Charge disorder and screening in graphene

Sayanti Samaddar

▶ **To cite this version:**

Sayanti Samaddar. Charge disorder and screening in graphene. Quantum Physics [quant-ph]. Université Grenoble Alpes, 2015. English. NNT : 2015GREAY065 . tel-01310259

HAL Id: tel-01310259
https://theses.hal.science/tel-01310259

Submitted on 2 May 2016

HAL is a multi-disciplinary open access archive for the deposit and dissemination of scientific research documents, whether they are published or not. The documents may come from teaching and research institutions in France or abroad, or from public or private research centers.

L'archive ouverte pluridisciplinaire **HAL**, est destinée au dépôt et à la diffusion de documents scientifiques de niveau recherche, publiés ou non, émanant des établissements d'enseignement et de recherche français ou étrangers, des laboratoires publics ou privés.

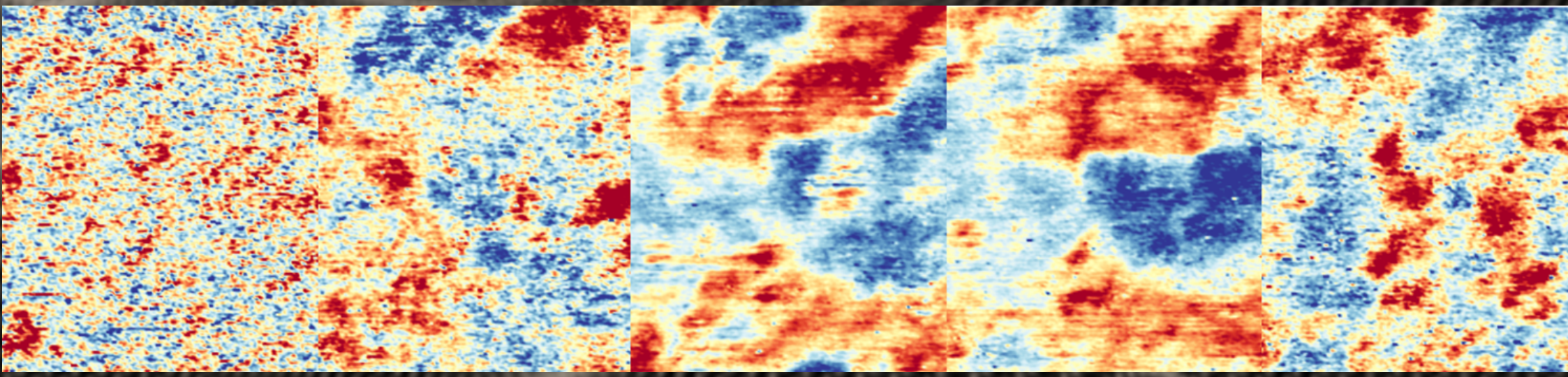

Charge Disorder and Screening in Graphene

Sayanti Samaddar

The charge carrier density of graphene on a dielectric substrate such as SiO_2 displays inhomogeneities, the so called charge puddles. Because of the linear dispersion relation in monolayer graphene, the puddles are predicted to grow near charge neutrality, a markedly distinct property from two-dimensional electron gases. By performing scanning tunneling microscopy/spectroscopy on a mesoscopic graphene device, we directly observe the puddles' growth, both in spatial extent and amplitude, as the Dirac point is approached. Self-consistent screening theory provides a unified description of both the macroscopic transport properties and the microscopically observed charge disorder.

Institut Néel
Université Grenoble Alpes

UNIVERSITÉ DE GRENOBLE

THÈSE

Pour obtenir le grade de

DOCTEUR DE L'UNIVERSITÉ DE GRENOBLE

Spécialité : **Physique/Nanophysique**

Arrêté ministériel : 7 août 2006

Présentée par

Sayanti Samaddar

Thèse dirigée par **Hervé Courtois**
et codirigée par **Clemens Winkelmann**

préparée au sein **Institut Néel**
et de **Ecole Doctorale de Physique**

Désordre de charge et écrantage dans le graphène

Thèse soutenue publiquement le **23 octobre 2015**,
devant le jury composé de :

Mr., Khaled Karrai
Directeur scientifique, Attocube systems, Président
Mr., Anjan Gupta
Associate Professeur, IIT Kanpur, Rapporteur
Mr., Thomas Ihn
Professeur, ETH Zurich, Rapporteur
Mr., Christian Loppacher
Professeur, Université de Aix-Marseille, Examinateur
Mr., Hervé Courtois
Professeur, U. Joseph Fourier/Institut Néel-CNRS, Directeur de thèse
Mr., Clemens Winkelmann
Maître de Conférences, Grenoble INP/Institut Néel-CNRS, Co-Directeur de thèse

The more I learn, the more I realize how much I don't know.

Albert Einstein (1879 – 1955)

Acknowledgment

It is often the case that the amount of knowledge that an individual acquires over the years is dense when one is young and gradually becomes sparse as one ages. Although I have no idea yet what my fate will be from here on, what I can most certainly ascertain is that in the last four years that I spent doing my PhD, I have matured as an individual to an extent that I never have in all the remaining years of my existence put together! I started as someone with very little research experience, someone who was mostly used to success. It was only during the course of my PhD that I got a taste of what real struggle meant. The innumerable hardships and failures encountered on the way, the lack of good results till the very end made things extremely difficult for me at times. Nevertheless, had it not been for these challenging times, I would have never figured out my full potential. This journey has left me exhausted but not without an overpowering sense of satisfaction and gratitude for those whose unending love and support as well as the faith they had in me were essential for getting me to this point. Hence, I would like to take this opportunity to sincerely thank these people whose contribution to this thesis and my life have been so much more than I could ever manage to sum up in a few words.

I have to start with my kind and loving supervisor whom I also consider to be my mentor and *guru*, Clemens Winkelmann. Right from filling up all my official documents (which were all in French!), arranging for my accommodation, accompanying me to various administrative offices to get me started...(the list goes on and on) to being an excellent guide..I need to thank him for everything and yet I know I can never thank him enough. I feel I am a slow learner, but I don't think he ever lost patience with me although I spent a lot of time anticipating an outburst! Instead, he showed incredible faith in my decisions and gave me full freedom to experiment. In fact, it has always been rather difficult for me to believe in myself...but it was this attitude of Clemens that has gone a long way to restore my trust in myself. Whenever I hit a dead end, I knew the way out was simply having a discussion with him. This gave me the much needed courage to sail through tough times. It was incredible how much he knew, the variety of activities he mastered and the number of languages he spoke. But what I found most amazing is how much he cared for each of his students and the extent to which he understood them..perhaps this is why he managed to get the best out of them. At the end of the day, I feel really fortunate and privileged to have him as my supervisor.

I also had the great fortune of having Hervé Courtois as the director of my thesis and my

official supervisor. I would like to sincerely thank him for accepting me as a PhD student in his group as well as for making me a part of the QNET (Quantum NanoElectronics Training) project which was a great learning experience in itself. The immense burden of administrative responsibilities bestowed on him as the director of the Nano department and later on the entire Institut Néel made it difficult for us to interact on a regular basis. Nevertheless, in our weekly group meetings, he always listened to our presentations with great attention and interest. I always found his suggestions extremely valuable that lent a fresh perspective to the problem at hand. I will never forget his help towards the end of my thesis. He made time to discuss my thesis chapters even during his holidays and was a major reason behind the success of my presentation at Defense.

During the course of my PhD, I had the privilege of interacting with several top level researchers both from Institut Néel as well as from other prestigious universities, research labs and industries from different parts of the world. Benjamin Sacépé, one of the most brilliant researchers I have ever met, was also part of our group. Though I always found myself rather intimidated by his strict nature, his guidance and brilliant ideas proved to be invaluable for this thesis; some of his advice even showed the way when nothing else worked. Johann Coraux, another renowned experimentalist from Institut Néel, was one of our strongest collaborators who provided us with samples of CVD grown graphene on iridium. Discussing with him has always been a pleasure as he never failed to infuse a fresh motivation and enthusiasm in us. I owe a lot to Benjamin Grévin of CEA (Grenoble) for explaining us the technique of Kelvin Probe Force Microscopy (KPFM). Not only did he perform some measurements for us in his sophisticated microscope but also inspired me to go ahead with the implementation of this technique in our combined AFM/STM setup. Since my initial project was to investigate superconducting proximity effect in superconductor-Graphene hybrid devices by STM, we had elaborate discussions with Claude Chapelier and Vincent Renard, also from CEA. Even though the project remained incomplete, I learnt a lot from these regular sessions. I was extremely lucky to have a chance encounter with the renowned theoretician Shaffique Adam of NUS, Singapore at the Graphene 2015 (Imagine Nano) conference in Bilbao, Spain. Our brief interaction there later on transformed into a strong collaboration which greatly benefitted us in interpreting my final results which form the main part of this thesis. I remain extremely grateful to him and his graduate student Indra Yudhistira for their support and help. Finally, I feel deeply honored for having the likes of Anjan Gupta, Prof. Thomas Ihn, Prof. Christian Loppacher and Khaled Karrai as the jury members for the evaluation of my thesis. This has turned out to be a rather long manuscript and I am indeed very thankful for their valuable time and sincere effort in correcting it. A very special thanks to Anjan Sir for coming to France all the way from India at my defence and recommending me to Hervé in the first place. Had it not been for him, I would have perhaps never known about Institut Néel.

As a young researcher in the QNET program, I was required to undertake *secondments*. In

this respect, I would like to sincerely thank Prof. Thomas Ihn and Khaled Karrai once again for hosting me in ETH Zutich and Attocube Systems (Munich) respectively for a period of one month each. It was an enriching experience that took my mind away from my own project for sometime and work in related topics in a new lab/industry under the guidance of a completely new set of researchers. I believe this whole experience had a strong influence in modifying my general outlook towards research. Thanks to Nikola Pascher, Fabrizio Nichele (ETH Zurich), Klaus Thurner and Pierre Braun (Attocube Systems, Munich) for giving me their valuable time and letting me participate in their projects, I really had a memorable time. Apart from the *secondments*, we had to attend the annual QNET meetings set at various prestigious labs spread over Europe, where we were required to present our work. I must admit, these meetings were truly a rare privilege and considerably improved our presentation skills. Each meeting was like a small conference that combined research and various training programs with good food, a taste of various cultures and most of all a chance to reunite with great friends. A very big thank you to all the QNET fellows: Angelo, Astghik, Marco, Priya, Robert, Anna, Timothé, Pauline, Nikola, Luca, Mano, Maria, Jonna and Jorge for making every single meeting something to look forward to and something to cherish forever.

I think no experimentalist can ever deny the selfless contribution and support of the lab technicians. In this respect, I would like to firstly thank our superb Nano-fab team comprising of the brilliant Thierry Crozes, the wise and caring Thierry Fournier, the skilled FIB expert Jean-Francois Motte (Jeff) and the extremely helpful trio: Bruno Fernandez, Gwénaëlle Julie, and Sébastien Dufresnes. The FIB-etched tungsten/Pt-Ir wire tips that have been extensively used in this work have been possible only because of the excellent craftsmanship of Jeff. Secondly, I owe my sincere gratitude towards the technicians of the mechanical workshop in the K building, especially Julien Jarreau and Laurent Del-Rey. Whenever in need of help, they never turned me down. They always did their best to help me out in the shortest time possible in spite of my poor communication skills in French. Finally, I remain indebted to the secretaries of the Nano department, in particular Véronique Fauvel, Sabine Gadal and Florence Pois. They were really like my administrative guardians and it is because of them that I managed to sail through the hurdle of complicated paper work typical of French administration.

The whole PhD adventure is incomplete and in fact impossible without friends. In this respect, I was enormously lucky to have met some of the finest people I know during the course of my PhD and have them as friends. Thanks to Aurélien (Fay) for being my first unofficial supervisor! Being the novice that I was, he was the one who took me by the hand and introduced me to the world of nano-fabrication. Sylvain (Martin): thanks a lot for transferring me your precious knowledge and expertise on Scanning Probe Microscopy with such dedication and all your help. I will never forget your generous hospitality when you invited me to celebrate Christmas with your family in my first year in Grenoble. Thanks to Amina for providing me with some great samples of CVD grown graphene on iridium. Thanks to David for teaching

me so much, for inspiring me to work harder and harder, to never give up and most of all for being there always. Thanks to Juliette for teaching me to accept things for what they are and making the best of situations. Thanks to Bruno (Kung) for giving me so many useful advice and suggestions and especially helping me in choosing the right silver epoxy for my AFM/STM probe. Thanks to Alessandro for all those niobium depositions, for all those useful discussions during the late evenings and weekends in office as well as for all your help. Johanna and Katrin: I really have no words to thank you.. from showing me the right way to exfoliate graphene (Katrin), placing manual contacts on graphene devices (Johanna) (even at crazy hours!) to treating me to some amazing food, organizing parties, shopping, sports like climbing/running/swimming and mentally supporting me through all my difficulties..the list goes on. You guys have really been the best friends one could ever wish for. Also, my sincere and hear-felt gratitude to Kevin, Vitto, Dipankar, Bivas, Aurélien (Nabet), Farida, Cornelia, Yani, Anna, Arunima, Ben and so many others who have helped me in innumerable ways during my PhD and have made this whole journey truly memorable.

In the very end, I would like to thank my parents and my dear twin, Srimoyee, without whose unending love and support, none of this would have been possible. Whatever I am today, whatever little I have achieved, I owe it to them. And one more person, whose constant presence in my life and selfless love has given me the strength to face all challenges head on...my loving husband, Gorky. My dearest, I dedicate this thesis to you.

Sayanti Samaddar

December, 2015

Abstract

Graphene presents a two-dimensional system whose charge carriers are subjected to a disordered potential created by random charge impurities trapped in the substrate. This impurity potential induces an inhomogeneous carrier concentration. On the other hand, the ability of single-layered graphene to screen this potential strongly depends on the charge carrier density. Thus the effect of the resulting charge disorder can be tuned with the backgate which manifests also in the transport properties of the device. By combining Scanning tunneling microscopy and spectroscopy with in-situ transport at dilution temperature, we probe a system of single-layered graphene on SiO_2. Local density of states maps on graphene, acquired at various carrier concentrations show gradual increase of spatial extent and amplitude of inhomogeneities as the Dirac point is approached. While the variations of the spatial extent of the fluctuations with back-gate show very good agreement with predictions, the observed amplitude of inhomogeneities show a larger than expected increase at low densities. We explain this as a result of the local gating effect exerted by the tip on graphene which amplifies any change in the intrinsic doping at low carrier concentrations. This is the first experiment bridging the gap between microscopic disorder and macroscopic transport properties of a graphene device.

Résumé

Le graphène héberge un gaz d'électrons bi-dimensionnel, sujet à un potentiel électrostatique désordonné dû aux impuretés de charge dans le substrat. Ce potentiel désordonné induit des inhomogénéités de la densité de porteurs de charge dans le graphène. Par ailleurs, l'écrantage dans le graphène mono-feuillet de ce potentiel dépend lui-même de la densité de porteurs de charge. L'effet du désordre de charge peut donc être modulé avec un potentiel de grille global, ce qui se manifeste en particulier dans la transconductance de dispositifs à base de graphène. Nous combinons des mesures par Microscopie/Spectroscopie à effet tunnel avec des mesures de transport in situ sur des dispositifs à base de mono-feuillets de graphène sur SiO_2, à basse température. Les cartes de la densité locale d'états du graphène, à diverses tensions de grille, mettent en évidence l'augmentation progressive des dimensions latérales ainsi que de l'amplitude des inhomogénéités au voisinage du point de Dirac. Alors que la dépendance en grille de la taille des inhomogénéités est en bon accord avec les prédictions, leur amplitude est plus forte qu'attendue au point de Dirac. Nous expliquons ce désaccord en prenant en compte l'effet de grille local produit par la pointe elle-même, qui a pour effet d'amplifier expérimentalement toute variation de la densité de porteurs de charge lorsque celle-ci elle faible. Cette expérience est ainsi la première mesure qui relie quantitativement les propriétés de désordre de charge à l'échelle microscopique aux propriétés de transport macroscopiques d'un dispositif à base de graphène.

Contents

Introduction 1

1 Resist Free Device Nanofabrication 7

1.1 Why avoid resist ? . . . 7

1.1.1 Nanostructures with Niobium for Scanning Probe . . . 8

1.1.2 Scanning probe compatible Graphene devices . . . 9

1.2 The Bilayer Metal Mask . . . 10

1.2.1 Fabrication . . . 11

1.2.2 Long Nb lines . . . 13

1.2.3 Nb-Au-Nb Proximity SQUIDs . . . 16

1.2.4 Furthur Developments . . . 18

1.3 The Mechanical Shadow Mask . . . 19

1.3.1 Substrate Preparation and Graphene Exfoliation . . . 19

1.3.2 Optical Detection & Raman Spectroscopy . . . 21

1.3.3 Surface Characterization by Atomic Force Microscopy . . . 22

1.3.4 Fabrication . . . 23

1.3.5 Contact materials and related challenges . . . 26

1.4 Conclusion . . . 27

2 Theory of Disorder and Screening in Graphene 29

2.1 Introduction . . . 29

2.2 Electronic Properties . . . 31

2.2.1 Lattice structure of single-layered graphene . . . 31

2.2.2 Energy Dispersion . . . 32

2.2.3 The Dirac Formalism . . . 34

2.2.4 Bilayer Graphene . . . 35

2.2.5 Electronic Density of States . . . 36

2.3 Many body effects in Graphene: Screening . . . 37

2.3.1 General introduction to Screening in a 3D electron gas . . . 38

2.3.2 Screening in Graphene . . . 42

2.4 From local Disorder to Macroscopic Carrier Transport in Graphene . . . 45

2.4.1 Charge Carrier Transport in Graphene . . . 46
2.4.2 Charge disorder and local correlations . . . 49
2.5 Conclusion . . . 59

3 The Cryogenic Scanning Probe Microscope 61
3.1 Introduction . . . 62
3.2 Elements of Scanning Probe Microscopy . . . 62
3.2.1 Scanning Tunneling Microscopy & Spectroscopy . . . 62
3.2.2 Atomic Force Microscopy . . . 67
3.2.3 Kelvin Probe Force Microscopy . . . 75
3.3 Experimental Setup . . . 78
3.3.1 The SPM Head . . . 78
3.3.2 The Inverted Dilution Fridge : Sionludi . . . 84
3.3.3 Magnetic Field . . . 90
3.3.4 Electronics . . . 90
3.4 The Needle Sensor . . . 97
3.4.1 Tips . . . 98
3.4.2 Implementation . . . 101
3.4.3 Temperature dependence of the Properties of the NS . . . 104
3.5 Applications of combining AFM with STM . . . 107
3.5.1 Experimental Determination of Sensitivity of NS . . . 108
3.5.2 Localizing a single nano-device on a chip . . . 110
3.6 Summary . . . 111

4 Charge Disorder in decoupled Graphene on a Metallic Substrate 113
4.1 Introduction . . . 114
4.1.1 Graphene on a Metallic Substrate . . . 114
4.1.2 Decoupling Graphene . . . 116
4.1.3 Graphene on Ir(111) . . . 118
4.2 Decoupled Graphene on Ir(111) . . . 120
4.2.1 Sample Preparation . . . 121
4.2.2 Large scale surface features . . . 122
4.2.3 Regions devoid of Graphene : Oxidised Ir . . . 123
4.2.4 Graphene Wrinkles . . . 125
4.3 Dynamics of Decoupling of Graphene . . . 131
4.3.1 Wrinkles as pathways for intercalation . . . 131
4.3.2 Electronic Properties of well-coupled vs decoupled graphene . . . 133
4.3.3 Conclusion . . . 134
4.4 Charge disorder in decoupled graphene . . . 134

4.4.1 STM/STS investigation of charge disorder . . . 135
4.4.2 Charge disorder by KPFM . . . 137
4.4.3 Origin of Disorder . . . 139
4.5 Conclusion . . . 140

5 Disorder and Screening in Graphene Devices 141
5.1 Introduction . . . 141
5.2 Charge Carrier Transport in Graphene . . . 142
5.2.1 Sample Description and Experimental Method . . . 143
5.2.2 Electric Field Effect . . . 145
5.2.3 RPA-Boltzmann Conductivity . . . 149
5.3 Local Field Effect with Scanning probe microscopy . . . 149
5.3.1 Experimental Method . . . 150
5.3.2 Contact Potential Difference with KPFM . . . 151
5.3.3 Tunneling Spectroscopy on graphene . . . 156
5.3.4 Local gating with the tip . . . 157
5.3.5 Tunneling Spectroscopy at different carrier density: The Experiment . . . 164
5.4 Electron-Hole Puddles in Graphene . . . 169
5.4.1 Imaging Electron-Hole Puddles . . . 170
5.4.2 Charge Disorder with Point to Point Tunneling Spectroscopy . . . 172
5.4.3 Gradual evolution of Charge disorder with Carrier Concentration . . . 179
5.4.4 Correlations at Different carrier densities . . . 186
5.5 Conclusion . . . 193

Conclusion 195

References 211

Introduction

GRAPHENE today defines a field in itself. The breakthrough achieved by Andre Geim and Konstantin Novoselov in 2004 [1] to isolate a single, atomically thin layer of graphene from stacks of graphite, had triggered an avalanche of scientific activity which today has reached a phenomenal magnitude unique in the history of science. It has been more than a decade since then but the field continues to evolve with scale of research growing with every passing year. The reason behind all this attention is simply because graphene is truly exceptional. Everything about graphene: its thickness, extreme toughness, high flexibility, superior thermal conductivity, extremely high mobility...is fascinating. What is especially interesting is its honeycomb lattice structure that gives rise to a linear dispersion, thus rendering a Dirac-like, relativistic nature to its charge carriers. This allows the study of quantum relativistic electrodynamics (QED) in table top experiments which has stimulated many important fundamental research such as the study of half integer Quantum Hall effect [2] and Klein tunneling [3], to name a few.

However, there is more to *real* graphene than this theoretical idealization of a single sheet of carbon, having a carrier density that is perfectly controlled by a backgate. Graphene sheets that are used to fabricate devices are usually placed on insulating substrates such as SiO_2/Si which contains random charge impurities trapped inside or on the surface. Hence under any practical situation, charge carriers in graphene are subjected to a disordered impurity potential. The response of the charge carriers in graphene to this potential depends on its screening properties. The impurity potential induces an inhomogeneous carrier concentration in graphene which in turn has the effect of screening out this potential in a completely self-consistent manner. At high carrier densities, screening is strong and the impurity potential is efficiently screened. But at low carrier concentrations, due to the weak screening response, the underlying disorder breaks up the system into electron-hole puddles. It is, therefore, the interplay of this disorder and screening that eventually determines the carrier dynamics in the end device. Transport theories based on this model of random charge impurities [**?**] were successful in solving the initial puzzle surrounding the absence of a universal minimum conductivity as had been predicted theoretically [4, 5].

Scanning tunneling microscopy and spectroscopy (STM/STS) offers, by far, the most sophisticated local probe technique to investigate such electronic inhomogeneities with atomic scale precision. STM/STS investigations on exfoliated graphene on SiO_2 have already shown the ex-

istence of the predicted doping inhomogeneities [6]. Such inhomogeneities showed no correlation with the topography, thus validating the concept of random charge impurities in the substrate as the probable origin of such a disorder. Further, these impurity induced inhomogeneities were shown to act as scattering centers that generated quasiparticle interferences (QPIs) which could be modulated by the voltage bias applied to the sample as well as the backgate. However, the important questions that remained unanswered were how the backgate would influence the induced inhomogeneities themselves, which are expected to change both in amplitude and lateral extent given the carrier dependent screening in graphene, and to what degree the local properties of the graphene device quantitatively match the macroscopic transport properties.

In this thesis, I have combined Scanning probe microscopy with in-situ transport to perform a complete investigation of the field effect in exfoliated, single-layered graphene on SiO_2/Si substrate at dilution temperatures. Charge carrier conductivity measured in transport gives the macroscopic properties of the device as well as allows us to quantitatively predict the amplitude and lateral scale of inhomogeneities using the theoretical model of scattering from random charge impurities. Whether these predictions are correct or not is verified by directly measuring the local density of states (LDOS) at different backgate, using STS. The metallic tip is found to play a surprisingly major role in influencing the measurements. Apart from graphene on an insulating substrate, charge disorder has also been investigated on graphene on a metallic substrate (iridium).

In the following sections, a brief outline of the different chapters have been presented.

1. Resist Free Device Nanofabrication

In this chapter, two different resist-free fabrication processes have been presented, specifically designed for creating nano-structures with thermally evaporated niobium that also ensure scanning probe compatibility. The reason for choosing niobium is that one of the initially planned targets was to investigate the superconducting proximity effect in graphene. Niobium formed the best choice for the superconducting material of the contacts because of its high superconducting transition temperature. The two different processes are shown in Figure 1. The first process involves a bilayer metal mask (Figure (a)) that substitute the role played by the organic resist in conventional lithography. To test the performance of this technique, we implemented it in the fabrication of long, thin Nb lines and Nb-Au-Nb DC proximity SQUIDs (Figure (b)). This process was published in [7] and is still intensively used in the group. The second method involves the mechanical masking of an exfoliated graphene flake with a $4\,\mu$m tungsten wire, as shown in (c). This process has been extensively used in this work, for placing two isolated electrical contacts on graphene.

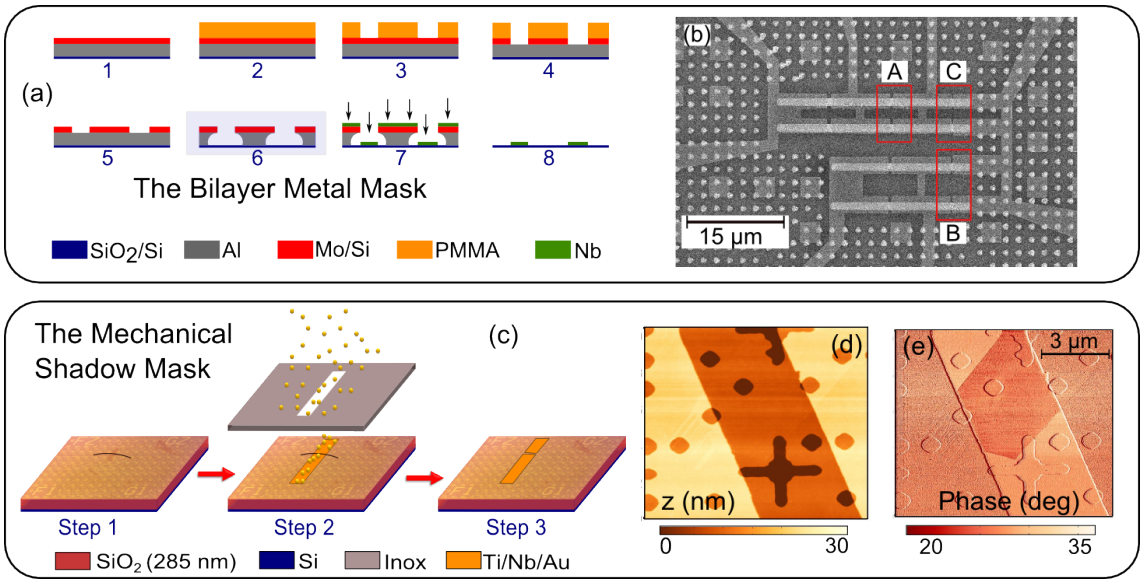

Figure 1: Resist free device nanofabrication. (a) Steps for device fabrication with thermally evaporated niobium using Bilayer metal mask technique. (b) Nb-Au-Nb SQUIDS fabricated with technique in (a). (c) Steps for contacting exfoliated graphene with two isolated electrical contacts using the mechanical shadow mask technique. (d) AFM topography and (e) Phase map of contacted graphene.

2. Theory of Disorder and Screening in Graphene

In this chapter, we discuss the theory required for understanding how the amplitude and lateral scale of doping inhomogeneities, induced in graphene by the disordered impurity potential, evolve as a function of the average carrier concentration controlled by the backgate. The carrier dynamics in graphene, determined by the interplay of disorder and screening, are discussed at high, intermediate and low carrier density regimes. This allows us to relate the local correlation functions of the screened disorder potential with parameters that are readily obtained from transport measurements.

3. The Cryogenic Scanning Probe Microscope

In this chapter, we introduce our experimental setup which is a Scanning probe microscope capable of operating down to dilution temperatures at magnetic fields upto 2 T. We first discuss the different microscopic techniques that can be implemented in this setup and has been thoroughly used throughout the course of this thesis. This is followed by the description of the key components of the setup i.e. the microscope itself, associated electronics and the inverted dilution fridge or *Sionludi* on which the microscope is installed. The scanning probe is introduced next with detailed description of its working principle, the way it is implemented in our setup and the change in its properties while cooling down from room to base temperature. Finally, we demonstrate important instances where the option to combine different microscopic techniques in our setup clearly proves to be a strong advantage.

4. Decoupled Graphene on a Metallic Substrate

In this chapter, we investigate the local properties of a system of graphene on iridium [GR/Ir(111)], prepared ex-situ by chemical vapour deposition (CVD). At first, the important topographic features on the GR/Ir(111) surface are introduced: i.e. the graphene itself, the regions devoid of graphene and the graphene wrinkles. Each of these features are characterized in detail by scanning probe microscopy. Next, we study a freshly prepared sample that has faced exposure to ambient conditions for a very small duration of time. This helps us to particularly understand the dynamics of the intercalation processes at work when exposed to ambient conditions and elucidates the role of the wrinkles, in particular, as pathways for such intercalation (Figure 2(a),(b)) [8]. Finally, we investigate the state of charge disorder in graphene that has been completely decoupled from the substrate due to sufficient exposure to ambient conditions. We find a strong correlation of this disorder with the topographic corrugations in STM (Figure 2(b)) which we relate to the presence of the intercalated molecular species between graphene and the metal substrate [9].

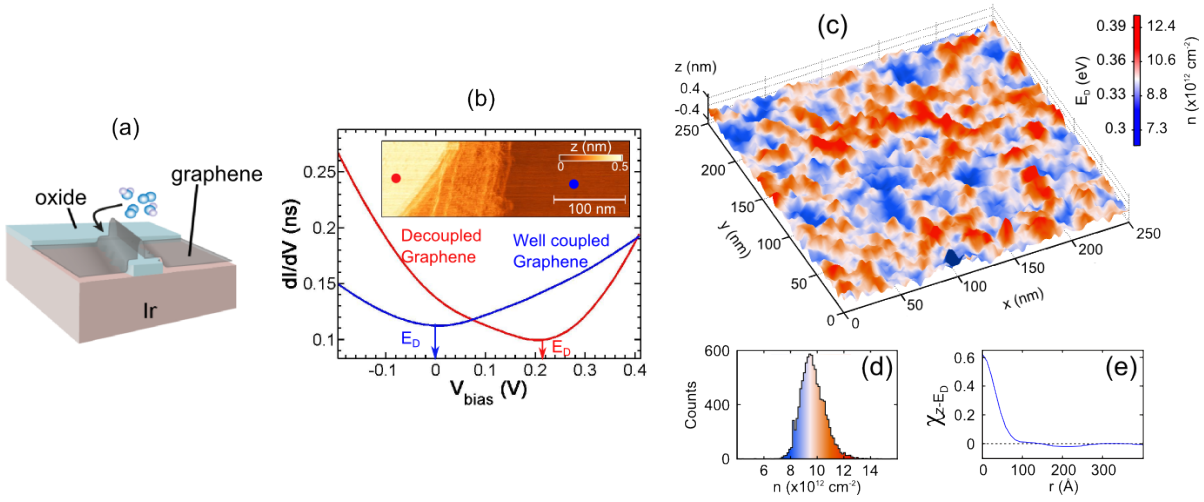

Figure 2: Charge disorder in decoupled graphene on iridium (111) substrate. (a) Schematic demonstrating the role of graphene wrinkles as pathways of oxygen intercalation [8]. (b) Differential tunneling conductance spectrum over well coupled and decoupled graphene. Inset presents the STM topograph showing the boundary between well coupled and decoupled graphene. (c) Dirac point map $E_D(\mathbf{r})$ superposed over simultaneously acquired STM topography $z(\mathbf{r})$. (d) Histogram of the doping fluctuations corresponding to the E_D map in (d). (e) Angular averaged, normalized cross-correlation between $z(\mathbf{r})$ and $E_D(\mathbf{r})$.

5. Disorder and Screening in Graphene Devices

In this chapter, we present a detailed investigation of the field effect in a single-layered graphene device by combining in-situ transport with scanning probe microscopy at dilution temperatures.

The chapter has been broadly divided into three sections. In the first section, the transport measurements have been presented and analyzed using the theoretical understanding gained in Chapter 2. The next section deals with the investigation of the field effect locally using two different techniques: Kelvin probe force microscopy (KPFM) and STS. The role of the metallic tip as a local gate has been discussed in detail to interpret the differential tunneling conductance spectrum in graphene and its response to the backgate (Figure 3(c)).

Finally, in the last section, we image the doping inhomogeneities in graphene by performing both point to point tunneling spectroscopy as well as mapping the tunneling conductance G_t at optimally chosen bias voltages. By performing this measurement at different backgate voltages, we track the evolution of this disordered landscape with the average carrier concentration induced by the backgate. This is followed by a detailed analysis of the $G_t(x, y)$ maps to extract the local correlations at different backgate voltages. This allows us to directly compare the experimentally measured correlations to what is predicted from the average properties extracted from transport. Here, once again, the role of the metallic tip as a local gate is invoked for a better understanding of the measurements.

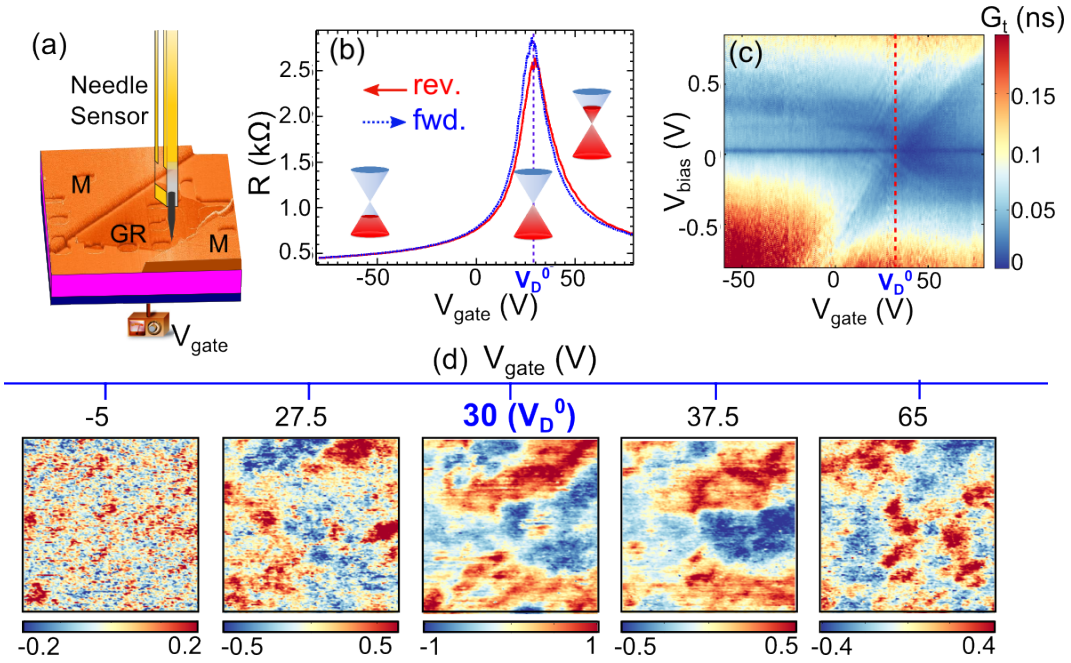

Figure 3: From macroscopic transport to charge disorder in graphene devices at various carrier concentrations. (a) Exfoliated graphene (GR) contacted with two isolated metal (M) contacts with a Needle sensor positioned on top: arrangement compatible for both transport and scanning probe microscopy. (b) Two-probe resistance as a function of V_{gate}. $V_D^0 = 30\,\mathrm{V}$ gives the charge neutrality point. (c) Differential tunneling conductance G_t as a function of V_{bias} and V_{gate}. (d) DOS maps at different V_{gate} over an area of $100 \times 100\,\mathrm{nm}^2$.

Chapter 1

Resist Free Device Nanofabrication

Contents

1.1 Why avoid resist ? **6**
1.1.1 Nanostructures with Niobium for Scanning Probe 7
1.1.2 Scanning probe compatible Graphene devices 8
1.2 The Bilayer Metal Mask **9**
1.2.1 Fabrication 10
1.2.2 Long Nb lines 12
1.2.3 Nb-Au-Nb Proximity SQUIDs 15
1.2.4 Furthur Developments 17
1.3 The Mechanical Shadow Mask **18**
1.3.1 Substrate Preparation and Graphene Exfoliation 18
1.3.2 Optical Detection & Raman Spectroscopy 20
1.3.3 Surface Characterization by Atomic Force Microscopy 21
1.3.4 Fabrication 22
1.3.5 Contact materials and related challenges 25
1.4 Conclusion **26**

1.1 Why avoid resist ?

Most of the nanofabrication done today involve the use of organic resists. Combined with the superior technology of a lithography system currently available, they allow one to pattern nanostructures with resolution as high as 5 nm and incredible precision. But not all nanofabrication is possible by following this standard route. As we will see below, for certain applications and for handling certain specific but extremely important materials, it becomes essential to take a detour.

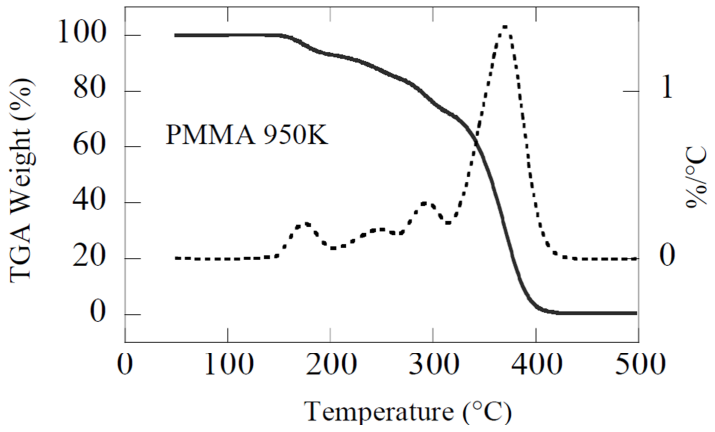

Figure 1.1: Thermogravity Analysis (TGA) results for PMMA polymer with a molecular weight $MW = 950.000\,\mathrm{g/mole}$. The full line indicates the weight loss vs. temperature in percent. The dashed line represents the derivative of the TGA curve and indicates degassing of volatile species which are particularly abundant in PMMA [10].

1.1.1 Nanostructures with Niobium for Scanning Probe

A strong motivation for this thesis has been to study superconducting proximity effect in Superconductor (S)- Normal(N)- Superconductor(S) junctions with the help of Scanning probe microscopy. As a choice for the superconducting material, niobium topped the list primarily because it offered the highest T_c ($\sim 9.2\,\mathrm{K}$ for bulk Nb) among elemental superconductors. This would imply a superconducting gap of about $1.3\,\mathrm{meV}$ ($\Delta(T = 0\,\mathrm{K}) = 1.764\,k_B T_c$) which in turn leads to a higher proximity-induced gap on the normal part thus increasing the chances of it falling well above the energy resolution of the scanning probe microscope. Also Nb is rather immune to the problem of aging making it a more suitable candidate over other higher T_c superconductors like lead or vanadium.

However, preparing nanostructures with niobium is not so straightforward. Niobium is a refractory metal with melting point of 2469°C. Therefore during electron beam deposition of niobium, extremely high temperatures are reached causing direct heating of the sample by radiation. The sample temperature can easily exceed 235°C which is the transition temperature for the frequently used e-beam resist PMMA as is shown in Figure 1.1 [10]. This can not only damage the resist but cause the resist mask to become unstable and collapse. Outgassing of the resist will lead to contamination of the niobium as well. It is well known that the T_c of niobium is extremely susceptible to contamination [11][12]. Only in the special condition that the niobium target is more than 40 cm away from the sample in the deposition chamber [13], can such a situation be avoided but this is often very difficult to realize in most setups. One way out of this problem could be to use a different technique of metal deposition like sputtering as it does not involve heating of the metal. This is a popular choice for most cases as it succeeds in producing high quality niobium films with its T_c preserved.

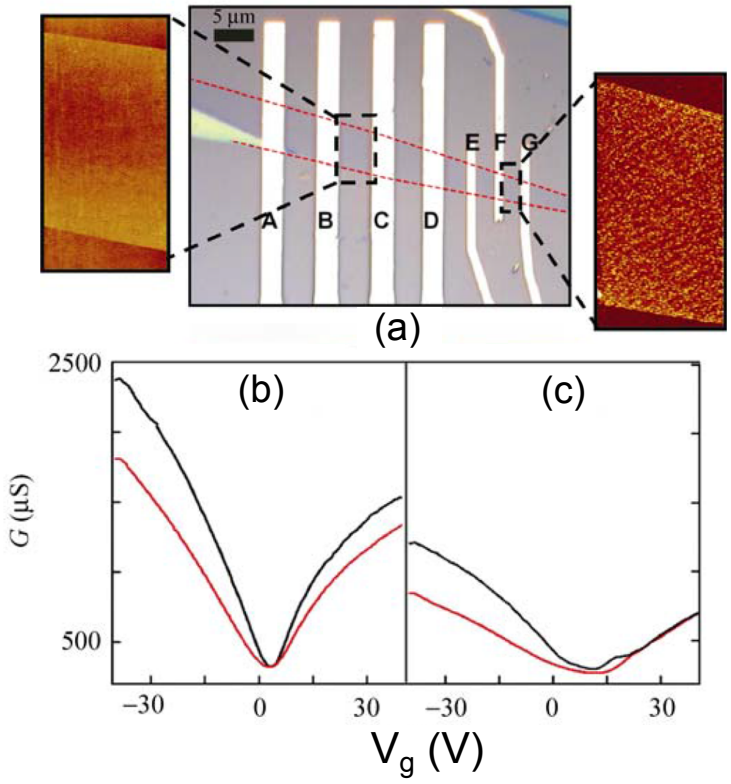

Figure 1.2: PMMA resist residues on graphene. Optical image of a single-layer graphene sheet device.The electrodes A, B, C, and D were deposited by evaporation through a shadow mask, and E, F, and G were fabricated using standard electron beam lithography. Plots of two-terminal conductance (G) vs back gate voltage (V_g) for the electrode pairs (b) B, C and (c) F, G at room temperature (red) and 4.2 K (black) [14].

But this was still not sufficient for our purpose. Sputtering is known to produce highly diffused edges at the interface. For the purpose of local investigation of the proximity effect, it is crucial to have a well defined interface with the bulk superconducting gap persisting up to the very edge and no diffusion of superconducting atoms in the normal part. E-beam deposition clearly scores in this respect over sputtering. Hence, keeping all these requirements in mind, the need of the hour was to come up with a fabrication technique that would avoid any organic resist at the stage of e-beam deposition of niobium.

1.1.2 Scanning probe compatible Graphene devices

In a widely studied two-dimensional system like graphene, where the surface constitutes the bulk, cleanliness of the surface is a serious issue to address during fabrication. Contamination of the graphene can fundamentally alter the properties of the end device limiting its mobility and hence leading to inferior device quality.

One important limitation associated with the use of organic resist is the difficulty in achieving a perfect lift-off. This is especially true in the case of graphene where the e-beam resist PMMA

shows a strong affinity towards the carbon molecules leading to surface contamination. This is nicely demonstrated in Figure 1.2 by Bao et al. [14]. The contamination of the surface by PMMA residues is clearly visible in the AFM image on the right inset as opposed to the image on the left inset of the same graphene flake that has not been exposed to PMMA. The state of cleanliness of the surface has a significant impact on the transport properties of the graphene as is evident from plots (b) and (c) of Figure 1.2 which shows a higher mobility and less intrinsic doping on the *clean* graphene compared to the *dirty* case .

This limitation is indeed an invincible obstacle for a surface scientist interested in probing the local properties of such a system. A clean sample surface is a very important pre-requisite in scanning probe microscopy. Insulating resist residues on the graphene surface can give rise to unstable scanning conditions in scanning tunneling microscopy for example, leading to a *tip-crash* or in other words damage of the probe. Ineviatably, this will lead to erroneous, irreproducible and incomprehensible results.

Cleaning the surface of residual resist debris after contacting the graphene is therefore of paramount importance. However, this continues to be a constant struggle for experimentalists working with graphene. Several techniques have been deviced for cleaning like annealing in a controlled environment, rinsing in organic reagents like acetic acid, chloroform, etc, using the AFM tip in contact mode to sweep away the contaminants. But none of the methods are really full proof and moreover they can give rise to additional complications.

In this case the best strategy is therefore to avoid any resist in the first place, if possible.

1.2 The Bilayer Metal Mask

To tackle the problem stated in section 1.1.1, there are several ways one might consider. A list of the different techniques adopted by different groups over the years is briefly outlined below.

1. Sputtering a thin film of niobium first and then patterning it by dry reactive ion etching as demonstrated in [15] for the fabrication of long DC proximity SQUIDs. However this process is rather customized for a given system and is incompatible for connecting niobium to fragile materials such as graphene, carbon nanotubes or thin sheets of topological insulators.

2. Replacing the conventional resist mask by a bilayer structure that remains thermally stable, undamaged and does not outgass at the high temperatures created in the evaporation chamber during niobium deposition. Dubos et al. [10] had used a bilayer consisting of a thermostable polymer (Poly Phenylene Ether Sulfone or PES) of high thermal and chemical stability as the base layer and silicon as the upper layer to fabricate Nb-Cu-Nb Josephson junctions.The use of these particular resists is nevertheless cumbersome; for instance, the ambient hygrometry has to be controlled during resist spinning.

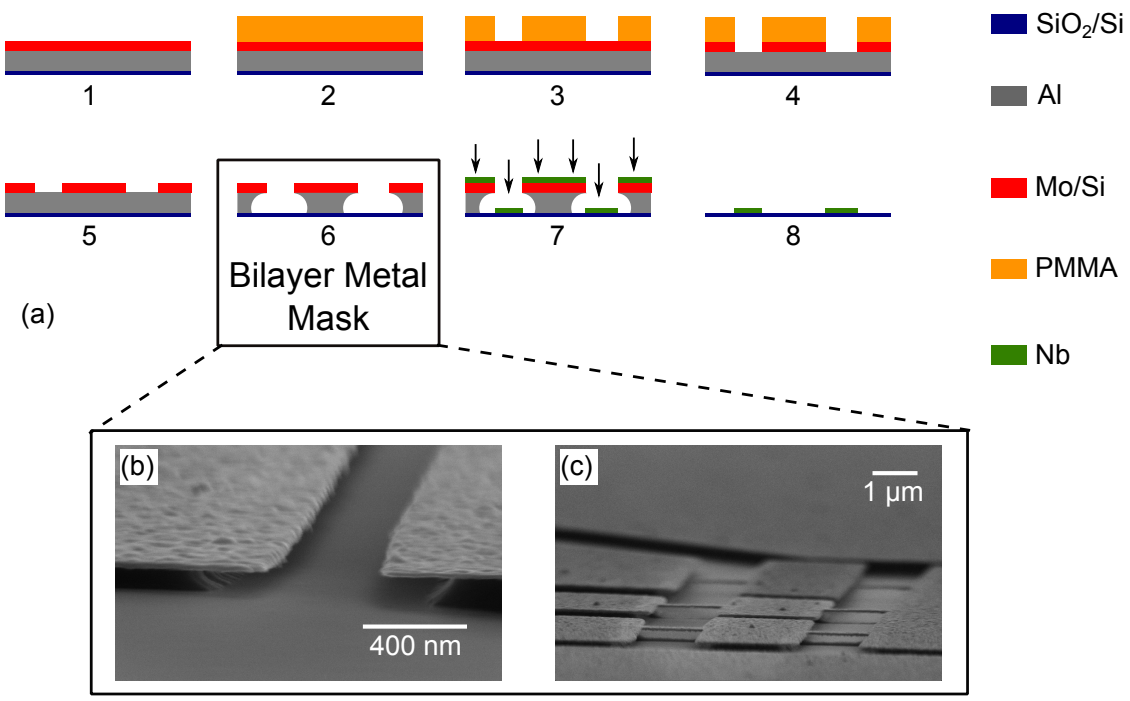

Figure 1.3: The Bilayer metal mask. (a) Steps for the fabrication of nanostructures with Niobium using bilayer metal mask. (b) SEM image of Al/Si (200 nm/30 nm) mask showing the well-defined undercuts in the Al sublayer. (c) Al/Si (200 nm/30 nm) mask showing Si bridges suspended over 2.2 μm with the Al underneath completely etched.

3. Non-organic evaporation stencil masks based on a suspended bilayer of Si_3N_4 and SiO_2 have been developed by Hoss et al. [16][17]. But in this case it is impossible to lift-off the mask after fabrication and hence is unsuitable for our purpose.

4. Using a metallic bilayer mask. As early as 1978, R. E. Howard [18], had experimented with a Nb stencil mask with a Copper sublayer whereas in [19] a lithography process based on an aluminium (Al)/chromium (Cr) bilayer was implemented to make arrays of micron sized Josephson junctions with Nb as the superconductor .

We choose the last route of using a completely metallic bilayer mask. In the following sections we demonstrate our own technique of fabricating nanostructures with high quality niobium films using a bilayer mask of molybdenum (Mo)/aluminium (Al).

1.2.1 Fabrication

As explained before, the main objective for choosing this direction of fabrication was to ensure a thermally stable mask at the time of niobium deposition that would not outgass and could easily withstand high temperatures ($> 500\,^{\circ}$C) produced inside the chamber during e-beam deposition of niobium. To facilitate an easy lift-off in the last stage with minimum damage to the edges of

the deposited nanostructures, a bilayered structure with an overhanging top layer with respect to the bottom layer is preferred. Figure 1.3(a) outlines the main fabrication steps while (b) and (c) shows two examples of the bilayer metal mask.

Since the top layer of the metallic mask is required to acquire the pattern from the PMMA mask above, metals like Mo, Si, Nb which are dry-etched by SF_6 in an anisotropic manner are suitable candidates. Anisotropic nature of the etch is important to ensure that the metal is etched much faster longitudinally than laterally which is important to preserve the dimensions of the designed structures. The prime requirement of the etchant is that it should have a significantly larger etch rate for the top metal than the PMMA for a successful pattern transfer. As for the choice of the bottom layer, we would need a metal that is easily soluble in one of the solvents available and accessible in the clean rooms. The chosen solvent must act on this layer isotropically to give rise to undercuts as desired.

For the top layer, we experimented with Mo and Si. Both satisfied the requirement of forming a thermally stable, robust and easily patterned upper layer. However, with Si, a problem was encountered in the final lift-off stage. During lift-off, once the Si overlayer collapsed on the SiO_2 substrate underneath, it was impossible to remove it even by strong ultrasonication. Aluminium was our choice for the bottom layer since Al nanostructures are isotropically etched by the readily available basic solutions of MF-26A or MF-319 (2.35 % solutions of tetramethyl ammonium hydroxide in water, pH $\approx$ 13) to create well controlled undercuts. Once again these solvents preferentially act on the exposed Al regions leaving the regions protected by the Mo intact.

Here it should be noted that this basic developer is unable to completely remove thin films of Al spread over continuous, large areas but if this same area is fragmented with numerous hole like structures, it becomes possible to achieve a clean removal. Including regularly spaced holes in the initial lithographic pattern, as shown in Figure 1.4, clearly helped in lifting off the Al/Mo(200 nm/40 nm) bilayer mask in just 45 minutes without which it was impossible. The reaction mechanism for dissolution of Al seems to be increased when the surrounding structures force the solution to act on tiny areas rather than a bulk surface. This was found to make the etch rate somewhat sample design dependent. Hence the etch duration needs to be optimized each time a new design is tried out. A good starting point is about 90 s for 200 nm thick Al. Having a good control over the Al etch is crucial as an under-etch would not be favourable for the final niobium structure during lift-off whereas an over-etch would produce huge undercuts that would lead to the collapse of the upper Mo layer.

The different steps involved in this process have been summarized below. This is accompanied by optical images in Figure 1.4 showing the different steps using an Al/Si mask although eventually Mo was preferred due to reasons stated above. The parameters stated are taken after a successful fabrication process but might require minor changes for adapting the process to different systems as was discussed above.

1. Bilayer preparation by depositing 200 nm Al as the bottom layer and 40 nm of Mo as the

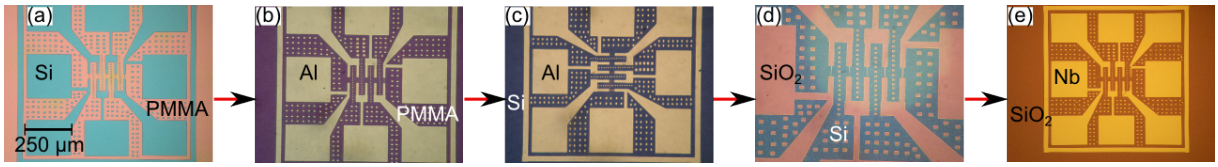

Figure 1.4: Optical Microscope images showing the different steps for Bilayer metal mask fabrication with the example of an Al/Si mask. (a) After development in MIBK/IPA (1:3) (b) after dry etch of Si (30 nm) top layer (c) after resist removal in acetone (d) after wet etch of Al (200 nm) (e) after metal deposition and lift-off.

top layer.

2. Spin-coating of organic resist PMMA 4 % (PolyMethyl-MethAcrylate) at 3000 rpm, 3000 rpm/s for 30 s. This ensured a resist thickness of ~ 350 nm. This is followed by baking at 180 °C for 5 minutes.

3. Patterning the resist by electron-beam lithography. This is followed by development in MIBK/IPA (1:3) for 35 s, rinsing in IPA for 5 s and finallly finishing off in another fresh bath of IPA for 90 s 1.4(a).

4. Pattern in the resist is transferred to the Mo layer by dry reactive ion etching with a 20 W SF_6 plasma for 2 minutes. This plasma preferentially attacks the exposed Mo 1.4(b).

5. Removal of the resist by immersing the sample in a bath of acetone for 45 minutes. It was found best to avoid ultrasonication to preserve fragile structures. This was followed by 5 minutes in 50 W O_2 plasma 1.4(c).

6. Removal of Al from the exposed parts by wet etching in a basic solution of MF-26A for about 90 s 1.4(d). The exposed substrate was then cleaned with 5 minutes of 50 W oxygen plasma before metal deposition. This gets rid of any organic contaminants on the substrate.

7. Metal (Niobium and/or other metals) deposition in an ultra high vacuum ($P \sim 10^{-10}$ torr).

8. Removal of the Al/Mo mask by wet etch in once again a basic solution of MF-319 for about 45 minutes 1.4(e).

1.2.2 Long Nb lines

As a first test, we have prepared narrow lines of niobium using the technique described above. In these samples, a 10 nm Ti layer was deposited *in situ* prior to deposition of 26 nm Nb, to improve adhesion and mimic the frequently used approach to contact a superconductor to novel low-dimensional materials. The presence of Ti however contributes to reducing the T_c of the wires due to inverse proximity effect. Atomic force microscopy (AFM) inspection of the Nb

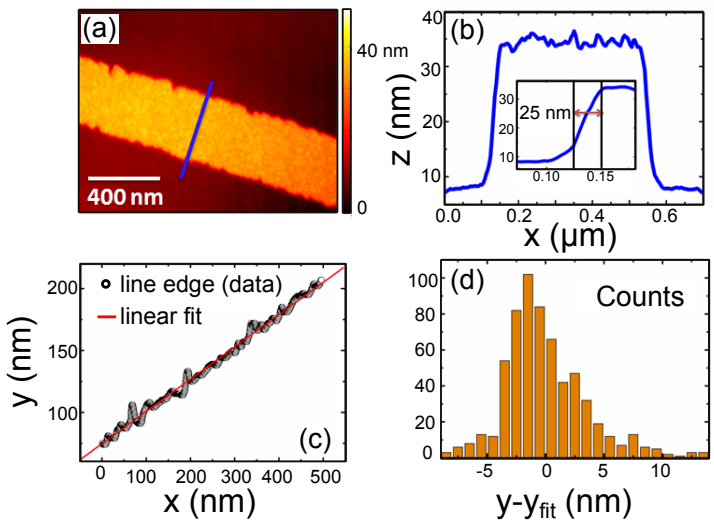

Figure 1.5: AFM analysis of the Line-edge roughness. (a) Atomic force microscopy (AFM) image of a 400 nm wide niobium line. (b)Profile along the straight line indicated in blue in (a). The inset indicates a zoomed in view of the line edge. The transition width of the edges is observed to be about 25 nm. (c) Edge contour of line along with a linear fit. (d) Histogram of line edge contour. Here $3\sigma = 10\,\text{nm}$.

lines obtained (Figure 1.5) shows that the edges are reasonably sharp and well defined. The 3σ (standard deviations) line edge roughness of the wires is 10 nm, which is of the order of the grain size in both the Nb film and the Si mask. This can perhaps be improved if the granularity of the Mo or Si layer is reduced which is possible by reducing the rate of deposition of the respective metal. Line edge smearing as indicated in Figure 1.5(b) is $\approx 25\,\text{nm}$ which is inferior to the lateral resolution of a standard AFM tip. The roughness of the Nb surface is about 1.1 nm.

We have performed transport measurements on these samples in a variable temperature (2˜300 K) cryostat, using a dc four-probe configuration. Figure 1.6(a) shows the optical microscope image of the sample consisting of long Ti/Nb lines ($L = 30\,\mu\text{m}$) of different widths. To measure the four probe resistance of a particular line, a biasing current $I_{bias} = 5\,\mu\text{A}$ was driven from sample pad 1 to 6 via the thin lines while the voltage was measured between pads on the two sides of the respective line. Hence, the resistance recorded for a particular line actually includes contribution from the adjoining broader structures. However, this does not necessarily pose a problem because, as we will see below, these broader structures undergo superconducting transitions at slightly higher temperatures and hence the resistance recorded after that corresponds to the resistance of the particular line alone.

The temperature dependence of the resistance R of the three narrowest lines of widths $W = 400\,\text{nm}, 700\,\text{nm}$ and $1\,\mu\text{m}$ have been shown in Figure 1.6(b) with the inset showing the variation of the normal state resistance (R_N) just before transition as a function of the aspect ratio of the lines. The slope of R_N vs L/W gives us the sheet resistance of the Ti/Nb film, $R_\square = 13.03\,\Omega/\text{sq}$

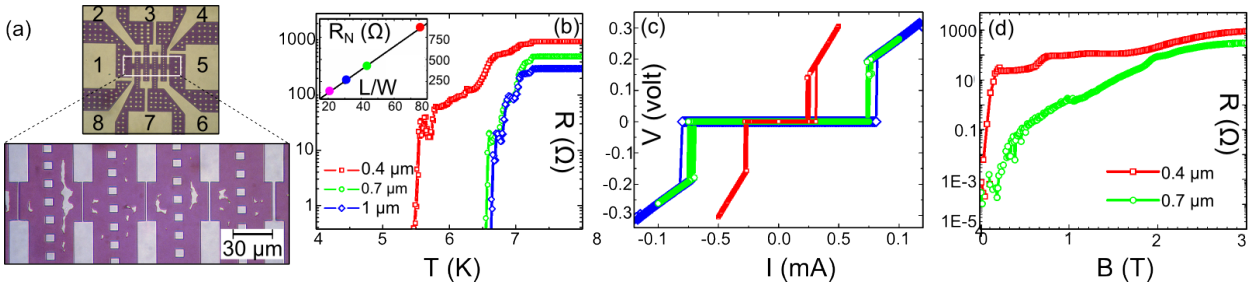

Figure 1.6: Characterization of niobium lines by transport. (a) Optical microscope image of the Ti/Nb (10 nm/26 nm) lines of length $L = 30\,\mu$m and widths $W = 400\,$nm, $700\,$nm, $1\,\mu$m, $1.5\,\mu$m and $2.5\,\mu$m from left to right. (b) Resistance versus temperature of the three narrowest lines ($I_{bias} = 5\,\mu$A). Inset shows the normal state resistance of the lines at $T = 4\,$K as a function of the aspect ratio, the different colors indicate the different line widths : $400\,$nm (red), $700\,$nm (green), $1\,\mu$m (blue) and $1.5\,\mu$m (magenta). The slope gives the sheet resistance $R_\square = 13.03\,\Omega$/sq. (c) Voltage versus current characteristics at $T = 4\,$K. These display hysteresis (as high as 32 % for the $400\,$nm line) as well as random fluctuations of the measured resistance at ($I \approx I_c$). (d) Resistance vs magnetic field B applied perpendicular to the plain of the lines.

which is quite reasonable. The lines display stepwise decrease of resistance below $T = 7.3\,$K which corresponds to the transition of the adjoining broader structures. The small resistance steps in the low-resistance region is probably related to pinning and depinning of residual vortices since niobium is a type II superconductor. The final rapid drop of R from the normal state value R_N to $R < 1\,\Omega$ corresponds to the critical temperature T_c of the narrowest part of each circuit. While the critical temperature T_c of the $400\,$nm wide line is considerably reduced, it is hardly affected for widths above $700\,$nm.

The $V(I)$ characteristics (Figure 1.6(c)) at $4.2\,$K show a marked resistive transition and some hysteresis. The latter is due to Joule heating in the Nb line once in the normal state, which elevates the local electronic temperature compared to the bath temperature [20]. As a result the critical current is reduced giving rise to hysteresis. Thermal hysteresis is enhanced in narrower structures due to higher Joule heating which in turn is a consequence of the higher normal state resistance of the narrower lines. The critical current density is about $J_c \approx 2 \times 10^{10}\,$A/m^{-2}.

R vs magnetic field B of the $400\,$nm and $700\,$nm lines have been shown in Figure 1.6(d). Since niobium is a type II superconductor, the bulk metal has two critical fields, the lower field $H_{c1} \approx 290\,$mT at which point magnetic flux penetration into the superconductor is initiated resulting in appearance of a finite resistance and an upper critical field H_{c2} which can be as high as $2\,$T or more beyond which the normal state resistance of the film is restored [21]. In the case of the two narrowest Ti/Nb lines, $H_{c2} \sim 2.5\,$T. The lower critical field, as marked by the sharp transition in resistance from $R < 1\,\Omega$ to $10\,\Omega$ is about $205\,$mT for the $400\,$nm line. However, for the case of $700\,$nm line, H_{c1} is difficult to identify.

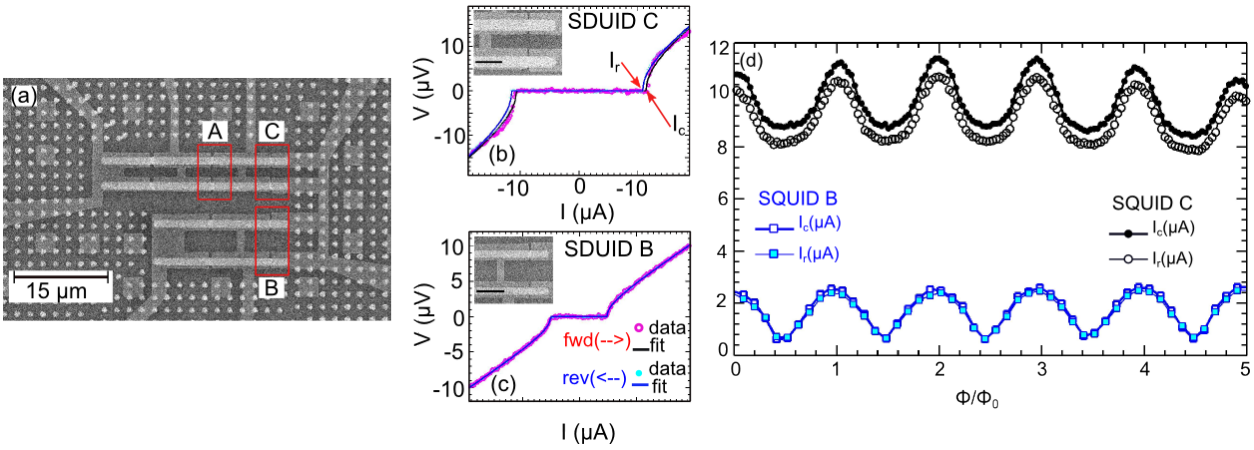

Figure 1.7: Oscillations of I_c and I_r with magnetic field. (a) SEM image of the entire sample consisting of five SQUIDs. (b) $V(I)$ characteristics of device C at $T = 135\,\mathrm{mK}$ and $B = 0.253\,\mathrm{mT}$ i.e. magnetic field corresponding to the third maxima of I_c at $\Phi/\Phi_0 = 2$ in (d). Inset shows the SEM image of SQUID C. Black line indicates the length scale of $2\,\mu$m (c) $V(I)$ characteristics of device D at $T = 125\,\mathrm{mK}$ and $B = 0.121\,\mathrm{mT}$ i.e. magnetic field corresponding to the second maxima of I_c at $\Phi/\Phi_0 = 1$ in (d). Inset shows the SEM image of SQUID B. Black line indicates the length scale of $3\,\mu$m. (c) Critical current I_c and retrapping current I_r oscillations vs applied magnetic field flux in SQUIDs B (squares, T = 125 mK) and C (bullets, T = 135 mK).

1.2.3 Nb-Au-Nb Proximity SQUIDs

We have further fabricated Nb–Au–Nb proximity SQUIDs (Figure 1.7(a)) using a two-step lithography process. We first patterned two long parallel lines of gold with a sticking layer of Ti, $1\,\mu$m wide and 30 nm thick, by conventional e-beam lithographic techniques. The metallic mask method described above is then used to pattern Nb proximity junctions on top of these. We deposited a 50 nm thick Nb layer without any sticking layer this time. Over the proximity junction, the metal mask is free hanging, as to form junctions as short as 200 nm. The device parameters of the three tested devices, labeled A, B and C, are summarized in table 1.1.

SQUID	$L\ (nm)$	$W\ (\mu m)$	$R_N\ (\Omega)$	$\rho_N\ (\mu\Omega cm)$	$D\ (cm^2/s)$	L_{th}	$I_c\ (\mu A)$	$\epsilon_c\ (\mu eV)$
A	430	0.98	1.99	13.6	29	160	-	10.2
B	340	1.00	1.04	9.20	42	190	2.7	24.1
C	210	0.98	0.89	12.4	31	170	11.8	46.7

Table 1.1: Device parameters of the Nb-Au-Nb SQUIDS. L is the geometrical length of the normal weak link. R_N is the normal state resistance of the weak link, measured at 4 K, ρ_N the corresponding resistivity and D the diffusion coefficient. I_C is the maximum critical current measured at 135 mK. $\epsilon_c = \hbar D/L^2$ is the Thouless energy assuming the weak link length is L.

In a hybrid Josephson junction made of a normal metal bridging two superconducting electrodes, as in the Au line between two Nb electrodes here, the length scale for inducing superconductivity in the normal metal is set by the normal metal thermal length given by

$$L_T = \sqrt{\frac{\hbar D}{2\pi k_B T}} \tag{1.2.1}$$

Here, D is the electronic diffusion coefficient in the normal metal. L_T is estimated to be about 180 nm at 135 mK while the junction lengths L are in the range 200˘400 nm.

Transport properties of the Nb–Au–Nb proximity SQUIDs were measured using a four-probe dc current bias scheme inside a dilution refrigerator. Each electrical lead to the samples was thoroughly filtered by individual 2 m long lossy coaxial lines thermalized at the cryostat base temperature. Figure 1.7(b) and (c) shows the $V(I)$ characteristics of SQUID C and SQUID B respectively at magnetic field corresponding to a critical current maxima for each. Out of the 5 SQUID devices, critical current is observed only for theses two devices i.e. ones with the shortest junction length L.

As proximity Josephson junctions have a vanishing capacitance, they are over-damped [22]. The $V(I)$ characteristic is thus expected to follow :

$$V = R_n\sqrt{I^2 - I_c^2} \;\; for\; |I| > |I_c| \tag{1.2.2}$$

The measured $V(I)$ characteristics showed a rather good agreement to this equation, see Figure 1.7(b) and (c). A small but finite hysteresis is nevertheless observed : 7 % for the highest I_c SQUID (device C) and 4 % for device B at the lowest temperatures. While sweeping the current down from large values $|I| > I_c$, the SQUID turns non-resistive at a retrapping current $I_r \leq I_c$. This hysteresis is known to be of thermal origin [20]: the Joule heat dissipated in the normal metal elevates the electronic temperature with respect to the phonon temperature as the electron–phonon coupling is the bottleneck for the electron thermalization to the bath. Retrapping happens when the bias current becomes of the order of the critical current at the current electronic temperature.

Our samples are in the long junction limit defined as a normal metal length larger than the superconductor coherence length: $L \gg \xi_s \approx 30$ nm. In this case, the relevant energy scale for the superconducting proximity effect is the Thouless energy

$$\epsilon_c = \frac{\hbar D}{L^2} \tag{1.2.3}$$

which is much smaller than the energy gap Δ. The evolution of critical current with temperature in a normal metal weak link at arbitrary temperatures can be understood by solving the Usadel equations. At low temperatures and in the long junction limit ($\Delta/\epsilon_c \to \infty$), the numerical solution to the Usadel equation can be approximated by [23]

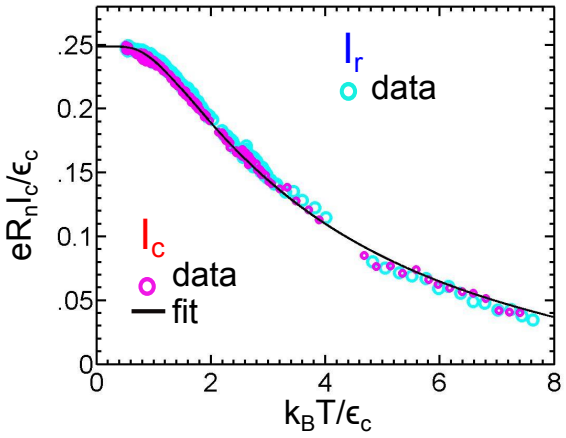

Figure 1.8: Temperature dependence of eR_nI_c/ϵ_c product for SQUID C for critical current I_c and retrapping current I_r along with fits with equation 1.2.4. Fitting parameters are η and ϵ_c. For I_c, best fit parameters are : $\eta = 0.023, \epsilon_c = 31.14\,\mu$eV. For I_r, best fit parameters are : $\eta = 0.023, \epsilon_c = 30.22\,\mu$eV.

$$\frac{eR_NI_c}{\epsilon_c} = \eta a\left[1 - b\exp\left(-\frac{a}{3.2}\frac{\epsilon_c}{k_BT}\right)\right] \tag{1.2.4}$$

where $a = 10.82, b = 1.30$ and $\eta = 1$ for perfectly transparent S–N interfaces. From the fit to the experimental data of SQUID C, shown in figure 1.8, values of $\epsilon_c = 31\,\mu$eV and $\eta \approx 0.023$ are found. Due to very small hysteresis, the values are almost the same for the I_r current branch. The estimate of ϵ_c agrees well with the value found from geometrical arguments, see table 1.1. The minor discrepancy can be understood as an effective junction length $\tilde{\mathrm{L}} = \sqrt{\hbar D/\epsilon_c} = 257\,$nm, slightly longer than the geometrical value [23]. The reduced value of η reflects a lower than ideal I_c, which is attributed to imperfect transmission at the Nb–Au interface. Argon plasma of the Au structures prior to Nb deposition should lead to improved contact transparencies.

1.2.4 Furthur Developments

This novel technique of nanofabrication using a bilayer metal mask has been significantly improved by the next graduate student in the lab [24]. By optimizing this process furthur so as to incorporate the possibility of angled evaporation of metals, this process could be successfully implemented in the fabrication of S-N-S interfaces with both the superconductor (S = Nb) and the normal part (N = Au) deposited one after the other without breaking vacuum of the deposition chamber. This technological advancement led to dramatic increase in interface transparencies by almost 35 times the value obtained in case of the SQUIDs! Figure 1.9(a) shows the metal mask for the SNS structure while (b) shows the end device.

The next goal would be to implement this process to fabricate superior quality Superconducting interfaces on graphene but this remains to be realized by future students.

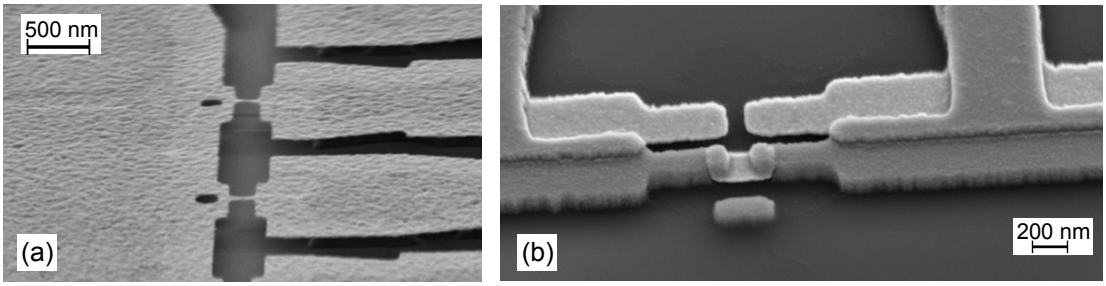

Figure 1.9: Nb-Au-Nb Josephson Junctions. (a) Scanning electron micrograph (SEM) of Al/Mo (290 nm/45 nm) bilayer mask for fabrication of Nb-Au-Nb junctions. (b) SEM image of the final junctions consisting of 90 nm Nb and 30 nm Au [24].

1.3 The Mechanical Shadow Mask

As had already been discussed in subsection 1.1.2, the primary limitation of applying conventional lithography methods for contacting graphene involving organic resists is that it is impossible to recover uncontaminated graphene devoid of resist afterwards. Since a clean graphene surface is essential for studying it by STM and AFM, we devised another technique to achieve the same which is once again quite different from the technique presented in section 1.2. This method does not involve any lithography process but is simply based on the method of mechanical masking of the graphene flake.

1.3.1 Substrate Preparation and Graphene Exfoliation

The graphene in our devices is obtained by the process of mechanical exfoliation of *Kish* graphite by the popularly used scotch-tape method [25],[1]. Although labour intensive, we found exfoliated graphene more suitable for our purpose rather than CVD grown graphene. This is because as far as sample quality in terms of surface cleanliness and large crystal domains is concerned, there is simply no other substitute for graphene prepared by mechanical exfoliation.

Graphene exfoliation is carried out on $SiO_2(285\,nm)/Si$ substrate. The thickness of the oxide is crucial for detection of few layer graphene (FLG) flakes by an optical microscope [26], [27]. FLG is actually visible as a shadow in the optical microscope whose contrast increases with the number of layers. The shadow is produced by the interference between light waves reflected from the graphene and the Si/SiO_2 interface. For 300 nm oxide thickness, the optimal contrast is obtained for the green light.

The treatment of the substrate prior to exfoliation is very important as it is a major determining factor for the size and number of FLG flakes obtained. Moreover, cleaning the surface thoroughly ensures reduction of concentration of charged impurities which are known to have a significant influence on the electronic characteristics of the flakes [29]. In order to ensure maximum removal of contaminants, the substrates were first ultrasonicated in a bath of acetone

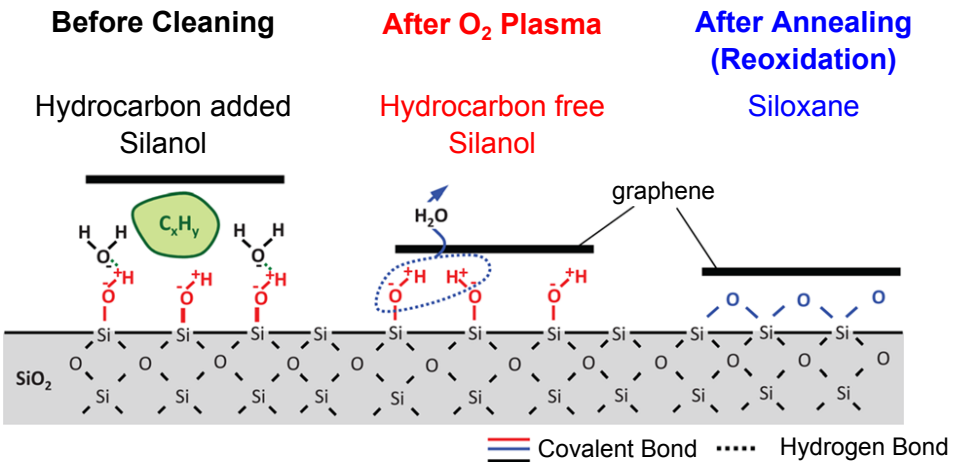

Figure 1.10: Schematic of the SiO_2 surface after different surface treatments. Hydrocarbons usually present are removed by oxygen plasma exposing negatively charged silanol groups. Re-oxidation occurs on annealing at 1000 °C for 5 minutes in 100 % O_2 flow leading to the formation of siloxane groups on the surface [28]

for about 10 mins followed by IPA rinse and then in RBS solution (soap). This is followed by 5 minutes in oxygen plasma (50 W) which renders the surface hydrophilic. Figure 1.10 shows a schematic illustrating the substrate environment after each cleaning step. Organic contaminants or hydrocarbons that usually exist on the substrate are removed by oxygen plasma, exposing negatively charged silanol groups that possess great affinity towards C molecules [28]. The ensuing high surface-graphene interaction is expected to reduce the van der Waals interaction between the bottom and the second carbon layers thus increasing the chances of occurance of single-layered graphene (SLG) with large dimensions. To take maximum advantage of the hydrophilic nature of the substrate, exfoliation was done within an hour of plasma treatment.

It should be noted here that the above technique of substrate preparation by O_2 plasma treatment scores over other commonly used methods because of yielding substrates that have a higher affinity towards C molecules. In fact the graphene is so well 'stuck' to the substrate, that for people trying to prepare BN-Graphene-BN stacks, it is indeed a nuisance as it is impossible to detach the graphene from the substrate afterwards. But for our purpose, it is quite an advantage since as we will see in section 3.5.2, the SiO_2/Si substrates that is required for our experiment is not flat but covered with a dense distribution of holes, crosses and markers $\approx$ 10 nm deep that have been patterned into the SiO_2 layer by deep UV lithography. This makes the adhesion of flakes on the substrate comparatively difficult. The inset in Figure 1.11 shows an optical image of an exfoliated flake on such a substrate. This is why the attractive nature of the substrate surface developed after O_2 plasma cleaning is important as it is able to somewhat redeem the situation. Other prevalent methods like annealing of the substrate or piranha cleaning (which causes reoxidation of the silanol groups forming siloxane), although are expected to give better

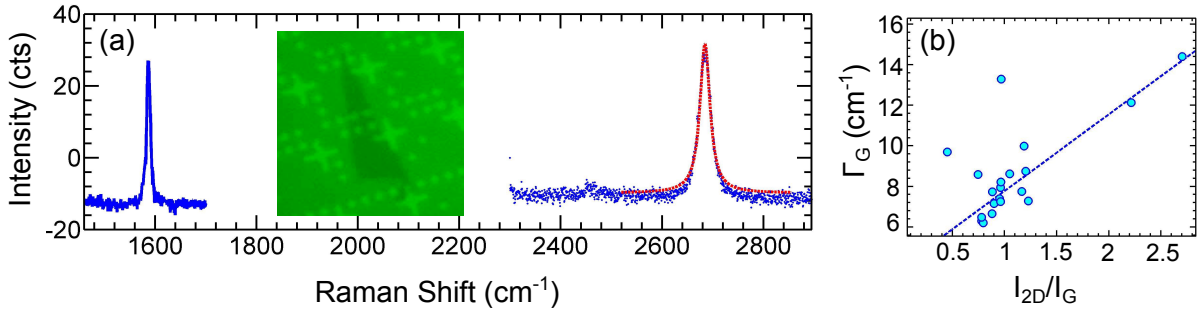

Figure 1.11: Identification of number of layers by Raman Spectroscopy. (a)Plot shows the G Peak at 1587 cm^{-1} and the 2D Peak at 2684 cm^{-1}. Blue dots indicate measured data points while the red curves indicate a lorentzian fit of the 2D intensity peak with a broadening of 24 cm^{-1}. Inset shows the optical micrograph of the corresponding graphene captured in green light for best contrast ($\approx 9\,\%$). (b) Broadening or FWHM (Γ) as a function of intensity ratio of 2D peak to that of G Peak (I_{2D}/I_G) for 20 monolayers (SLG) right after exfoliation. The blue dashed line is just a guide to eye to emphasize the positive correlation between Γ_G and I_{2D}/I_G .

quality flakes [28], could not be implemented on our substrates due to the significantly lower yield.

1.3.2 Optical Detection & Raman Spectroscopy

After exfoliation, the samples are scanned optically for single-layered graphene flakes (SLG) although some experiments were also conducted on multilayers. The optical contrast already gives us a rough estimate about which flakes could be monolayers. It was seen that with green light, SLGs showed a contrast of about $8 - 10\,\%$ while bilayers about $16 - 20\,\%$ and so on. After this pre-selection step, the suspected SLGs were put to test under a 514 nm laser light for analyzing the Raman Spectra of the reflected signal, which provides a definitive identification of monolayers [30].

Figure 1.11 (a) shows the Raman spectra of one of the monolayers prepared, whose optical image is shown in the inset. The Raman spectra of the entire graphite family i.e starting from few layer flakes to the bulk crystal, are characterized by an intensity peak at Raman shift $\approx 1580\,\mathrm{cm}^{-1}$ which is called the G Peak and another peak at $\approx 2700\,\mathrm{cm}^{-1}$ called the 2D Peak. The G Peak is caused by the doubly degenerate zone center E_{2g} mode while the 2D Peak is a second order effect created by zone-boundary phonons. But what sets the monolayer spectra apart from the rest of the graphite family is the distinct Lorentzian shape of the 2D peak with a broadening (FWHM) $\approx 30\,\mathrm{cm}^{-1}$.

The power of Raman spectroscopy as a probe for graphene physics is not merely limited to monolayer and bilayer identification. One can also have insights into the structure, doping and disorder of a particular flake with the help of this technique [31][32][33]. The position, broadening

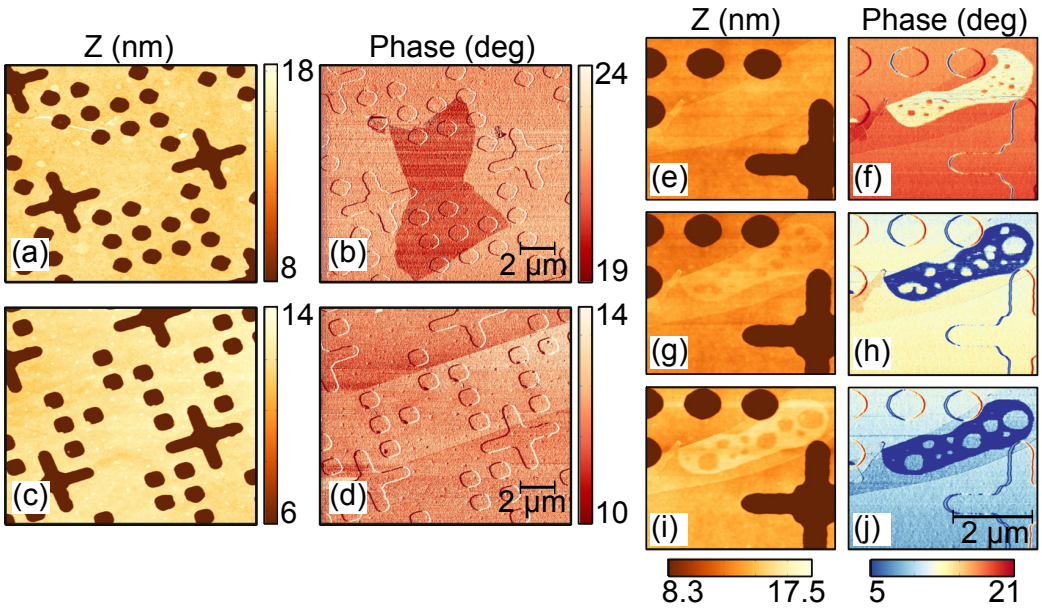

Figure 1.12: Surface characterization of exfoliated graphene by atomic force microscopy in tapping mode. (a) AFM topograph and (b) Phase signal map of a given monolayer (SLG 1). (c) Topography and (d) Phase signal map of a second monolayer (SLG 2). (e),(g),(i) Topography and (f), (h), (j) Phase signal map of a third monolayer (SLG 3). (e)-(j) Each row from top to bottom have been recorded one after the other.

(Γ_G) and the intensity ratio of the 2D peak to that of the G Peak (I_{2D}/I_G) are all related to the doping level of the graphene flake [32][34]. An undoped sheet of graphene will have the G Peak located at $\approx 1584\,\mathrm{cm}^{-1}$ with $\Gamma_G \approx 16\,\mathrm{cm}^{-1}$ and $I_{2D}/I_G \sim 3$. Doping the flake results in G Peak stiffening, decrease in linewidth as well as decrease in I_{2D}/I_G. Figure 1.11(b) shows a plot of FWHM of the G peaks vs the corresponding values of I_{2D}/I_G for 20 SLGs prepared by the exfoliation technique presented above. As expected, the two quantities do show a positive correlation for most of the flakes i.e. less the doping, more is the broadening and higher the ratio of the intensity maxima. The two points which fall completely off the straight line correspond to flakes with were not entirely single-layered. Contributions from the milti-layered regions could account for the observed discrepancy.

From 1.11(b), it is also quite clear that most of the flakes exfoliated by the above process are already doped. The average values of the G Peak Position, G peak broadening (Γ_G) and intensity ratio (I_{2D}/I_G) are $1589\,\mathrm{cm}^{-1}$, $8\,\mathrm{cm}^{-1}$ and 1 respectively; all indicative of a rather high doping. Since the Raman observations were conducted prior to metal deposition, we can conclude that the substrate environment has a significant influence in the overall properties of the flakes.

1.3.3 Surface Characterization by Atomic Force Microscopy

After selecting the monolayers from millions of flakes by a combination of optical means and Raman spectroscopy, the surface of each individual selected flake was characterized by Atomic

Force Microscopy (AFM) in tapping mode. This was primarily done to ensure a clean surface free from glue from the tape, cracks, tears or any other kinds of contamination. For such a surface characterization, AFM is the perfect probe as it is both non-invasive and unlike SEM, non-contaminating. However, it is difficult to identify the precise number of layers by this technique. For a monolayer which should theoretically have a thickness of 0.3 nm, the step height recorded can be upto about 1 nm while quite often they are hardly visible in the AFM topography as can be seen in the examples shown in Figure 1.12 (a) and (c). This ambiguity in step height detection happens because the topography in AFM is influenced by the nature of the tip-sample interaction which can be very different on the graphene compared to that on the surrounding substrate at a given tip-sample distance.

Figure 1.12 shows examples of AFM characterization done on three monolayers. It is quite evident that while the flakes are vaguely visible in the topography, they prominently stand out in the Phase signal because the latter is directly sensitive to the nature of the tip-sample interaction. Hence it serves as a very useful probe for the direct visualization of the condition of the graphene. The three examples shown in this figure demonstrate the variety of contrasts that can be seen in the Phase signal ; from a decrease in phase over the graphene (SLG 1) to a relative increase (SLG 2) or sometimes to a spatial distribution of both (SLG 3). Figure 1.12 (e)-(j) tracks the evolution of the SLG 3 with consecutive scans from top to bottom. From a comparison of topography with Phase, it appears that regions on the flake which are closer to the substrate produce a higher phase change of the scanning cantilever probe or in other words have a higher influence on the cantilever than regions lying furthur away. Hence the phase image qualitatively produces a map of the spatial variations of the substrate-graphene distance. Moreover, what is even more interesting is that, this process of scanning the flakes with the probe in intermittent contact with the surface (tapping) can sometimes even induce changes in this distance as we see in the case of SLG 3.

1.3.4 Fabrication

After the finalization of the graphene flake to be contacted, it's time to implement the process of Mechanical Masking to pattern two contacts on it that are isolated electrically. This process has been demonstrated schematically in Figure 1.13. It involves positioning a thin tungsten (W) wire on top of the flake to partially mask it before placing it in the chamber for metal deposition. The steps are enumerated below :

1. Clean (ultrasonicated in acetone/IPA) W wire strands $(3-4)$ of diameter $4\,\mu$m and length of about $500-600\,\mu$m are placed on the sample substrate.

2. One of the wires is positioned on top of the selected graphene flake. This is done by pushing the W wire with a second thicker W wire ($d \sim 100\,\mu$m) fixed at the edge of a micromanipulator capable of precise movement in three dimensions as shown in Figure

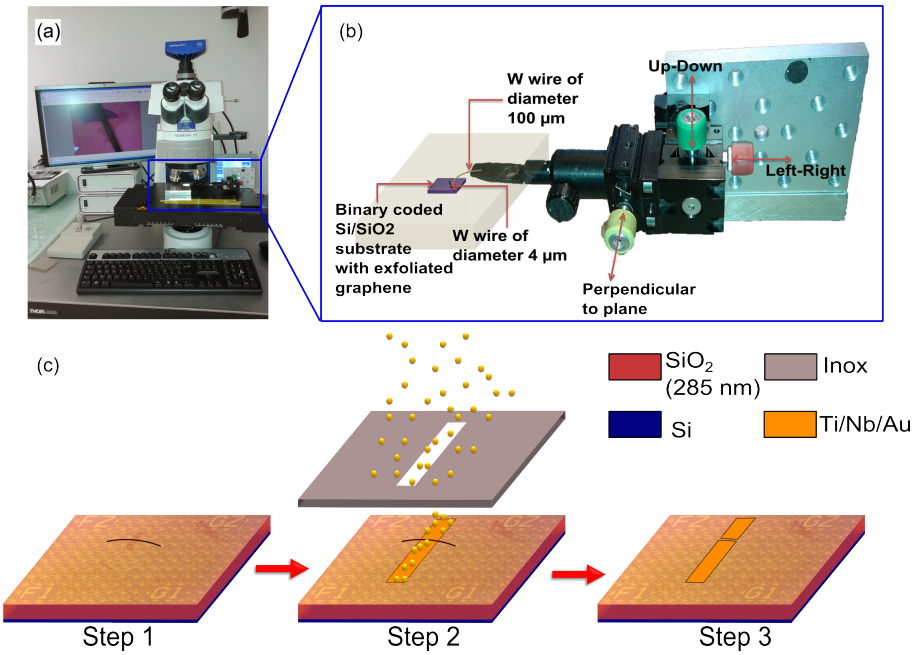

Figure 1.13: Contacting Graphene by Mechanical masking. (a) Photograph showing the setup used for manual alignment of a W wire mask over the graphene consisting of a micromanipulator placed under an optical microscope. (b) Schematic explaining the working of the micromanipulator. (c) Fabrication steps for placing two isolated electrical contacts on exfoliated graphene. Step 1: Positioning 4 μm W wire on the selected flake. Step 2: Deposition of metal through a rectangular slit of size 0.3 mm × 2 mm placed on top of the wire. Step 3: Contacted graphene after removing the wire and the second mask.

1.13(b). The wires adhere to the substrate rather strongly due to van der Waal's interaction and do not detach even on flipping the substrate.

3. A second metallic mask containing a rectangular window of size 0.3 mm × 2 mm is now carefully positioned on top of the flake in a way such that the flake position is adjusted to the center of the window.

4. After securely clamping the sample to the sample holder, with the mechanical mask on top, it is placed inside an ultra high vacuum chamber with pressure of about 10^{-10} mbar for metal deposition.

5. The sample is then annealed at 150 °C for half an hour and kept in UHV overnight to allow sufficient time for outgassing.

6. This is followed by metal deposition consisting of a sticking layer of titanium (1.5 nm), niobium as the superconducting material (10 nm) and finally a thin layer of gold (2 nm) to protect against surface oxidation.

7. After deposition, the metal and the wire masks are manually removed. The wire can simply be removed with the help of once again a thicker W wire.

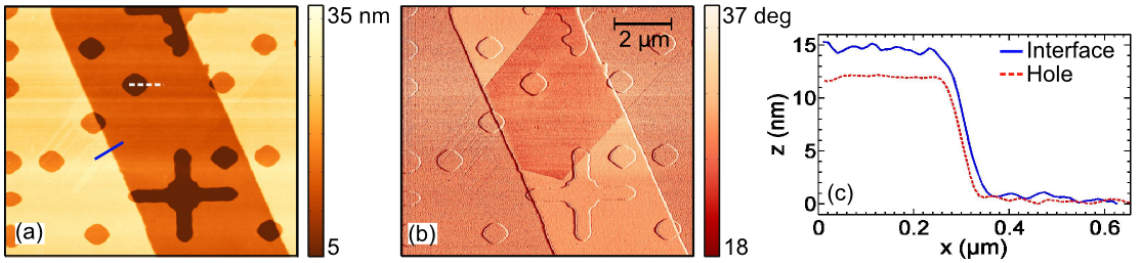

Figure 1.14: AFM Characterization of the Metal-Graphene Interface. (a) AFM Topography and (b) Phase map of a SLG contacted by the Ti/Nb/Au (1.5 nm/10 nm/2 nm) using the technique of mechanical masking. The roughness measured on the graphene is ~ 0.6 nm, over an area of $1\,\mu\text{m} \times 1\,\mu\text{m}$ while that on the SiO_2 substrate is about 0.3 nm and that on the metal is ~ 0.8 nm for the same area. (c) Comparison of edge sharpness between graphene-metal interface (blue) created by the wire mask and a marker hole (red dashed line in plot and white dashed line in topography image (a)) patterned by deep UV lithography.

It should be noted that, the length of the W wires should not be higher than $\sim 600\,\mu$m as otherwise the wires were found to be displaced. This was probably due to the fact that at the high temperatures to which the sample was subjected to, the adhesion of the wire to the substrate is weakened. Hence, this causes an upper bound to the length of the wire. At the same time, length should not be shorter than $\sim 400\,\mu$m keeping in mind the $300\,\mu$m width of the upper metallic (stainless steel) mask.

This process of contacting flakes was found to be rather efficient with a high success rate. And what is more is that with this technique we managed to achieve our main objective which was the production of contamination free graphene surface that has never seen any organic resist and hence perfectly compatible for scanning probe measurements.

Figure 1.14 shows the AFM image of an exfoliated graphene flake conatcted by the above method. It is quite evident that the surface is very clean and devoid of any contaminants. Also, region close to the interface is found to be free of any metal grains diffusing into the graphene. Figure 1.14(c) shows the edge sharpness of the metal-graphene interface in comparison to that of a marker hole patterned by deep UV lithography as measured by an AFM tip in tapping mode. The slope of the former is about 0.12 while that of the latter is about 0.14 which is only a minor difference. The measurement of edge sharpness in this way is, of course, not accurate but limited by the finite radius of the AFM tip apex. Nevertheless, the close similarity with edges created by conventional lithography definitely implies the success of this technique to create nearly perfect metal-graphene interfaces.

Even if we were to assume that the spatial width of transition from the graphene to the metal is equal to what is observed in AFM i.e. ~ 100 nm, this would still be sufficient for our purpose. For the purpose of investigation of Superconducting proximity effect near the interface, with reasonable interface transparency, the thermal length L_T (relevant length scale for proximity superconductivity) in graphene is expected to be far greater than 100 nm. Hence,

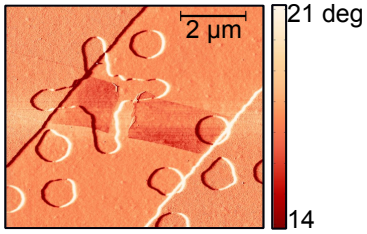

Figure 1.15: Rupture of Graphene under strain. Phase map (AFM) of a contacted (Ti/Nb/Au) (1.5 nm/10 nm/2 nm) monolayer flake found to be torn from the middle right after deposition.

for the objectives that we set our for, this was rather satisfactory.

1.3.5 Contact materials and related challenges

Although this method of contacting the graphene by partially masking it by a metallic wire was quite easy to implement, there were some difficulties encountered on the way. These were mostly related to our choice of Niobium as the superconducting contact metal and our decision to deposit this by electron-beam deposition for reasons already explained (see Section 1.1.1). The extremely high temperatures that are produced during electron-beam deposition of niobium $\sim$ 3000 °C, subjects the graphene to a very high compressive strain induced by a thermal expansion coefficient (TEC) mismatch between graphene and the underlying substrate as well as the deposited metals. This is because graphene has a negative TEC of about $-8 \times 10^{-6}\,\mathrm{K}^{-1}$, while SiO_2 and the metals, all have a positive TEC [35]. This may even cause the graphene to slip as the tensile force can exceed the weak van der Waal's foces that usually hold the graphene to the substrate. Figure 1.15 shows an example of a SLG flake that was found in a ruptured state right after metal deposition.

This problem of rupturing of the flakes could be solved by paying attention to the graphene dimensions. It was observed that graphene with a high Length:Width aspect ratio ($\gtrsim 3$) were particularly susceptible to being torn. Hence, care was taken to avoid such flakes.

Another major problem was the poor adhesion of the metal to the graphene. As a solution to this, we realized that reducing the thickness of the metal contacts from 3 nm/30 nm/4 nm (Ti/Nb/Au) (Figure 1.16(a)) to 1.5 nm/10 nm/2 nm (Figure 1.16(b)) significantly improved the metal - graphene interfaces. Figure 1.16(c) shows the comparison of interface profiles (AFM) of graphene devices with different thickness of metal contacts. Of course, reducing the thickness meant reduction of superconducting critical temperature (T_c) of the metal combination Ti/Nb/Au as well. For this optimum thickness, we measured the T_c to be about 5.9 K which was still sufficiently high for our purpose.

The change in metal thickness also brought about a marked difference in the electronic transport properties of the end devices. Figure 1.16(d) shows the normalized conductance of two SLGs with different metal thicknesses, plotted as a function of the applied voltage bias (V_{bias}). With a higher metal thickness, the conductance was always found to decrease for $|V_{bias}| < 2\Delta/e$,

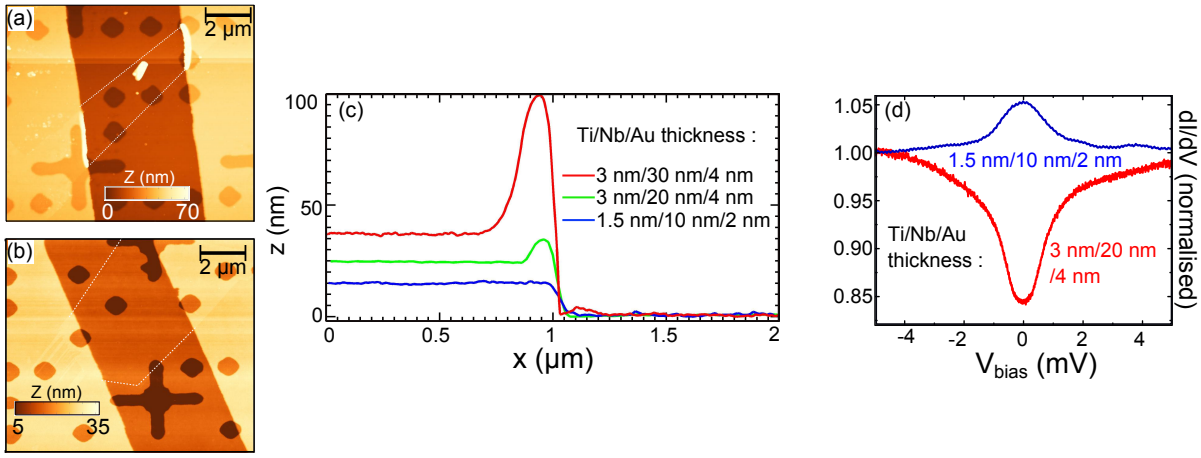

Figure 1.16: Interface improvement with reduced metal thickness. (a) AFM topograph of a metal-graphene-metal junction with poor adhesion of the contacts to the graphene. (b) AFM topograph of another sample with reduced metal thickness that shows much better contact with the SLG. (c) Gradual improvement of interfaces with lower metal thickness deposited. Plot shows the Z profiles (AFM) of Au/Nb/Ti - Graphene interfaces for different thicknesses of the metal deposited. (d) Normalised conductance measured by transport as a function of voltage bias across the sample for two different metal thicknesses at zero backgate voltage which corresponded to a intrinsic positive doping in both cases (T = 130 mK).

where $\Delta \sim 900\,\mu$eV is the superconducting gap of Ti/Nb/Au, irrespective of the doping level of the graphene. This implied a poor interface transparency. With the reduced thickness, for high doping, there was an increase in conductance for V_{bias} below $2\Delta/e$ which was a clear signature of the occurrence of second order Andreev processes that account for the transport of Cooper pairs across a SNS interface and hence contribute to a rise in conductance. Thus, we conclude that reducing the thickness of contact metals definitely helps in increasing the interface transparency.

1.4 Conclusion

In this chapter, two distinct fabrication procedures have been discussed : firstly, the Bilayer Metal mask technique for creating nanostructures with thermally evaporated niobium and secondly, the Mechanical shadow mask for contacting graphene. Both methods adopt the non-organic resist route to pattern niobium electrodes via electron beam deposition to achieve *uncontaminated* Superconductor - Normal metal/Graphene interfaces that are compatible for investigation by scanning probe.

Even though the mechanical shadow mask technique offers an efficient way of achieving clean superconductor-graphene-superconductoe junctions, the width of the junctions are limited to the tungsten wire diameter. To achieve versatile contact designs with controllable electrode spacing, the eventual aim is to implement the bilayer metal mask technique in contacting the graphene

flakes. This work is in progress by new students in the group who have found it best to replace the aluminium sublayer by copper. This is because the etchant MF-319 needed for developing aluminium is found to affect graphene. Copper satisfies all the criteria required to form the underlying metallic layer and moreover it is etched easily by mild reagents like ammonium persulphate which do not have any adverse effect on graphene. Successful optimization of the bilayer metal mask technique to fabricate graphene based devices would lead to significant progress in local study of mesoscopic graphene based devices by scanning probe.

Chapter 2

Theory of Disorder and Screening in Graphene

Contents

2.1 Introduction **28**
2.2 Electronic Properties **30**
2.2.1 Lattice structure of single-layered graphene 30
2.2.2 Energy Dispersion 31
2.2.3 The Dirac Formalism 33
2.2.4 Bilayer Graphene 34
2.2.5 Electronic Density of States 35
2.3 Many body effects in Graphene: Screening **36**
2.3.1 General introduction to Screening in a 3D electron gas 37
2.3.2 Screening in Graphene 41
2.4 From local Disorder to Macroscopic Carrier Transport in Graphene **44**
2.4.1 Charge Carrier Transport in Graphene 45
2.4.2 Charge disorder and local correlations 48
2.5 Conclusion **58**

2.1 Introduction

It was sometime in the fall of 2002, when Andre Geim in his lab at the Manchester university realized the power of the scotch tape to isolate a single sheet of graphene from a stack of graphite [36]. Being completely two dimensional, graphene was believed by many to be just a theoretical model as 2D crystals were thought to be thermodynamically unstable based on a loose interpretation of the powerful Mermin Wagner theorem [37]. It has been more than a decade since then

and in that time graphene has ushered in a revolution with active participation from various branches of scientific research. The properties of graphene are fascinating from every angle; it is the thinnest and at the same time the toughest material ever measured (150 times stronger than an equivalent weight of steel), it is extremely flexible (can stretch to 120% of its length), it has the best mobility (more than 100 times that of Si) and the highest current density (million times that of copper) beats even diamond in thermal conductivity and the list goes on. Efforts continue to harness these potentials in building high performance field effect transistors, opto-electronic devices like photo-voltaics [38], touch-screens [39] etc, for biding sensors like bio and gas sensors and also in biological applications like tissue engineering [40] and detecting neural activity [41] in brains. With the success in scaling up graphene production [39], its industrial future seems rather promising.

But from a more fundamental point of view, the interest in graphene stems from the relativistic nature of its charge carriers which arises due to its honey-comb lattice structure. This allows the possibility to study relativistic electrodynamics in table-top experiments like half-integer quantum Hall effect [2], Klein tunneling [3] and scattering [42], atomic collapse [43], gauge fields and topological defects [44], etc. What came as a surprise in the starting years was the failure to observe a theoretically predicted suppression of anti-localization [45] and a universal minimum conductivity [5] in graphene. This was part of a bigger question of what actually limits the mobility in graphene. It was gradually realized that the role of electrostatic potential fluctuations or *disorder* to which the graphene is subjected is crucial in determining the transport properties of its carriers especially at low carrier densities. With the help of sophisticated scanning probe techniques like scanning single electron transistor [46] and scanning tunneling microscopy and spectroscopy [6], the presence of an inhomogeneously doped landscape or electron-hole puddles in graphene on SiO_2 was revealed. Understanding the origin of this disorder is really at the heart of graphene research and the most accepted explanation in this respect has been the model of scattering by random charge impurities embedded in the substrate [29].

In this chapter, we theoretically look into the problem of how carriers in graphene respond to a disordered potential of Coulombic origin and its effects both locally and macroscopically, based on theoretical work by S. Das Sarma and Adam et. al [47][29] [48]. We start with the fundamental electronic properties that are intrinsic to graphene. When many-body interactions are turned on, we see how these properties give rise to a screening behavior that is strikingly different from other two dimensional systems. We then move on to consider the implications of this unique carrier dependent screening when subjected to an electrostatically disordered environment. By assuming a disordered potential created by random charge impurities in the substrate, we quantitatively discuss the bulk transport properties of the carriers in graphene both at high and low carrier densities. This will allow us to identify the important length and energy scales in the problem and the parameters that determine them. With this knowledge, we will finally build up the local correlations of the screened disordered potential of the system and see how this changes as the

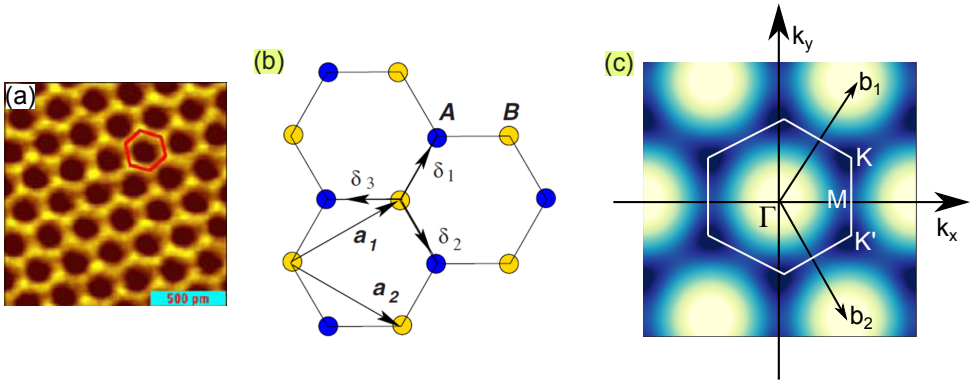

Figure 2.1: Honeycomb lattice of Graphene and its Brillouin Zone. (a) Atomically resolved STM image showing the hexagonal arrangement of atoms in a unit cell of graphene [50]. (b) Schematic of the honeycomb lattice consisting of two inter-penetrating triangular sublattices. a_1 and a_2 are the lattice unit vectors while $\delta_i, i = 1, 2, 3$ are the nearest neighbour vectors. (c) Corresponding Brillouin zone. The Dirac cones are located at $\mathbf{K}$ and $\mathbf{K}'$ points while $\mathbf{b_1}$ and $\mathbf{b_2}$ indicate the reciprocal lattice vectors [49]. The background color plot gives energy $E(\mathbf{k})$ of the conduction band in units of the hopping energy [Eq.(2.2.6)].

carrier density is tuned from the high density limit right up to charge neutral Dirac regime.

2.2 Electronic Properties

To understand the end result of any interesting experiment related to graphene, or for that matter any system in condensed matter, the importance of understanding the basics of the electronic structure leading to the dispersion relation cannot be overemphasized. Hence, in this section we revisit the basics of this fascinating system to appreciate the unique features in the energy dispersion that sets this material apart. All derivations presented in this section are taken from the review by A. H. Castro Neto [49] and S. Das Sarma et al. [47].

2.2.1 Lattice structure of single-layered graphene

P.R. Wallace had used the concept of graphene for the first time, back in 1947 [51], as a theoretical construct to calculate the band structure of graphite. It consists of a single sheet of carbon atoms arranged in the form of a honeycomb lattice. Figure 2.1(a) shows an STM image of graphene lattice which beautifully captures the hexagonal arrangement of the carbon atoms in a unit cell. Since each C atom is shared by three unit cells, each unit cell effectively contains two atoms. Hence, an alternate way to look at it would be as two triangular inter penetrating sub-lattices as shown in Figure 2.1(b), blue and the yellow circles representing each individual sub-lattice. The lattice vectors are given by :

$$\mathbf{a_1} = \frac{a}{2}\left(3, \sqrt{3}\right), \ \mathbf{a_2} = \frac{a}{2}\left(3, -\sqrt{3}\right), \tag{2.2.1}$$

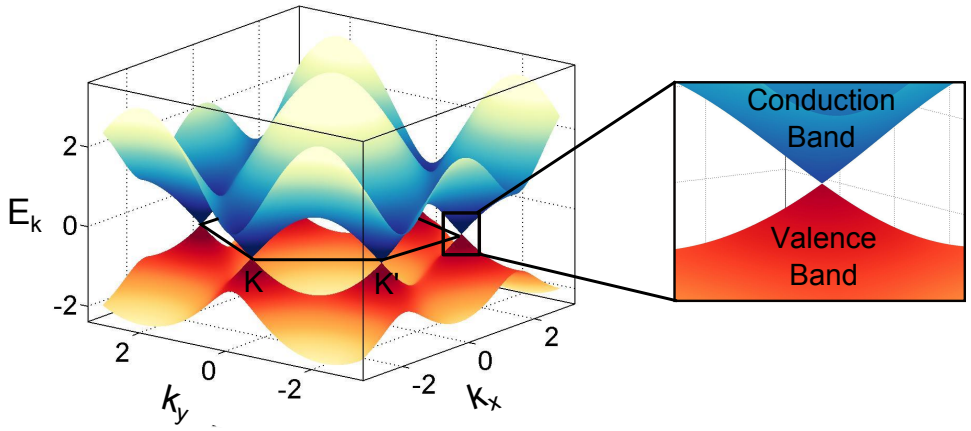

Figure 2.2: Electronic band structure of Graphene. Energy spectrum (in units of t) with finite values of t and t': $t = 2.7\,\text{eV}$ and $t' = -0.1t$ in this case. Inset shows the zoom-in of the energy bands close to one of the Dirac Points.

where $a \approx 1.42$ Åis the nearest neighbour distance between two carbon atoms. The three nearest neighbour vectors in real space are given by

$$\delta_{\mathbf{1}} = \frac{a}{2}\left(1, \sqrt{3}\right), \; \delta_{\mathbf{2}} = \frac{a}{2}\left(1, -\sqrt{3}\right), \; \delta_{\mathbf{3}} = -a\,(1, 0)\,. \tag{2.2.2}$$

From the graphene unit cell, it is now straightforward to construct the corresponding reciprocal lattice [52] (Figure 2.1(c)) with reciprocal vectors

$$\mathbf{b_1} = \frac{2\pi}{3a}\left(1, \sqrt{3}\right), \; \mathbf{b_2} = \frac{2\pi}{3a}\left(1, -\sqrt{3}\right). \tag{2.2.3}$$

The Wigner-Seitz primitive cell of this reciprocal lattice gives the first Brillouin zone. The corners of the Brillouin zone indicated as $\mathbf{K}$ and $\mathbf{K'}$ points in Figure 2.1(c) are known as the Dirac Points. Their positions in momentum space are given by

$$\mathbf{K} = \frac{2\pi}{3a}\left(1, \frac{1}{\sqrt{3}}\right), \; \mathbf{K'} = \frac{2\pi}{3a}\left(1, -\frac{1}{\sqrt{3}}\right). \tag{2.2.4}$$

2.2.2 Energy Dispersion

The Hamiltonian of this system according to the tight-binding model considering nearest neighbour and next-nearest neighbour hopping of electrons has the form [49]

$$\mathcal{H} = -t \sum_{<i,j>,\sigma} \left(a^{\dagger}_{\sigma,i} b_{\sigma,j} + H.c.\right) - t' \sum_{<<i,j>>,\sigma} \left(a^{\dagger}_{\sigma,i} a_{\sigma,j} + b^{\dagger}_{\sigma,i} b_{\sigma,j} + H.c.\right), \tag{2.2.5}$$

where $a_{i,\sigma}$ ($a^{\dagger}_{i,\sigma}$) is the operator for creating(annihilating) an electron with spin $\sigma(\sigma \uparrow\downarrow)$ on site $\mathbf{R_i}$ on sub-lattice A, similarly for sub-lattice B. $t \approx 2.8\,\text{eV}$ is the hopping energy between

nearest neighbours (inequivalent sub-lattices) and t' is the next nearest neighbour hopping energy (same sub-lattice). The corresponding energy bands are given by [49]

$$\begin{aligned} E_{\pm}(\mathbf{k}) &= \pm t\sqrt{3+f(\mathbf{k})} - t'f(\mathbf{k}), \\ f(\mathbf{k}) &= 2\cos\left(\sqrt{3}k_y a\right) + 4\cos\left(\frac{\sqrt{3}}{2}k_y a\right)\cos\left(\frac{3}{2}k_x a\right), \end{aligned} \tag{2.2.6}$$

where the plus sign gives the conduction band or π^* band and the minus sign gives the lower valence band or π band. It is easy to see that a finite value of t' would result in an asymmetry between the π and π^* bands. Figure 2.2 shows the band structure of graphene with this slight asymmetry due to a finite value of $t' = -0.1t$ [1].

As such Eq.(2.2.6) gives the full dispersion for single-layered graphene and in principle we are done here. Nevertheless, to appreciate the uniqueness of this band structure, we have to zoom-in close to the **K** points of the Brillouin zone (inset of Figure 2.2) where most of the excitement around graphene is centered. If we expand Eq.(2.2.6) about $\mathbf{k} = \mathbf{K} + \mathbf{q}$ ($|\mathbf{q}| << \mathbf{K}$) upto second order in q/K [49]

$$E_{\pm}(\mathbf{q}) \approx 3t' + \hbar v_F|\mathbf{q}| - \left(\frac{9t'a^2}{4} \pm \frac{3ta^2}{8}\sin(3\theta_{\mathbf{q}})\right)|\mathbf{q}|^2, \tag{2.2.7}$$

where $v_F = 3ta/2\hbar = 0.97 \times 10^6\, m/s$ (with $t = 3\,\text{eV}$ and $a = 0.142\,\text{nm}$) gives the Fermi velocity of graphene and

$$\theta_{\mathbf{q}} = \arctan\left(\frac{q_y}{q_x}\right) \tag{2.2.8}$$

is the angle in momentum space. With $t' = 0$ and retaining t upto the linear term, we arrive at the famous linear dispersion of graphene i.e.

$$E_{\pm}(\mathbf{q}) = \pm\hbar v_F|\mathbf{q}|. \tag{2.2.9}$$

This linear dispersion relation implies an energy independent group velocity $v_{group} = \frac{1}{\hbar}\frac{\partial E}{\partial q} = v_F$ which is very different from the usual parabolic dispersion for free electrons in a metal $\epsilon(q) = q^2/2m$ where the velocity $v = \sqrt{2E/m}$ changes substantially with energy. Most importantly, we note that this energy dispersion resembles the energy of massless particles which are quantum mechanically described by the Dirac Equation. This is also the reason behind naming the **K** points of the Brillouin zone as the Dirac Points.

We also note that this linear dispersion is a long-wavelength continuum property of graphene carriers valid only for $q << K$. A good way to estimate a cut-off wave vector q_c would be to demand that the carrier energy $E_c < 0.4t\,(\sim 1\,\text{eV})$ so that one can ignore the lattice effects. This leads to $k_c = 0.25\,\text{nm}^{-1}$.

[1] The value of t' is not well known but *ab initio* calculations have shown $0.02t \lesssim t' \lesssim 0.2t$. Experiments on cyclotron resonance have found $t' \approx 0.1\,\text{eV}$ [49]

2.2.3 The Dirac Formalism

It is possible to recast the tight-binding Hamiltonian of Equation 2.2.5 in the following form assuming $t' = 0$ and some more involved algebra [49],

$$\mathcal{H} = -i\hbar v_F \int dxdy \left[\hat{\Psi}_1^\dagger(\boldsymbol{r})\boldsymbol{\sigma}\cdot\nabla\hat{\Psi}_1(\mathbf{r}) + \hat{\Psi}_2^\dagger(\mathbf{r})\boldsymbol{\sigma}^*\cdot\nabla\hat{\Psi}_2(\mathbf{r})\right], \tag{2.2.10}$$

where $\sigma = (\sigma_x, \sigma_y)$ are the Pauli matrices and $\hat{\Psi}_i^\dagger(\mathbf{r}) = (a_i^\dagger, b_i^\dagger)\,(i = 1, 2)$ i.e. the set of creation operators at the $\mathbf{K}$ and $\mathbf{K}'$ points respectively. This exactly resembles superposition of two copies of massless Dirac like Hamiltonians, one holding for momentum $\mathbf{p}$ around $\mathbf{K}$ point and the other for $\mathbf{p}$ around $\mathbf{K}'$ point. The two-component electron wave function $\psi(\mathbf{r})$ close to the $\mathbf{K}$ point will then obey the 2D Dirac equation.

$$-i\hbar v_F\sigma\cdot\nabla\psi(\mathbf{r}) = E\psi(\mathbf{r}). \tag{2.2.11}$$

Combining the two equations for both $\mathbf{K}$ and $\mathbf{K}'$ points and re-writing in momentum space

$$\hbar v_F k \begin{pmatrix} \sigma\cdot\hat{\mathbf{k}} & 0 \\ 0 & \sigma^*\cdot\hat{\mathbf{k}} \end{pmatrix} \begin{pmatrix} \psi_{\mathbf{K}}(\mathbf{k}) \\ \psi_{\mathbf{K}'}(\mathbf{k}) \end{pmatrix} = \pm E \begin{pmatrix} \psi_{\mathbf{K}}(\mathbf{k}) \\ \psi_{\mathbf{K}'}(\mathbf{k}) \end{pmatrix}. \tag{2.2.12}$$

Here, $E = \pm\hbar v_F k$ are the eigen energies for the π^* and π bands respectively. The corresponding solution spinors around $\mathbf{K}$ and $\mathbf{K}'$ points are given by [53]

$$\psi_{\pm,\mathbf{K}}(\mathbf{k}) = \frac{1}{\sqrt{2}}\begin{pmatrix} 1 \\ \pm e^{i\theta_{\mathbf{k}}} \end{pmatrix},\ \psi_{\pm,\mathbf{K}'}(\mathbf{k}) = \frac{1}{\sqrt{2}}\begin{pmatrix} 1 \\ \pm e^{-i\theta_{\mathbf{k}}} \end{pmatrix}. \tag{2.2.13}$$

where $\theta_{\mathbf{k}}$ is given by Eq.(2.2.8). The following important conclusions can be derived from the above eigen solutions.

1. $\psi_{\pm,\mathbf{K}}(\mathbf{k})$ and $\psi_{\pm,\mathbf{K}'}(\mathbf{k})$ are related by time reversal symmetry.

2. A Berry's Phase of π can be derived from the eigen states in Eq.(2.2.13) [53] which is a characteristic of spinors.

3. Both wave-functions are also eigen functions of the helicity operator $\hat{h} = \frac{1}{2}\sigma\cdot\frac{\mathbf{p}}{|\mathbf{p}|}$ which is defined as the projection of the pseudospin σ along the direction of the momentum. This is so because $\hat{h}$ is proportional to the Hamiltonian for both $\mathbf{K}$ and $\mathbf{K}'$ as it is evident from eqn. 2.2.12.

$$\hat{h}\psi_{\mathbf{K}}(\mathbf{r}) = \pm\frac{1}{2}\psi_{\mathbf{K}}(\mathbf{r}),\ \hat{h}\psi_{\mathbf{K}'}(\mathbf{r}) = \mp\frac{1}{2}\psi_{\mathbf{K}'}(\mathbf{r}). \tag{2.2.14}$$

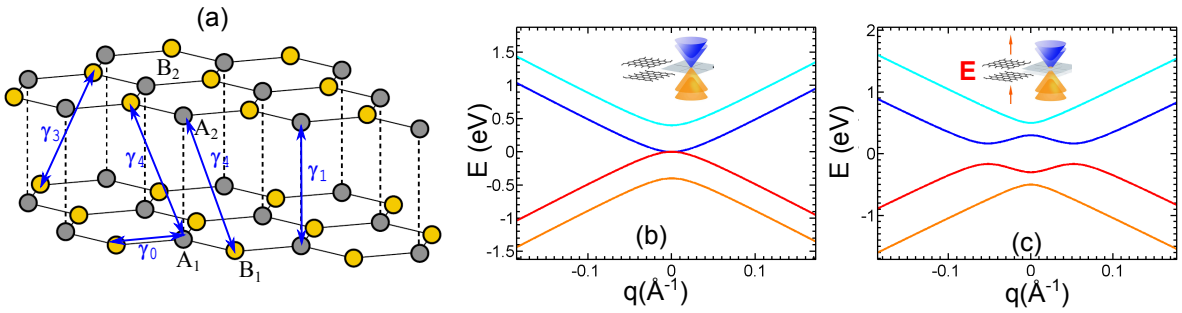

Figure 2.3: Lattice structure and energy dispersion relation in bilayer graphene. (a) Lattice structure of Bernal (A-B) stacked bilayer graphene. γ_i, $i = 1, 2, 3, 4$ indicates the inter and intra-layer hopping parameters, see text [54]. (b) The four energy bands (different colors) corresponding to $V = 0\,\text{eV}$ and (b)$V = 0.3\,\text{V}$. Intra-plane, nearest neighbour (NN) hopping parameter $\gamma_0 = t = 3\,\text{V}$ and inter-plane, NN hopping energy $\gamma_1 = t_\perp = 0.4\,\text{eV}$. The insets show a three dimensional schematic for each case.

Therefore the electrons (holes) have a positive (negative) helicity at **K** point and negative (positive) helicity at the **K′** point. In other words, the electron or hole states have a well-defined helicity or chirality.

2.2.4 Bilayer Graphene

Bilayer graphene consists of two graphene monolayers that are weakly coupled by inter-layer carbon hopping. Figure 2.3(a) shows the lattice structure for A-B or Bernal stacked bilayer graphene. The tight-binding approach used to derive the dispersion relation in SLG can also be applied in this case. The different inter and intra-layer hopping terms have been indicated in (a). The intra-layer, nearest neighbour hopping energy is $\gamma_0 = t \approx 3\,\text{eV}$ while the interlayer hopping energies are $\gamma_1 = t_\perp \approx 0.4\,\text{eV}$, $\gamma_3 = 0.3\,\text{eV}$ and $\gamma_4 = 0.04\,\text{eV}$. If γ_3 and γ_4 are ignored ($\gamma_{3,4} < t_\perp$), then for A-B stacking of the graphene layers, the low energy, long-wavelength dispersion relation for bilayer graphene [47] is given by

$$E_\pm(q) = \pm\left[V^2 + \hbar^2 v_F^2 q^2 + t_\perp^2/2 \pm \sqrt{4V^2\hbar^2 v_F^2 q^2 + t_\perp^2 \hbar^2 v_F^2 q^2 + t_\perp^4/4}\right]^{1/2}, \tag{2.2.15}$$

where $v_F = 3ta/2\hbar$, V is the potential difference between the two C layers which can exist when an external electric field is applied perpendicular to their plane. This will lead to the opening of an energy gap in the band structure as shown in Figure 2.3. The four energy eigen values $E(q)$ for a given value of q stated above, reflects the four degrees of freedom (two equivalent sub-lattices in each layer) associated with tight-binding Hamiltonian of bilayer graphene, indicated by the four different color curves in Figure 2.3(a) and (b).

For $V = 0$, Eq.(2.2.15), reduces to a simple parabolic dispersion for small q, ($\hbar v_F q << t_\perp$):

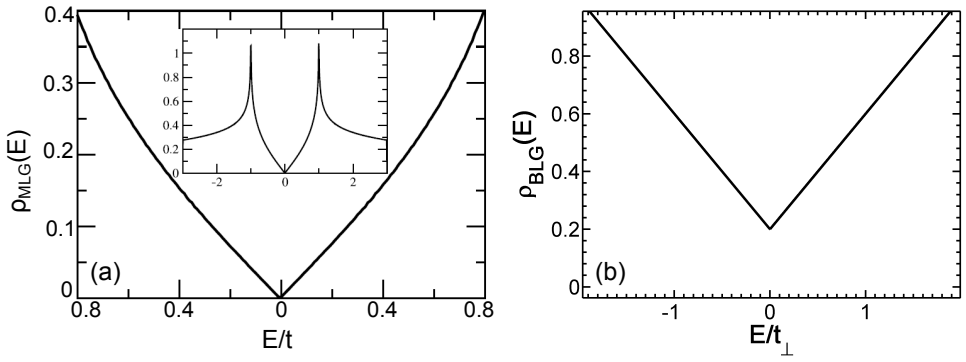

Figure 2.4: Electronic density of states (DOS) of single-layered (SLG) and bilayer (BLG) graphene. (a) DOS of SLG close to the Dirac point. Inset shows the DOS for the full bandwidth [49]. (b) DOS of BLG for $V = 0$ ($v_F = 10^6\,\mathrm{ms}^{-1}$, $t_\perp = 0.4\,\mathrm{eV}$), calculated using Eq.(2.2.20).

$E(q) \approx \hbar^2 v_F^2 q^2/t_\perp = \hbar^2 q^2/2m$, where $m = t_\perp/(2v_F^2) \approx (0.03 - 0.05)m_e$, m_e being the electronic mass. For large q ($\hbar v_F q >> t_\perp$): $E(q) \approx \hbar v_F q$, exactly the same as for SLG. This parabolic to linear cross-over at $V = 0$ is best described by re-writing eqn 2.2.15 in the following form

$$E_{BLG} = \mp m v_F^2 \pm m v_F^2 \left[1 + \left(\frac{q}{q_0}\right)^2\right]^{1/2}, \tag{2.2.16}$$

where $q_0 = t_\perp/(2\hbar v_F) \approx 0.3\,nm^{-1}$ for $m \approx 0.03 m_e$.

The charge carriers in BLG continue to be chiral due to A/B sub-lattice symmetry resulting in conservation of the pseudospin index.

2.2.5 Electronic Density of States

With the energy dispersion relations for both monolayer and bilayer graphene at our disposal, it is now straight-forward to calculate the respective DOS. We begin by writing down the general expression for charge carrier density at temperature T.

$$n(T) = \int_0^\infty \rho(E) f(E,T) dE \tag{2.2.17}$$

where $f(E,T)$ is the Fermi distribution function and $\rho(E)$ is the DOS. For 2D system like graphene, DOS is given by

$$\rho(E) = \frac{g_s g_\nu}{2\pi} \left| k(E) \frac{dk(E)}{dE} \right| \tag{2.2.18}$$

Here g_s, g_ν stands for spin and valley degeneracy respectively, both being = 2 for SLG and BLG.

Substituting $k(E)$ from the linear dispersion relation Eq.(2.2.9) that holds for SLG, in the low energy, long-wavelength limit ($k \ll K$), in the above equation, we arrive at the following expression for DOS.

$$\rho(E) = \frac{g_s g_\nu}{2\pi} \frac{|E - E_D|}{(\hbar v_F)^2} \tag{2.2.19}$$

where E_D represents the Dirac point energy. Figure 2.4(a) shows the DOS for monolayer graphene derived using the full dispersion relation [Eq.(2.2.6)]. The zoom-in shows the variation over a larger energy bandwidth where it is clear that at higher energies, $\rho(E)$ shows significant deviation from this linear dependence on E found at energies close to E_D.

For bilayer graphene, the DOS for the lowest energy bands (red and blue curves in Figure 2.3(b)) can be calculated using the simplified dispersion expression given in eqn. 2.2.16 for $V = 0$.

$$\rho(E) = \frac{g_s g_\nu}{2\pi} \frac{1}{(\hbar v_F)^2} \left(|E - E_D| + \frac{t_\perp}{2} \right) \tag{2.2.20}$$

Note that the DOS (shown in Figure 2.4(b)) is still linear for BLG with the important difference that even at $E = E_D$, there is still a finite DOS, which is not the case for SLG.

Finally, all that remains is to find the total charge carrier density n by plugging in $\rho(E)$ in Eq.(2.2.17). For simplicity, we assume $T = 0$. Hence, for SLG,

$$n = \int_0^{E_F} \rho(E) dE = \frac{g_s g_\nu}{4\pi} \left(\frac{E_F - E_D}{\hbar v_F} \right)^2 \tag{2.2.21}$$

In case of BLG, using the dispersion relation for $V = 0$, i.e. eqn.2.2.16, we obtain the following expression for carrier concentration,

$$n = \frac{g_s g_\nu}{2\pi} \frac{1}{(\hbar v_F)^2} \left(\frac{(E_F - E_D)^2}{2} + \frac{t_\perp}{2} |E_F - E_D| \right) \tag{2.2.22}$$

For $|E_F - E_D| \ll t_\perp$, the quadratic term can be dropped after which we obtain the following simplified expression.

$$n = \frac{g_s g_\nu}{2\pi} \left(\frac{m}{\hbar^2} \right) |E_F - E_D| \tag{2.2.23}$$

With this we have revisited the basic electronic properties of both monolayer and bilayer graphene that will provide the foundation necessary for an efficient understanding of the remainder of this chapter.

2.3 Many body effects in Graphene: Screening

In our formulation of the tight-binding Hamiltonian for both single-layered and bilayer graphene which ultimately led to the linear dispersion in the former case, we have completely ignored the effect of electron-electron interactions in the system. Including these interactions will modify the dispersion relation and therefore the fundamental properties of these 2D systems will be affected. The simplest and the most important manifestation of electron-electron interactions in a material is the phenomenon of screening. In this section, we discuss the concept of screening and then see

how screening in graphene differs from screening in other two-dimensional systems. To derive the basics, we follow the standard text book on Solid State Physics by Ashcroft and Mermin [55] while to understand screening in graphene, we resort to the theory chapter on Graphene carrier transport by Shaffique Adam [56] with whom we collaborated to understand the results presented in Chapter 5.

2.3.1 General introduction to Screening in a 3D electron gas

Let us consider the simple picture of a rigidly held positive charge placed in a medium of an electron gas. It will obviously attract electrons from the neighborhood, creating a surplus of negative charges around it which will have the effect of reducing its electric field. This damping of electric fields caused by mobile charge carriers in a system is referred to as *screening*. The electrostatic potential arising from this positive charge (volume charge density $\rho(\mathbf{r})$) alone is given by Poisson's equation,

$$-\nabla^2\phi^{ext}(r) = \frac{\rho^{ext}(\mathbf{r})}{\epsilon_0}, \tag{2.3.1}$$

where $\epsilon_0 = 8.85 \times 10^{-12}\,\mathrm{Fm}^{-1}$ is the permittivity of free space. Let us define the charge density induced in the medium as $\rho^{ind}(\mathbf{r})$ and the total charge density as $\rho(\mathbf{r})$. Then the total potential will be given by

$$-\nabla^2\phi(r) = \frac{\rho(\mathbf{r})}{\epsilon_0}, \tag{2.3.2}$$

where $\rho(\mathbf{r}) = \rho^{ext}(\mathbf{r}) + \rho^{ind}(\mathbf{r})$. By analogy with the theory of dielectric media, we make two assumptions. Firstly, the external potential $\phi^{ext}(r)$ and the overall potential $\phi(r)$ are linearly related in the manner $\phi^{ext}(r) = \int d\mathbf{r}'\epsilon(\mathbf{r},\mathbf{r}')\phi(r')$, where $\epsilon(\mathbf{r},\mathbf{r}')$ is called the static dielectric function and is the quantity that represents the screening properties of a given system. For an isotropic system, $\epsilon(\mathbf{r},\mathbf{r}')$ can depend only on the separation between the two points $\mathbf{r}$ and $\mathbf{r}'$. Hence, $\epsilon(\mathbf{r},\mathbf{r}') = \epsilon(\mathbf{r}-\mathbf{r}')$. Therefore, we can write

$$\phi^{ext}(r) = \int d\mathbf{r}'\epsilon(\mathbf{r}-\mathbf{r}')\phi(r'). \tag{2.3.3}$$

Invoking the convolution theorem for Fourier transformations, we can relate the Fourier coefficients of $\phi^{ext}(r)$ and $\phi(r)$ in the following manner.

$$\phi^{ext}(q) = \epsilon(q)\phi(q). \tag{2.3.4}$$

Secondly, we assume that the induced charge distribution $\rho_{ind}(\mathbf{r})$, also depends linearly on $\phi(\mathbf{r})$ (valid for a sufficiently weak ϕ). In that case, their Fourier transforms will satify the following relation.

$$\rho^{ind}(q) = \chi(q)\phi(q), \tag{2.3.5}$$

where $\chi(q)$ is defined as the dielectric susceptibility of the medium. Eventually, by plugging every thing together, we arrive at the following equation that relates the dielectric function $\epsilon(q)$ to the susceptibility $\chi(q)$.

$$\epsilon(q) = 1 - \left(\frac{1}{\epsilon_0 q^2}\right)\chi(q) = 1 - \left(\frac{1}{\epsilon_0 q^2}\right)\frac{\rho^{ind}(q)}{\phi(q)}. \tag{2.3.6}$$

The above equation can be re-written in the following form which will be useful later (section 2.3.2)

$$\epsilon(q) = 1 + V(q)\Pi(q). \tag{2.3.7}$$

where $V(q) = \frac{e^2}{\epsilon_0 q^2}$ is just the Fourier transform of the Coulomb potential $V(r) = \frac{e^2}{4\pi\epsilon_0 r}$ and $\Pi(q)$ is called the dielectric polarizability function which is related to susceptibility by $\Pi(q) = -\chi(q)/e^2$.

As is evident from the above equation, to solve the problem of the total charge induced in the medium by the external potential, all that remains is to calculate $\chi(q)$ for the medium. The two most widely prevalent approaches to do this are the Thomas-Fermi theory which is the semi-classical limit of the Hartree theory (quantum many body theory, [55]). The other way is the Lindhard method or the Random Phase Approximation (RPA) which offers an exact Hartree calculation of the induced charge density in the presence of a self-consistent field of the external charge and the electron gas of the medium.

Thomas-Fermi Theory

In the presence of an external potential $\phi(r) = \phi^{ext}(r) + \phi^{ind}(r)$, the total number density of charged carriers in the system will be given by

$$n(r) = \int \frac{d\mathbf{k}}{4\pi^3} \frac{1}{e^{\beta\left(\frac{\hbar^2 k^2}{2m} - e\phi(r) - \mu\right)} + 1}, \tag{2.3.8}$$

where μ is the chemical potential or the Fermi energy of the system. Here, we have made an important assumption. The energy eigen value of a given state $\mathbf{k}$ has been considered as

$$\varepsilon(k) = \frac{\hbar^2 k^2}{2m} - e\phi(r). \tag{2.3.9}$$

But this description makes sense only in terms of wave-packets with a typical spread in position of $1/k_F$. It is therefore required that $\phi(r)$ should vary slowly on the scale of the Fermi wavelength. In terms of Fourier components, this means that the calculations of $\chi(q)$ will be reliable for $q \ll k_F$.

From Eq.(2.3.8), we can express the total number density of charge carriers $n(r) = n_0(\mu) + n^{ind}(r)$ where

$$n_0(\mu) = \int \frac{d\mathbf{k}}{4\pi^3} \frac{1}{e^{\beta\left(\frac{\hbar^2k^2}{2m} - \mu\right)} + 1} \tag{2.3.10}$$

is the total number of charge carriers in the system in the absence of the potential $\phi(\mathbf{r})$ or equivalently can be looked upon as the density of background positive charges and $n^{ind}(\mathbf{r})$ is the number density of charges induced in the system by this positive background. Hence, the total induced charge can be written as

$$\rho^{ind}(r) = -e\left[n_0(\mu + e\phi(r)) - n_0(\mu)\right]. \tag{2.3.11}$$

This is the basic equation of non-linear Thomas-Fermi theory. If we furthur make the assumption that $\phi(r)$ is small enough, then $n_0(\mu + e\phi(r)) \approx n_0(\mu) + e\phi(r)\frac{\partial n_0}{\partial \mu}$, by Taylor expansion about μ. Therefore, we obtain

$$\rho^{ind}(r) = -e^2 \frac{\partial n_0}{\partial \mu}\phi(r) \tag{2.3.12}$$

The proportionality factor gives us $\chi(q)$ i.e.

$$\chi(q) = -e^2 \frac{\partial n_0}{\partial \mu} \tag{2.3.13}$$

Hence, finally, we arrive at the expression for the dielectric function of the electron gas in three dimensions.

$$\epsilon(q) = 1 + \left(\frac{e^2}{\epsilon_0 q^2}\right)\frac{\partial n_0}{\partial \mu} = 1 + \frac{q_{TF}^2}{q^2} \tag{2.3.14}$$

Here we introduce the quantity q_{TF} which is called the Thomas-Fermi wave vector given by

$$q_{TF}^2 = \left(\frac{e^2}{\epsilon_0}\right)\frac{\partial n_0}{\partial \mu} = \left(\frac{e^2}{\epsilon_0}\right)\nu(\mu) \tag{2.3.15}$$

where $\nu(\mu) = \frac{\partial n_0}{\partial \mu}$ is simply the DOS at Fermi level, provided we assume that temperature $T \ll T_F$.

The significance of q_{TF} is that it translates into a damping factor for the Coulomb potential in real space. For example if we consider the external potential due to a point charge Q, i.e. $\phi^{ext}(r) = \frac{Q}{4\pi\epsilon_0 r}$, then the corresponding Fourier transform is $\phi^{ext}(q) = \frac{Q}{\epsilon_0 q^2}$. The total potential will then be $\phi(q) = \frac{1}{\epsilon(q)}\phi^{ext}(q) = \frac{1}{\epsilon_0}\left(\frac{Q}{q^2 + q_{TF}^2}\right)$. Transforming back to real space, we get the resultant potential as

$$\phi(r) = \frac{1}{4\pi\epsilon_0}\frac{Q}{r}e^{-(rq_{TF})} \tag{2.3.16}$$

Hence the total potential is the starting Coulomb potential multiplied by a damping term that renders the total potential negligible beyond a distance $\gg 1/q_{TF}$.

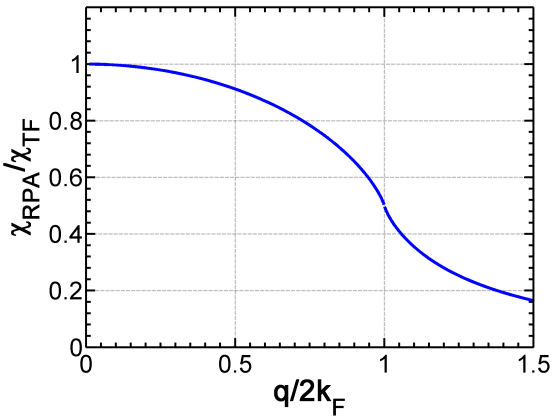

Figure 2.5: Ratio of susceptibilities determined from Thomas-Fermi and Lindhard or Random Phase Approximation (RPA) theory of screening.

So, to summarize, Thomas-Fermi theory provides a reasonable estimate of the screening response of a system to a slowly varying potential by formulating the analytical expression for the dielectric function of the system.

Lindhard Theory or Random Phase Approximation (RPA)

In this approach, we return to the one-electron Schrödinger equation in the presence of potential $\phi(\mathbf{r})$

$$-\frac{\hbar^2}{2m}\nabla^2\psi_i(\mathbf{r}) - e\phi(\mathbf{r}) = \varepsilon_i\psi_i(\mathbf{r}). \tag{2.3.17}$$

But unlike in the TF approach, no assumption about the slow varying nature of ϕ is made in this case. Instead, we start with the fact that the induced carrier density is needed only to linear order in ϕ. To do this, the above equation is solved perturbatively. Expanding the single electron wave function using the first-order stationary perturbation theory, we have

$$\psi_{\mathbf{k}} = \psi^0_{\mathbf{k}} + \sum_{\mathbf{k}'}\frac{1}{\varepsilon_{\mathbf{k}} - \varepsilon_{\mathbf{k}'}}\left\langle\psi^0_{\mathbf{k}'}\right|\phi\left|\psi^0_{\mathbf{k}}\right\rangle\psi^0_{\mathbf{k}'}. \tag{2.3.18}$$

The total charge density can be written as

$$\rho(\mathbf{r}) = -e\sum f_k\left|\psi_{\mathbf{k}}(\mathbf{r})\right|^2 = \rho^0(\mathbf{r}) + \rho^{ind}(\mathbf{r}), \tag{2.3.19}$$

where $f_{\mathbf{k}}$ is the equilibrium Fermi distribution of a free electron. With a little algebra, it can be shown that the Fourier transform of the induced charge density upto the linear order in ϕ is given by

$$\rho^{ind}(\mathbf{r}) = -e^2\int\frac{d\mathbf{k}}{4\pi^3}\frac{f_{\mathbf{k}-\frac{1}{2}\mathbf{q}} - f_{\mathbf{k}+\frac{1}{2}\mathbf{q}}}{\varepsilon_{\mathbf{k}-\frac{1}{2}\mathbf{q}} - \varepsilon_{\mathbf{k}+\frac{1}{2}\mathbf{q}}}. \tag{2.3.20}$$

Finally it can be shown that at $T = 0\,K$, the quantity $\chi(q) = \rho^{ind}(q)/\phi(q)$ is given by

$$\begin{aligned} \chi(q) &= -e^2\nu(\mu)\left[\frac{1}{2} + \frac{1-x^2}{4x}\ln\frac{1+x}{1-x}\right], \quad x = \frac{q}{2k_F} \\ \Rightarrow \frac{\chi(q)}{\chi_{TF}} &= \left[\frac{1}{2} + \frac{1-x^2}{4x}\ln\frac{1+x}{1-x}\right]. \end{aligned} \tag{2.3.21}$$

where $\chi_{TF} = -e^2\nu(\mu)$ is the value of $\chi(q)$ according to Thomas-Fermi theory. The above ratio is important as it highlights the differences between the two approaches used, TF and RPA, and has been plotted in Figure 2.5. We observe that for $q \to 0$, $\chi_{TF} = \chi_{RPA}$ as expected (section 2.3.1). However as $q \to 2k_F$ (scattering of electrons close to the Fermi level), the two theories increasingly deviate. In this regime, the RPA theory gives more insight into the nature of screening than the TF. The decay of a Coulomb potential will no longer be just a Yukawa type decay as predicted by TF theory but rather $\phi(r) \sim \frac{1}{r^3}\cos 2k_F r$, hence there is considerably more structure in the screened potential at large distances.

2.3.2 Screening in Graphene

So far what has been presented about *screening* strictly applies to electron gases in three dimensions. Although, it has familiarized us with the basic concepts, there will be some major differences as far as graphene is concerned. The band structure of graphene leading to the Dirac like dispersion of its charge carriers as well as its two dimensional nature will result in these differences. In this sub-section, we try to look into theses differences to gain a deeper understanding of the screening properties of the charge carriers in graphene.

Peculiarities in Screening properties for SLG and BLG

We start with the introduction of the interaction parameter : r_s or in case of SLG, what is more correctly called the fine-structure constant. Its importance lies in the fact that it quantifies the strength of electron-electron interactions in a system. It is defined as the ratio of the potential energy to the kinetic energy of the charge carriers.

$$r_s = \frac{V}{E_{KE}} \tag{2.3.22}$$

The interaction potential energy is given by $V = \frac{1}{4\pi\epsilon_0\kappa}\frac{e^2}{<r>}$ where κ is the background dielectric constant and $< r >$ is the average inter-atomic separation. In a two dimensional system, it can be shown that $< r >= 1/\sqrt{\pi|n|}$. The Kinetic energy E_{KE} is given by the Fermi energy of the system which for SLG $E_F = \hbar v_F\,\mathrm{sgn}(n)\sqrt{\pi|n|}$, as obtained from Eq.(2.2.21) and for BLG, $E_F = \frac{\hbar^2\pi n}{2m}$, as obtained from Eq.(2.2.23). Therefore, r_s in these two systems is given by

$$r_s^{SLG} = \frac{e^2}{4\pi\epsilon_0\kappa\hbar v_F} \approx 0.8, \qquad r_s^{BLG} = \frac{e^2}{4\pi\epsilon_0\kappa}\left(\frac{2m}{\hbar^2}\right)\frac{1}{\sqrt{\pi n}} \tag{2.3.23}$$

We straightaway note that for SLG, r_s is independent of carrier concentration n, implying that the strength of electron-electron interactions remain fixed. This is a most peculiar property in SLG which is a direct outcome of its linear dispersion. Since the dielectric constant κ can vary in the range $1 \leq \kappa \leq \infty$, r_s is bounded i.e. $0 \leq r_s < 2.2$. Hence, it is a weakly interacting system. Nevertheless, for graphene deposited on SiO_2, which is currently, the standard system for graphene based devices, $r_s \approx 0.8$ and this is still far greater than 1/137 which is the fine-structure constant in relativistic systems in QED. Hence, interactions are weak but cannot be treated non-perturbatively in SLG. In direct contrast to it is the case of BLG or 2D electron gases (2DEGs) where the interaction strength increases with decrease in carrier concentration.

Next, we look into the screening properties of the two graphene systems. In two dimensions, the Thomas-Fermi vector (that was defined for the 3D case by Eq.(2.3.15)), is given by

$$q_{TF} = \frac{e^2}{2\kappa\epsilon_0}\nu(E_F), \tag{2.3.24}$$

where $\nu(E_F)$ is the DOS at Fermi energy. By inserting the DOS of SLG and BLG given by Eq.(2.2.19) and Eq.(2.2.20) respectively, in the above equation, we find

$$q_{TF}^{SLG} = g_s g_\nu \left(\frac{e^2}{4\pi\epsilon_0\kappa\hbar v_F}\right)\sqrt{\pi n}, \qquad q_{TF}^{BLG} = g_s g_\nu \left(\frac{e^2}{4\pi\epsilon_0\kappa}\right)\frac{m}{\hbar^2} \tag{2.3.25}$$

Here, n is the charge carrier concentration. What is important to note is that q_{TF} for SLG increases with n whereas for bilayer graphene and also for 2D electron gases, it is independent of the charge carrier concentration. The dielectric function in two-dimensions can be written as

$$\epsilon(q) = 1 + \frac{q_{TF}}{q}. \tag{2.3.26}$$

For $q = k_F$, which is the case for electronic states contributing in charge transport, $\epsilon(q)$ depends on the ratio $q_s = q_{TF}/k_F$. This quantifies the strength of screening. In SLG, we can show that $q_s = 4r_s$ (using Eq.(2.3.25) and Eq.(2.3.23)), which implies a constant dielectric function $\epsilon = 1 + 4r_s$ since r_s is constant. This means that the functional form of the screened potential $\tilde{V}(q) = \frac{V(q)}{\epsilon(q)} = \frac{V(q)}{1+4r_s}$ is exactly the same as the unscreened potential $V(q)$. This is yet another peculiar property arising from the linear dispersion in SLG. In contrast for BLG and 2D electron gases, $q_s = \frac{e^2}{4\pi\epsilon_0\kappa}\left(\frac{4m}{\hbar^2}\right)\frac{1}{\sqrt{\pi|n|}}$ which can be obtained by considering $E_F = \hbar^2 k_F^2/2m$ in BLG (2.2.4) and using Eq.(2.2.23) for E_F and Eq.(2.3.25) for q_{TF}^{BLG}. This implies that screening becomes stronger in BLG as carrier density reduces and that it behaves like an unscreened system at high carrier densities. This counter-intuitive behavior is also true for other 2D systems like 2DEGs but is opposite of the screening in 3D metals [47].

Screening in SLG using RPA model

Here, we find out the screening properties of graphene using the Random Phase approach that has been briefly discussed in section 2.3.1. Within RPA, the dielectric function of the system is

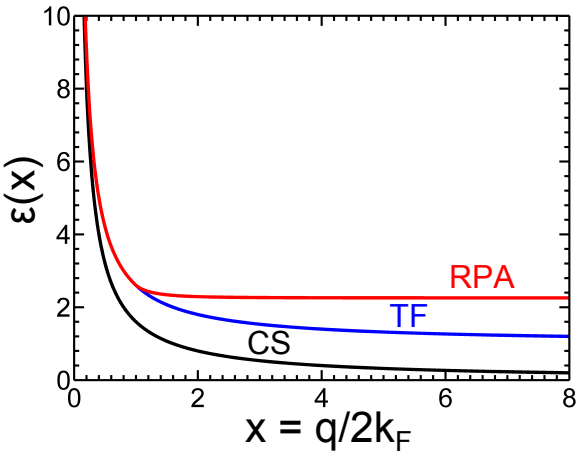

Figure 2.6: Dielectric function of graphene calculated using the three different approaches : Thomas-Fermi (TF), Random Phase Approximation (RPA) and Complete Screening (CS).

defined as in Eq.(2.3.7) using the dielectric polarizability function $\Pi(q)$. Following the procedure of Hwang et al. [57], this function is given by

$$\Pi(q) = \frac{g_s g_\nu}{L^2} \sum_{k,s,s'} \frac{f_k^s - f_{k'}^{s'}}{\varepsilon_{s,k} - \varepsilon_{s',k'}} \frac{1 + ss' \cos\theta_{k,k'}}{2} \tag{2.3.27}$$

where $\mathbf{k}' = \mathbf{k} + \mathbf{q}$ is the wave vector corresponding to the scattered state and $\theta_{\mathbf{k},\mathbf{k}'}$ is the angle between state $\mathbf{k}$ and $\mathbf{k}'$. What is different for single-layered graphene is the sum over both electron bands ($s = 1$) and hole bands ($s = -1$) and the overlap between the spinor components of the wave-function.

Without going into the detailed derivation which can be found in [57], we come to the final expression for polarizability

$$\frac{\Pi(q = 2k_F x)}{\nu(E_F)} = \begin{cases} 1, & \text{for } x \leq 1 \\ 1 + \frac{\pi x}{4} - \frac{x}{2} \arcsin\left(\frac{1}{x}\right) - \frac{1}{2x}\sqrt{x^2 - 1}, & \text{for } x \geq 1 \end{cases} \tag{2.3.28}$$

Incorporating $\Pi(q)$ into eqn. 2.3.7, we get the full analytic expression for the dielectric function of graphene. This has been plotted in Figure 2.6 (red curve) along with $\epsilon_{TF} = 1 + \frac{q_{TF}}{q}$ (blue) as well as in the complete screening limit (black) where it is assumed that $q_{TF} \gg q$ and hence $\epsilon_{CS} = \frac{q_{TF}}{q}$. This importantly signifies the following two main points.

1. For $q \ll 2k_F$, $\epsilon \to \infty$, i.e. screening is perfect. For $q < 2k_F$, TF and RPA coincide for single-layered graphene. This is also consistent with what we saw in the case of three-dimensional electron gases (section 2.3.1).

2. For $q \gg 2k_F$, RPA alone gives a proper description for screening. At these high q values, graphene screens like a dielectric insulator with constant ϵ.

Eq.(2.3.28) can be simplified to obtain the following approximate expression for the dielectric function in SLG [29]

$$\epsilon(q) = \begin{cases} 1 + \frac{q_{TF}}{q}, & \text{for } q \leq 2k_F \\ 1 + \frac{r_s \pi}{2} & \text{for } q > 2k_F. \end{cases} \tag{2.3.29}$$

2.4 From local Disorder to Macroscopic Carrier Transport in Graphene

Upto this point, we have built up a picture of graphene that in reality is little more than a scientific concept. A single sheet of carbon atoms with a Dirac like dispersion, isolated from all kinds of interactions both from the external world as well as electron-electron interactions from within, is clearly a simple theoretical construct. To take this concept from the confines of its theoretical framework and plant it in reality, we have to plug in these perturbations one by one. Switching on the interactions from within i.e. electron-electron (e-e), electron-phonon (e-ph) and electron-plasmon (e-pl) interactions have the effect of renormalizing graphene electronic structure as well as creating new inelastic excitation tunneling channels [58][59][60]. Hence, the screening properties that have been discussed in the previous section with the linear dispersion in mind, might have to undergo some modifications.

Further, the graphene that we deal with in our day to day experiments, in particular graphene on SiO_2 is not really a single atomic sheet with a homogeneously defined carrier density that we control with the backgate. Random charged impurities on the substrate [61], rippled morphology of the graphene [62] or even defects in the graphene lattice [63] will render the effective charge distribution inhomogenous. Although extraneous in the sense that graphene linear dispersion is not affected, the effect of this disorder is by no means negligible with major implications in the dynamics of carrier transport in graphene. Figure 2.7 shows a simulated projection of the disordered potential on the substrate giving rise to carrier inhomogeneities in the graphene sheet.

The effect of this disordered potential becomes more important at low carrier densities. In this scenario, the doping fluctuations induced by the underlying disorder, exceed the average carrier density of the graphene, leading to the formation of electron-hole puddles that render the Dirac point inaccessible to experiments. Such puddles have been measured experimentally [46][6]. Hence, this low density regime is especially governed by the physics of the interplay of disorder and screening rather than the exotic Dirac physics that people had hoped for. In fact, this is the simple explanation behind the absence of a universal minimum conductivity in graphene devices with a theoretically predicted value $\sigma = 4e^2/\pi h$ [4][5].

In this section, we start by discussing the basic transport properties of the charge carriers in graphene using the Drude-Boltzmann model. We will see that, assuming scattering by random charge impurities, this model gives the correct description for conductivity at high carrier

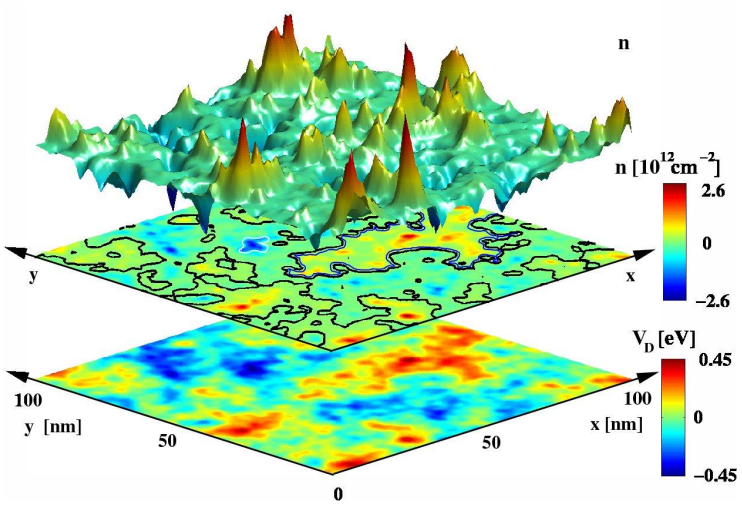

Figure 2.7: Doping inhomogeneities induced in graphene by disordered impurity potential. Lower color plot shows the spatial distribution of the disordered potential V_D due to charged impurities. Upper plot traces the distribution of the induced carrier concentration n, also shown above in 3D. The black lines define the boundary of e-h puddles [64].

densities but the low density regime remains rather vague. To understand this regime, we need to quantitatively analyze the statistics of the local charge disorder. In this context, the local correlation function of the screened disordered potential is introduced. Using a self-consistent approach, we will then extract the amplitude of fluctuations both for charge and screened potential disorder and find a length scale characterizing the decay of these local correlations (the puddle size). All derivations shown in this section are based on the theoretical work by Adam et al. [29][48][56].

2.4.1 Charge Carrier Transport in Graphene

Main Features in Experimental Field Effect Curves

Measurement of the Field effect is one of the most basic and at the same time highly important characterization of graphene devices as it provides a direct way to estimate the dynamic properties of its charge carriers. Figure 2.8 shows the field effect curves measured by Chen et al. [61] for different concentration of charged impurities adsorbed on graphene. We observe the following main features that are common to all of them:

1. Finite minimum conductivity σ_0.
2. σ_0 occurs at a non-zero gate voltage V_D^0 that gives the Charge neutrality point.
3. Finite broadening about the minimum at V_D^0.
4. Away from V_D^0, σ scales almost linearly with backgate voltage (at least for high impurity concentrations).

In the subsequent sections, we discuss the reasons behind each of these features.

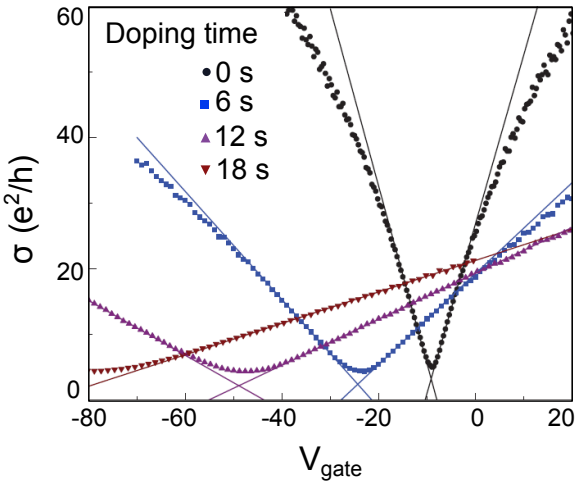

Figure 2.8: Change of conductivity σ dependence on backgate V_{gate} with increased impurity concentration (by depositing potassium atoms at $T = 20\,K$ in UHV). Lines represent fits to Eq.(2.4.6) in accordance with Drude-Boltzmann model [61].

Drude-Boltzmann model for carrier transport at high densities

Transport of charge carriers in graphene in the high density regime can be treated using the semi-classical Drude-Boltzmann formalism [29]. The theory is valid in low-disorder systems where $k_F l_e \gg 1$, l_e being the electronic mean free path of the charge carriers. In case of graphene $k_F l_e \geq 4$ for low carrier densities (n) and ≈ 100 for high n and hence application of this formalism is justified. Moreover, it is the standard theory used to describe Coulomb scatterers in 2D systems which happens to be the case in graphene as we shall see shortly.

The conductivity is given by Einstein's relation

$$\sigma = e^2 \nu(E_F) D \tag{2.4.1}$$

where $\nu(E_F)$ is the DOS at Fermi energy and $D = v_F^2 \tau/2 = v_F l_e/2$ is the diffusion constant in two dimensions, τ being the scattering time. Substituting these values in the above equation, we have the final expression

$$\sigma = \frac{2e^2}{h} k_F l_e \tag{2.4.2}$$

Using the Boltzmann transport theory, the scattering time can be evaluated.

$$\frac{\hbar}{\tau} = \frac{4}{\pi} \frac{k_F}{v_F} \int_0^1 d\eta \sqrt{1-\eta^2} \left| \frac{V(2k_F\eta)}{\epsilon(2k_F\eta)} \right|^2 \tag{2.4.3}$$

where $V(q = 2k_F\eta)$ is the bare scattering potential and $\epsilon(q = 2k_F\eta)$ is the static dielectric function. What becomes clear straight away is that graphene transport is governed by the interplay between the disordered potential and screening in the system and each individually can

have a major impact in the overall behaviour. In this context, let us have a brief look at what this means for unscreened Coulomb scatterers and delta-correlated short range scatterers.

1. For unscreened Coulomb scatterers ($\epsilon = 1$), $V(q) \propto q^{-1}$ which implies $\tau \propto k_F$ implying that for a given n_{imp}, mean free path gets smaller and smaller as the Dirac point is approached $k_F \to 0$.

2. For short-range, delta correlated scatterers, $V(q) \sim q^0$ implying $\tau \sim 1/k_F$ causing the mean free path to increase and ultimately diverge at the Dirac point.

For a disordered potential $V(\mathbf{r})$ created by random charge impurities (which are Coulomb scatterers) trapped in the substrate and considering the static dielectric function according to RPA approximation as given in Eq.(2.3.29), it can be shown that [29]

$$\sigma \approx A[r_s]\frac{e^2}{h}\frac{n}{n_{imp}} = 20\frac{e^2}{h}\frac{n}{n_{imp}} \quad \text{for } r_s = 0.8 \tag{2.4.4}$$

where $A[r_s] = F_1[x = 2r_s]^{-1}$ and

$$\frac{F_1(x)}{x^2} = \frac{\pi}{4} + 3x - \frac{3x^2\pi}{2} + x(3x^2 - 2)\frac{\arccos[1/x]}{\sqrt{x^2 - 1}} \tag{2.4.5}$$

The linear dependence of σ on n as obtained in this semi-classical model, considering Coulomb scattering, explains the fourth feature of the experimentally observed field effect curves 4. This is a strong indication that scattering processes at work in present graphene samples (on SiO_2 for example), are indeed Coulombic in origin which once again justifies the use of the Drude-Boltzmann approach.

Conductivity in the full range of carrier density

Although, the linear dependence of conductivity on carrier density n is explained well by the Drude-Boltzmann model, the origin of the other features remain ambiguous. Nevertheless, based on our knowledge of the conductivity at high n, we can roughly extrapolate this dependence upto the low density limit at the charge neutrality point V_D^0.

$$\sigma(n) = \begin{cases} 20\frac{e^2}{h}\left(\frac{n^*}{n_{imp}}\right) & \text{if } n_g < n^* \\ 20\frac{e^2}{h}\left(\frac{n_g}{n_{imp}}\right) & \text{if } n_g > n^* \end{cases} \tag{2.4.6}$$

where n_g is the total carrier concentration and is given by $n_g = \alpha(V_{gate} - V_D^0)$, $\alpha = K\epsilon_0/et \approx 7.57 \times 10^{10}\,\mathrm{cm^{-2}V^{-1}}$ for a Si/SiO_2 substrate with the gate oxide thickness $t = 285\,\mathrm{nm}$ and dielectric constant $K = 3.9$. The carrier concentration induced by the gate voltage to achieve charge neutrality is given by $\bar{n} = \alpha V_D^0$. n^* is the residual carrier density at $V_{gate} = V_D^0$ which takes care of the finite minimum conductivity and the finite width of the plateau at minimum conductivity. The origin of this residual charge density and the reason for this finite broadening

of the conductivity observed at charge neutrality will become clear in the upcoming sections. Before moving on, we note that more advanced theories exist like the Effective Medium Theory (EMT) which are able to describe the full cross-over from high and low n [65]. But for our purpose, the above method based on RPA-Boltzmann model is sufficient.

Here is a short summary of the different important concentrations that we have discussed so far as well as those that will be needed shortly.

Quantity	Definition
n_{imp}	Concentration of charge impurities in the substrate.
$\bar{n}$	Carrier concentration induced by V_{gate} at which the impurity potential is neutralized. This is related to the charge neutrality point V_D^0 by $\bar{n} = \alpha V_D^0$.
n^*	Residual charge density at CNP.
n_g	Carrier concentration induced by the gate voltage with $n_g = 0$ at CNP. In general, $n_g = \alpha(V_{gate} - V_D^0)$.
$n(\mathbf{r})$	Total carrier concentration at position $\mathbf{r}$.
n_{rms}	Root mean square of the fluctuations in $n(\mathbf{r})$.

Table 2.1: Summary of the different charged particle concentrations.

2.4.2 Charge disorder and local correlations

We have seen in the last section how scattering from the disordered potential created by randomly charged impurities on the substrate, combined with the screening response of the carriers, determines the dynamics of transport at high carrier densities. At low carrier densities, this disorder will induce fluctuations in the doping giving rise to puddles of electron and holes. Intuitively it might still appear puzzling as to how carrier transport could continue in such a disordered system with innumerous pn junctions. It is due to the quantum relativistic phenomenon called Klein tunneling [3] that allows the chiral carriers in graphene to get transmitted across such barriers with 100 % efficiency on normal incidence (Figure 2.9). This ensures a finite non-vanishing conductivity close to the Dirac point.

To understand the low-carrier density regime, we have to start by acknowledging the fact that the carrier density is not homogeneous across the graphene sheet. We therefore introduce a spatially varying quantity $n(\mathbf{r})$ to describe the carrier concentration at position $\mathbf{r}$. The underlying disordered potential $V(\mathbf{r})$ created by random charge impurities embedded in the substrate is responsible for inducing fluctuations in $n(\mathbf{r})$. A quantitative measure of these fluctuations is the standard deviation in $n(\mathbf{r})$ i.e. n_{rms}. These fluctuations in turn have the effect of screening out this potential in a self-consistent manner resulting in a screened potential $\tilde{V}(\mathbf{r})$. This resultant

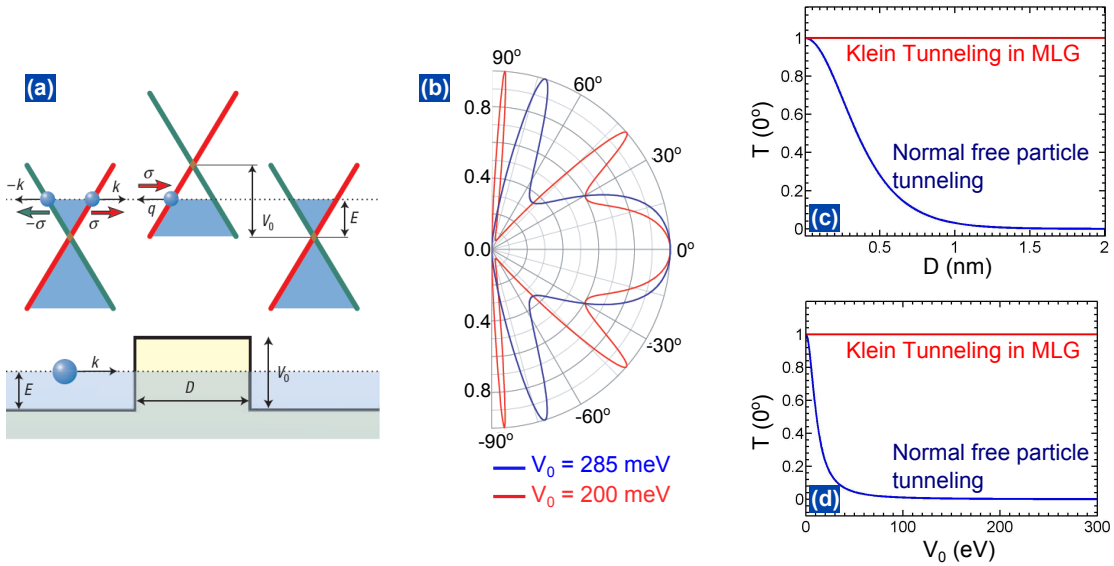

Figure 2.9: Klein tunneling of Dirac quasiparticles in graphene. (a) Schematic showing the tunneling of an electron, with energy E and pseudospin σ parallel to its momentum ($\mathbf{k}$), between two electron doped regions via a hole-doped region. (b) Transmission probablity T through a barrier of width $D = 100\,nm$ and height V_0 as a function of the incident angle. (c) T at normal incidence as a function of D ($V_0 = 285\,\text{meV}, E = 80\,\text{meV}$) and (d) V_0 ($D = 0.01\,\text{nm}, E = 80\,\text{meV}$) for Klein tunneling in graphene and normal quantum mechanical tunneling for a free electron in a square potential [3].

potential is manifested as shifts in the local Dirac point $E_D(\mathbf{r}) = -\hbar v_F\,\text{sgn}[n(\mathbf{r})]\sqrt{\pi|n(\mathbf{r})|}$.

A good way to characterize $\tilde{V}(\mathbf{r})$, is by considering its angular averaged auto-correlation function.

$$C(r) = \frac{1}{2\pi}\int_0^{2\pi} C(\mathbf{r})d\phi \tag{2.4.7}$$

where $C(\mathbf{r})$ is the 2D auto-correlation function given by

$$C(\mathbf{r}) = \int_{\mathbf{r}'} \tilde{V}(\mathbf{r}'+\mathbf{r})\tilde{V}(\mathbf{r}')d\mathbf{r}'. \tag{2.4.8}$$

The value of this auto-correlation function at $\mathbf{r} = 0$ is related to the RMS amplitude of the fluctuations in $\tilde{V}(\mathbf{r})$ in the following manner.

$$C(0) = \int_{\mathbf{r}'} \tilde{V}(\mathbf{r}')\tilde{V}(\mathbf{r}')d\mathbf{r}' = \left\langle \tilde{V}^2 \right\rangle = [\tilde{V}_{rms}]^2 + \left\langle \tilde{V} \right\rangle^2 \tag{2.4.9}$$

Hence if $\left\langle \tilde{V} \right\rangle = 0$ which is the case close to charge neutrality, then

$$C(0) = [\tilde{V}_{rms}]^2. \tag{2.4.10}$$

We note that $C(0)$ has no spatial dependence. Plugging this back in the expression for the angular averaged correlation function $C(r)$, we have

$$C(r) = C(0) \times A(r). \tag{2.4.11}$$

$A(r)$ is the normalized correlation function (because $A(0) = 1$) and is solely responsible for accounting for the spatial variation of $C(r)$. Writing $C(r)$ in this way is useful as it helps us to separate the spatial variations of the fluctuations in $\tilde{V}(\mathbf{r})$ from its RMS amplitude.

Theoretical Correlation function for Screened Coloumb Potential

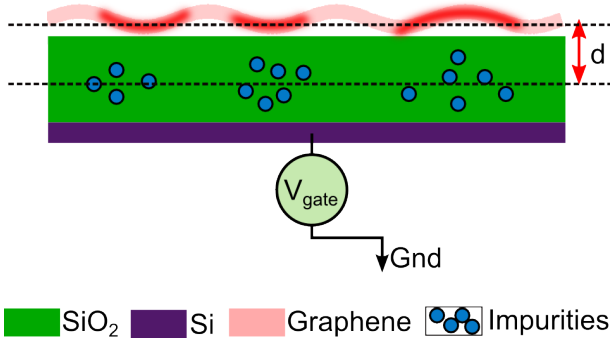

Figure 2.10: Sketch of charged impurity induced doping in Graphene. Reddish regions in the graphene indicate higher positive doping due to the negatively charged impurities embedded in the substrate.

Let us now theoretically calculate the correlation function. To do so, we make two assumptions. Firstly, $V(\mathbf{r})$ is created by a distribution of charged impurities n_{imp} embedded in the substrate at an average distance d from the plane of graphene as shown in Figure 2.10. The inhomogeneities in $n(\mathbf{r})$ induced by $V(\mathbf{r})$ will in turn induce a spatial variation in the screening properties of the graphene. This brings us to the next assumption that it is still possible to find a global dielectric function $\epsilon(q, n)$ which adequately describes these variations.

For a single charged impurity (with charge +e), Fourier transform of the potential created by it on a 2D plane at a distance d from it in a medium with dielectric constant κ is (in CGS units) is

$$\phi(q) = \frac{2\pi e^2}{\kappa}\left(\frac{e^{-qd}}{q}\right). \tag{2.4.12}$$

The corresponding screened potential is

$$\tilde{\phi}(q, n) = \frac{\phi(q)}{\epsilon(q, n)}. \tag{2.4.13}$$

The Correlation function for the screened potential created by an impurity concentration n_{imp} will be then given by [56]

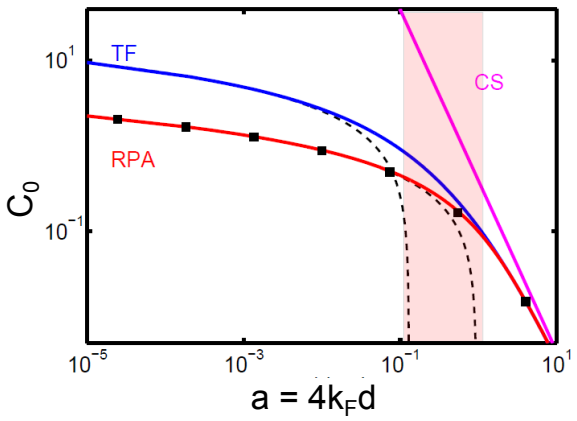

Figure 2.11: Comparison of $C_0(r_s = 0.8, a = 4k_F d)$ using different screening approximations [29]. All approximations agree in the high density regime but show major differences in the low density regime. Dashed lines represent small density analytic asymptotes for the Thomas Fermi and RPA. Squares show numerical evaluation of Eq.(2.4.14) using exact dielectric function reported in [57]. Highlighted (red) window approximately shows the regime accessible by experiments ($d = 1\,\text{nm}$).

$$\begin{aligned} C(r) &= n_{imp} \int \frac{d^2q}{(2\pi)^2} \left[\tilde{\phi}(q,n)\right]^2 e^{-i\mathbf{q}\cdot\mathbf{r}} \\ &= 2\pi n_{imp} \left(\frac{e^2}{\kappa}\right)^2 \int_0^\infty q \left[\frac{1}{\epsilon(q,n)} \frac{e^{-qd}}{q}\right]^2 J_0(qr)\, dq \end{aligned} \tag{2.4.14}$$

where $J_0(qr) = \frac{1}{2\pi}\int_0^{2\pi} e^{-iqr\cos\theta} d\theta$ is the Bessel function of zeroth order. Hence, close to the Dirac point, the RMS fluctuations of the screened disordered potential will be given by

$$\begin{aligned} [\tilde{V}_{rms}]^2 = C(0) &= 2\pi n_{imp} \left(\frac{e^2}{\kappa}\right)^2 C_0(r_s, a = 4k_F d) \\ \text{where } C_0(r_s, a = 4k_F d) &= \int_0^\infty q \left[\frac{1}{\epsilon(q,n)} \frac{e^{-qd}}{q}\right]^2 dq \end{aligned} \tag{2.4.15}$$

Here $r_s = \frac{e^2}{\kappa \hbar v_F}$ is the interaction parameter and ≈ 0.8 for graphene. $k_F = \sqrt{\pi |n(\mathbf{r})|}$ is the amplitude of the local Fermi wave-vector. So, C_0 and $C(0)$ both essentially signify the RMS fluctuations in the screened disordered potential, the main difference being that C_0 does not directly depend on the impurity concentration n_{imp}.

In Figure 2.11, $C_0(r_s, a)$ has been plotted as a function of $a = 4k_F d$ using the dielectric function $\epsilon(q, n)$ calculated using all the three methods discussed in section 2.3.2. We see that while all three approximations agree in the high density regime, there are significant deviations near charge neutrality. Although the Thomas-Fermi approach captures the right qualitative behaviour, it grossly underestimates the effect of screening. Hence, we shall follow the RPA method in future calculations. The exact analytic expression for $C_0(r_s, a)$ within the RPA approximation

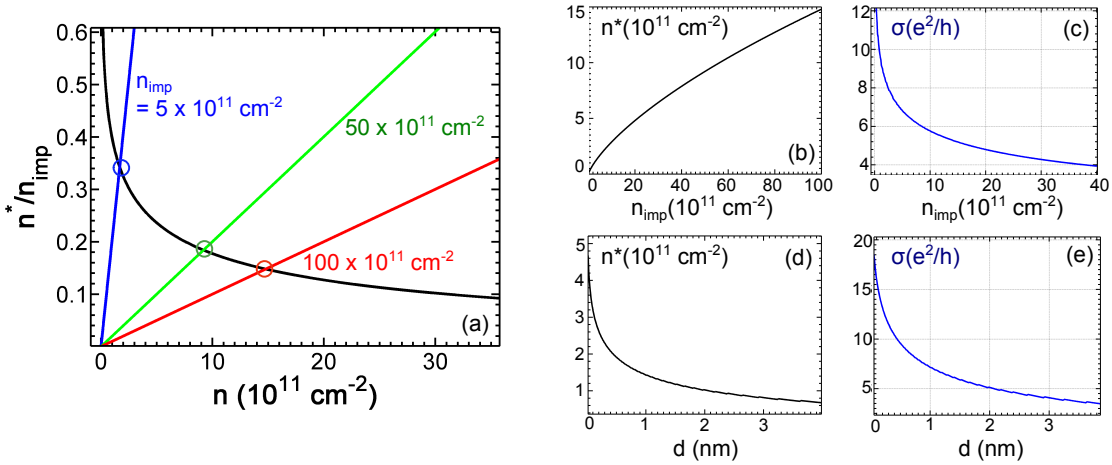

Figure 2.12: Residual charge density and Minimim conductivity. (a) Finding n^* self-consistently. Black curve represents the RHS of Eq.(2.4.17) and the straight lines represent the LHS for the indicated values of n_{imp}. The intersections give the solution n^*. (b) Variation of n^* and (c) minimum conductivity σ_0 with n_{imp} for $d = 1\,\text{nm}$. (d) Variation of n^* and (e) σ_0 with d for $n_{imp} = 4.0 \times 10^{11}\,\text{cm}^{-2}$.

is available in literature [29]. Since C_0 is proportional to the magnitude of the screened disorder potential fluctuations, this plot shows how the disorder is increasingly screened by higher number of charge carriers in the graphene which is expected.

Using this correlation function, we are now in a position to quantitatively analyze the remaining features in the field effect curves of graphene (section 2.4.1).

The Residual Charge carrier density at CNP: Self-Consistent Approach

As the system approaches Charge neutrality i.e. $V_{gate} \to V_D^0$, the fluctuations in $n(\mathbf{r})$ exceeds its mean value. These fluctuations do not allow the total carrier concentration to be absolutely zero but pin it to a minimum value which we define as the residual charge density n^*. In a more quantitative manner, it is defined as the charge carrier density at which the RMS fluctuations in the screened disordered potential becomes equal to the mean Dirac point[2] i.e.

$$\begin{aligned} \langle E_D(n^*)\rangle^2 &= \left[\tilde{V}_{rms}\right]^2 \\ \Rightarrow (\hbar v_F)^2 \pi n^* &= 2\pi n_{imp} \left(\frac{e^2}{\kappa}\right)^2 C_0(r_s, 4d\sqrt{\pi n^*}) \end{aligned} \tag{2.4.16}$$

This directly leads to the self-consistent equation to find n^*.

$$\frac{n^*}{n_{imp}} = 2r_s^2 C_0(r_s, a = 4d\sqrt{\pi n^*}) \tag{2.4.17}$$

[2] $\tilde{V}_{rms}$ here is in units of energy

The method to solve this equation has been graphically demonstrated in Figure 2.12(a). We find that n^* increases with increasing n_{imp}. This is expected since the higher the impurity concentration, the larger is the residual charge induced by it. But if n^* increases, one might naively expect σ_0 to increase with n_{imp} as well which is the opposite of what actually happens. This is understood by considering that there are two competing effects :(1) Increase in n^* means large number of charge carriers, hence larger conductivity σ_0. (2) On the other hand, large n^* also means stronger screening of the disorder. In the clean limit, n^* is too small so that the second effect can be neglected resulting in an overall increase of σ_0. However, in dirty samples, n^* is large resulting in strong screening and the two effects compete to produce a net decrease in σ_0. This also explains why the minimum conductivity σ_0 is found to vary from sample sample and not have a universal value of $4e^2/\pi h$ as expected in the quantum ballistic limit. Figure 2.12(d),(e) show that both n^* and σ_0 decrease as distance of impurities from graphene plane is increased which is what one would expect.

The concept of this residual charge density is very important in understanding the properties of graphene close to charge neutrality. It essentially represents the screened disorder potential $\tilde{V}(\mathbf{r})$. Besides being useful in finding the value of the finite minimum conductivity in graphene, it allows us to realize the following:

1. It gives the limiting carrier density below which the physics of charge disorder takes over. Hence the plateu width about the Dirac point is $\approx 2n^*$.

2. The shift in the plateau position of Charge neutrality from zero induced by the substrate impurities i.e. V_D^0 is related to n^* and can be calculated.

$$V_D^0 = \frac{\bar{n}}{\alpha} = \frac{1}{\alpha}\left(\frac{n_{imp}^2}{4n^*}\right) \tag{2.4.18}$$

3. The RMS fluctuations in $n(\mathbf{r})$ at the Dirac point or the charge disorder can also be calculated from n^*.

$$n_{rms} = n^*\sqrt{3} \tag{2.4.19}$$

The Complete Screening Limit

In the complete screening limit, achieved at very high carrier concentrations when the gate voltage is tuned far away from V_D^0, all three screening approximations give the same result for C_0 as seen in Figure 2.11. This can be obtained from Eq.(2.4.14) by substituting $n = n_g$ (carrier concentration induced by the backgate) as the effective carrier concentration. This is a valid approximation because in this regime $n_g \gg n_{rms}$. The expression for C_0 in this limit is

$$C_0^{CS} = \frac{1}{(2dq_{TF})^2} = \frac{1}{(2r_s a)^2} \tag{2.4.20}$$

Complete screening is achieved when $a > 1$ i.e.

$$n_g > \left(\frac{1}{16d^2\pi}\right) \tag{2.4.21}$$

For $d \sim 1\,\text{nm}$ which is a reasonable value for graphene on SiO_2, to reach the complete screening limit $n_g > 2 \times 10^{12}\,\text{cm}^{-2}$ which is still possible in experiments. But even if d drops to say $0.1\,\text{nm}$, n_g has to exceed about $200 \times 10^{12}\,\text{cm}^{-2}$, which is not at all feasible. Hence, most of the current experiments with graphene devices fall in the intermediate regime which we will discuss in the next sub-section.

Nevertheless, the complete screening limit is theoretically well understood and hence, it is important to calculate the charge disorder n_{rms} in this case.

$$n_{rms} = \frac{2}{\pi(\hbar v_F)^2} \,|\, \langle E_D(n_g)\rangle \,|\, |\delta E_D| \tag{2.4.22}$$

By setting $\langle E_D(n_g)\rangle = -\hbar v_F\,\text{sgn}(n_g)\sqrt{\pi|n_g|}$ and $\delta E_D = \tilde{V}_{rms} = \sqrt{[C(0)]}$, we arrive at the following expression for charge disorder.

$$n_{rms} = \left(\frac{n_{imp}}{8\pi d^2}\right)^{1/2} \tag{2.4.23}$$

The Intermediate Regime

Although the behaviour of graphene is well understood at the two extreme limits, i.e. near charge neutrality and in the limit of complete screening, the regime which is accessible to current experiments is the regime intermediate between these two as mentioned in the last section. Unfortunately, the theory for this cross-over region is not yet well developed.

The way charge disorder n_{rms} is calculated in this case is by extrapolating between the low density [Eq.(2.4.19)] and high density [Eq.(2.4.23)] limits and adding the two contributions in quadrature and solving for n_{rms} self-consistently [48]. This gives

$$n_{rms} = 2r_s\sqrt{n_{imp}C_0}\left[2n_g + 3r_s^2 n_{imp}C_0\right]^{1/2} \tag{2.4.24}$$

The above equation has been solved and the resultant charge disorder has been plotted in Figure 2.13 as a function of n_g. To do so, we evaluate C_0 using RPA approximation provided in [29]. The following steps have been followed to find n_{rms} at a given value of n_g.

1. For a given value of n_{imp} and d, we find the residual charge density n^*.
2. We assume a starting value of $n_{rms} = n^*\sqrt{3}$ [Eq.(2.4.19)].
3. A Gaussian distribution of n is set up ranging from $(n_g - 5n_{rms})$ to $(n_g + 5n_{rms})$ with mean $< n >= n_g$ and standard deviation n_{rms}.
4. C_0^{RPA} is evaluated for the whole distribution.
5. The average value of C_0^{RPA} is plugged in Eq.(2.4.24) to find n_{rms}.
6. This process is repeated till a consistent solution is found for n_{rms}.

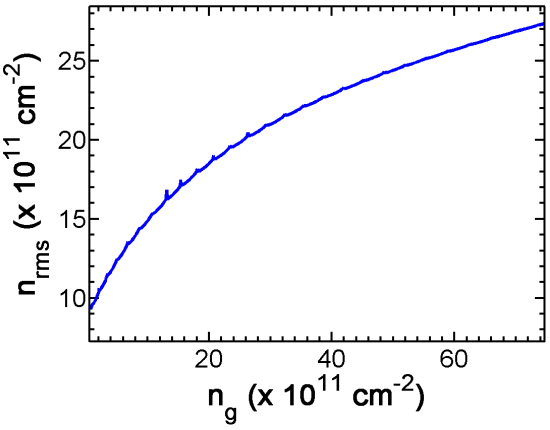

Figure 2.13: Charge disorder as a function of carrier density solved self-consistently, see text. $n_{imp} = 8.56 \times 10^{11}\,\mathrm{cm}^{-2}$ and $d = 2.09\,\text{Å}$.

Lateral extent of Disorder

So far we have concentrated on the amplitude of the screened disorder potential $\tilde{V}(\mathbf{r})$ and the magnitude of the charge disorder n_{rms} induced by it. Now, we move to the second part of the local correlation function in Eq.(2.4.11) which contains the spatial dependence or in other words, the normalized correlation $A(r) = C(r)/C(0)$.

The color plot in Figure 2.14(a) shows A for a disordered potential landscape created by Coulombic impurities [Eq.(2.4.14)], as a function of carrier concentration n_g and distance r. Each correlation curve has been obtained by numerically solving Eq.(2.4.14) since a closed analytic form does not exist. The RPA dielectric function $\epsilon(q, n)$ has been used as given by Eq.(2.3.29) to account for the screening. We observe that away from the charge neutrality ($n_g = 0$), $A(r)$ is characterized by a sharp decay whereas close to it, the correlations persist over longer distances. In Figure 2.14(b), $A(r)$ has been shown at the two extreme cases together with Gaussian functions that give the closest fit. Whereas at high n_g, the curves can be well described by a Gaussian, at low n_g, there is significant deviation from this Gaussian like decay with more structure persisting at quite high distances.

Nevertheless, it is important to extract a decay length for each $A(r)$ and we settle for the Gaussian function of the form

$$A^{G}_{fit}(r) = \exp\left[-\frac{|r|^2}{2\xi^2}\right]. \tag{2.4.25}$$

Figure 2.14(c) shows the correlation length ξ as a function of n_g both with RPA and TF screening, extracted in this way. The divergence of the decay length close to the Dirac point can be understood as a natural consequence of the small number of carriers in the system that result in very weak screening and the effect of any potential fluctuation can therefore be felt at long distances. At high carrier densities, the strong screening results in a rapid decay of any

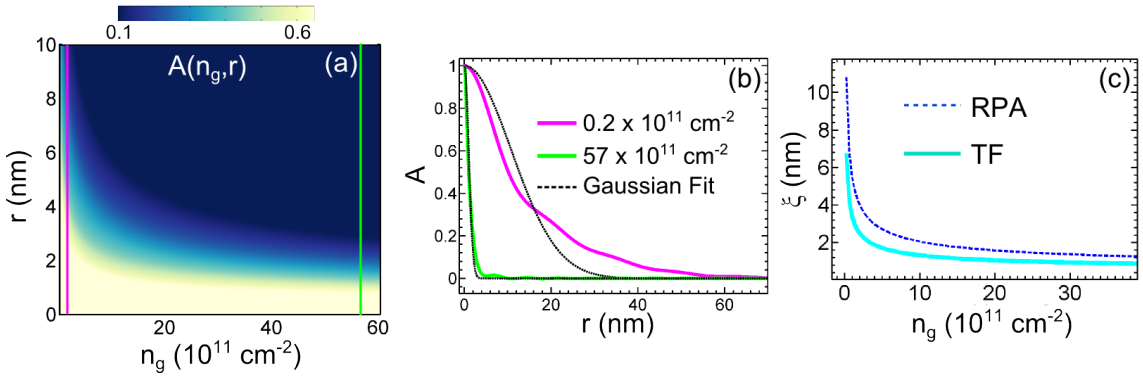

Figure 2.14: (a) Normalized auto-correlation of screened Coulomb potential as a function of n_g and distance r by numerically solving Eq.(2.4.14) ($n_{imp} = 4 \times 10^{11}\,\mathrm{cm}^{-2}$ and $d = 0.23\,\mathrm{nm}$). (b) Two cuts of $A(r)$ along lines indicated in (a) corresponding to two different values of n_g, along with the respective Gaussian fits. (c) Variation of correlation length ξ as a function of n_g, extracted as standard deviation of the best-fitting Gaussian, see text.

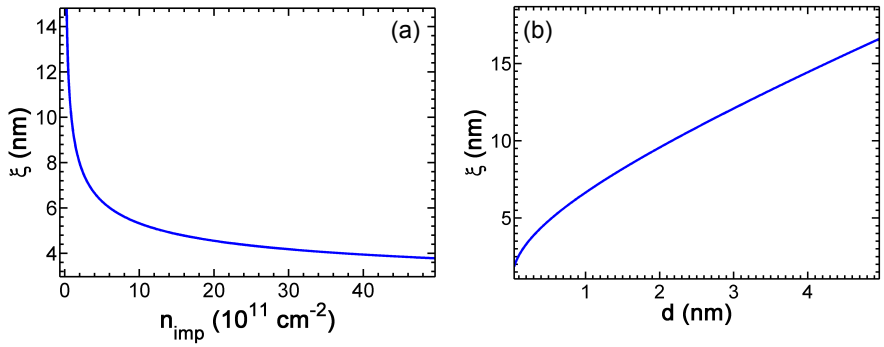

Figure 2.15: Variations in Correlation length ξ at $n_g = 0$ with (a) impurity concentration n_{imp} and (b) distance of the impurities from the plane of graphene using Eq.(2.4.26).

perturbations and hence explains the small values of ξ.

A more mathematical way to carry out this Gaussian mapping has been presented in [56]. For our purpose, it is sufficient to use the main results which are discussed below.

Firstly, we obtain the dependence of correlation length on the impurity concentration and distance of impurities from the graphene plane which is given by

$$\xi = \frac{1}{\sqrt{n_{imp}}} \frac{D_0}{4\pi r_s^2} \left[C_0(r_s, 4d\sqrt{\pi n^*}) \right]^{-3/2} \tag{2.4.26}$$

where full analytic expressions for D_0 and C_0 within the RPA approximation are available in literature [56]. In Figure 2.15, this dependence have been plotted.

Decrease of ξ with increase in n_{imp} is expected since the larger number of carriers induced produces stronger screening and hence smaller puddle size. Also, higher n_{imp} causes a higher density of inhomogenieties in the first place which also results in decrease of ξ. The reason for

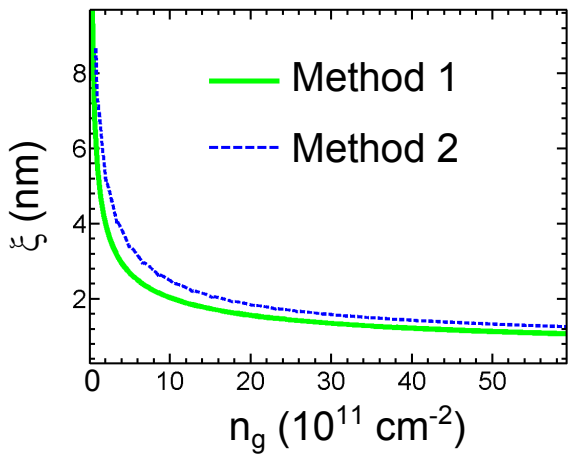

Figure 2.16: Correlation length as a function of carrier concentration n_g found using two different methods. In Method 1, ξ is found by Gaussian fitting of the $A(r)$ given by Eq.(2.4.14). In Method 2 Eq.(2.4.27) is used which incorporates the effect of changing charge disorder at different carrier concentrations.

the monotonic increase of ξ with d can be understood by considering the exponentially decaying nature of the single impurity potential $\tilde{\phi}(q,n) \propto e^{-qd}$ which implies a higher distance upto which a finite correlation persists.

Secondly, we also get an important relationship between the charge disorder n_{rms} and the correlation length.

$$\xi = \left[\pi n_{imp}\left\{\left(\frac{n_{rms}}{n^*}\right)^2 - 3\right\}\right]^{-1/2} \tag{2.4.27}$$

Using this relationship, ξ as a function of n_g has been replotted in Figure (2.16), marked as 'Method 2'. 'Method 1'just plots ξ extracted by direct Gaussian fitting of the theoretical $A(r)$ curves as illustrated in Figure 2.14. We see that the two are not exactly the same. This is because in 'Method 2', we need to find n_{rms} first using the procedure described in 6. This therefore incorporates the changing charge disorder at each carrier density whereas 'Method 1'does not take this into account.

Hence, with this we have completely characterized the local fluctuations in the screened impurity potential, the longitudinal as well as the spatial extent at different carrier densities. In this respect, we have obtained the four most fundamental quantities that define this disorder: $C(0)$, n_{rms}, n^* and ξ and numerically calculated their relationship to other known system parameters. We realize at this point that all these quantities are ultimately dependent on just two free parameters n_{imp} and d, both of which can be determined from the measurement of charge carrier transport. So, as it stands, this should be sufficient to completely predict the macroscopic transport as well as the microscopic correlations in the system.

2.5 Conclusion

The honey-comb structure of the graphene lattice gives rise to the Dirac-Weyl like dispersion of its charge carriers similar to quantum relativistic particles. However, unlike these systems, interactions in graphene are non-perturbative due to its rather high fine-structure constant (or interaction parameter r_s) of about 0.8 in comparison to 1/137 in the former case. This calls for a self-consistent approach to treat the effect of the disordered potential created by charged impurities trapped in the substrate. More specifically, the charge inhomogeneities induced by the underlying disorder will screen out this potential that created it in the first place. This leads to a subtle interplay between disorder and charge carrier response in graphene that ultimately determines the carrier dynamics in the entire system.

While in the high density regime, charge transport is diffusive, and the scattering from Coulombic impurities can be well described by the Drude Boltzmann model, in the low density regime the physics of disorder takes over. The properties of charge carriers in graphene are well understood in both these extreme limits. However, for intermediate carrier concentrations where the majority of experiments are conducted today, the scenario still remains rather ambiguous. The best way this cross-over regime is understood is by interpolating the results at the two extreme limits. But whether this approach is correct or not can only be decided by carefully designed experiments that can combine and correlate macroscopic with microscopic properties of the system.

As we have seen, existing theory dictates that all the important quantities characterizing screened disorder fluctuations like n_{rms}, n^*, ξ and $C(0)$ are ultimately related to n_{imp} and d, both of which can be extracted by conducting transport measurements on the sample. On the other hand, local measurements like scanning probe microscopy can directly measure the above quantities with high energy and spatial resolution. Hence, performing these two different kinds of measurements in parallel, will help us to test the existing theories and hence strengthen our understanding of the fundamental properties of one of the most widely investigated systems today.

Chapter 3

The Cryogenic Scanning Probe Microscope

Contents

3.1 Introduction **60**

3.2 Elements of Scanning Probe Microscopy **60**

3.2.1 Scanning Tunneling Microscopy & Spectroscopy 60

3.2.2 Atomic Force Microscopy 65

3.2.3 Kelvin Probe Force Microscopy 73

3.3 Experimental Setup **76**

3.3.1 The SPM Head 76

3.3.2 The Inverted Dilution Fridge : Sionludi 82

3.3.3 Magnetic Field 88

3.3.4 Electronics 88

3.4 The Needle Sensor **95**

3.4.1 Tips 96

3.4.2 Implementation 99

3.4.3 Temperature dependence of the Properties of the NS 102

3.5 Applications of combining AFM with STM **105**

3.5.1 Experimental Determination of Sensitivity of NS 106

3.5.2 Localizing a single nano-device on a chip 108

3.6 Summary **109**

3.1 Introduction

In this chapter, we introduce our experimental setup which is a Scanning probe microscope capable of operating down to dilution temperatures at magnetic fields up to 2 T. We first discuss the different microscopic techniques that can be implemented in this setup and has been thoroughly used throughout the course of this thesis. This is followed by the description of the key components of the setup i.e. the microscope itself, associated electronics and the inverted dilution fridge or *Sionludi* on which the microscope is installed. The scanning probe is introduced next with detailed description of its working principle, the way it is implemented in our setup and the change in its properties while cooling down from room to base temperature. Finally, we demonstrate important instances where the option to combine different microscopic techniques in our setup clearly proves to be a strong advantage.

3.2 Elements of Scanning Probe Microscopy

When Binnig, Rohrer, Gerber and Weibel invented the Scanning Tunneling Microscope in 1982 [66] followed by the Atomic force microscope four years later by Binnig, Quate and Gerber [67], not only did they lead the way into the world of atoms but simultaneously opened the floodgates for a whole new family of powerful experimental techniques - the Scanning probe microscopies that could address the local fluctuations of physical properties of a given system.

The fundamental difference with other microscopies like optical or scanning electron microscopy in which the sample surface is probed with photons or electrons, is that scanning probe microscopy involves the use of a local probe and hence the name. The kind of probe used determines the local property of the surface that can be investigated. For example a metallic tip can measure the local density of states of the sample surface, a resonator like a cantilever or tuning fork can detect the tip-surface interaction, a Hall probe or a SQUID can be used to detect the local magnetization, etc. Each type of probe defines a new technique which all fall under the broad category of Scanning probe microscopy. In the following sections, we introduce and discuss the three different scanning probe techniques that can be implemented in our setup.

3.2.1 Scanning Tunneling Microscopy & Spectroscopy

The Scanning Tunneling Microscope today has become one of the most widely used experimental techniques in probing the local electronic properties of surfaces. As the name suggests, it is based on the phenomenon of quantum mechanical tunneling of electrons between two electrodes separated by a thin potential barrier. The idea is rather simple although realizing a Scanning Tunneling Microscope is quite an experimental challenge!

Figure 3.1 shows a cartoon explaining very simply the main working principle of a STM. A sharp, metallic tip, mounted on a piezoelectric scanner capable of three-dimensional positioning

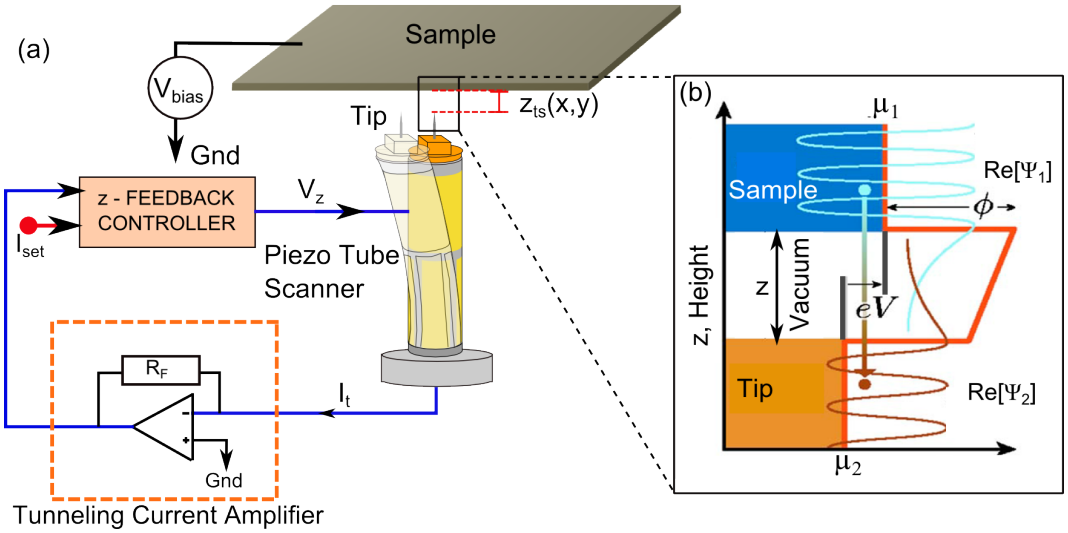

Figure 3.1: Schematic showing the working of a Scanning Tunneling Microscope. A metallic tip mounted on a piezo tube scanner scans over a conducting sample with the tip-sample distance maintained by a feedback loop controlled by the tunneling current flowing between the two surfaces. (b) Schematic showing the tunneling process occurring between the tip and the sample across an insulating (vacuum) barrier fo width z [68].

with picometric precision, is placed extremely close (of the order of a few Å) to a conducting sample surface. The electrons on the two sides (tip and sample surface) are therefore separated by a finite potential barrier of width of the order of their Fermi wavelength and hence, small enough to allow a finite overlap of their wave-functions. This leads to a non-zero probability for them to *tunnel* through this barrier resulting in a finite current flow between the tip and the sample on applying a small voltage difference (V_{bias}) between the two. This tunneling current I_t constitutes the main imaging signal of this microscopy technique.

The reason for the remarkably high vertical resolution of this microscope of a few hundredths of an angstrom is due to the exponential dependence of I_t on the tip-sample distance z_{ts}:

$$I_t \propto e^{-z_{ts}/z_0}, \quad \frac{1}{z_0} = 2\sqrt{\frac{2m\phi}{\hbar^2}} \approx \sqrt{\phi(\text{eV})}\text{Å}^{-1} \tag{3.2.1}$$

The work-function (ϕ) of a typical metal is about 5 eV which implies that I_t decreases by an order of magnitude for only a change of 1 Å of the tip-sample separation.

This high sensitivity of I_t to z_{ts} is made use of in maintaining the tip at a constant separation from the sample surface while scanning. A feedback loop where I_t serves as the input parameter is used to regulate the voltage applied to the z electrode of the piezo-scanner V_Z such that I_t remains fixed. The changes produced in V_Z can be directly converted to give the changes produced in the vertical position of the tip *z(x,y)*. Spatial variations of z produce an image of the sample surface which gives the topography of the surface. This method of imaging the surface is known as the *Constant-current imaging mode*. Since this method of scanning is dependent on the control of

the tip-sample distance by the z-feedback, the scan speed is limited by the bandwidth of the feedback loop which is usually in the kHz range. Another common mode of surface imaging is the *Constant-height mode* in which the z-regulation is kept off while scanning. In this case, local surface corrugations would produce variations of I_t and hence positional map of I_t will reflect the surface topography. Of course, since the tip-sample distance is not regulated, the latter method is faster but more risky and should be implemented only after ensuring small surface roughness to prevent collision of the tip with surface protrusions. Also, the I_t modulations produce only a qualitative map of topography since $\delta z \propto \ln I_t(x,y)/\sqrt{\phi}$, so for a quantitative comparison, local value of ϕ must be known.

Nevertheless, images of the surface produced in both these STM modes is not just the real topography of the surface. In particular, they contain influences of the variations in the local density of states (LDOS) as well. This is because the tunneling current I_t, that constitutes the imaging signal, depends both on the tip-sample distance and the convolution of the density of sates of the sample ρ_s and the tip ρ_{tip}, as explained in the following section.

Quantum Mechanical Tunneling

If we assume elastic tunneling of electrons, then within the independent particle approximation, we can write down the following expression for I_t as a function of voltage bias V_{bias} and tip-sample distance z:

$$I_t(V_{bias}, z) = \frac{4\pi e}{\hbar} \int_{-\infty}^{\infty} |M|^2 \rho_{tip}(E - eV_{bias}) \rho_s(E, \mathbf{r}) \left[f(E - eV_{bias}, T) - f(E, T) \right] dE \qquad (3.2.2)$$

In the above expression :

1. $|M|^2$ represents the tunneling matrix element which is proportional to the transmission probability of the electron across the insulating barrier $T(E, z)$ and is responsible for the exponentially decaying nature of I_t with the width of the barrier i.e. the tip-sample distance z_{ts}. Under the assumption that $V_{bias} << \Phi$, we can safely assume $|M|$ to be independent of energy.

2. $f(E, T)$ represents the Fermi-Dirac distribution function which gives the probability of an electronic state at energy E being filled at temperature T. We assume here that the electronic temperature for both the tip and the sample is the same.

$$f(E, T) = \frac{1}{\exp\left(\frac{E - E_F}{k_B T}\right) + 1} \qquad (3.2.3)$$

where E_F is the Fermi energy and $k_B = 1.38 \times 10^{-23} JK^{-1}$ is the Boltzmann constant.

3. $\rho_s(E,\mathbf{r})f(E,T)dE$ gives the position dependent number of electronic states of the sample that are filled between energy E and $E+\delta E$ whereas $\rho_{tip}(E-eV_{bias})\left[1-f(E-eV_{bias},T)\right]dE$ gives the number of states that are available in the tip in the same energy interval when a voltage V_{bias} is applied to the sample. Hence, the total current flowing from sample to tip will be given by :

$$I_{s\to tip} \propto \int_{-\infty}^{\infty} |M|^2 \rho_s(E,\mathbf{r}) f(E,T) \rho_{tip}(E-eV_{bias}) \left[1-f(E-eV_{bias},T)\right] dE \tag{3.2.4}$$

4. Similarly, current flowing from tip to sample will be given by :

$$I_{tip\to s} \propto \int_{-\infty}^{\infty} |M|^2 \rho_s(E,\mathbf{r}) \left[1-f(E,T)\right] \rho_{tip}(E-eV_{bias}) f(E-eV_{bias},T) dE \tag{3.2.5}$$

5. Now from equations 3.2.4 and 3.2.5, the above expression for the effective tunneling current flowing between the tip and the sample 3.2.2 can be easily recovered.

$$I_t(V_{bias},z) = I_{tip\to s} - I_{s\to tip} \tag{3.2.6}$$

Scanning Tunneling Spectroscopy

The fact that the tunneling current is dependent on the local density of states of the sample makes it possible to use this signal as a probe to sense it. This forms the basis of the other important use of the microscope : Scanning Tunneling Spectroscopy or STS. Here, the signal which assumes the key role is the derivative of the tunneling current dI_t/dV_{bias} or the tunneling conductance.

$$\frac{dI_t}{dV_{bias}} = \frac{4\pi e}{\hbar} \int_{-\infty}^{\infty} |M|^2 \rho_s(E,\mathbf{r}) \frac{\partial}{\partial V_{bias}} \left[\rho_{tip}(E-eV_{bias}) f(E-eV_{bias},T)\right] dE \tag{3.2.7}$$

If we choose a metallic tip (most often the case in STS) and restrict ourselves to energies close to the Fermi level i.e. eV_{bias} is small enough to approximate $\rho_{tip}(E-eV_{bias})$ to be independent of energy, then we can simplify the above expression to get the following.

$$\frac{dI_t}{dV_{bias}} = \frac{4\pi e^2}{\hbar} |M|^2 \rho_{tip} \int_{-\infty}^{\infty} \rho_s(E,\mathbf{r}) \left[\frac{\partial f(E-eV_{bias},T)}{\partial(eV_{bias})}\right] dE \tag{3.2.8}$$

The expression $\frac{\partial f(E-eV_{bias},T)}{\partial(eV_{bias})}$ is just a bell-shaped weighting function peaked at $E=eV_{bias}$ with weight k_BT and unit area under the curve. In fact at $T=0\,K$, it exactly corresponds to a Dirac delta function and in this situation, dI_t/dV_{bias} becomes exactly proportional to the DOS of the sample.

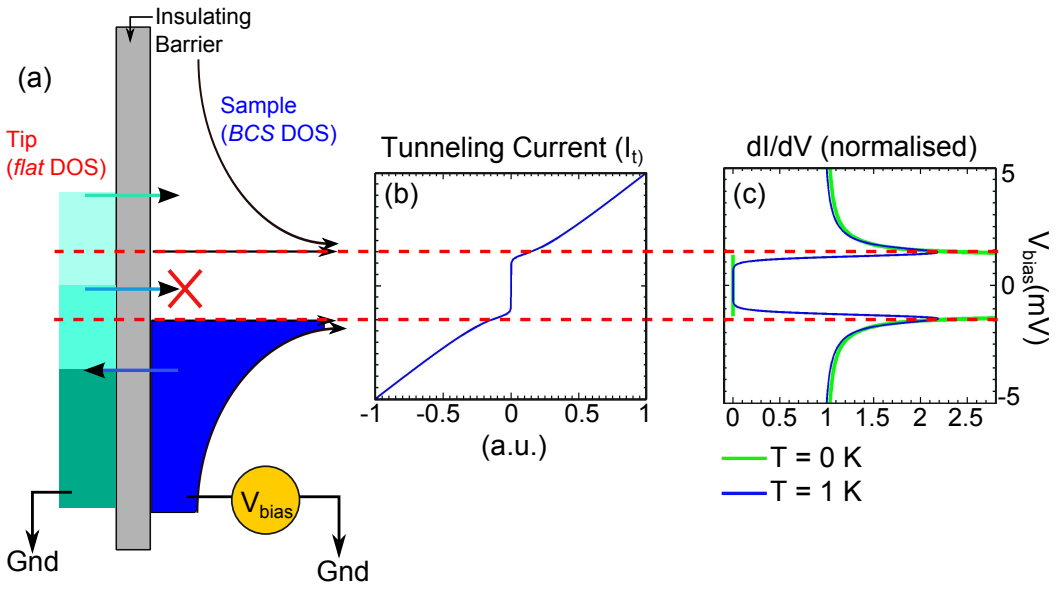

Figure 3.2: Scanning Tunneling Spectroscopy. (a) Schematic demonstrating elastic tunneling of quasiparticles from a metallic tip (left) with a flat DOS to a superconducting sample with a BCS like DOS (right) through an insulating (vacuum) barrier. By tuning the bias (V_{bias}) applied to the sample, relative position of the Fermi levels of tip and sample changes giving access to different parts of the sample DOS. (b) Tunneling current as a function of V_{bias} at $T = 1\,K$. (c) Tunneling conductance as a function of V_{bias} at $T = 1\,K$ (blue) and $T = 0\,K$ (green).

$$\frac{dI_t}{dV_{bias}} = \left[\frac{4\pi e^2}{\hbar}|M|^2\rho_{tip}\right]\rho_s(eV_{bias}, \mathbf{r}) \tag{3.2.9}$$

Figure 3.2 shows an example of using STS to measure the DOS of a superconducting sample having a BCS type DOS [69]. At $T = 0\,K$, the measurement produces an accurate description whereas at higher temperatures, the dI_t/dV_{bias} will produce an approximate value that will be subjected to a smearing of about $4k_BT$.

To perform tunneling spectroscopy, one way is to simply measure I_t as a function of V_{bias} and then to find its derivative numerically. Another popular way is the *lock-in technique*. In this method, a small sinusoidal ac modulation $V_{ac}sin(\omega t)$ (from the lock-in amplifier output) is superimposed with the dc bias voltage supplied to the sample. The frequency of the modulation ω is carefully chosen such as to avoid typical domains of mechanical vibrations or electronic noise for example multiples of $50\,Hz$ should be avoided to ensure minimum influence from the $50\,Hz$ electrical noise. The tunneling current can then be written as (using Taylor expansion):

$$I_t(V) = I_t(V_{bias}) + \left|\frac{dI_t}{dV}\right|_{V=V_{bias}} V_{ac}sin(\omega t) + \mathcal{O}(V_{ac}^2) \tag{3.2.10}$$

The resultant signal is once again measured with the help of the lock-in amplifier which gives back the amplitude and the phase corresponding to the reference frequency ω of the supplied

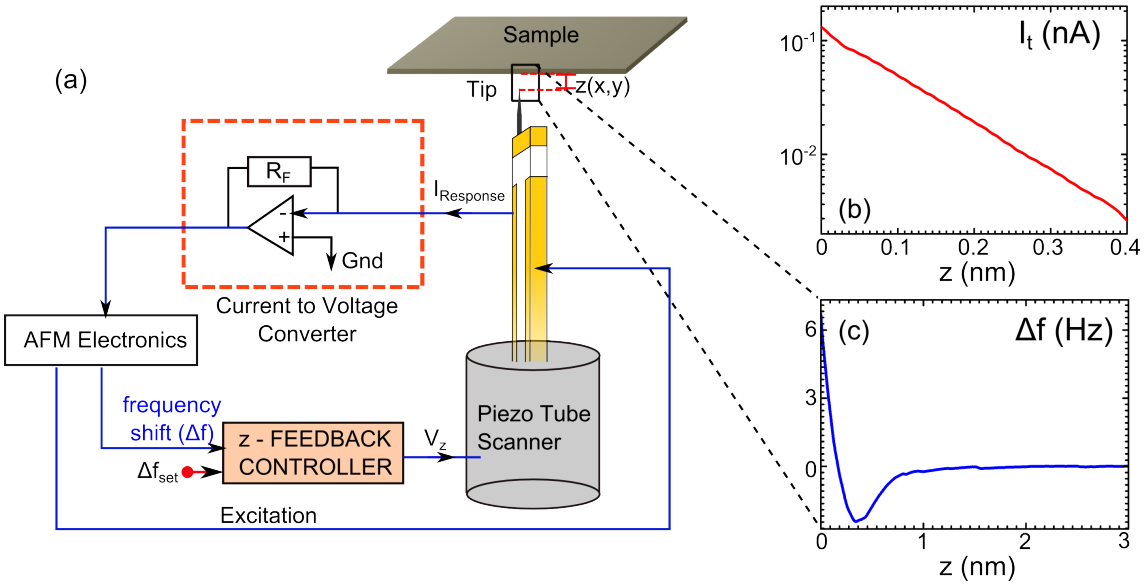

Figure 3.3: Atomic Force Microscopy. (a) Schematic explaining the basic working principle of the Atomic force microscope. Here, the needle sensor has been depicted as the force sensor, see section 3.4. (b) I_t vs z sensitivity curve, on gold surface at room temperature with a Pt/Ir coated Si cantilever tip, the decay length is about $100\,pm$. (c) Δf vs z sensitivity curve, recorded also on gold with a FIB shaped tungsten tip mounted on a needle sensor at $4\,K$ ($Q = 54300$, $f_0 = 993.864\,kHz$, $A = 400\,pm$). For both (b) and (c), $z = 0$ corresponds to the starting position determined by the set-point parameters.

voltage modulation i.e.

$$A_{lock-in} = V_{ac} \left| \frac{dI_t}{dV} \right|_{V=V_{bias}} \tag{3.2.11}$$

Or in other words, the lock-in directly gives the tunneling conductance. Since this method gives the freedom to measure in the least noisy domain of the I_t signal spectrum, it often results in very clean measurements with less noise. However, due to smearing effect of the voltage modulation, one should be careful to keep V_{ac} significantly small compared to any physical feature (of width $\approx \delta E$) present in the DOS of the sample being investigated, i.e. $eV_{ac} \ll \delta E$. Also, if possible, $V_{ac} \ll 4k_BT$ to keep the resulting smearing lower than the thermal smearing.

3.2.2 Atomic Force Microscopy

Even though the STM is unparalleled as a tool for imaging the local electronic properties of surfaces with spatial resolution down to atomic scale, it suffers from a serious drawback : its range of application is limited to conducting surfaces. This limitation is easily overcome in an Atomic Force Microscope or AFM.

The basic ingredients of AFM are essentially the same as that of STM. Figure 3.3(a) shows a schematic of the basic idea and layout of an atomic force microscope. Here the tip-sample

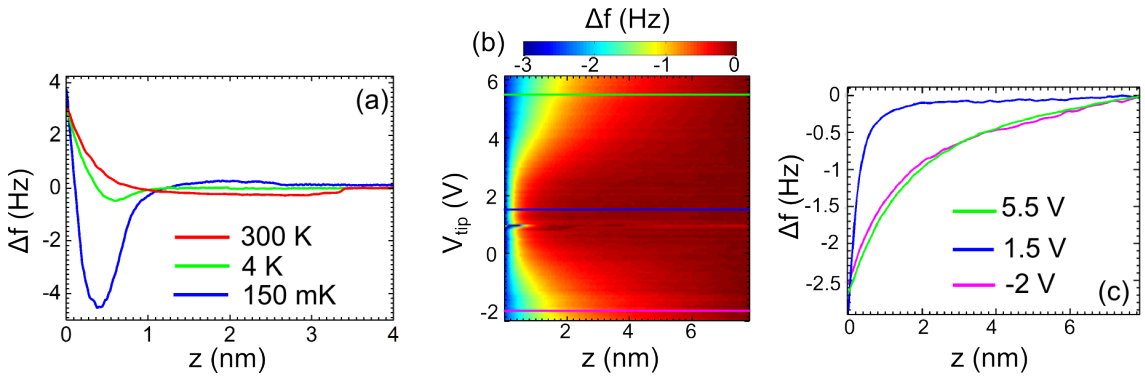

Figure 3.4: Experimentally measured tip-sample interactions under different conditions. (a) Frequency shift Δf vs tip-sample distance z at $T = 300\,\mathrm{K}$ ($P \approx 10^{-4}\,\mathrm{mbar}$), 4 K and 150 mK. (b) Δf as a function of z and tip voltage V_{tip}. (c) Δf vs z at three different tip voltages with (sample grounded), along the horizontal cuts in (b). (Sample: gold, tip: W tip mounted on LER, $T = 4\,\mathrm{K}$)

distance dependent forces play the role analogous to that played by the tunneling current I_t in STM. Quite naturally, this requires the scanning probe to be a force sensor capable of detecting changes in these forces or force gradients. Cantilevers or quartz resonators are popular choices for this purpose as their natural oscillating frequencies change when subjected to these tip-sample forces. This shift in the natural frequency of the resonator Δf constitutes the main imaging signal in frequency modulated AFM (FM-AFM) which is the mode in which AFM is implemented in our setup.

Figure 3.3(b) shows the sensitivity of Δf to tip-sample distance (measured with a needle sensor) as compared to the sensitivity of I_t in STM. The lower sensitivity combined with the non-monotonic change of Δf with z does make it difficult to achieve the spatial and vertical resolution that is possible in STM. Nevertheless, the accessibility to practically any kind of surface whether conducting or not and the power of the force sensors to sense them from a distance at least ten to even hundred times further than that possible in STM, makes this technique much more versatile.

Tip-Sample Forces

The tip-sample interactions may be short-range or long range. The short range forces mainly comprise of chemical binding forces (relevant at distances $< 5\,\text{Å}$) and the van der Waals forces (distances up to $5 - 7\,\mathrm{nm}$ in air) while the long range contributions are electrostatic or magnetic in nature. For extremely small tip-sample distances z, the interaction is repulsive. This is because of the Pauli exclusion principle for the overlapping electron clouds of the tip and sample atoms. At slightly larger distances, the attractive van der Waals force takes over. It results from the interaction between electrostatic dipoles induced by electromagnetic field fluctuations in the environment [70]. At yet larger distances, the short-range contributions disappear and

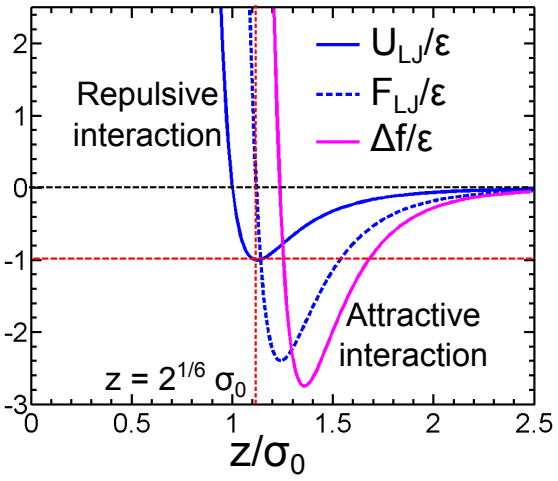

Figure 3.5: The Lennard Jones' potential U_{LJ}, corresponding force $F_{LJ} = -\frac{dU_{LJ}}{dz}$ and the frequency shift given by Eq.(3.2.17) as a function of tip-sample distance z.

any remaining interaction is attractive and dominated by long range electrostatic (if tip and sample surfaces are conducting) or magnetic (if tip and sample surfaces are magnetized) forces. Figure 3.4(a) shows the experimentally measured frequency shift Δf of scan probe (derivative of tip-sample interaction) as a function of tip-sample distance at room temperature and at 4 K where we observe the range of interaction to reduce at low temperatures. In (c), the blue curve results from the attractive van de Waals interaction while on increasing electrostatic interaction (changing V_{tip}), the interactions are found to persist up to longer distances.

The emperical way to represent the short-range tip-sample interactions is by the Lennard Jones' potential [71] given by

$$U_{LJ}(z) = 4\epsilon \left[\left(\frac{\sigma_0}{z} \right)^{12} - \left(\frac{\sigma_0}{z} \right)^{6} \right], \tag{3.2.12}$$

where $z = 2^{1/6}\sigma_0$ is the equilibrium distance and ϵ is the minimum value of this potential i.e. $\epsilon = -(U_{LJ})_{min}$ corresponding to equilibrium. The positive, rapidly decaying term describes the repulsive part while the negative, slowly decaying term gives the attractive part of the potential. The component of the tip-sample force perpendicular to the sample surface is then $F_{LJ} = -\frac{dU_{LJ}}{dz}$. In Figure 3.5, U_{LJ} and the corresponding force F_{LJ} has been plotted as a function of tip-sample distance z. For $z > \sigma_0$, the interaction is attractive while it is repulsive at distances smaller than σ_0.

In non-contact AFM, the probe-sample distances are maintained in the attractive regime unlike in contact or tapping mode AFM where the probe is placed in contact with the surface.

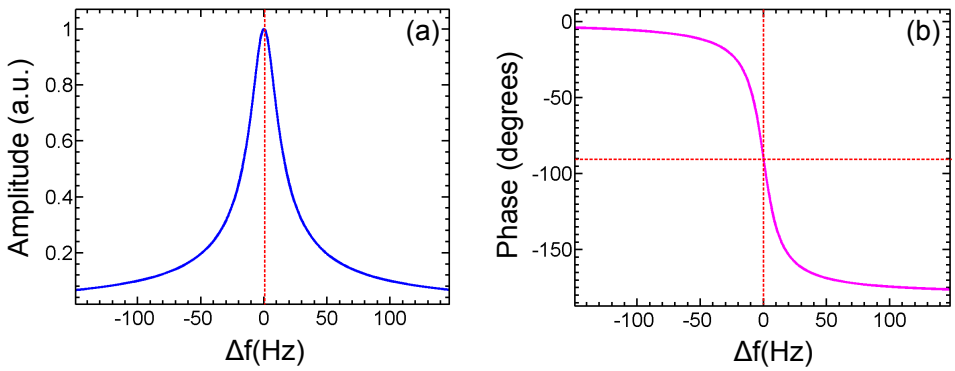

Figure 3.6: Calculated steady state response characteristics of a forced, harmonic oscillator with $f_0 = 1\,\text{MHz}$ and $Q = 50000$. (a) Amplitude vs frequency shift. (b) Phase vs frequency shift.

Detection of Tip-sample Interactions in FM-AFM

As already mentioned, an AFM probe constitutes of a cantilever or a quartz resonator with a characteristic eigen frequency of oscillation $\omega_0 = 2\pi f_0$ that changes under the influence of the tip-sample force F_{ts}. This can be simply understood by considering the probe as a damped harmonic oscillator subjected to a periodic force $F_0 \cos(\omega_d t)$ (to maintain its oscillations) and the tip-sample interaction. The equation of motion is then given by

$$m\ddot{z} + \frac{m\omega_0}{Q}\dot{z} + k_0 z = F_{ts} + F_0 \cos(\omega_d t) \tag{3.2.13}$$

where Q is the quality factor, m is the effective mass of the resonator and k_0 is the spring constant. In the absence of F_{ts}, the eigen frequency of the system is just $\omega_0 = 2\pi f_0 = \sqrt{\frac{k_0}{m}}$. The steady state solution to Eq.(3.2.13) is described by a resultant amplitude and phase given by

$$A = \frac{|A_{drive}|}{\sqrt{\left(1 - \frac{f_d^2}{f_0^2}\right)^2 + \left(\frac{f_d}{f_0 Q}\right)^2}}, \tag{3.2.14a}$$

$$\phi = \arctan\left[\frac{f_d}{f_0 Q\left(1 - \frac{f_d^2}{f_0^2}\right)}\right]. \tag{3.2.14b}$$

Here $A_{drive} = F_0/m\omega_0$. We note that at resonance i.e. $f_d = f_0$, amplitude $A = QA_{drive}$ is maximum and phase $\phi = 90°$ as shown in Figure 3.6.

For an infinitesimally small tip displacement z, F_{ts} can be written as (by Taylor expansion of tip-sample interaction potential U_{ts})

$$F_{ts}(z) = -\frac{dU_{ts}}{dz} = -\frac{d}{dz}\left[U_{ts}(0) + \left(\frac{dU_{ts}}{dz}\right)_{z=0} z + \left(\frac{d^2U_{ts}}{dz^2}\right)_{z=0} \frac{z^2}{2} + \mathcal{O}(z^3)\right] \approx -\left(\alpha_0 + k_{ts} z\right). \tag{3.2.15}$$

where $\alpha_0 = \left(\frac{dU_{ts}}{dz}\right)_{z=0}$ is a constant and $k_{ts} = \left(\frac{d^2U_{ts}}{dz^2}\right)_{z=0}$. Inserting this back in Eq.(3.2.13), we obtain

$$m\ddot{z} + \frac{m\omega_0}{Q}\dot{z} + (k_0 + k_{ts})\, z = F_0 \cos(\omega_d t) - \alpha_0. \tag{3.2.16}$$

This shows that the motion of the oscillator remains harmonic but the eigen frequency changes to $\omega = \sqrt{\frac{k_0 + k_{ts}}{m}}$. If the oscillator is sufficiently stiff i.e. $k_0 \gg k_{ts}$, then the shift in frequency is approximately given by

$$\Delta f = f - f_0 \approx \frac{f_0}{2k_0} k_{ts} = \frac{f_0}{2k_0}\left(\frac{d^2U_{ts}}{dz^2}\right)_{z=0}. \tag{3.2.17}$$

In Figure 3.5, the magenta curve shows the variation of frequency shift calculated from the above equation. Here we note that this equation is only valid for infinitesimally small amplitude of oscillation A. In practice however, this is seldom the case and Δf generally shows a dependence on A as seen in Figure 3.7.

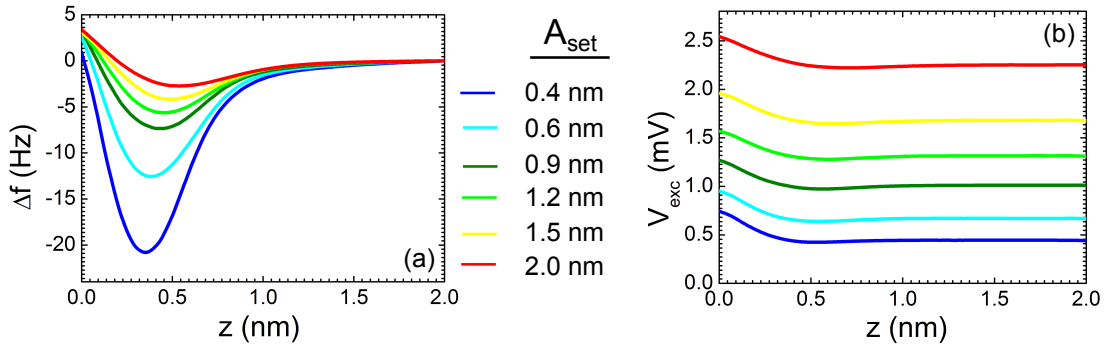

Figure 3.7: Experimental z spectroscopy for different amplitude of oscillations. (a) Δf vs tip-sample distance z for different amplitude of oscillations A_{set} (Sample: graphene on iridium (111), tip: Pt/Ir coated Si cantilever tip mounted on LER, $T = 4\,\mathrm{K}$. (b) Excitation voltage V_{exc} supplied to probe to maintain a constant amplitude set-point, as a function of z. $z = 0$ is the tip position where z-feedback is switched off and $z > 0$ implies tip withdrawal.

A more general expression for Δf is given by [72]

$$\Delta f = \frac{f_0}{2k_0}\langle k_{ts}\rangle, \quad \text{where } \langle k_{ts}\rangle = \frac{2}{\pi}\int_{-1}^{1} k_{ts}(z + \zeta A)\sqrt{1-\zeta^2}\, d\zeta \tag{3.2.18}$$

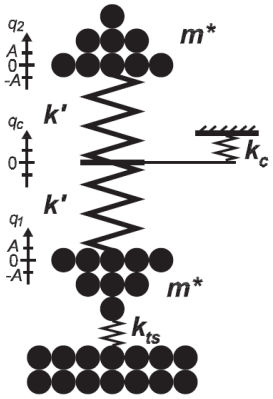

Figure 3.8: Mechanical analog of a coupled oscillator used as a force sensor. There are three degrees of freedom: the deflection of the central mount q_c and the deflections of the two coupled oscillators $q_{1,2}$ [72].

At large amplitudes, the above expression can be approximated to

$$\Delta f = \frac{f_0}{k_0}\frac{1}{A^{3/2}}\gamma_{ts}, \tag{3.2.19}$$

where $\gamma_{ts} \approx 0.4F_{ts}\sqrt{\lambda}$ is the normalized frequency shift that is independent of A, F_{ts} being the tip-sample interaction and λ being the decay length. The above equation suggests a decrease in Δf with increase in A which is what we find in Figure 3.7. We also measure the excitation voltage supplied to the tip V_{exc} in order to maintain a constant amplitude set-point, to increase at small tip-sample distances. This implies the presence of a non-conservative component in the tip-sample interaction that leads to dissipation, something that is not included in the Lennard Jones' model. This is further discussed on section 4.2.4.

Nevertheless, the frequency shift produced in the oscillator in response to the tip-sample interaction, has a high sensitivity to the tip-sample distance and this forms the basis for its use as a force sensor in AFM.

Frequency shift in Coupled oscillators

The most common quartz oscillators used today as AFM probes, are coupled oscillators, like the tuning fork [73] [74] and the length extensional resonator [75] [76]. Since in our microscope, the latter is implemented, it is important to understand the influence of the tip-sample force on the dynamics of such a coupled system. The detailed derivation is presented in [72] from which we look at the main results.

Figure 3.8 shows the schematic of a coupled oscillator in which one of the resonators is subjected to the tip-sample force while the other is free to oscillate. In such a system, there are three degrees of freedom: the displacement of the center of mass $q_c(t)$ and the displacement of the oscillators $q_{1,2}(t)$. The equation of motion is given by

$$m\ddot{q_1} = -k_{ts}q_1 - k_0(q_1 - q_c) \tag{3.2.20a}$$

$$m\ddot{q_2} = -k_0(q_2 - q_c) \tag{3.2.20b}$$

$$m\ddot{q_c} = -k_c q_c - k_0(q_c - q_1) - k_0(q_c - q_2) \tag{3.2.20c}$$

Since the center of mass has to be in equilibrium, $\ddot{q_c} = 0$. Thus, from Eq(3.2.20c), we find $q_c = \kappa(q_1 + q_2)$ where $\kappa = 1/(2 + \frac{k_c}{k_0})$. Hence, we are left with a system having two independent degrees of freedom which can be diagonalized and accurately solved to find two eigen frequencies. Under the assumption that $\kappa > 1/3$ (which is reasonable because generally $k_c < k_0$) and $k_{ts} \ll k_0$, the solutions are as follows:

1. A high frequency, antiparallel motion with frequency

$$\omega_1^2 \approx \omega_0^2 \left\{1 + \frac{1}{2}\left(\frac{k_{ts}}{k_0}\right) + \frac{1}{8\kappa}\left(\frac{k_{ts}}{k_0}\right)^2\right\} \tag{3.2.21}$$

2. A low frequency, parallel motion

$$\omega_2^2 \approx \omega_0^2 \left\{1 - 2\kappa + \frac{1}{2}\left(\frac{k_{ts}}{k_0}\right) - \frac{1}{8\kappa}\left(\frac{k_{ts}}{k_0}\right)^2\right\} \tag{3.2.22}$$

The antiparallel motion is used in AFM. Therefore, the frequency shift is given by

$$\Delta f = \frac{f_0}{4k_0} k_{ts}. \tag{3.2.23}$$

to the first order. This means that the frequency shift produced in response to a given tip-sample force is reduced to half the value than in case of a single harmonic oscillator. We can still use Eq.(3.2.17) to obtain the frequency shift provided the individual stiffness of the oscillators k_0 is replaced by an effective stiffness $k = 2k_0$.

Frequency Modulated AFM

So far we have discussed about the tip-sample forces and their influence on the scanning oscillator. What follows next is how this sensed frequency shift can be measured and implemented in controlling the tip-sample distance. There are mainly two different ways this can be done: amplitude modulation (AM) and frequency modulation (FM). In AM-AFM, the probe is excited at a constant frequency slightly off resonance. A change in frequency would result in a decrease or increase of the amplitude of oscillation A which therefore serves as a measure of Δf. The input for the z-feedback loop is controlled by A. The major limitation of this technique is that the available bandwidth is limited by the quality factor of the probe since the response time of the system is given by $\tau = 2Q/\omega_0$.

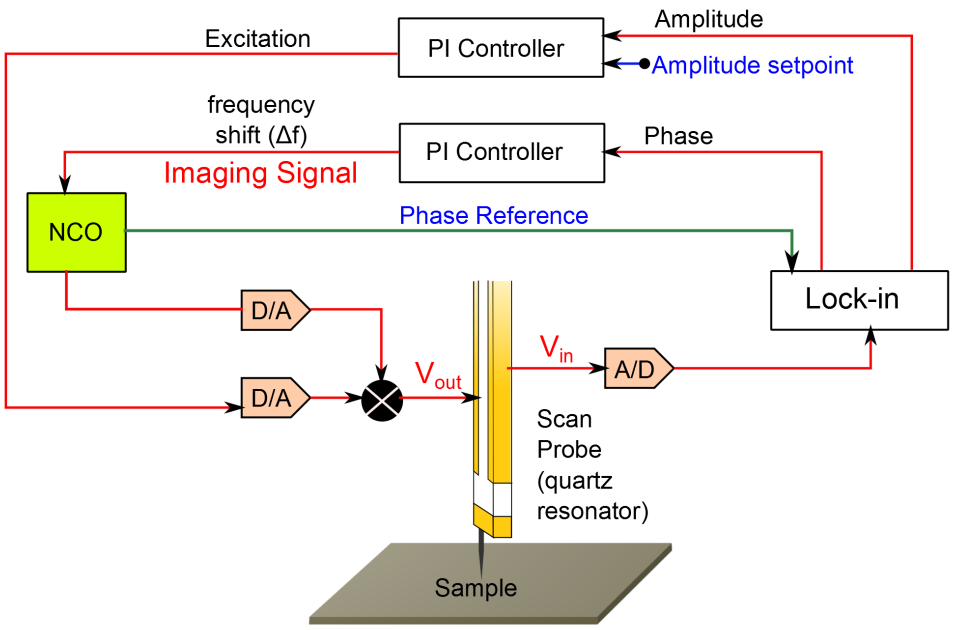

Figure 3.9: Block diagram of the Frequency Modulation AFM (FM-AFM) feedback loop for maintaining the scan probe at resonance while scanning. NCO is a Numerically Controlled Oscillator.

The technique of frequency modulation was introduced by T. R. Albrecht et al. [77]. It overcomes the above limitation and is the AFM mode implemented in our setup. In Frequency-modulated (FM) atomic force microscopy, a phase-locked loop (PLL) is used to always maintain the oscillator probe at resonance while scanning as it, itself forms the frequency determining component of an oscillator in the detection electronics. Figure 3.9 shows the block diagram of the actuation and detection system implemented in currently available frequency-modulated systems. The steps are outlined below :

1. The analog input signal V_{in} from the scanning resonator is converted into a digital signal via an analog to digital converter.

2. The digital signal is analyzed by a lock-in amplifier which outputs its amplitude and phase separately. The phase is calculated wrt. a reference phase (Φ_{ref}) that is common for the whole feedback circuit and is chosen such that it is zero when the scan probe is oscillating at resonance, far away from the influence of the tip-sample force.

3. The amplitude signal enters as the input to a feedback circuit called the Amplitude Controller (one part of the PLL) which regulates on the drive to be supplied to the scan probe. The feedback acts on the *Excitation* to ensure that amplitude of oscillation of the probe is maintained at a set value (Amplitude setpoint).

4. The phase signal enters a separate feedback circuit called the Phase Controller (other part

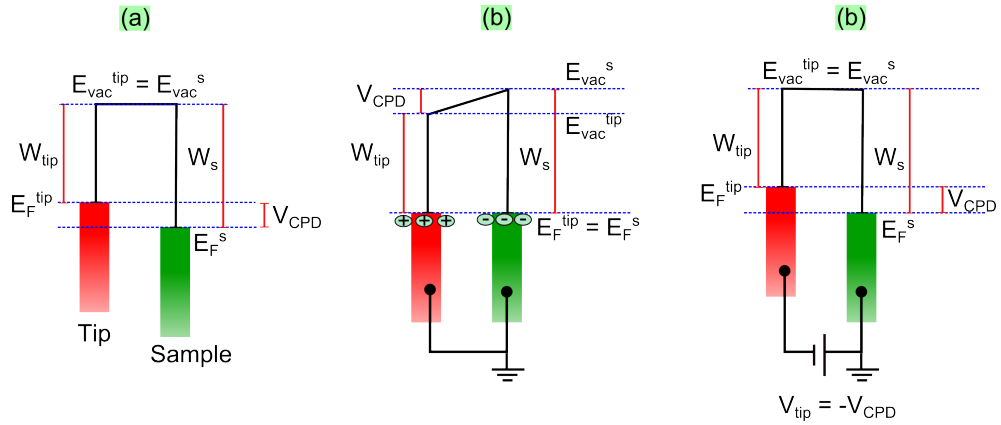

Figure 3.10: Schematic explaining measurement of contact potential difference (CPD) between tip and sample in Kelvin probe force microscopy (KPFM). Alignment of the different energy levels in the sample wrt. the tip when (a) they are electrically disconnected, (b) electrically connected and (c) a voltage $V_{tip} = -V_{\mathrm{CPD}}$ is applied to the tip where V_{CPD} is the CPD of the sample wrt. the tip. E_F represents the Fermi level, E_{vac}: the vacuum level and W: the work-function of tip/sample as indicated by superscript/subscript.

of the PLL). Based on the difference between the phase input and the Φ_{ref}, the circuit acts on the frequency of an oscillator: the *NCO* or the Numerically Controlled Oscillator. The NCO directly controls the frequency of the output voltage V_{out}. A non-zero phase would imply the probe had encountered a frequency shift, hence the Phase Controller will act to provide maximum positive feedback at the new resonance frequency of the probe and hence change the frequency of the NCO accordingly. In the process, the change in frequency recorded Δf to maintain the probe at resonance forms the main Imaging Signal.

5. Finally, the *Excitation* and the frequency shift information are converted to analog signals and combined to produce the resultant drive for the scan probe.

With this, we have more or less discussed the important aspects on the working of the FM-AFM. Now all that remains is the introduction and characterization of the scan probes for combined AFM/STM that will be taken up in 3.4.

3.2.3 Kelvin Probe Force Microscopy

Kelvin probe force microscopy or KPFM is a combination of nc-AFM and the Kelvin probe technique developed by Lord Kelvin in 1898 for the measurement of the contact potential difference (CPD) between two surfaces. The origin of this contact potential difference lies in the different work-functions of the two surfaces which leads to different positions of the respective Fermi levels E_F (Figure 3.10(a)). When the two surfaces are electrically connected, this electrochemical potential imbalance (different E_F) will cause a transfer of charge between them till the Fermi levels are aligned leading to equilibrium (Figure 3.10(b)). The electrostatic potential difference,

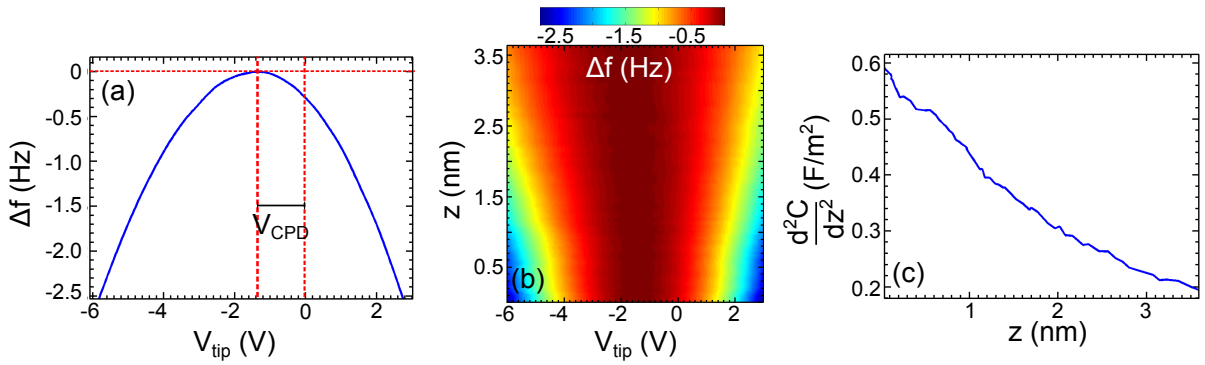

Figure 3.11: Measurement of V_{CPD} by force spectroscopy at different tip-sample distances. (Sample: gold, Probe: W tip mounted on LER). (a) Parabolic dependence of Δf on V_{tip}. (b) Δf as a function of V_{tip} and tip-sample distance z. $z = 0$ refers to the sarting point. (c) Change of $\frac{d^2C}{dz^2}$ as a function of z where C is the tip-sample capacitance.

thus built up in this process, is the contact potential difference V_{CPD}. This potential difference will give rise to an ac current if one of the surfaces is vibrated wrt. the other due to the changing capacitance. The current can be nullified if a compensating voltage $= V_{\mathrm{CPD}}$ is supplied to one of the surfaces so that the effective potential difference between the two is zero (Figure 3.10(c)). This forms the basis of detection of CPD by Kelvin probe.

In Kelvin probe force microscopy, the local CPD of the surface is measured with the AFM probe. However, unlike in the Kelvin probe technique, the detected signal is force instead of current. The CPD difference between the tip and the sample causes an electrostatic force which can be detected as a frequency shift by the AFM probe as discussed in section 3.2.2. The CPD is then measured simply by nullifying this force using a compensating tip voltage $V_{tip} = -V_{\mathrm{CPD}}$ (Figure 3.10(c)).

In particular, we note that, with the sample grounded and voltage applied to the tip,

$$V_{\mathrm{CPD}} = \frac{W_{sample} - W_{tip}}{|e|}. \tag{3.2.24}$$

where W_{sample} and W_{tip} are the work-functions of the sample surface and scan probe respectively.

Implementation

There are mainly three ways of measuring the local CPD of the surface using KPFM: (1) point to point force spectroscopy, (2) amplitude modulated KPFM and (3) frequency modulated KPFM. In our setup, the first technique can be implemented. Nevertheless, our collaboration with Benjamin Grévin in CEA enabled us to closely experience the working of frequency modulated KPFM and in chapter 5, CPD measurements by Dr. Grévin using FM-KPFM have been presented. Therefore, we briefly discuss the first and third method to understand the measurements

discussed in subsequent chapters.

In point to point force spectroscopy, the frequency shift of the scan probe, which is the derivative of the tip-sample force, is measured as a function of voltage applied to the tip. The voltage at which the frequency shift is minimized then gives the CPD. The tip-sample system can be considered as a capacitor. The electrostatic potential is then given by

$$U_{el} = \frac{1}{2} C \left(V_{tip} + V_{\mathrm{CPD}}\right)^2 \tag{3.2.25}$$

where C is the tip-sample capacitance. Using Eq.(3.2.17), the frequency shift resulting from this electrostatic interaction can be calculated.

$$\Delta f = \frac{f_0}{4k} \frac{d^2C}{dz^2} \left(V_{tip} + V_{\mathrm{CPD}}\right)^2 . \tag{3.2.26}$$

Here k is the effective stiffness constant of the scanning resonator. In deriving the above equation, we have considered only the electrostatic force component perpendicular to the tip-sample surface which has the dominant contribution in AFM. We have also ignored the short range van der Waals contribution which is justified if the spectroscopy is performed sufficiently far $> 10\,\mathrm{nm}$ from the sample surface. Figure 3.11 shows an example of force spectroscopy performed on a gold surface with a tungsten tip mounted on a LER at 130 mK. Figure (a) shows the parabolic dependence of Δf as a function of V_{tip} as expected according to Eq.(3.2.26). The Δf values are negative implying the attractive nature of the electrostatic force. The position of the maximum of the parabola gives the V_{CPD}. Figure (b),(c) shows the decreasing curvature of the parabola as the tip-sample distance is increased due to the expected decrease of the tip-sample capacitance.

In frequency modulated KPFM, an ac signal $V_{ac}\cos(\omega_{ac}t)$ is superposed on the dc tip signal i.e. $V_{tip} = V_{dc} + V_{ac}\cos(\omega_{ac}t)$. This produces three distinct spectral components of the frequency shift.

$$\Delta f_{dc} = \frac{f_0}{4k} \frac{d^2C}{dz^2} \left[\left(V_{dc} + V_{\mathrm{CPD}}\right)^2 + \frac{V_{ac}^2}{2}\right] \tag{3.2.27a}$$

$$\Delta f_{\omega_{ac}} = \frac{f_0}{2k} \frac{d^2C}{dz^2} V_{ac} \left(V_{dc} + V_{\mathrm{CPD}}\right) \cos(\omega_{ac}t) \tag{3.2.27b}$$

$$\Delta f_{2\omega_{ac}} = \frac{f_0}{8k} \frac{d^2C}{dz^2} V_{ac}^2 \cos(2\omega_{ac}t) \tag{3.2.27c}$$

The dc component is just added to the topography signal. A lock-in amplifier tuned to the frequency of the ac bias then measures the corresponding component in the frequency shift i.e. Eq.(3.2.27b) which is proportional to $V_{dc} + V_{\mathrm{CPD}}$. A feedback loop then adjusts the dc bias V_{DC} to minimize $\Delta f_{\omega_{ac}}$ which directly gives the local CPD.

This brings us to the end of the discussion about the different scanning probe microscopies that can be implemented in our setup. The ability to combine these three powerful techniques in a single setup which is capable of operating at dilution temperatures opens up a whole range of possibilities, only a small fraction of which has been explored in this thesis.

3.3 Experimental Setup

In this section we will discuss about our Scanning probe microscope (SPM) and the associated experimental environment. The microscope was built by Sylvain Martin under the supervision of Clemens Winkelmann and the full details have been presented in his thesis [78]. Here a more concise description is provided. We first describe the SPM head. This is followed by the description of the cryogenic arrangement that enables the operation of the SPM at dilution temperatures i.e. via inverted dilution. Finally we end our discussion with the associated electronics required to probe and measure the local properties of a given sample.

3.3.1 The SPM Head

The SPM head forms the central element of a scanning probe microscope as well as the part that is the most challenging to build. Since the main target is to realize a spatial resolution high enough to image atoms by maintaining a probe at Å scale distances from the sample surface, mechanical vibrations need to be much smaller than the atomic corrugation. Moreover, operation at low temperatures imply lower thermal drift and better energy resolution but at the same time the cryogenic arrangements required for this purpose tend to increase the mechanical vibrations. A suitable design of the head with proper choice of component materials that results in higher structural resonance frequencies significantly helps in damping these low frequency vibrations. Therefore, the SPM head needs to be very rigid and at the same time, compact and light for compatibility with cryogenic arrangements. Keeping these requirements in mind, we chose the Pan design [79].

General Description

The schematic in Figure 3.12(a) shows the lateral view of the STM head while in (b)-(e), optical images of the corresponding parts are shown. The microscope is equipped for top loading of sample with face downwards while the scan probe, facing upwards, is made to vertically move up to reach the sample. The sample holder is inserted on an assembly of two movable wagons which facilitates displacement of the sample in the horizontal plane. The probe is fixed on a metallic (phosphor bronze) tip holder that is detachable from the microscope. This assembly of the probe and the tip holder fits into a receptacle that is present on the top of the piezo scanner. Figure (c) shows a top view of the scanner with the tip holder receptacle. The scanner essentially consists of a piezo tube (Figure (d)), fixed on a macor (machineable ceramic) base and housed inside a macor tube which in turn is housed inside a sapphire prism. The vertical coarse approach mechanism involves the side walls of the microscope, a spring plate (Figure (c), part 10), six piezo stacks (Figure (e)) with ceramic surface (4 fixed on the side walls and two on the spring plate) and the sapphire vertical shaft.

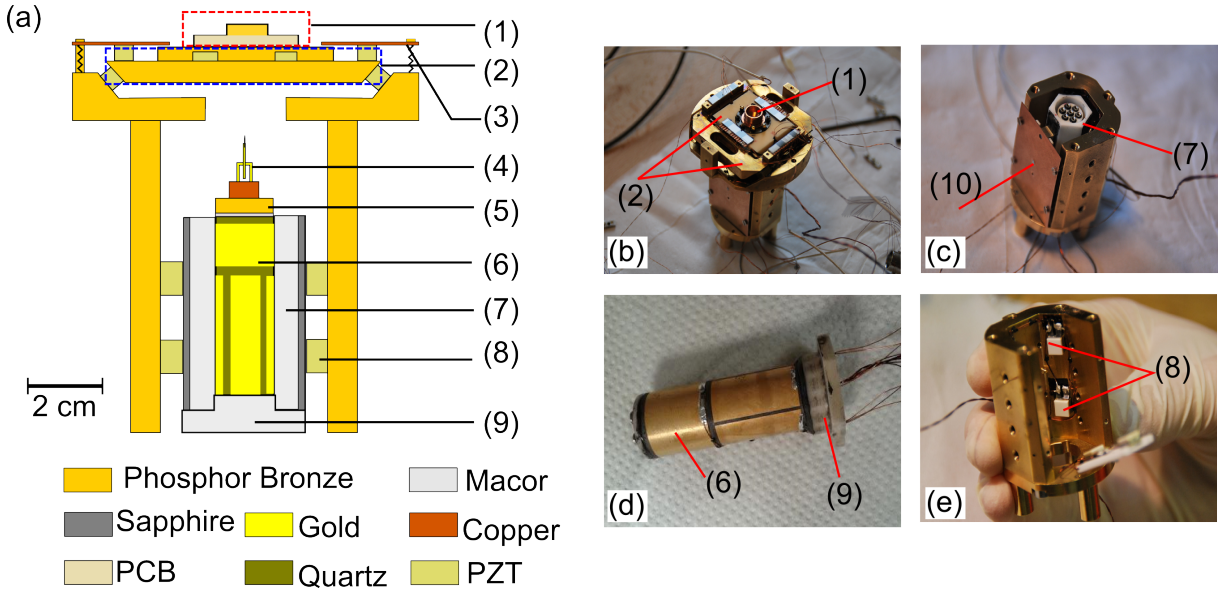

Figure 3.12: General assembly of the SPM head. (a) Schematic explaining the basic structure of the SPM head. (1) Sample holder, also in (b). (2) Wagons for displacement of sample holder in the horizontal plane, also in (b). (3) in (a) and (10) in (c): Spring plates for piezo actuators. (4) Scan probe (tip on LER). (5) Tip holder. (6) Piezo tube scanner, also in (d). (7) Macor prism with sapphire outer plates for movement along Z direction, also shown in (c). It also forms the outer protective case of the piezo-tube scanner. (8) Piezo-electric acctuators for coarse motion along Z, also in (e). (9) Macor base plate of scanner assembly, also in (d).

Choice of materials

For operation at dilution temperatures, the choice of the materials of the microscope head is very important. There are several factors that should be taken into account. Firstly, the chosen materials should be good conductors of heat down to base temperature so that the different parts are well thermalised. Hence, materials that turn superconducting at temperatures higher than the base temperature must be avoided as in the superconducting state, these metals are bad thermal conductors. Secondly, the thermal expansion coefficients of the different parts should be well matched to prevent wear and damage on cooling down. Finally, magnetic materials cannot be used as the STM head is placed inside a magnetic coil which might induce large forces on the head due to magnetization. Keeping all these requirements in mind, our choice for the material of the body of the microscope is gold plated phosphor bronze which is an alloy of copper with $3.5 - 10\%$ tin and up to 1% phosphorous. It is a good thermal conductor down to base temperature, harder than copper and retains a good thermal expansion coefficient matching to macor and piezoelectric material (PZT) which are the other important materials used (Figure 3.12(a)). Table 3.1 lists the value of the relevant thermal properties of the different materials used in the microscope.

Materials	Thermal expansion coefficient $\frac{\Delta l}{l}$ at 300 K ($\times 10^{-6}\,\mathrm{K}^{-1}$)	Thermal conductivity at 300 K $Wcm^{-}K^{-1}$	Thermal conductivity at 100 mK $Wcm^{-}K^{-1}$
Copper	16.4	4	10^{-1}
Bronze	18.9	1.2	6×10^{-4}
Phosphor Bronze	17.5	0.5	2.2×10^{-3}
Macor	9.3	1	5×10^{-5}
Titanium Ta6V	8.9	0.058	10^{-6}
PCB	14		2×10^{-4}
Inox	13	0.16	1.5×10^{-4}
PZT	4-6	0.011	
Quartz	8.1	0.013	1.5×10^{-4}
Sapphire	8.4	0.4	
Stycast®2850 FT	35	1.2	
Epotex®H21D	26		
Constantan	14.9	0.19	5×10^{-1}
Ecosorb	63		

Table 3.1: Thermal properties of the principle materials used in the microscope [80, 81]

Piezoelectricity

The crucial ingredient of a scanning probe microscope is the accurate control of the position of the local probe wrt. the sample in three dimensions. This would not have been possible without the discovery of Piezoelectricity by Jacques and Pierre Curie in 1880. It is the property of certain crystalline materials to generate an electric field when mechanically stressed. Or conversely, they respond to an applied electric field by undergoing mechanical deformation which is called the inverse piezoelectric effect. Its origin is related to the fact that in certain crystalline materials with a non-uniform charge distribution, mechanical deformation can give rise to separation of geometric centers of positive and negative charges resulting in electric polarization **P**. The piezoelectric effect can be described by the strain-charge coupled tensorial equations:

$$\begin{aligned} \mathbf{S} &= [s]\mathbf{T} + [d]^t\mathbf{E} \\ \mathbf{D} &= [d]\mathbf{T} + [\epsilon]\mathbf{E}, \end{aligned} \tag{3.3.1}$$

where **S** and **T** are the six-component mechanical strain and stress vectors respectively (3 longitudinal and 3 in shear mode) and **E**, **D** are the three component electric field and electric displacement vectors respectively. **S** and **T** are related by the tensor $[s]$ (6×6) called the mechanical compliance, similarly **D** and **E** by the dielectric permittivity $[\epsilon]$ (3×3) while **S** and **E** are coupled by $[d]$ (3×6) which is the symmetric, piezoelectric coupling matrix . The coefficient $d_{\mathrm{i,j}}$ gives the induced strain in direction $j \in (1, 6)$ per unit of electric field applied in direction $\mathrm{i} \in (1, 3)$. Usually the 3^{rd} direction is considered as the polarization direction **P** of the crystal.

Figure 3.13 demonstrates the normal and shear mode mechanical deformations induced in a

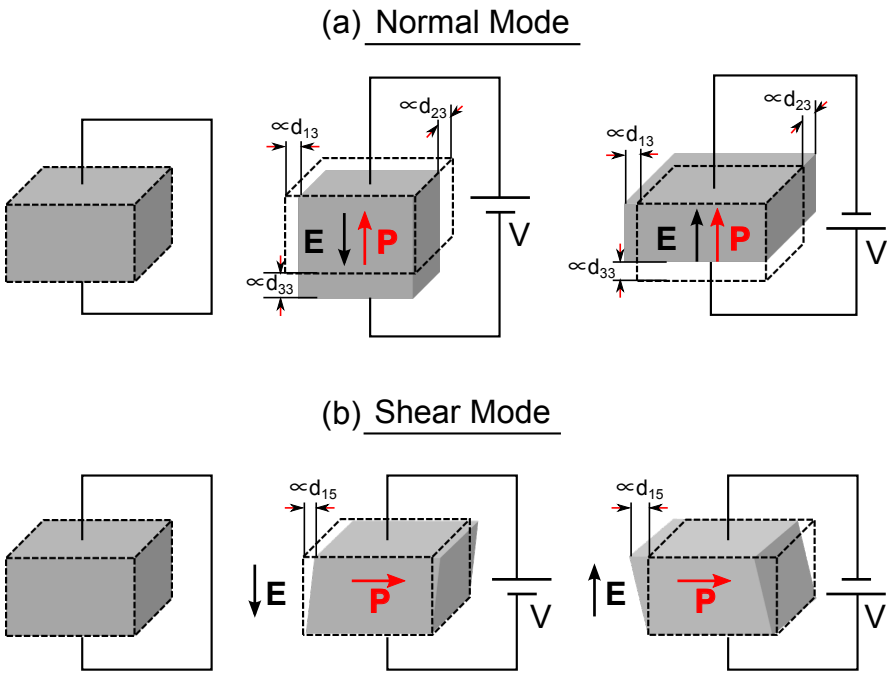

Figure 3.13: (a) Normal mode and (b) shear mode of operation of piezoelectric materials.

piezoelectric. In normal mode of operation, **E** is applied parallel to **P** that induces extension (contraction) in the direction of **P** accompanied by a contraction (expansion) in the plane perpendicular to **P**. The additional deformations in the perpendicular plane are described as the transverse piezoelectric effect and consequently (d_{13}, d_{23}) are called the transverse piezoelectric coefficients. In shear mode of operation, **E** is applied perpendicular to **P** which yields a shear deformation in the direction of **P** as shown in Figure (b). The shear deformation coefficients are normally the largest piezoelectric coefficients.

In the microscope, two different piezoelectric materials have been used: quartz and $Pb\,(Zr_xTi_{1-x})\,O_3$ (PZT). Table 3.2 lists the transverse piezo electric coefficient of these materials at room temperature and at 4 K. Quartz is a naturally occurring piezo-electric, possible to produce with very good quality and is a natural choice for the material for the resonators used in the scanning probe (section 3.4). However, from table 3.2, we see that its piezoelectric coefficient is rather small which limits its application as an actuator. PZT, an artificially synthesized ceramic with far greater d_{31} than quartz, is a suitable choice for constructing strong actuators needed for three dimensional movement of the tip. However, unlike quartz, its piezoelectric properties are dependent on temperature and this gives rise to hysteresis and thermal drift.

The Piezoelectric Scanner

The piezoelectric scanner used in our microscope is made by PI [82]. It essentially consists of a hollow, cylindrical tube made of PZT as shown in Figure 3.14(a). Two pairs of electrodes placed on opposite sides of the tube control its X-Y movement while an electrode going round

	Transverse piezoelectric coefficient d_{13} (10^{-12} m/V)	
	300 K	4 K
Quartz	1	1
PZT	200	$\approx 20 - 40$

Table 3.2: Transverse piezoelectric coefficient of materials used in the microscope [78].

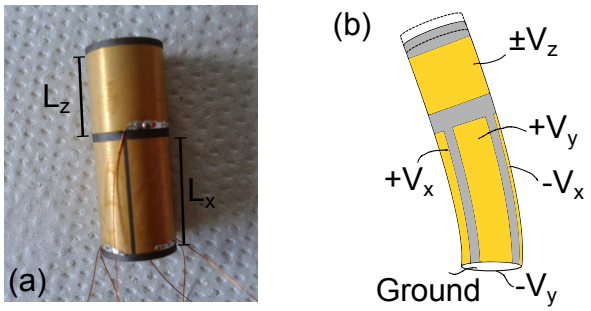

Figure 3.14: Schematic of the piezoelectric tube. The side electrodes (connected to $\pm V_x$ and $\pm V_y$) cause bending motion of the tube for scanning in the horizontal X-Y plane. The top electrode (connected to $\pm V_z$) together with the interior grounded plane is responsible for longitudinal extension and contraction of the tube.

the tube controls its Z-movement. The capacitance of the X,Y and Z plates wrt. ground is 5, 5 and 10 nF respectively at RT while at low temperatures, the capacitances drop to 1.1, 1.1 and 2.2 nF respectively. The thickness of the tube is $t \approx 0.5$ mm and its interior diameter $d \approx 9$ mm. The length of the X,Y electrodes are $L_x, L_y = 14$ mm and for the Z electrode is $L_z = 10$ mm. For elongation or contraction along Z, a voltage V_z is applied to the outer Z electrode while the interior of the tube is maintained at ground (cold). The radial electric field, thus applied, is parallel to the direction of polarization of the tube which induces mechanical strain radially. Hence the walls of the tube are thinned (thickened) and to maintain constant volume, an elongation (contraction) along Z is simultaneously produced. Lateral displacement in the X-Y direction also uses this transverse piezoelectric effect. A voltage of opposite polarity is $\pm V_x$ and $\pm V_y$ is applied to the X and Y plates respectively. A positive voltage would cause an elongation of the corresponding side of the tube while a negative voltage to the opposite electrode would cause a contraction, thus leading to a bending of the tube laterally.

	300 K	100 mK	Calculated at 300 K
ΔX/ΔV(nm/V)	40	6.5	39.2
ΔZ/ΔV(nm/V)	3.5	0.7	3.6

Table 3.3: Measured sensitivity of Piezo-electric tube using a calibration sample and from theoretical estimate [78].

Table 3.3 lists the lateral and longitudinal deforming capability or the sensitivity of the piezoelectric tube in our microscope at room temperature and at 4 K. At room temperature, the

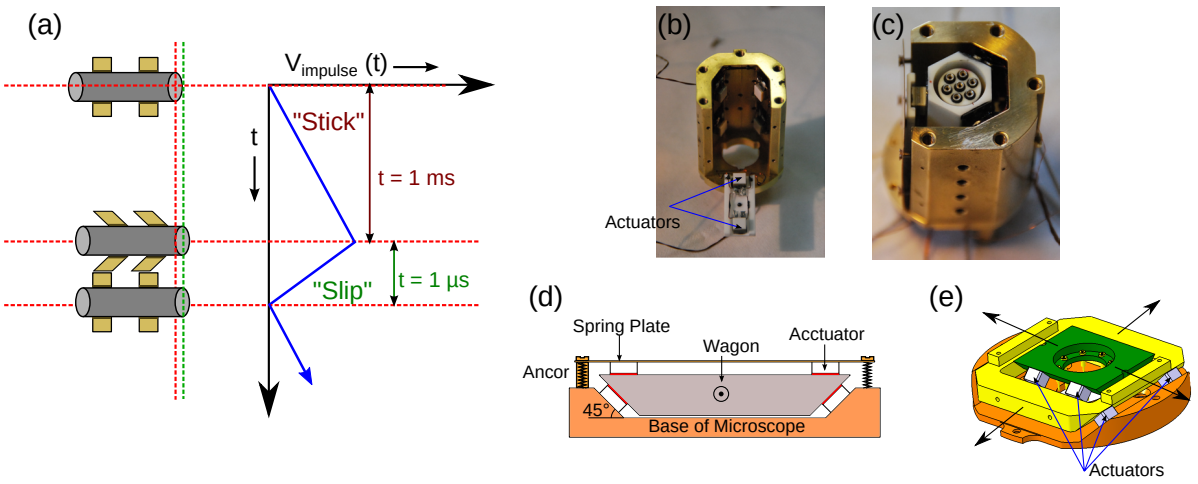

Figure 3.15: Coarse motion. (a) Movement by 'Slip-stick' mechanism. (b) Optical microscope image showing the piezo actuators attached to microscope body for coarse motion in z direction. (c) Top view of the assembly of piezo scanner, outer macor tube and outermost sapphire shaft held inside the microscope body by the spring plate. (d),(e) Schematic for the wagons for the displacement of the sample in the horizontal plane.

maximum voltage that is applied to the tube electrodes is ±150 V. This implies a maximum scan range of 12 μm and a maximum longitudinal deformation of 1.050 μm. Although the electronics used (Nanonis) allows a maximum output voltage of ±400 V, we found it safe to restrict the applied voltage to ±150 V as application of too high voltages could lead to depolarization of the tube. At 4 K or lower, we apply a maximum of ±310 V which gives a maximum scan range 4 μm. The maximum voltage applied to the Z electrode at low temperatures is about ±280 V which gives a maximum longitudinal deformation of 396 nm.

These high scan ranges are required for the purpose of localization of our sample by AFM (section 3.5.2). Nevertheless, this does compromise the spatial resolution achievable by the microscope to some extent. The Nanonis electronics is a 16 bit system with maximum output of ±10 V and gains 4, 15 and 40. Hence, the highest resolution achievable with gain 4 is about $\delta V = 1.2$ mV which corresponds to a spatial resolution of $\delta X = \frac{\Delta X}{\Delta V}\delta V = 50$ pm and longitudinal resolution of $\delta Z = \frac{\Delta Z}{\Delta V}\delta V = 4.3$ pm at room temperature. At low temperatures, both spatial and Z resolution is enhanced to 7 pm and 0.8 pm respectively due to reduction of the piezoelectric coefficient at low temperatures. The electrical noise associated with the high voltage amplifier is about 1 mV which contributes to a noise in δX of about few tens of pm at room temperature. This is acceptable but not ideal for permitting a good resolution in STM. Once again, this is reduced by a factor of $5 - 10$ at low temperatures.

Coarse Motion

The coarse motion of the piezoelectric scanner in the vertical direction and the sample in the horizontal plane is brought about by the piezo-actuators, also made of PZT, operated in shear mode (section 3.3.1). Figure 3.15(b) shows the six actuators for Z-displacement of the piezo tube, four attached to the microscope body and two attached to the spring press plate while (c) shows the image of the complete arrangement for vertical motion. The frictional force between the actuators and the sapphire shaft of the scanner can be adjusted by adjusting the pressure exerted by the spring press plate on the scanner. In a similar fashion, the X and the Y wagons are acted on by six actuators each, four on the microscope base and two on spring press plates (Figure 3.15(d),(e)). The dimension of each actuator is $5 \times 5\,\mathrm{mm}^2$ and consists of three piezo stacks with a total capacitance of 10 nF.

The coarse motion is based on the "slip-stick" mechanism as demonstrated in Figure 3.15(a). A saw-tooth voltage $V_{impulse}(t)$, consisting of a slow rise ($t = 1\,\mathrm{ms}$) and a sharp drop ($t \approx 1\,\mu\mathrm{s}$), is applied to the face of the actuators in contact with the part to be moved (scanner/X-Y wagons) while the other face is maintained at ground potential. During the slow rise of $V_{impulse}(t)$, the shear force on the actuators is perfectly balanced by the static friction. This implies that the part to be moved "sticks" to the actuators and gets dragged along the direction of deformation. When $V_{impulse}(t)$ suddenly drops to zero, the static friction is unable to overcome the resulting large acceleration and this causes the actuators to "slip" wrt. the scanner/wagons and return to their original position. This, therefore imparts a net displacement to the piezoelectric scanner and the X-Y wagons.

The time taken to drop $V_{impulse}$ to zero during the rapid face is very important as it determines the acceleration imparted to the scanner or the wagons. This time is limited by the intrinsic time constant of the actuator circuit τ. With $C = 10\,\mathrm{nF}$ and the resistance of the lines being $R = 70\,\Omega$, the time constant is about $\tau = 0.7\,\mu\mathrm{s}$. At room temperature, 100 V pulses are applied at a frequency of 1 kHz which generates a displacement of $\approx 250\,\mathrm{nm/pulse}$ in X/Y and $\approx 100\,\mathrm{nm/pulse}$ in Z, towards the sample and $\approx 350\,\mathrm{nm/pulse}$ away from the sample (supported by gravity since in the downward direction). At 4 K or lower, $200 - 250\,\mathrm{V}$ pulses at the same frequency are used. While displacement produced in the X-Y direction is about $\approx 75\,\mathrm{nm/pulse}$, towards the sample along Z direction, it is about $\approx 40\,\mathrm{nm/pulse}$ and away from sample, it is about 120 nm/pulse. However, these measures are highly subjected to the pressure exerted by the spring plates and can be optimally adjusted for higher efficiency.

3.3.2 The Inverted Dilution Fridge : Sionludi

The cryostat used in the experiment belongs to the second generation (2008) of *Sionludi* or Inverted Dilution cryostat developed here in Institut Néel [83]. It operates in a completely reversed manner compared to a standard dilution refrigerator, hence the name. Whereas in

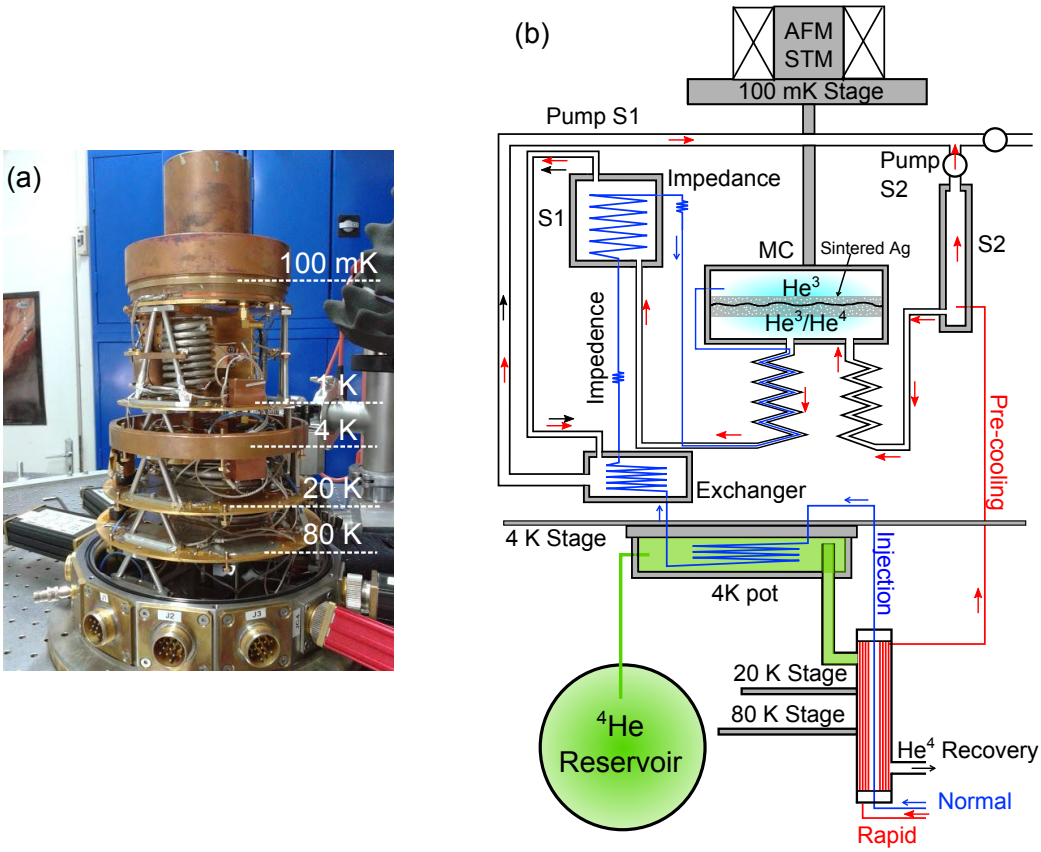

Figure 3.16: The Inverted Dilution fridge or *Sionludi*. (a) Optical image with the five stages of thermalisation indicated. (b) Schematic explaining the working of the *Sionludi* [78]. MC stands for mixing chamber, S1 for Still 1 and S2 for Still 2.

the latter, the cryostat is inserted top-down inside a helium bath, inverted dilution requires the cryostat to be mounted on top of a ^{4}He reservoir. This is particularly convenient for scanning probe experiments as it provides an easy access to the sample and the tip. However, since the cryostat is in a room temperature environment, heavy shielding and a good vacuum is essential to reduce the heat load on the dilution stage.

The whole cryostat is housed inside a vacuum chamber, located on top of the ^{4}He reservoir. There are a total of five stages for thermalisation, stacked one on top of the other, at: 80 K, 20 K, 4 K, 1 K and 100 mK (from bottom to top), as shown in Figure 3.16(a). The different stages are isolated thermally by stainless steel legs that ensure a good mechanical stability. Gold plated copper screens installed at 80 K and 20 K help to isolate the 4 K and colder stages from thermal radiation.

The schematic shown in Figure 3.16(b) explains the functioning of the *Sionludi*. The cryostat possesses a ^{4}He circuit (secondary circuit) that is distinct from the circuit of the mixture ^{3}He/^{4}He (primary circuit). The cooldown of the cryostat from 300 K to 100 mK is achieved in two stages. The first stage involves cooldown of the mixture to 4 K by creating a strong thermal contact

between the mixture and the ^{4}He circuit while in the second stage this thermal contact is cut off and the mixture is cooled down further by the process of dilution [84]. The different steps involved are listed below:

1. An overpressure of 100−300 mbar maintained on the ^{4}He reservoir causes the ^{4}He to flow up into the 4 K pot, thus cooling the lower stages on the way. It then flows downwards through a counter-flow heat exchanger where it comes into thermal contact with the mixture circuit. The ^{4}He vapours thus formed, then flow into the recovery.

2. A very small quantity of the ^{3}He/^{4}He mixture (7 l STP) is injected at high pressure (≈ 1.3 bar and flow rate of 11 l/min STP) into the rapid injection path, indicated by the red arrows in (b). At this stage, Still 2 is directly pumped. This causes the cooled mixture (cooled by the thermal contact with ^{4}He at the counter-flow heat exchanger) to directly flow into Still 2, then to the mixing chamber, Still 1 and finally pumped out. This gradually cools the upper stages to 4 K. The whole process takes about 15 hours.

3. Once everything is at 4 K, direct pumping of Still 2 is stopped. The rest of the mixture from the tank is now gradually injected into the circuit via normal injection, indicated by the blue line in Figure 3.16(b). The mixture therefore flows from the 4 K pot into Still 1 via a narrow capillary which provides a high impedance, then into the upper part of the mixing chamber (MC) via a second high impedance. The sudden expansion into the broad space of the MC from the narrow high impedance path causes significant cooling by Joule Thompson effect. The colder mixture exits the MC and flows back into Still 1, then another exchanger, thus cooling the inflowing mixture on the way, and then finally pumped out. This process causes the temperature to gradually lower from 4 K to 1 K.

4. By 1 K, the mixture in the MC has condensed and separates into an upper ^{3}He rich phase (practically 100% ^{3}He) and a lower dilute phase (6.6% ^{3}He+93.4% ^{4}He). To cross the phase boundary, ^{3}He molecules from the concentrated phase absorb heat from the surroundings and flow into the dilute phase. This endothermic process of dilution is the key process for creating temperatures as low as 100 mK. The cold ^{3}He then leaves the MC in the dilute phase and on its way out cools the incoming mixture. In Still 1, the ^{3}He flows through superfluid ^{4}He which is at rest, and is pumped out. Finally, all the ^{4}He in the mixture is trapped as superfluid ^{4}He in the MC and Still 1 while the pumping ensures a constant circulation of ^{3}He in the primary circuit [1].

With the microscope installed, our cryostat can cool down to a base temperature of 130 mK with the stills at a temperature of about 1.1 K and the injection pressure dropping down to about 1 bar. This enables us to turn off the compressor and only one pump is sufficient to maintain the mixture circulation.

[1] This is in ideal case. In practical case, some ^{4}He keeps circulating.

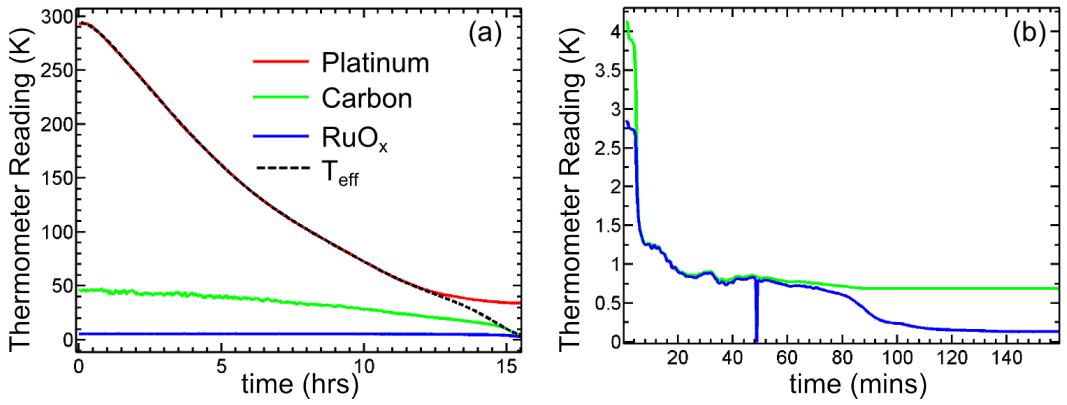

Figure 3.17: Temperature of mixing chamber recorded by different thermometers. (a) During cooldown from room temperature to 4 K and (b) during condensation. T_{eff} gives the effective temperature estimated by considering the Pt thermometer reading from 300 K to 40 K and the C thermometer reading from 10 K to 4 K and then extrapolating between the two by a polynomial fit (order 9) to get the readings in the range $T \in (40\,\mathrm{K}, 10\,\mathrm{K})$.

Thermometry

Resistance based thermometers are installed at different stages of the cryostat to monitor the temperature during the cooling process from room temperature to 4 K and then further down to base temperature. Table 3.4 lists the different types of resistors used as thermometers and their respective locations in the cryostat.

Location	Type of thermometer
80 K	Platinum resistor
20 K	Platinum resistor
4 K	Platinum and Carbon resistor
Still 1	Carbon resistor
Still 2	Carbon resistor
Mixing Chamber	Platinum, Carbon and RuO_x resistors

Table 3.4: Thermometers installed at different locations.

Three different types of resistors have been used which function as thermometers at different temperature ranges. Figure 3.17 shows the temperature of the mixing chamber recorded simultaneously by the three different thermometers installed at the dilution stage during cooldown to 4 K and then during condensation. Platinum resistors are sensitive to temperature in the range $T \in (300\,\mathrm{K}, 40\,\mathrm{K})$ beyond which it saturates. The carbon thermometers gives the correct temperature value from 10 K to about 700 mK beyond which the RuO_x thermometers are operational up to the lowest temperature of the cryostat.

Between 40 K and 10 K, there is no direct access to the temperature of the mixing chamber. But we are able to deduce the intermediate temperatures by considering the Pt thermometer reading from 300 K to 40 K and then the C thermometer reading from 10 K to 4 K. By ex-

trapolating between the two sets of readings by means of a polynomial fit, we can extract the temperature of the mixing chamber in the range (40 K, 10 K). In Figure 3.17(a), the effective temperature T_{eff} extracted in this manner has been plotted.

The measurement of the thermometer resistances is done by electronics and accompanying labview interface developed by the electronic service in the lab [85].

Wiring

Three shielded cables of length ≈ 1 m each have been used to electrically connect the different components of the SPM head located at the 100 mK stage to Jaeger connectors located at the outermost stage of the cryostat at room temperature [2]. Each cable consists of 15 constantan (alloy of 55% copper and 45% nickel) wires of diameter 0.1 mm ($R \approx 73\,\Omega$) with a plastic insulation and shielded outside by $7 * 16$ braids of constantan. The outer shield of the cables have been thermally anchored at every thermalisation stage to successively reduce the heat load. Additionally, the wires have been directly thermalised at stages 4 K, 1 K [3] and at 100 mK. Table 3.5 lists the length of the wires between the different stages and the corresponding thermal power transmitted (crudely estimated assuming a thermal conductivity of 19.5 $\mathrm{Wm^{-1}K^{-1}}$ for constantan).

Temperature	Length of wire	Thermal power
300 K $->$ 80 K	20 cm	2.35 mW
80 K $->$ 20 K	10 cm	1.28 mW
20 K $->$ 4 K	10 cm	0.34 mW
4 K $->$ 1 K	30 cm	21.4 μW
1 K $->$ 100 mK	30 cm	6.4 μW

Table 3.5: Thermal powers conducted by each shielded cable of 14 constantan wires between each thermalisation stage.

For reducing noise in the tunneling current line, we have dedicated a single low noise, coaxial cable just for this purpose. Apart from this there are three separate capillaries with 12 wires each for the thermometers.

Filtering

For low temperature cryogenic operation, it is extremely important to filter high frequency electromagnetic radiations which can disturb the thermal equilibrium of the electrons in the circuit. The gold-plated copper shields installed at the different stages cut off a significant fraction of these radiations. However, the electrical lines serve as good wave guides for transmission of

[2] The existing wiring at the beginning of my PhD had to be redone because several important connections showed significant leakage to ground

[3] At 4 K and 1 K stage, thermalisation of the wires have been done inside closed copper boxes using Kapton tapes glued with Eccobond (good thermal conductor but electrically insulating.)

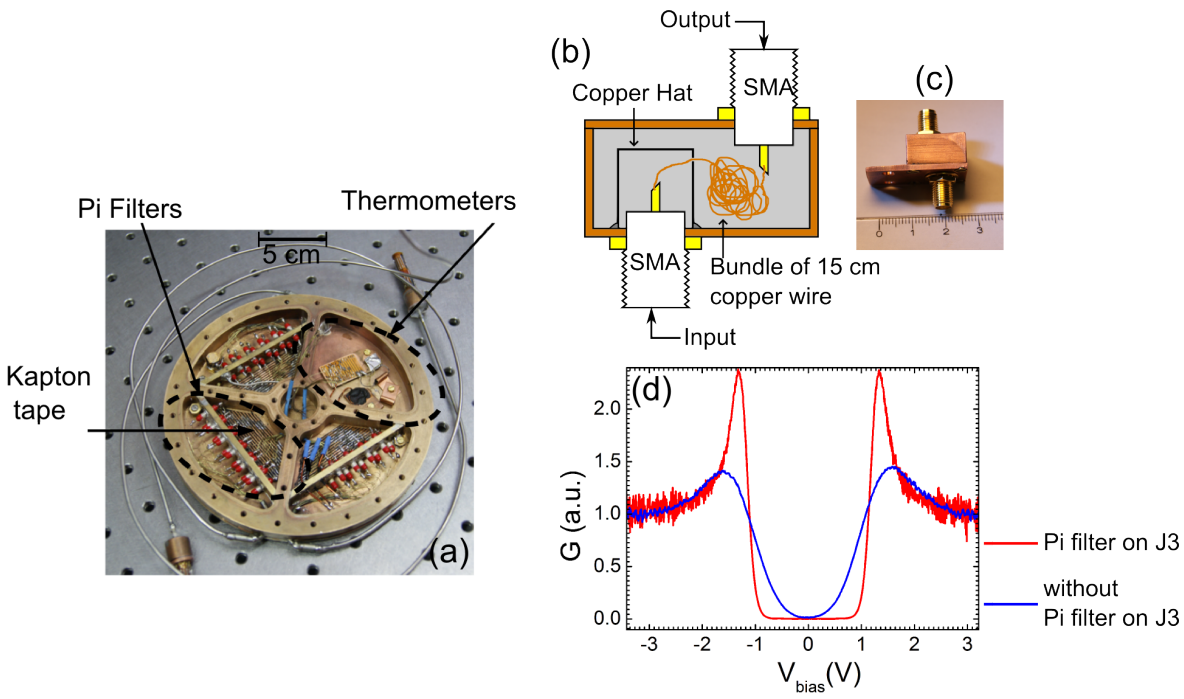

Figure 3.18: Filters. (a) 6.5 nF pi-filters inserted at the dilution stage. (b) Schematic and (c) optical image of the filter of the tunneling current line at the 1 K stage [78]. (c) Normalized differential tunneling conductance spectra over Ti/Nb/Au (3 nm/30 nm/4 nm) at $T = 180$ mK, with and without an external feed-through pi-filter (bandwidth < 100 kHz) on the high voltage lines (J3).

these high frequency waves and hence must be additionally filtered. For this purpose, at the dilution stage, a circular box with four compartments have been installed as shown in Figure 3.18(a). Three compartments are dedicated for accommodating the filtering and thermalisation arrangements for each of the three shielded cables while the fourth compartment houses the thermometers. Each of the three compartments is in turn divided into two sub-compartments, the outer one housing the inputs of the filters while the wires exit the filter outputs in the inner compartment where they are then thermalised on tracks of Kapton tape. The filter installed at each electrical line consist of a feed-through, low-pass pi filter (cut-off frequency ≈ 350 kHz at room temperature and ≈ 1.5 MHz at 100 mK). However, the lines connected to the piezo-actuators for coarse motion have not bee filtered at this stage because the increased capacitance would enhance the relaxation time of the actuators and this could lead to a reduction of their efficiency. Also, the two lines required for AFM operation (section 3.3.4) have not been filtered as the electronics involved for this purpose demands a low line capacitance.

The tunneling current line have been treated in a special manner as very small currents of the order of pA needs to be measured. A single low noise, coaxial line with a stainless steel core serves this purpose. The core is surrounded by an insulating sheath of PTFE (commonly

called Teflon) coated with carbon and then an outer metallic braid. Since stainless steel is a bad conductor of heat, the heat load transmitted by the line is less. SMA connectors have been used for better electrical connection and better shielding. The line runs from room temperature directly to the 1 K stage with the outer metallic braid thermalised at the different stages at intermediate temperatures. At the 1 K stage, it enters a filter made of a small copper box (Figure 3.18(c)). The inner cavity of the box is fragmented into two sub-compartments by a copper partition, one housing the input and the other the output (Figure (b)). The input and the output is simply connected by a bundle of copper wire 15 cm long that causes dissipation of the electromagnetic signals. Further the box is filled up with Eccosorb which is also a very good filter. The tunneling current line then continues to the cold stage with an intermediate thermalisation that additionally dampens any remaining vibration. In the filtering compartment for the other lines (Figure (a)), the tunneling current line is not filtered further. It is isolated from the other lines and continues to the microscope.

Since the high voltage lines connected to the piezo actuators are not filtered, this does affect the measurements as the unfiltered radiations transmitted cause a higher electronic temperature than the base temperature of the cryostat. The situation is seen to improve by including an external feed through pi-filter (equipped for 12 lines, cutoff frequency ≈ 100 kHz) [85] on the high voltage lines (represented by J3). Figure 3.18(c) shows the differential tunneling conductance spectrum on Ti/Nb/Au (3 nm/30 nm/4 nm) showing the superconducting DOS, with and without pi-filter on J3. The remarkable improvement of the measurement, characterized by the well-developed coherence peaks and sharper drop at $V_{bias} = \Delta$, clearly indicated a lower electronic temperature after including the pi filter in the high voltage lines.

3.3.3 Magnetic Field

The cryostat is equipped with a superconducting magnet constituted by a coil of niobium titanium (NbTi) woven around a copper shield that is installed at the 4 K stage. The magnetic field provided by it is 160 mT/A. The current source used to drive these coils can provide a maximum of 10 A, thus giving a maximum magnetic field of 1.6 T.

However, due to local damage in the coil, the maximum magnetic field that could be achieved in the later part of my PhD, was restricted to 320 mT. It is currently under repair.

3.3.4 Electronics

For overall control of the microscope operation, we have utilized Nanonis electronics made by Specs [86]. It is equipped with a PC which has a real time operating system and 2 NI-FPGA cards that enables data acqusition, analysis and implementation. The PC communicates with the main computer of the experiment by ethernet. The Nanonis is a 16 bit, fully digital system and consists of three modules:

1. The SPM Controller: It controls all the basic STM operations like scan control, Z-control, data acquisition, data monitoring, spectroscopy etc. The generic analog interface provides 48 live signals: 8 inputs, 8 outputs and 32 internal signals. The maximum voltage that can be obtained from each output is ±10 V.

2. The Oscillation Controller with PLL: It provided the excitation voltage to the AFM resonator, measures the response generated by it and utilizes this signal in the manner described in section 3.2.2. The AFM operation is controlled by this module.

3. The High voltage amplifier: This is a low noise amplifier with gains 4, 15 and 40. This is used to amplify the voltages supplied to the X,Y,Z electrodes of the piezo tube scanner as well as one extra channel.

4. The Piezo driver: It supplies the voltage pulses to the piezo actuators for coarse motion, at an amplitude and frequency that can be set by the user.

The Nanonis interface provides a user-friendly environment for scanning probe measurements. It additionally includes several modules that can be easily integrated in labview programming to perform experiments as per user requirement. This feature has been extensively utilized throughout the course of my PhD to automate various experiments; tip approach in AFM mode, performing Bias and Z spectroscopy, LDOS mapping at different back gate voltages (Chapter 5), recording temperature dependence of sample and tip properties during cooldown, are a few examples.

Apart from the overall control by the Nanonis, there are two important home-built electronic components: (1) the tunneling current amplifier and (2) the AFM electronics that control the signals involving the scan probe in the STM and AFM mode of operation respectively. We discuss this next.

Tunneling Current Amplifier

The tunneling current amplifier must allow the measurement of currents with a precision less than pA and a band-pass of about 1 kHz (sufficient for imaging 10 atoms/nm at a speed of 100 nm/s). It constitutes of a very low noise current to voltage operational amplifier implemented in the inverted configuration, as shown in the schematic in Figure 3.19(a). The output voltage produced by a tunneling current I_t is given by:

$$V_{out} = -Z_{fb} I_t = -\left(\frac{R_{fb}}{1 + j\omega R_{fb} C_p}\right) I_t, \tag{3.3.2}$$

where R_{fb} is the feedback resistor, C_p is the parasitic capacitance and ω is the frequency of I_t. As is evident, the low frequency gain of the amplifier is given by $-R_{fb}$ with a cut-off frequency $f_c = 1/(2\pi R_{fb} C_p)$. Therefore, although a larger R_{fb} increases the gain of the amplifier, it is

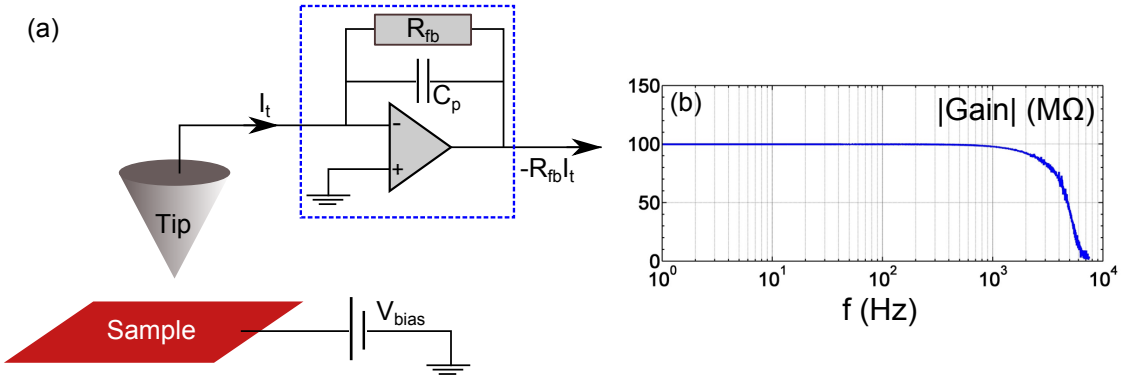

Figure 3.19: (a) Schematic showing the implementation of the tunneling current amplifier. R_{fb} is the feedback resistor and C_p is the parasitic capacitance. (b) Gain of the amplifier as a function of frequency showing a cut-off at about 3 kHz.

at the cost of reducing the bandwidth. An optimum value of R_{fb} is, hence, required which is usually chosen to be about $10 - 100\,\mathrm{M\Omega}$. The thermal voltage noise density associated with R_{fb} is given by the Johnson-Niquist formula [87],

$$n_R = \sqrt{4k_B T R_{fb}}, \tag{3.3.3}$$

where $k_B = 1.38 \times 10^{-23}\,\mathrm{J/K}$ is the Boltzmann's constant and T is the temperature where R_{fb} is installed.

In our tunneling current amplifier $R_{fb} = 100\,\mathrm{M\Omega}$ and installed at room temperature. Figure 3.19(b) shows the measured transfer characteristics which indicates a cut-off frequency of about 3 kHz. The parasitic capacitance is therefore $C_p \approx 0.5\,\mathrm{pF}$. The Johnson-Niquist noise density at 300 K is $1.29\,\mu\mathrm{V}/\sqrt{\mathrm{Hz}}$. This gives a current noise

$$S_{I_t} = \frac{n_R\sqrt{B}}{R_{fb}} = \sqrt{\frac{4k_B T B}{R_{fb}}} \tag{3.3.4}$$

where B is the acquisition bandwidth with a maximum $= f_c$. $S_{I_t} \approx 0.7\,\mathrm{pA}$ in our case at $T = 300\,\mathrm{K}$ and $B = f_c$. Using Eq.(3.2.1), we can find the corresponding vertical noise in z_{ts} given by

$$S_{z_{ts}} = \frac{S_{I_t}}{\left|\frac{\partial I_t}{\partial z_{ts}}\right|} = z_0 \frac{S_{I_t}}{I_t}. \tag{3.3.5}$$

If we assume $z_0 \approx 1\,\text{Å}$, then for $I_t = 100\,\mathrm{pA}$, the vertical noise in z_{ts} is $\approx 0.7\,\mathrm{pm}$ which is well below the vertical resolution required to image atoms.

AFM Amplifier

The design of the AFM electronics depends on the choice of the AFM resonator and the manner in which it is excited. In many cases like cantilevers or quartz resonators, the signal generated in

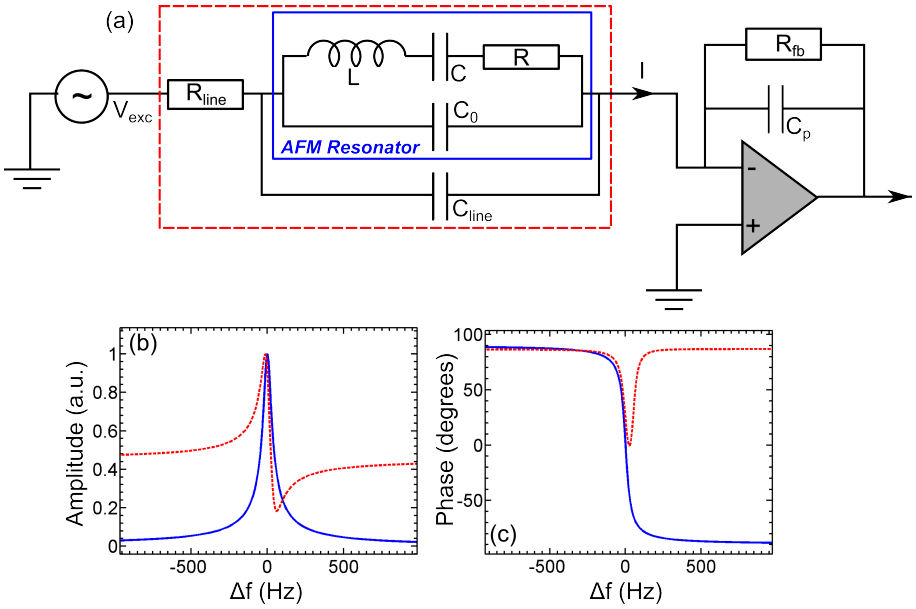

Figure 3.20: Effect of electrical line on AFM signal. (a) Circuit diagram for AFM resonator (enclosed by blue rectangle) connected to a current to voltage converter. (L, C, R) are the inductance, capacitance and resistance respectively of the AFM resonator, C_0 is the capacitance between the electrodes and (C_{line}, R_{line}) are capacitance and resistance of the electrical line respectively. (b) Amplitude of current, with (red) and without (blue) line contribution, as a function of $\Delta f = f - f_0$ where f is the drive frequency and $f_0 = 993.75\,\text{kHz}$ is the eigen frequency of the resonator. (c) Phase of I vs Δf. ($L = 1.9\,\text{H}$, $C = 13.5\,\text{pF}$, $R = 600\,\Omega$, $C_0 = 1\,\text{pF}$, $R_{line} = 70\,\Omega$ and $C_{line} = 131\,\text{pF}$ [88, 89]).

response to a given excitation (electrical/mechanical) is electric current. Therefore, the electronics required to measure this response signal essentially consists of a current to voltage converter just like in STM operation. However, unlike STM, the response signal is composed of extremely high frequencies, especially for quartz based resonators ($> 30\,\text{kHz}$). The choice of our AFM probe is the Length Extensional Resonator or LER (section 3.4) which has an eigen frequency of $f_0 \approx 1\,\text{MHz}$. There are two standard ways to measure this: (1) by using a current to voltage amplifier with higher bandwidth, but reduced gain. Since the current to be measured is of the order of tens of nA, the reduced gain does not pose a problem. However, the current noise is increased [Eq.(3.3.4)]. (2) By using a charge amplifier [4], as is the case for Femto amplifiers by SPECS [88].

However, one major problem in measuring the high frequency response of the resonators is that the effect of the line capacitance and resistance ($C_{line} \approx 131\,\text{pF}$, $R_{line} \approx 70\,\Omega$) is significant since $C_{line} \gg C$. Figure 3.20(b) shows the response characteristics of a LER (value of (L, C, R) and C_0 taken from manual for the Kolibri sensor [88]) as well as the response considering electrical line contributions. As can be seen clearly, the intrinsic resonance properties of the probe are subdued which hinders its capability to efficiently respond to changes in the tip-sample force

[4] current to voltage converter operated beyond the cut-off frequency

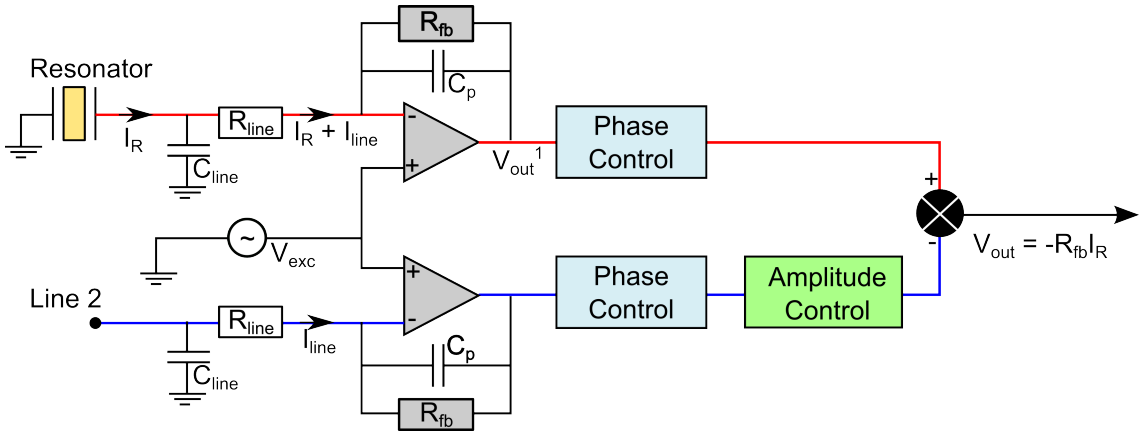

Figure 3.21: Measuring response of the AFM resonator with line compensation. Schematic of the electronics used to cancel the contribution from the electrical lines. I_R is the current generated by the resonator in response to the excitation voltage V_{exc} and I_{line} is the current contribution from the electrical line. $R_{fb} = 22\,\mathrm{k\Omega}$ gives the overall gain and $C_p \approx 1\,\mathrm{pF}$ is the parasitic capacitance.

gradient.

To circumvent this problem, we use a measurement scheme in which the contribution from the electrical line is compensated by using the signal from another identical line (Line 2), starting from room temperature and ending at the dilution stage (well thermalised but remains floating there). The schematic of the necessary electronics is shown in Figure 3.21. It was made by Daniel Leppoitevin from the electronic service in Institut Néel. In this measurement technique, the resonator is excited and the generated response measured from the same electrode while the other electrode is maintained at ground (room temperature) by the tunneling current amplifier (section 3.3.4). Hence, only one electrode of the scan probe is sufficient for implementation of AFM. This technique has the additional advantage that a good compensation can be achieved irrespective of temperature since the AFM line is identical to Line 2 and their properties change in an identical manner while cooling down.

To cancel the contribution of the electrical line, the signal in the two branches, i.e. the AFM line and line 2, is matched at a frequency far away from resonance. A perfect match would completely nullify the voltage at the output of the electronics. The way this matching is done is by using a phase and amplitude controller as shown in Figure 3.21 which enables adjustment of the phase and amplitude of one signal wrt. the other. These adjustments are continued till the output signal is minimized. Conducting a frequency sweep now, should give us the completely compensated resonator response as shown by the blue curve in Figure 3.20(b),(c). If not, the above process is repeated at a far off frequency at the other extremity. Repeating the whole process two-three times leads to a very good match and hence complete recovery of the intrinsic resonator response.

Figure 3.22(a) and (c) shows the electronic circuit of the Phase and amplitude controller respectively. The Phase controller essentially consists of a low pass filter with a capacitance

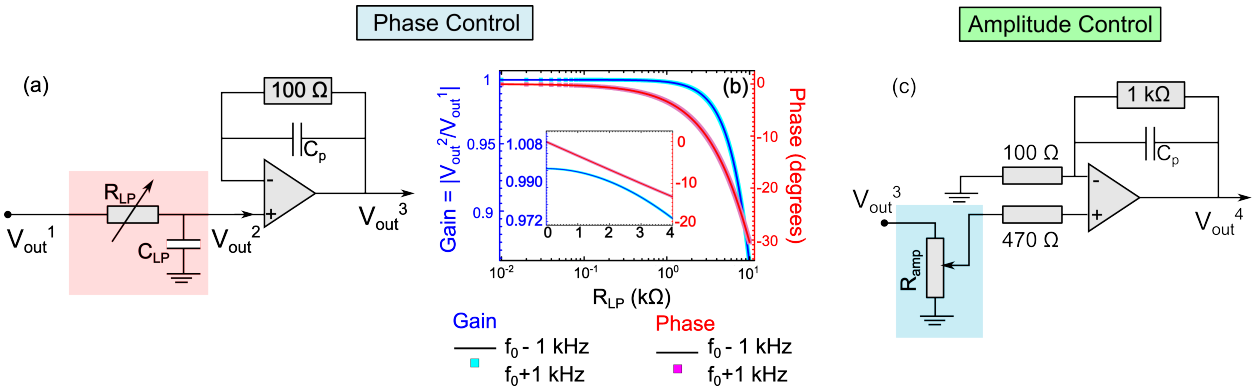

Figure 3.22: Phase and Gain control in AFM electronics. (a) Electronic circuit for controlling the phase of the line contribution. (b) Change in gain and phase of V^2_{out}/V^1_{out} with change in R_{LP} at the two extreme frequencies $f_0 \pm \Delta f_0/2$ ($f_0 = 993.75\,\text{kHz}$, $C_{LP} = 9.4\,\text{pF}$). (c) Electronic circuit for controlling the amplitude of the line contribution.

$C_{LP} = 9.4\,\text{pF}$ and an adjustable resistance R_{LP} having a maximum of $10\,\text{k}\Omega$. Tuning R_{LP} causes its cut-off frequency to vary down to 1.7 MHz which is just above the resonating frequency of the LER ($\sim 1\,\text{MHz}$). A characteristic property of low pass filters is that close to its cut-off, the phase at the output changes linearly with frequency although the gain remains close to unity. This is shown in Figure 3.22(b) for two frequencies located at the two sides of f_0 (where the adjustments are made). This demonstrates the working principle of the Phase controller. The amplitude controller simply makes use of the principle of a voltage divider. Tuning a variable resistor R_{amp} (maximum $10\,\text{k}\Omega$), causes a change in the voltage division and consequently a change in the amplitude of the output voltage.

The compensation achieved at a given frequency far off resonance, in this manner, continues to persist at all frequencies in the neighborhood of f_0 i.e. $|f - f_0| \lesssim \eta \Delta f_0/2$ (Δf_0 is the FWHM) where η can be as large as 20 or even more. This is not so obvious given the frequency dependence of the electrical line signals. This is partially explained by the fact that since the two lines are very similar, if not perfectly identical, their electrical properties should evolve with frequency in a similar manner; hence once matched at a particular frequency, they should remain that way for other frequencies as well. There is another reason which becomes clear if we consider the mathematical expression for the output at the exit of the first amplifier at a far off frequency (Figure 3.21);

$$V^1_{out} = \left(\frac{Z_{fb} + Z_{line}}{Z_{line}}\right) V_{exc}, \tag{3.3.6}$$

where Z_{fb} is the feedback impedance [Eq.(3.3.2)] and $Z_{line} = R_{line} - j\left(\frac{1}{\omega C_{line}}\right)$ is the impedance of the electrical line. This has been plotted in Figure 3.23 where we clearly see that the contribution of the line amounts to an additional amplitude and phase that changes very little with frequency,

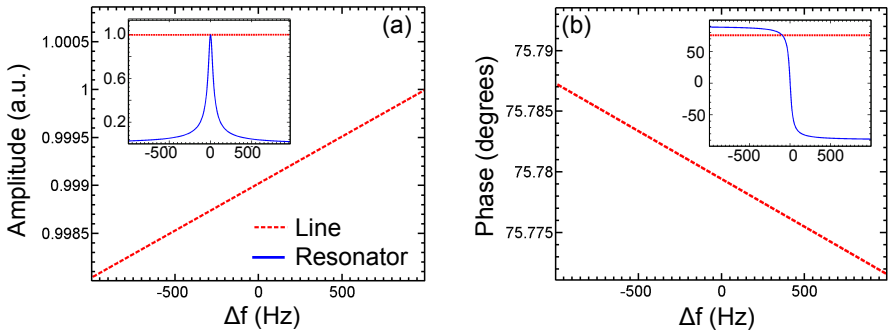

Figure 3.23: Contribution from the electrical line. (a) Amplitude of V^1_{out}/V_{exc} due to electrical line given by Eq.(3.3.6) as a function of $\Delta f = f - f_0$ ($C_p = 1\,\mathrm{pF}$, $R_{fb} = 22\,\mathrm{k\Omega}$ and the rest of the parameters are same as in Figure 3.20). Inset shows the simultaneous variation in the amplitude of the resonator response. (b) Phase of V^1_{out}/V_{exc} as a function of Δf. Inset shows the simultaneous variation in the phase of the resonator response.

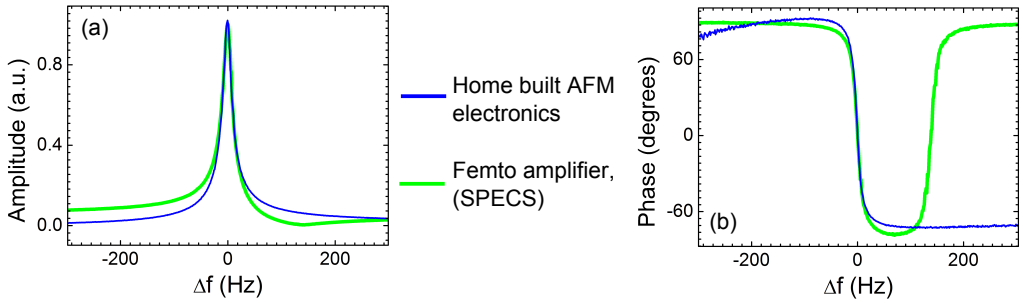

Figure 3.24: Response characteristics of LER measured by home-made AFM electronics and Femto amplifier by SPECS ($f_0 = 993.89\,\mathrm{kHz}$, $Q = 62090$, $T = 300\,\mathrm{K}$ and $P = 10^{-4}\,\mathrm{mbar}$). (a) Amplitude and (b) Phase vs Δf.

in comparison to the intrinsic response characteristics of the resonator. Therefore, even if the lines are not perfectly identical, this small variation with frequency ensures that the compensation method described persists over a broad range of frequencies (about f_0), far higher that what is required in AFM.

Therefore the AFM electronics, described above, provides a way to perfectly compensate the contribution from the electrical lines. Any imbalance appearing as a result of changing temperature and pressure during cooldown, can be compensated by simply tuning the phase and the amplitude controller. Hence this provides an efficient way to recover the intrinsic resonator response and therefore, fully harness its potential as a force sensor. Figure 3.24 shows the response characteristics of a LER measured with the Femto amplifier from SPECS [88] and by our AFM electronics that brings out the advantage offered by the latter.

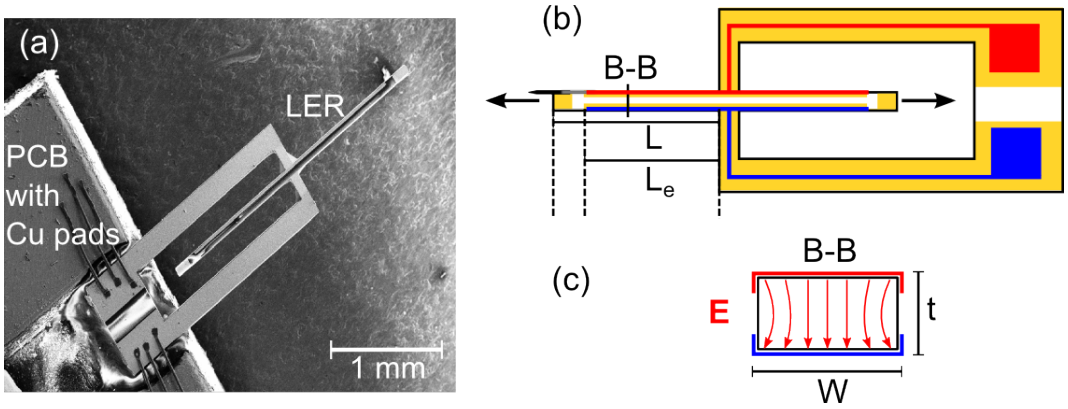

Figure 3.25: The Needle Sensor (NS). (a) SEM image of the Needle Sensor based on a length extensional resonator (LER). (b) Schematic explaining the geometry of the NS. The black arrows indicate the direction of oscillation. $L = 1340\,\mu$m is the total length of each beam of the resonator, $L_e = 1100\,\mu$m is the length of the electrode starting from the support in the middle. (c) Cross-section of the LER (B-B) indicated in (b). $W = 130\,\mu$m is the width and $t = 70\,\mu$m is the thickness of the LER beams. The red arrows indicate the direction of the applied electric field **E**.

3.4 The Needle Sensor

As force sensors in AFM, commercially available quartz based oscillators like the tuning fork (TF) [90] or the length extensional resonator (LER) [91] are being increasingly used. The natural piezoelectric property of quartz renders them self-actuating and self-sensing, thus eliminating any need to include complicated detection systems. This makes them compact and easy to implement, particularly well-suited for cryogenic applications. Moreover, the intrinsic frequency stability of quartz ensures minimum fluctuations and thermal drift compared to other force sensors like the Si cantilevers, for example [5]. Additionally, the high quality factor found in such resonators (can easily exceed 600 000 at low temperatures) reduces noise contributions (thermal and oscillator noise) in the Δf signal which consequently improves the quality of measurement.

Out of the two quartz resonators available, we chose the LER based Needle Sensor (NS) [75, 76]. Figure 3.25(a) shows an SEM image of the NS while (b) demonstrates its geometrical dimensions. The quartz rod supported in the middle and free to oscillate longitudinally at the ends, constitute a system of two coupled electromechanical oscillators, whose oscillation dynamics had been discussed in section 3.2.2. An oscillating electric field applied between the two side electrodes (red arrows in (c)) induces mechanical oscillations by transverse piezoelectric (inverse) effect 3.3.1 (therefore self-actuating). By the reverse piezoelectric effect, the periodic mechanical deformations in turn induce a periodic surface charge at the electrodes and hence current which can be easily measured (hence, self-sensing). The stiffness of each beam is $k_0 \approx 540\,$kN/m, therefore the effective stiffness of this coupled system is $k = 2k_0 \approx 1080\,$kN/m 3.2.2. This is

[5] For Si, $\Delta f/f_0 \approx -35\,$ppm/K at RT whereas for quartz it is 1 ppm/K [72]

about 600 times larger than the qPlus sensor which is based on the tuning fork oscillator [6]. Table 3.6 lists the relevant properties of the NS and the qPlus.

	k_0 (N/m)	k (N/m)	f_0 (Hz)
Needle sensor	540 000	1 080 000	1 000 000
qPlus sensor	1800	1800	32 768

Table 3.6: Important oscillating properties of the NS and the qPlus sensor. k_0 is the stiffness of each electromechanical oscillator (each beam in NS and each prong in qPlus), k is the effective stiffness of the system and f_0 is the eigen frequency [72].

The high stiffness of the NS reduces its sensitivity to tip-sample force gradients Eq.(3.2.17) as well as increases the noise level in the measurements, especially thermal and oscillator noise, compared to the qPlus [72]. Nevertheless, this high stiffness protects the probe against instabilities like 'jump to contact'. Since our main aim is to combine STM with AFM, the tip is required to be extremely close ≈ 1 Å to the surface in STM than in AFM and hence is subjected to far stronger tip-sample forces. Operations like sudden switching of tip voltage in STM mode, can also result in very high electrostatic forces. Therefore, a high probe stiffness is of paramount importance to prevent the probe from snapping to contact. Even in AFM, the higher stiffness makes it possible to work with smaller amplitudes ~ 100 pm which increases the signal-to-noise ratio and reduces the sensitivity to unwanted long-range force contributions.

This essentially justifies our decision to choose the Needle sensor as our scan probe.

3.4.1 Tips

In STM, the importance of the tip cannot be overemphasized. A clean, atomically sharp tip with stable tunneling conditions is key to achieving reproducible, superior quality measurements with high spatial and energy resolution that are free from artifacts. The important requirements for the material for an STM tip is that it should have a high conductance, hence passive against surface oxidation and high stiffness in order to withstand the strong tip-sample forces operational at tunneling distances. To combine AFM with STM, the metallic tip needs to be mounted on the force sensor. Hence, it must be light enough so that the oscillation dynamics of the sensor is not severely affected. For the qPlus sensor, this is not so stringent since it is essentially used as a cantilever, but for the NS, the weight of the tip is absolutely critical as it introduces asymmetry between the otherwise identical beams of the LER .

Tungsten (W) and platinum-iridium (Pt/Ir) are the most popular choices for STM tips. While W tips have a higher stiffness, they are prone to surface oxidation while Pt/Ir is comparatively soft, nevertheless inert to oxidation. Hence W tips are more suitable for operation under UHV conditions with sophisticated tip-preparation arrangements like FIM (Field Ion Milling) where

[6] A tuning fork with one prong fixed and the other, containing the metallic tip, free to oscillate, constitutes the Q-Plus. It therefore operates as a cantilever. Therefor $k = k_0$ in this case.

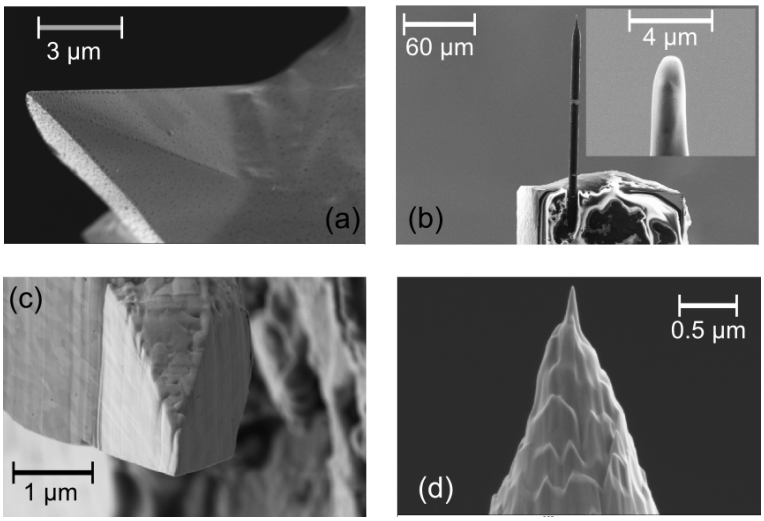

Figure 3.26: SEM images of different conducting tips for combined AFM/STM used during my the PhD. (a) Pt/Ir coated silicon cantilever tip. (b) Electrochemically etched carbon fiber tip (diameter $\approx 4\,\mu$m) [*Courtesy A. De-Cecco*]. Inset shows a zoomed-in view of tip apex. (c) Tungsten wire (diameter $\approx 4\,\mu$m), shaped with focused ion beam (FIB) in the form of a pyramid. (d) Conical W tip, shaped with FIB. *Courtesy J. F. Motte.*

the surface oxide layer can be evaporated by the application of a high electric fields. For moderate vacuum conditions, like ours, Pt/Ir is more suitable.

However, for the purpose of mounting the tips on the LER, the wire diameter is required to be very small, of the order of few microns, to ensure minimum degradation of the Q-factor. In this regard, $15\,\mu$m Pt/Ir wires were first tried. They were already quite tricky to handle given the small size and the tendency to curl up (low stiffness). Moreover, the success rate was very low with maximum probes showing poor Q-factors afterwards. The tips are then shaped with Focussed ion beam (FIB) by Jean Francois Motte of the Nanofab department in Institut Néel. Etching of $15\,\mu$m wires also proved to be rather time consuming. Using smaller diameter Pt/Ir wires $\sim 5\,\mu$m would perhaps have been a far better choice. It was not tried but manipulating such thin wires with low stiffness is anticipated to be rather challenging. Thin ($\sim 4\mu$m) tungsten wires, on the other hand, could be manipulated with relative ease, because of their higher stiffness (do not curl up). The success rate was quite high ($75-80\%$) for the probes to retain a reasonable Q-factor afterwards and FIB in the final stage, was also way faster. We opted for FIB instead of electrochemical etching of W for tip sharpening, as is commonly done, because of mainly two reasons. Firstly, the electrochemical etching process oxidizes the tip apex, which can be several nm thick. Secondly, the tip-apex produced is extremely sharp and often curls up on touching the surface (see [78], Pg. 48, for example). Moreover, FIB sharpening removes any nascent oxide from the tip apex. Quickly transferring the tip to the setup ($\sim 2-3$ days) or stored in vacuum, yielded reasonable tunneling conditions both at room and low temperature.

Apart from W tips, others tried were Pt/Ir coated Si cantilever tips and carbon fibers [92].

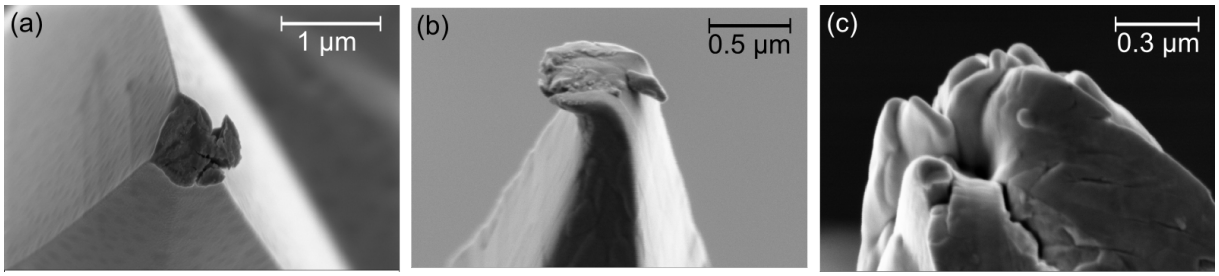

Figure 3.27: SEM images showing some examples of the nature of tip damage occurring during use as a scan probe. (a) Pt/Ir coated Si cantilever tip. (b) Pyramid shaped (FIB) W tip (4 μm). (c) FIB shaped W wire tip, initially with a conical tip apex.

Figure 3.26 shows the SEM images of some of the different kind of tips that were experimented with. Among the W tips, two different shapes were tried: (1) pyramidal tip apex as shown in (c) and (2) conical tip apex as shown in (d). Although the conical design yielded sharper tip apex, the success rate was less compared to the more robust pyramidal shape. Figure 3.27(c) shows the state of a conical W tip after use. The sharp tip-apex is rather fragile and is almost never recovered after scanning. The pyramidal tips are seldom damaged. Figure 3.27(b) shows an example of a damaged pyramidal tip (rare occurrence). Pt/Ir coated Si cantilevers were used at the beginning of my work. Their light weight is a major advantage, resulting in minimum/no reduction in Q-factor. But, the major problem with these is that the conductive Pt/Ir coating at the tip-apex is fragile and would be easily lost while scanning, as shown in Figure 3.27(1), thus resulting in the absence of a tunneling current at low temperature (when the remaining Si at the apex is not/less conducting). Therefore, in view of all the different advantages and problems for the different tips, we decided in favour of the pyramidal shaped W wire tip.

Towards the end, we started experimenting with carbon fiber tips, shown in Figure 3.26(b). This work is in progress in terms of optimizing tip fabrication procedure and performance testing at dilution temperatures. Our interest in the carbon fibers stem from their electrical and mechanical properties that make them seem quite promising material for STM/AFM tips [92]. They are electrically conducting up to dilution temperatures [7], resistent to corrosion, robust against tip crash and incredibly stiff (remains straight over centimeters!) as is clear from Figure 3.26(b). Hence, very thin fibers ($\sim 5\,\mu$m) are quite easy to manipulate. These tips can be electrochemically etched without undergoing oxidation (Inset of Figure 3.26(b)), therefore FIB is not required (which is quite expensive and time consuming). The only disadvantage is that they have a parabolic DOS, unlike conventional metallic STM tips with flat DOS near Fermi energy. For investigating small, low energy features in the DOS, like the superconducting DOS or the induced gap in superconducting proximity effect, this does not pose any problem. But for investigating gate dependent features in the DOS of graphene, for example, might be difficult.

[7] $R \approx 3.3\,\mathrm{k}\Omega$ [93]. Stable tunneling current exists at 16 K. STM at base temperature remains to be verified.

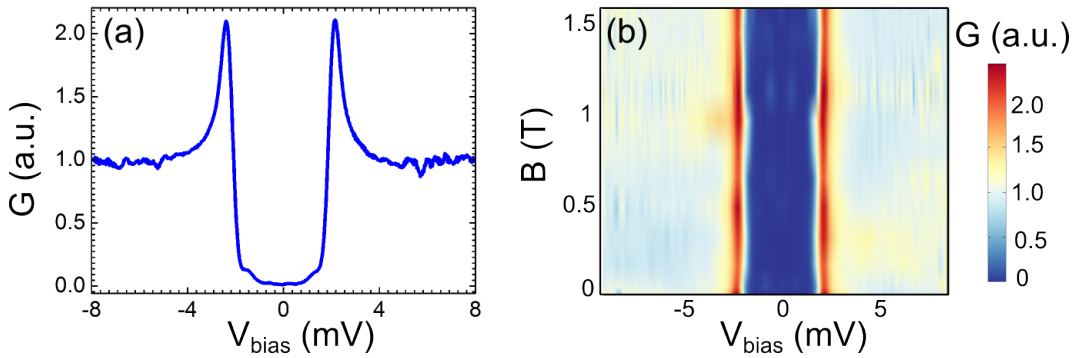

Figure 3.28: Scanning tunneling spectroscopy on a normal metal with a superconducting tip (50 nm NbN sputtered on Pt/Ir wire of diameter 250 μm). (a) Normalised differential tunneling conductance spectrum on gold at temperature $T = 120$ mK and magnetic field $B = 0$ T. (b) G (normalised) as a function of sample bias V_{bias} and magnetic field.

Another ongoing project is the fabrication and implementation of superconducting STM tips, done together with Arunima Sethi [93]. The tips are made by Dr. Max Hofheinz of CEA, by sputtering about 50 nm of niobium nitride (NbN) on a Pt/Ir (250 μm) wire. NbN is an intensively studied superconductor with a T_c of about 16 K (disorder dependent). Figure 3.28(a) shows the normalized differential tunneling conductance spectrum acquired on gold which has a normal DOS, at a cryostat temperature of 120 mK. The spectrum clearly reveals the superconducting DOS of the tip with superconducting gap $\Delta \approx 2.26$ meV [8] which implies a $T_c \approx 14.9$ K [9]. Figure 3.28(b) shows the evolution of the tunneling spectrum with magnetic field. We see almost no change in the superconducting DOS with magnetic field which is expected because the upper critical field in NbN can go up to 35 T [95], depending on the extent of disorder. Nevertheless, more work needs to be done towards optimization and characterization of the tips and finding suitable applications where such tips can be implemented.

3.4.2 Implementation

The length extensional resonators are purchased from Microcrystal [96]. To construct the Needle sensor from the LER, several intermediate steps are involved which has been presented below.

1. Using araldite (quickly drying, insulating glue), the LER is fixed to a PCB substrate, in between two metallic contact pads made of copper (Figure 3.25 and Figure 3.29(a),(b)).

2. The two LER electrodes are electrically connected (microbonded) to the nearest Cu pad.

3. The response characteristics is checked. At this stage $f_0 \approx 998$ kHz and Q factor is about $13\,000 - 17\,000$.

[8] Roughly estimated by considering the difference between the coherence peaks.
[9] Using $\Delta \approx 1.764 k_B T_c$ [94].

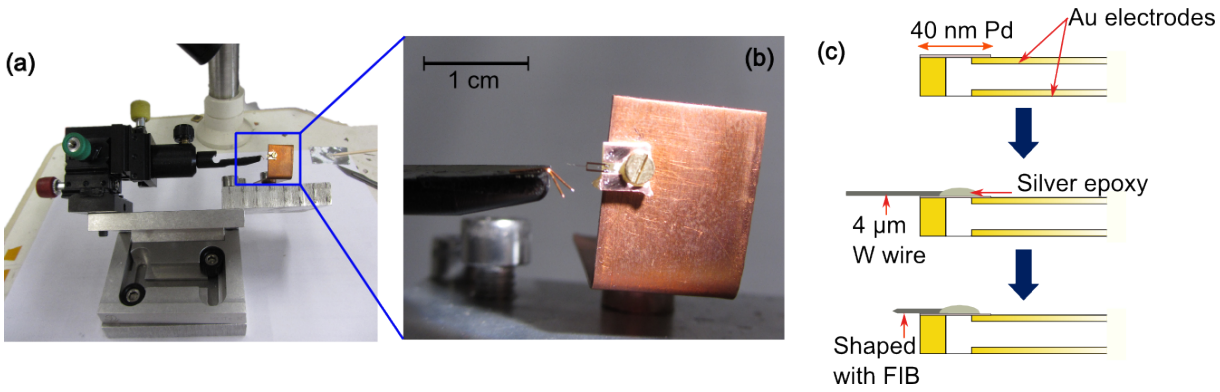

Figure 3.29: Implementation of the Needle Sensor. (a) SEM image of a Length Extensional Resonator (LER) fixed to a PCB with two isolated copper contacts. (b) Schematics showing the different steps after fixing the LER to the copper chip, see text.

4. Since the metallic tip will be fixed on the right side, the top electrode of the LER needs to be electrically connected to the right side electrode [10]. This is done by depositing about 40 nm of palladium (Pd). Figure 3.30 shows the schematic of the necessary arrangement to implement this step. The LERs are fixed on an Al block with the right side facing towards the Pd target. Al foils, placed over the right side cover most of the LER except the small region which needs to be connected. Such an arrangement is necessary to prevent any short between the two side electrodes.

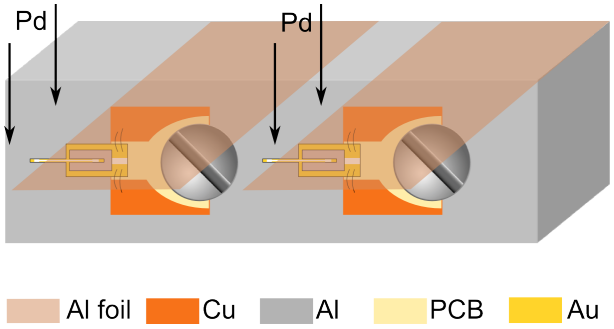

Figure 3.30: Stand for Pd deposition on LERs

5. The response characteristics is checked once again. f_0 drops by about 600 Hz while the Q-factor remains unchanged. In some cases, it is even observed to increase slightly.

6. The W wire is now glued on the right side of the LER with two-component silver epoxy. Figure 3.29(a) shows the arrangement necessary to do this. The W wire (diameter $= 4\,\mu$m and length $\approx (200-300)\,\mu$m) and two other Cu wires (diameter $\approx 250\,\mu$m) are first placed on the extended arm of the micro-manipulator. The set of these three wires can be precisely

[10] The length of the tip is not long enough to reach the side electrode. This is done to keep the weight to a minimum

moved in 3D. The LER is fixed on a Cu stand. With one of the copper wires a very small amount of silver epoxy is placed at the top of the right side electrode. The W wire is then gently placed over this epoxy and the arm of the manipulator removed from the bottom, thus leaving the wire fixed on the LER. This is followed by annealing in an oven to cure the epoxy. The steps have been schematically shown in Figure 3.29(c).

7. The response of the LER is checked yet again. This time the Q-factor is seen to be severely affected and f_0 drops to $987 - 990\,\text{kHz}$. Only those LERs showing a Q factor greater than 1000 are handed over to J. F. Motte for sharpening by FIB.

8. In FIB, the tip length protruding out is kept between $10 - 30\,\mu\text{m}$ and the angle between the slanting edges to about 35°.

9. After FIB, high Q factors are recovered $\approx 5\,000 - 15\,000$. Sensors with $Q < 2000$ are difficult to use and hence discarded.

Under vacuum (pressure $< 0.01\,\text{mbar}$), Q-factors rise to about $3-4$ times the value at ambient pressure. Lowering of temperature generally causes a sharp increase. The maximum achieved at 130 mK was about 650 000.

We would like to mention here, that a serious problem of lack of tunneling current at low temperatures was noted on several occasions, although perfect tunneling conditions existed at room temperature. Replacing the initially used Pt/Ir coated Si cantilever tips with FIB etched W wire tips increased the success rate but did not completely eliminate the problem. The atmospheric oxidation of the W tip apex could be a reason as in certain cases, tunneling current was found to occur only at very high voltages ($> 10\,\text{V}$). In these cases, recovery of a good tip was possible by field effect. In many other cases, tunneling current was absent up to the maximum sample bias applied, even if the tip was placed into physical contact with the surface. Strangely, the signal returns at about $T = 150\,\text{K}$ as shown in Figure 3.31.

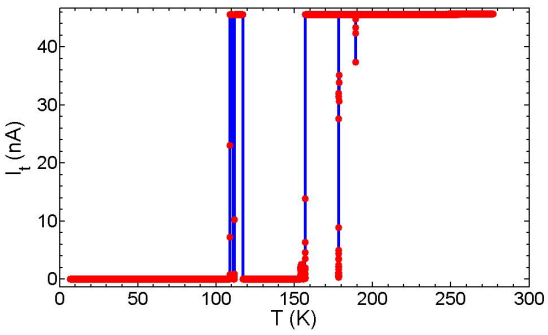

Figure 3.31: Current in the tunneling current line, as a function of temperature while warming up. The tip is placed in physical contact with the sample .

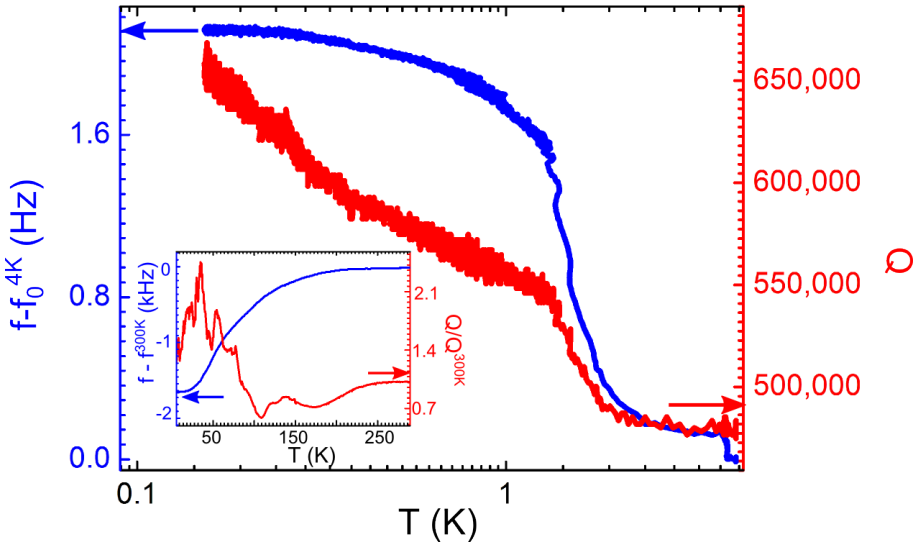

Figure 3.32: Change of the eigen frequency f_0 and Q factor of the Needle sensor from $4\,K$ to 130 mK ($f_0^{4\,\mathrm{K}} = 991107\,\mathrm{Hz}$). Inset shows the corresponding variation from room temperature to 4 K ($f_0^{300\,\mathrm{K}} = 991107\,\mathrm{Hz}$ and $Q^{300\,\mathrm{K}} = 21000$) (The two measurements are done for two different needle sensors.)

This tends to imply a weak electrical connection at some point in the tunneling current circuit. The silver epoxy (silver granules dispersed in a solvent) and/or the deposited Pd layer could therefore be a reason. Replacing the initially used silver epoxy [97] with a new one [98], seemed to work better (two out of two times). However, more tests are required to confirm this. What could be a good solution to the problem is if the tip is directly placed from the copper pad in the PCB up to the LER end, hence eliminating the need for both the Pd layer or the silver epoxy. Efforts are on in this direction to implement this technique without hampering the Q-factor.

3.4.3 Temperature dependence of the Properties of the NS

For the implementation of the Needle sensor at cryogenic temperatures, it is important to understand their properties at these temperatures and how they respond to changes in temperature. Many important properties like the eigen frequency, stiffness, quality factor, sensitivity etc, which directly affect their role as the scan probe in STM/AFM, are different at dilution temperatures than at room temperature. Therefore a knowledge of the temperature characteristics of these properties will allow us to recalibrate the scan or other measurement parameters which is important for performing quantitatively accurate, reproducible and precise measurements at different temperatures.

To characterize the properties of the needle sensor with changing temperature, we track the eigen frequency f_0 and the quality factor Q while cooling down the setup from room temperature to 4 K in the first step and then from 4 K to base temperature of 130 mK in the subsequent step

(section 3.3.2). In the first step, complete frequency sweeps are recorded from which (f_0, Q) are extracted using Eq.(3.2.14). Each sweep takes about 3 min during which T can change by about 1.5 K at maximum (Figure 3.17(a)). In the second step, since the temperature drop from 4 K to 130 mK proceeds faster (Figure 3.17(b)), the Phase locked loop (section 3.9) is used to record the frequency shift Δf_0 wrt. the starting frequency at 4 K and the driving voltage V_{exc} required to keep the probe oscillating with a set amplitude. f_0 and Q are then extracted from Δf and V_{exc} respectively. About 26 sensors were studied in this manner. Figure 3.32 shows the recorded variation in the temperature range $T \in (4\,\mathrm{K}, 130\,\mathrm{mK})$ while the inset shows the same in the range $T \in (300\,\mathrm{K}, 4\,\mathrm{K})$. We summarize the main findings below:

1. f_0 decreases with temperature by about 1.64 kHz from room temperature to 4 K. On further cooling to 130 mK, it *turns around* and increases slightly reaching a saturation again.

2. Thermal drift in f_0 is minimum at the maximum point at $T \approx 300$ K and at the minimum at $T = 4$ K. These temperatures are called the turnover temperatures T_p [72] and is determined by the crystal cut. The T_p of quartz sensors is kept about 300 K on purpose to ensure maximum temperature stability of f_0 at RT where they are usually used.

3. The quality factor Q shows a non-monotonic change with T from 300 K to 4 K. In majority of the NS investigated, a drop in Q occurs at around 100 K followed by an increase, reaching a maximum at about $40-50$ K after which it decreases till 4 K. In some cases, Q is observed to drastically decrease below 40 K such that the sensor is not usable at low temperature.

4. In most of the other cases, below 4 K, Q increases monotonically and does not reach saturation even at base temperature of 130 mK, as clearly observed in Figure 3.32.

5. The relevant thermal expansion co-efficient for the NS $\alpha_\perp = \frac{1}{L}\left(\frac{dL}{dT}\right)$ is related to the relative change in f_0 in the following manner [99]:

$$\frac{\partial f_0}{\partial T} = f_0\left[-\alpha_\perp + \frac{1}{v_s}\left(\frac{\partial v_s}{\partial T}\right)\right] \tag{3.4.1}$$

   where v_s is the velocity of sound that remains independent of T below 10 K. If we assume that v_s remains constant in the whole range of temperature from 300 K to 4 K then $\alpha_\perp \approx -\frac{1}{f_0}\left(\frac{\partial f_0}{\partial T}\right)$. This has been plotted in Figure 3.33(c) for three different NS. We once again find a non monotonic change in $\alpha_\perp$ wrt. T with a minimum at $T = 40-50$ K. This implies that the NS expands rapidly up to $40-50$ K after which the rate of expansion reduces. Interestingly, this temperature coincides with the point of maximum Q.

The decrease in f_0 of 1.64 kHz from room temperature to 4 K that we find is consistent with what is reported by T. An et al [100] which is about 1.7 kHz. However, they do not provide the complete Δf_0 vs T profile for the NS. For the quartz tuning fork (TF), J. Rychen et al. [101]

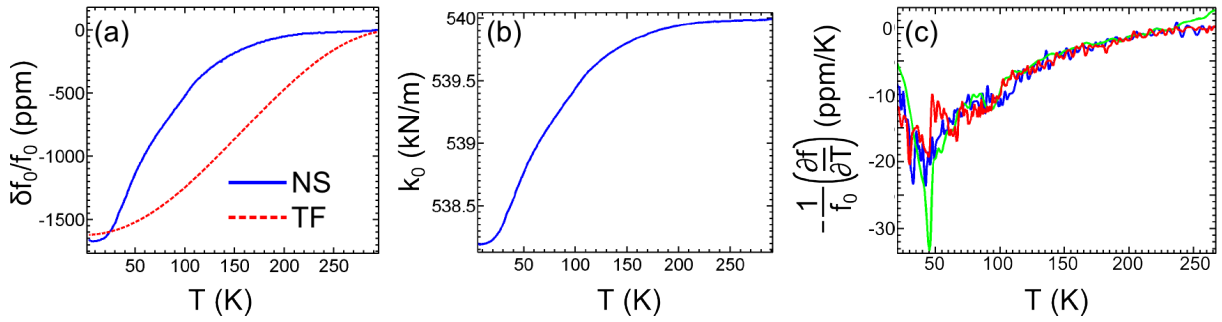

Figure 3.33: (a) Relative frequency change with T for the NS (same as in the inset of Figure 3.32) in comparison to a quartz TF [Eq.(49) of [72]]. (b) Variation of longitudinal stiffness of one of the beams on the NS with T, assuming $k_0(300\,\mathrm{K}) = 540\,\mathrm{kN/m}$, table 3.6. (c) Change of $-\frac{1}{f_0}\left(\frac{\partial f_0}{\partial T}\right) \approx \alpha_\perp$ with T, using Eq.(3.4.1) for three different NS (indicated by the different colors).

and S. Hembacher et al. [102] had measured the change of f_0 with T from room temperature up to 1.56 K in the former case and up to 4 K in the latter.

Figure 3.33(a) shows the f_0 vs T for the NS compared to that of a TF as measured in [102]. We find that the two sensors show considerable difference while being cooled to lower temperatures. The change in f_0 is more slow about 300 K for the NS than for the tuning fork. However, for both, turnover temperatures T_p occur at 4 K and at room temperature, which gives a low thermal drift near both these temperatures, particularly advantageous for SPM operation. At lower temperatures (Figure 3.32), f_0 increases and once again stabilizes at about 130 mK which is once again to our advantage.

Nevertheless, implementing AFM at such low temperatures was found much more challenging than at room temperature. One explanation is the excessively high Q-factors, found on some occasions, makes it tricky to optimize the scan conditions. Also, we see that although f_0 stabilizes, the Q factor of the NS remains highly sensitive to temperature at 130 mK. So, although the different thermal properties are comparatively more stable at 4 K and at 130 mK than at other temperatures, room temperature by far offers the best environment in terms of intrinsic thermal stability of the probe.

Finally, this measurement allows us to estimate the change in sensitivity of the needle sensor from room temperature to 4 K, based on the changed eigen frequency, stiffness and geometrical dimensions. The sensitivity is defined as the current produced by maximum deformation of the beams of the NS. This is given by [72],

$$S_{NS} = 4\pi f_0 d_{31} k_0 \frac{L}{t} \sin\left(\frac{\pi L_e}{2L}\right), \tag{3.4.2}$$

where $d_{31} = 2.31\,\mathrm{pC/N}$ is the transverse piezoelectric coupling co-efficient for quartz (section 3.3.1) and can be assumed to be temperature independent. By deducing the thermal expansion

coefficient of a given NS from its f_0 vs T variation [Eq.(3.4.1)], we can estimate the change in length L and thickness t due to lowering of temperature.

This gives small changes in L and t, about $1.5\,\mu$ and 80 nm respectively and the changed longitudinal stiffness is about 538 kN/m (Figure 3.33(b)). The corresponding sensitivity is then about 283.4 nA/nm which corresponds to a change of only 0.5%. We note here that this is only the theoretical sensitivity. For a proper characterization, the sensitivity must be measured experimentally. Both F. J. Giessibl [74] and T. An et al [76] had found an experimentally measured sensitivity for the qPlus and the NS respectively, that was half the theoretically expected value. They attributed the discrepancy to non ideal effects occurring at the edges of the electrodes.

In conclusion, we have measured the eigen frequency and the quality factor of the NS from room temperature to dilution temperature of 130 mK. This thermal characterization, conducted for several sensors, gives insight into the stability and performance of the sensor at various temperatures. The thermal stability is found to be maximum at room temperature while good stability is also attained at the low operational temperatures in our microscope i.e. $T \to 4\,\mathrm{K}$ and $T \to 130\,\mathrm{mK}$. The thermal expansion co-efficient $\alpha_\perp$ is found to be negative and changes non-monotonically with temperature with maximum ($|\alpha_\perp|$) occurring at about $40 - 50\,\mathrm{K}$. This temperature coincides with the maximum attained by the quality factor which also shows a non-monotonic change. Further, the measurement allows us to find the theoretical sensitivity of the sensor at different temperatures which gives us a change of only 0.5%.

3.5 Applications of combining AFM with STM

Both AFM and STM are individually very powerful tools to probe the properties of the sample surface at a local scale, as we must have realized by now. Combining these two techniques in a single microscope helps to overcome the individual limitations and opens the possibilities for a vast number of applications that could not have been achieved otherwise. Relationship between tunneling current in STM and attractive forces in AFM can be investigated, which can further give insights into dissipation occurring at the atomic scale [103]. Another interesting application is the technique of dynamic STM, i.e. STM with an oscillating tip, which could provide enhanced stability and resolution in comparison with only STM for studying molecular assemblies [104]. Simultaneous measurements of force and tunneling conductance over nano-sized metallic adsorbates can also help in understanding the nature of short-range chemical forces [105]. The list can go on.

In this section, we present two important applications in which both STM and AFM are directly employed. While the first application offers a way to experimentally measure the sensitivity of the NS, the second application involves using the AFM feature of the probe to locate a nano-device on an insulating substrate [106]. This second application is fundamental to my PhD work and forms the main motivation behind combining the two microscopies.

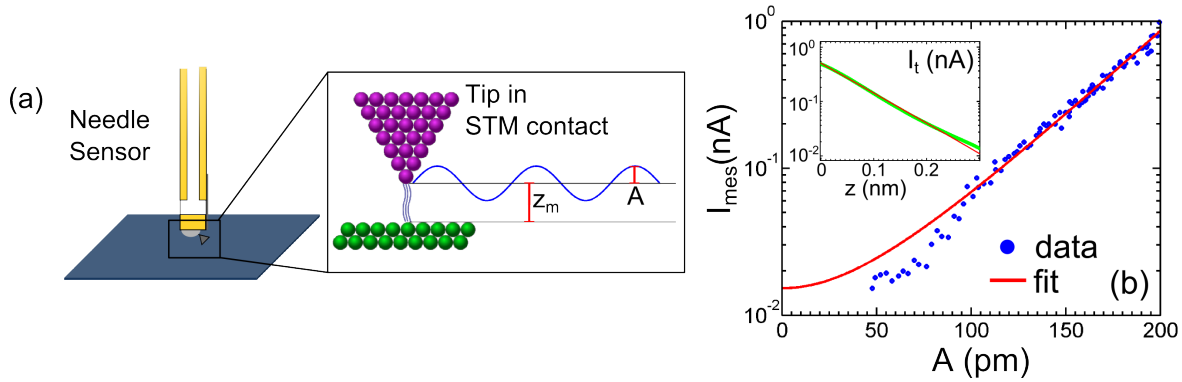

Figure 3.34: (a) Schematic explaining the method employed to determine the sensitivity of the NS[11]. (b) Average tunneling current measured I_{mes} vs A on a sample of graphene on iridium (111) at $T = 130\,\text{mK}$. Red line indicates fit with Eq.(3.5.2) [fit parameter: $\eta = 2.3$]. Inset shows variation of tunneling current I_t with tip-sample distance z recorded just prior to measurement of I_{mes} vs A. Green dots represent data points and red line indicates fit with Eq.(3.2.1). Fit parameter: $z_0 = 0.080\,\text{nm}$.

3.5.1 Experimental Determination of Sensitivity of NS

We present here a method to experimentally measure the sensitivity of the needle sensor S_{NS} [Eq.(3.4.2)] by using the superior sensitivity of the tunneling current I_t to tip-sample distances z_{ts}. This offers an elegant way to perform an in-situ calibration of the oscillations of the needle sensor at various temperatures.

Figure 3.34(a) schematically demonstrates the process employed. The NS, vibrating with an amplitude A at its eigen frequency f_0 is approached towards the sample surface in STM mode. The tunneling current set-point is kept sufficiently low ($< 25\,\text{pA}$) so that the tip does not touch the surface. The oscillating tip-sample distance $z = z_m + A\sin 2\pi f_0 t$ will induce a modulation in the tunneling current I_t at frequency f_0 given by (using Eq.(3.2.1))

$$I_t(t) = I_0 \exp\left(-\frac{z_m + A\sin(2\pi f_0 t)}{z_0}\right) = I_t(0)\exp\left(-\frac{A}{z_0}\sin(2\pi f_0 t)\right). \tag{3.5.1}$$

However, these modulations cannot be measured by the tunneling current amplifier because its bandwidth is about $3\,\text{kHz} \ll f_0$ (section 3.3.4). Hence, what is measured is the average i.e. $I_{mes} = \langle I_t \rangle$. It can be shown that this average value is related to the amplitude of oscillations in the following manner [78]:

$$I_{mes} = I_t(0) J_0\left(i\frac{A}{z_0}\right), \tag{3.5.2}$$

where J_0 is the zeroth order Bessel's function. Hence if the excitation voltage supplied to the sensor is changed so as to change A at a rate much smaller than the bandwidth of the tunneling current amplifier [12], then I_{mes} changes according to the above equation, and this change can be

[12] In the measurements presented, integration time $\tau = 100\,\text{ms}$

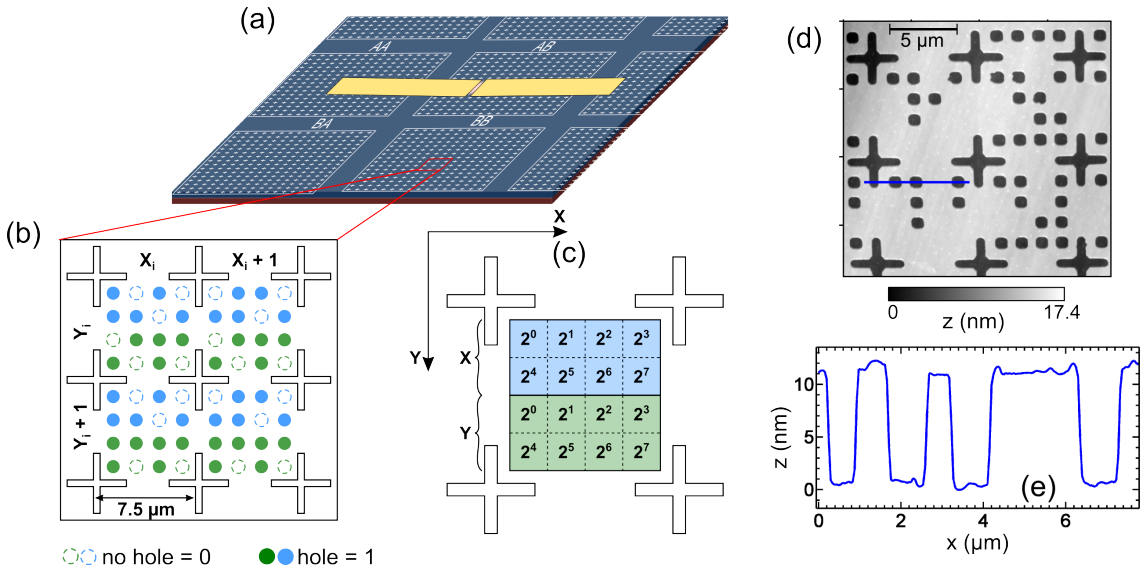

Figure 3.35: The Binary code. (a) Schematic of a *coded* Si/SiO_2 substrate with a contacted graphene flake positioned close the center. (b) Zoom-in showing the 16 bit code, represented by a systematic sequence of holes, enclosed within the four crosses. First two rows denote the X co-ordinate while the last two rows denote the Y co-ordinate. (c) Interpretation of binary code to convert it to the corresponding decimal number [78]. (d) AFM (tapping mode) image of a substrate with the code. (e) Height profile along blue line indicated in (d). The dimension of the holes is about 750 nm, distance between them is about 1.5 μm and the depth is about 10 nm.

used to extract the actual amplitude of oscillations A_{real}.

Figure 3.34(b) shows the variation of the measured tunneling current with the apparent amplitude of oscillation A at a temperature of 130 mK on a sample of graphene on iridium (111). A is obtained assuming a calibration of $G = 140\,\text{nm/V}$, implying a sensitivity of $S_{NS} = 325\,\text{nA/nm}$ (gain of our AFM amplifier is $R_{fb} = 22\,\text{k}\Omega$, Figure 3.21). We consider the real amplitude of oscillation to be linearly related to A i.e $A_{real} = \eta A$. By substituting A with A_{real} in Eq.(3.5.2), the data is fitted with this equation using η as a fit parameter.

We find $\eta \approx 2.3$ which implies an actual calibration of $G_{real} = 325\,\text{nm/V}$ and a sensitivity of $S_{NS} = 1/(G_{real}R_{fb}) = 140\,\text{nA/nm}$. This is marginally higher than what has been reported in literature of about 125 nA/nm [76] at room temperature.

We must note that, while fitting the observed dependence to Eq.(3.5.2), we have assumed a constant tunneling current decay length z_0 which we find by measuring the exponential decay of I_t with tip-sample distance (insets of Figure 3.34), both before and after measurement of I_{mes} vs A. In the presented measurement z_0 is found to differ by about 10% between forward and backward sweeps which is quite normal in STM operation. However, this hysteretic behaviour would give rise to an error of the order of 10% in the measured sensitivity.

3.5.2 Localizing a single nano-device on a chip

Our primary motivation for combining AFM with STM in our setup is to be able to perform local tunneling spectroscopy of nano-devices located on mm-sized insulating substrates. In the absence of elaborate optical arrangements, which are incompatible with cryogenic arrangements, it becomes important to have an alternative scheme in place to locate the measurement site on the vast sample surface. By simple eye-estimation one can at best align the tip within few hundreds of microns from the target location which is not good enough and will evidently result in a tip-crash in STM. In AFM, this is of course not a problem and this is what makes it worthwhile to have this additional ability to scan the surface by sensing the tip-sample force. T. Quaglio et al. [106] had used a substrate with markers pointing towards the sample. Hence, successive AFM images can gradually guide us to our destination. H. le Sueur [107] used a different coding scheme that allows us to precisely identify the present location of the tip wrt. the sample from the very first AFM image. We adopt this system for an efficient localization of the target device.

The substrates (Si/SiO_2) are engraved with a 16 bit coding scheme using deep UV lithography. The fabrication steps have been listed in [78]. Figure 3.35(a) shows a schematic depicting the coded substrate with the device located close to the center. Each big square block of coded positions spans an area of $1920 \times 1920\,\mu m^2$. Within each block, the position can be accurately determined with the help of a sequence of holes and crosses. The elementary unit of the code consists of a square region enclosed between four crosses over an area of $7.5 \times 7.5\,\mu m^2$, as depicted in (b) and (d). Each square region contains a sequence of 'holes' and 'no holes' organized into a 4×4 matrix. The first two rows represent the X co-ordinate while the last two rows represent the Y co-ordinate. The first element of the first row represents the least significant bit (LSB) while the last element of the second row represents the most significant bit (MSB). Figure 3.35(c) demonstrates the way to convert the code to the corresponding decimal form. For example in (a) $X_i = (10110101)_2 = (181)_{10}$ and $Y_i = (01011110)_2 = (94)_{10}$. The X co-ordinates increase from left to right while the Y co-ordinates increase from top to bottom.

The tip position wrt. the sample is changed by moving the sample stage with the help of piezo-actuators (section 3.3.1). Hence, particular care is taken to fix the sample to the sample holder in a specific orientation which ensures that the X/Y directions of the code is parallel to the X/Y directions of the microscope (depends on the designated direction of the piezo actuators) and that right/left/top/bottom of code also has exact correspondence to that of the microscope. Care is also taken to ensure that both the target device in the sample and the tip is well-centered wrt. the sample holder. A good centering is crucial for the efficient localization of the target (can be done within two hours!). This is not only because the tip is already in close proximity to the target but also because the functioning of the actuators work best and in a reproducible manner in this situation. The movement calibrations have been mentioned in section 3.3.1. However, it is recommended to calibrate the movement at the beginning of each search.

At room temperature, the scan range is about $12\times12\mu m^2$ which is sufficient for understanding the present location from one single image. However, at low temperature, the maximum scan range should not exceed $4 \times 4\,\mu m^2$ 3.3.1. Therefore one single image is often not sufficient to understand the location. In fact, locating the desired position is a challenge at low temperatures given the small scan range and the reduced efficiency of the piezo actuators. The following steps were found useful to speed up the search at low temperatures:

1. Sample is located at room temperature.
2. The tip is now moved $15\,\mu m$ to the right (2 squares of binary code) and $45\,\mu m$ down (6 squares of code). This should compensate for the relative displacement occurring between tip and sample while cooling down because of the different thermal contractions of the different parts of the microscope. This compensation ensures that at low temperatures, the tip is within one/two squares off at maximum.
3. AFM images are acquired till the present position is accurately understood. In the process, the X/Y movement is continuously calibrated. This often resembles putting pieces of a puzzle together and one might efficiently make use of the hint that the target is very close. This really helps in excluding a vast number of possibilities.
4. Based on the average movement calibration done in the previous step, the tip is now displaced to reach the target. In most cases, this is sufficient to reach the target. If not, the previous step is once again repeated. After two or three iterations, the target is definitely achieved.

This, therefore, offers a simple yet efficient technique for an optics free localization of the target device. This technique was implemented in finding contacted graphene flakes (section 1.3), the measurements on which will be presented in Chapter 5.

3.6 Summary

Scanning probe microscopy has been discussed in detail in this chapter, the several aspects which have been particularly useful in the course of my PhD. The microscope assembly, the different scanning probe techniques that can be implemented, the cryogenic arrangements supporting the low temperature operation, the electronics involved, the needle sensors for combining AFM with STM, the different kinds of tips and finally localizing a nano-sized target device on a mm-sized insulating substrate; in short, these have formed the several highlights. This forms the backbone for the significant bulk of the measurements that has been presented in subsequent chapters.

Chapter 4

Charge Disorder in decoupled Graphene on a Metallic Substrate

Contents

4.1 Introduction **111**
4.1.1 Graphene on a Metallic Substrate 111
4.1.2 Decoupling Graphene 113
4.1.3 Graphene on Ir(111) 115
4.2 Decoupled Graphene on Ir(111) **117**
4.2.1 Sample Preparation 118
4.2.2 Large scale surface features 119
4.2.3 Regions devoid of Graphene : Oxidised Ir 120
4.2.4 Graphene Wrinkles 122
4.3 Dynamics of Decoupling of Graphene **128**
4.3.1 Wrinkles as pathways for intercalation 128
4.3.2 Electronic Properties of well-coupled vs decoupled graphene 130
4.3.3 Conclusion 131
4.4 Charge disorder in decoupled graphene **131**
4.4.1 STM/STS investigation of charge disorder 132
4.4.2 Charge disorder by KPFM 134
4.4.3 Origin of Disorder 136
4.5 Conclusion **137**

4.1 Introduction

The method to isolate free-standing graphene from graphite has only been realized in 2004 [1]. But in an adsorbed form on metal surfaces, graphene has been known for at least forty years. During the preparation of single crystal surfaces of certain metals like Ru or Pt, graphene formation was observed when the metals were annealed at high temperatures that caused the carbonaceous impurities to segregate from the bulk to the surface [108]. Alternatively, graphitic carbon deposition on metal surfaces was already known for quite sometime as the leading cause of deactivation of the catalytic activity of the metal in industrial heterogenous catalysis reactions involving the decomposition of hydrocarbons [109]. The avalanche of scientific activity in graphene physics triggered by the breakthrough of 2004 also led to a revival of interest in graphene deposited on metal surfaces.

The system of graphene on a metallic substrate is appealing for a number of reasons. Firstly, from the point of view of industrial applications, these systems are highly important as they currently offer the only solution to large scale growth of graphene of different thicknesses and extraordinary quality that can be later transferred to polymers/insulating substrates. Secondly, from a technical point of view, it is important to understand the role of metal contacts in doping the graphene which will eventually influence the transport properties of the end device [110]. Finally, from a more fundamental point of view, there are certain aspects of these systems which remain quite ambiguous: How does the graphene layer interact with the metal, what is the nature of bonding at the graphene-metal interface? How is the electronic structure of graphene affected by the metal? If it is, is it possible to completely decouple the graphene from the influence of the metal? What is the state of doping in such decoupled graphene, is it homogenous or disordered?

From the large family of metal-graphene systems currently available, the system that forms the subject of this chapter is decoupled graphene on an iridium (111) substrate. But before we delve into the details of this specific case, we first try to develop a better understanding of metal-graphene systems in general in order to understand the significance of the key questions.

4.1.1 Graphene on a Metallic Substrate

Graphene on a metallic substrate comes very close to the text-book like graphene that we have in mind: single sheet of carbon atoms arranged in a honey-comb lattice with very close, if not perfect, lattice matching with the metallic substrate underneath. Figure 4.1 shows atomically resolved STM images of two such graphene-metal systems; (a) GR/Ni(111) and (b) GR/Ir(111). In the case of one class of systems like GR/Ni(111) [111] or GR/Co(0001) [114], it is possible to have a perfect registry between the carbon lattice of graphene and that of the metal as shown by the Low Energy Electron Diffraction (LEED) image in the inset of Figure 4.1(a) where the reciprocal space of the two respective lattices are superposed. In most other cases like Pt(111) [115], Ir(111) [116] or Ru(0001) [117], a slight lattice mismatch exists which give rise to

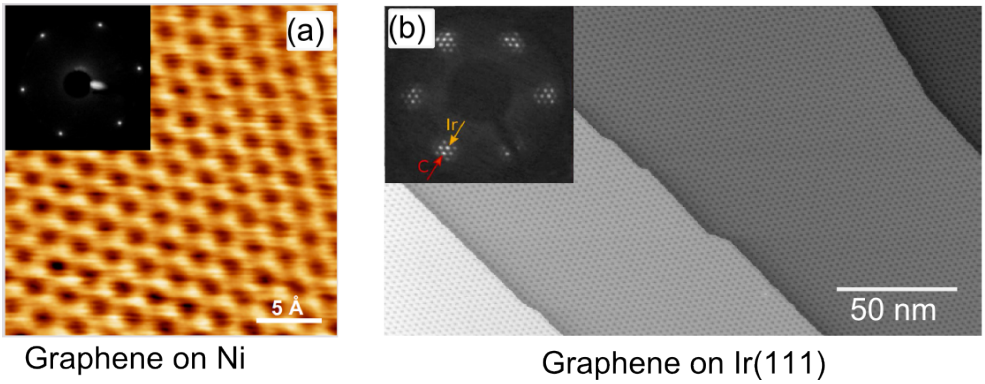

Figure 4.1: Graphene on metallic substrates. (a) Atomically resolved, constant current STM image of graphene on Ni(111) showing the perfect graphene lattice. Tunneling parameters: $V_{bias} = 2\,\text{mV}$ and $I_t = 48\,\text{nA}$. The inset shows a LEED image obtained at 63 eV [111]. (b) STM topograph of graphene grown on Ir(111) at 1320 K. The moiré pattern due to lattice mismatch between graphene and the Ir substrate is clearly visible, extending over several Ir steps. Tunneling parameters: $V_{bias} = 100\,\text{mV}$ and $I_t = 30\,\text{nA}$ [112]. The inset shows the LEED pattern for graphene on Ir where additional intensity spots of the moiré are visible surrounding the graphene and Ir integer spots [113].

incommensurate moiré superstructures. We see an example of this in the STM image of GR/Ir (Figure 4.1(b)) as well as in the LEED image in the inset where the moiré patterns beautifully manifest themselves as additional intensity spots around the main integer spots of C and the metal lattice.

In spite of the apparent structural perfectness of graphene in these systems, the linear dispersion of its charge carriers is not guaranteed. This is because of the metal-graphene interaction which can significantly influence the intrinsic properties of graphene in some cases. Based on the strength of interaction with graphene, there can be broadly two class of metals : Strongly interacting like Co, Ni, Ru, Rh and Re and weakly interacting like Cu, Ag, Ir, Pt and Au.

Strongly interacting metal-graphene systems are characterized by: (1) a genarally high lattice-matching, if not then a buckling of more than 1 Å is observed in the graphene, (2) high metal-graphene bonding strength (for example $0.132\,\text{eV/C} - \text{atom}$ in case of GR/Co(0001) [119]), (3) very small graphene-metal distance $2.1 - 2.2\,\text{Å}$ which is even smaller than the inter-plane separations of carbon atoms in graphite and (4) most importantly, linear dispersion in graphene is significantly disrupted due to strong hybridization between the d states of the metal and the π states of graphene; in particular, shift to higher binding energy of $1 - 3\,\text{eV}$ and opening of a band gap as shown in Figure 4.2(a) in the case of GR/Ni(111) [118]. In short, what we are left with is no longer graphene but more of a graphene-metal hybrid system.

In contrast, weakly interacting systems are characterized by: (1) a higher rotational mismatch between the graphene and the metal lattice, (2) weaker, inhomogeneously distributed metal-graphene bonding strength ($0.05\,\text{eV/C} - \text{atom}$ in case of GR/Ir(111), [119]), (3) larger

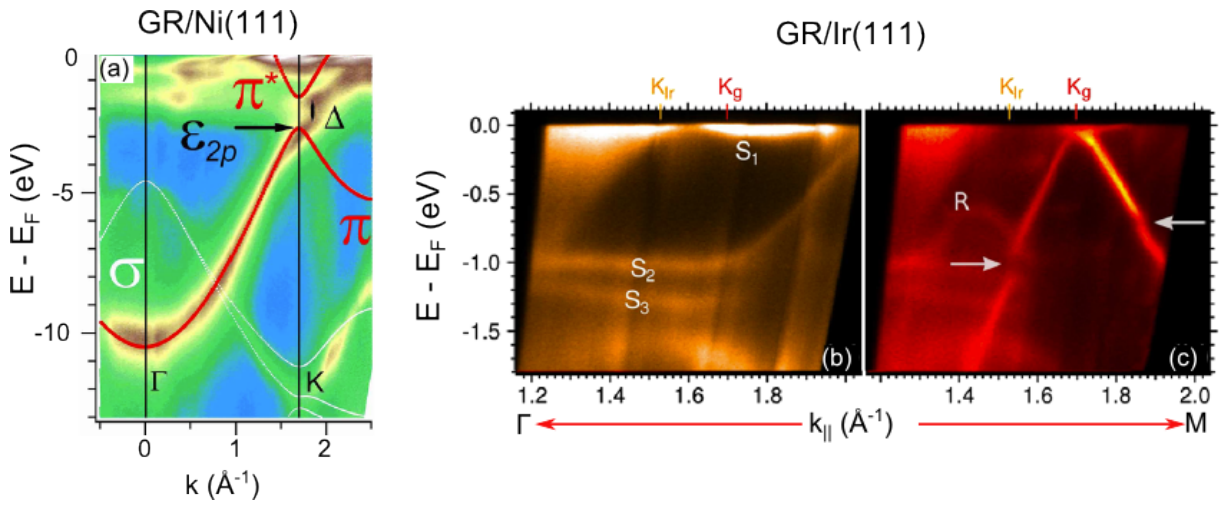

Figure 4.2: Effect of metallic substrate on graphene band structure. (a) ARPES intensitiy map of the band structure of graphene monolayer on Ni(111). The red lines represent π and $\pi*$ bands while the thin white line represent the σ band according to tight-binding (TB) calculations. ϵ_{2p} depicts the on-site energy and Δ represents the energy gap between the π and $\pi*$ bands due to the influence of Ni surface states [118]. (b) ARPES spectrum of bare Ir(111). **K** points of Ir and graphene are marked as $\mathbf{K_{Ir}}$ and $\mathbf{K_g}$, respectively. $S_1 - S_3$ represent surface states. (b) ARPES spectrum of single-layered graphene on Ir(111). Horizontal arrows point to the minigap in the primary Dirac cone [113].

metal-graphene separations of about $3.6 - 3.8$ Å and (4) effect of metallic substrate on the electronic properties of the charge carriers in graphene is not as pronounced as in the case of strongly interacting systems but more complicated to understand. The linear dispersion is almost preserved. However, minor discrepancies can arise as in the case of GR/Ir(111), evident from the ARPES spectrum shown in Figure 4.2(c), to be dealt with in detail later, (section 4.1.3). Apart from this, one important effect is that the work-function mismatch between the metal and the graphene results in an overall p-type or n-type doping [120].

4.1.2 Decoupling Graphene

From the above section, it becomes quite clear that for graphene-metal systems, the influence of the metal plays a crucial role and has a significant impact on the electronic band structure of graphene. For most practical purposes, this pronounced influence of the metal substrate is unwanted as it obscures the unique electronic properties of the charge carriers in graphene. At the same time, it is easy to achieve graphene growth on these strongly interacting metals.

A standard route adapted by experimentalists to quench the strong influence of the metallic substrate and hence recover the linear dispersion, is to intercalate weakly interacting molecular species in between the graphene sheet and the underlying metal. One prominent example is in the case of CVD grown graphene on Ni(111) where intercalation with Sn, Al [124], Au, Ag,

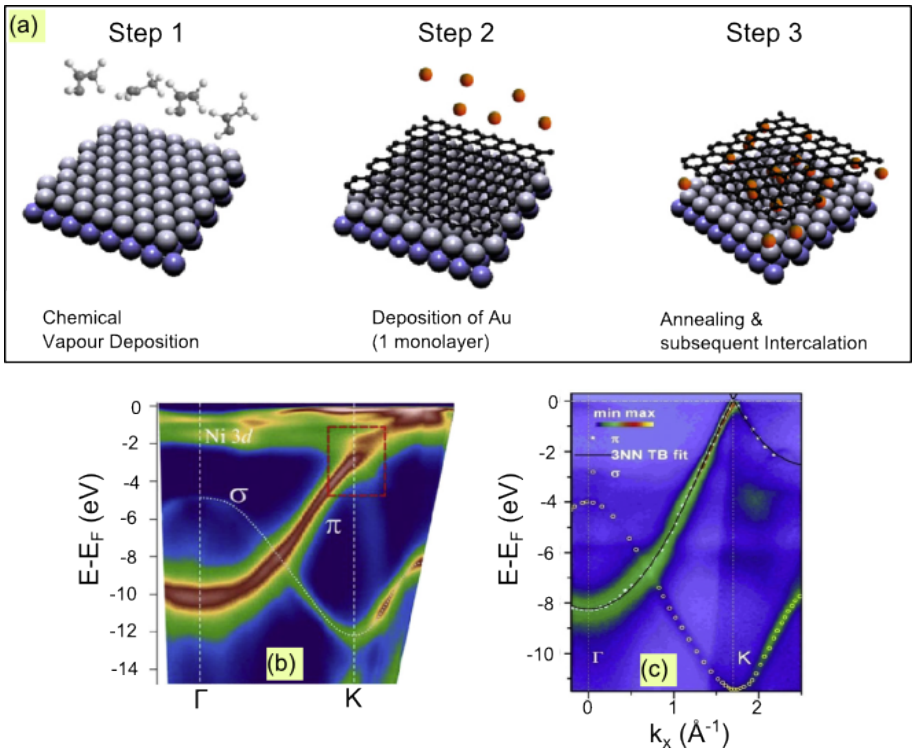

Figure 4.3: Decoupling of graphene from the metallic substrate by intercalation of molecular species. (a) Schematic depicting the process of obtaining free-standing graphene on a Ni substrate by depositing a gold monolayer that gradually intercalates between the graphene and the underlying metal, resulting in decoupling of the graphene sheet [121]. (b) ARPES spectrum of graphene on Ni(111) [122], (c) of graphene on Ni(111) with intercalated Au in between [123].

Cu [125], alkali atoms [118] etc has been tried to achieve various degrees of decoupling of the graphene from the metallic influence. The best results are obtained with gold intercalation in which case the graphene fully recovers the linear dispersion of the π bands with the complete disappearance of the band gap of 3 eV [126] about the Dirac point present in GR/Ni. Figure 4.3 (b) and (c) shows the ARPES spectrum on GR/Ni(111) before and after gold intercalation. Au intercalated graphene really resembles text-book like graphene. Other prominent examples include decoupling of graphene by controlled oxygen intercalation in GR/Ru(0001) [127] and GR/Ir(111) [128][129]. In the case of few layer graphene on metallic substrate, the lower carbon sheets can serve as the buffer that liberates the top layer from the influence of the lower metal which has been demonstrated in GR/Ru(111) [130].

A simple schematic of this process has been shown in Figure 4.3(a) which gives the three steps involved in this process in the case of GR/Ni(111) :(i) growth of monolayer graphene on Ni by decomposition of the hydrocarbon, propene or C_3H_6 (CVD), (ii) deposition of metal to be intercalated and finally (iii) annealing at high temperatures (depending on the intercalating metal) that causes the metal ions to penetrate through the graphene lattice and occupy the space underlying it. This is possible because Au monolayer in the intercalated form is energetically

more stable than in the adsorbed form as shown by DFT calculations [131]. The complete decoupling of graphene, achieved in some cases, suggests that the intercalated molecules are able to inter-diffuse and homogenously fill up the space between the graphene and the metal.

However, the intercalation process itself is not very clear and can proceed quite differently for different intercalating molecules. The energy required for a single atom to distort the carbon lattice of defect-free graphene in order to penetrate it is prohibitively high and hence the intercalation process has to occur through defects in the graphene sheet. There have been few studies so far, in the role of defects as pathways for intercalation, namely graphene free edges [127] and point defects [132][133][134]. But in all these cases, the intercalation had been performed under UHV conditions to enable optimum control over the process. Hence, some questions that remain are (i) whether there are other defects that could serve as intercalation pathways? (ii) Can molecular intercalation occur under ambient conditions? and (iii) If so, how different would it be from well-controlled intercalation under UHV conditions?

4.1.3 Graphene on Ir(111)

In this broad family of metal-graphene systems, the system of Graphene on iridium(111) features as one of the weakly interacting members as had been already mentioned in section 4.1.1. Hence, the graphene under consideration can be expected to retain its graphene-like electronic properties, in particular the linear band structure of its π bands, with only minor influences from the metallic substrate. Indeed, this seems to be verified if we come back to Figure 4.2(b),(c) which shows the ARPES spectrum of an *in-situ* prepared sample of GR/Ir(111) taken under UHV conditions. This figure alone reveals several important information about this system [113]:

1. Dirac cones show no sign of hybridization with substrate electronic bands. This suggests a weak bonding of graphene with the iridium surface.

2. The Fermi level passes through the valence band ($|E_D - E_F| = 0.10 \pm 0.02\,\text{eV}$), indicating an overall p-doping.

3. Minigaps in the graphene band structure (gap width $\approx 0.1 - 0.2\,\text{eV}$) and Dirac cone replicas are observed due to the superperiodic potential (potential amplitude $\approx 0.05 - 0.10\,\text{eV}$) created by the moiré lattices.

4. No conclusions could be drawn about the presence or absence of a band gap at the Dirac point since this point was not accessible with ARPES. However, if it does exist, it should be smaller than 0.2 eV.

Further density functional theory (DFT) calculations have shown the average graphene-Ir separation to be about 0.34 nm [135] which can account for the defect free growth of graphene over step edges.

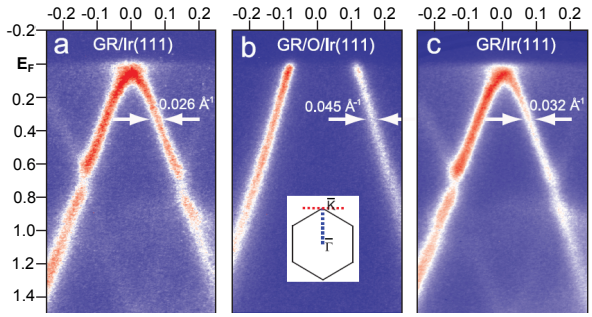

Figure 4.4: Effect of controlled oxygen intercalation and deintercalation of oxygen molecules on the electronic band structure of graphene. ARPES measurements of the spectral function along the direction perpendicular to the $\mathbf{\Gamma} - \mathbf{K}$ direction on (a) as-grown GR/Ir(111), (b) lifted graphene due to oxygen intercalation and (c) landed graphene following O-deintercalation [128]

Decoupling graphene by controlled oxygen intercalation

It is possible to recover fully the intrinsic properties of graphene by following the route of intercalation of molecules between the graphene and the underlying metallic substrate, as has been described in section 4.1.2. R. Larciprete et al, in 2012, demonstrated for the first time that an entire monolayer of epitaxial graphene, devoid of any cracks or holes, could be perfectly decoupled from the Ir substrate at a sufficiently high oxygen pressure of $\sim 5 \times 10^{-3}$ mbar and at a temperature between $500 - 520$ K [128] under UHV conditions. Since the graphene covered the entire substrate, verified by XPS (X-ray photo-emission spectroscopy), intercalation could only proceed via defects, domain boundaries or in the vicinity of wrinkles in the graphene sheet. This process can be reversed or in other words, the oxygen de-intercalated on annealing the sample above 600 K. Figure 4.4 shows the ARPES spectrum of GR/Ir(111), starting from the pristine sample to decoupled graphene obtained by oxygen intercalation followed by "landed" graphene or graphene after deintercalating oxygen. Following are the features in the spectra that are noteworthy:

1. The minigaps and the Dirac cone replicas due to weak coupling of the graphene to Ir and superperiodic potential imposed by the moiré lattice (section 4.1.3) completely disappear after the process of oxygen intercalation and reappear again after the removal of the oxygen molecules. This clearly demonstrates the role that oxygen molecules play in completely decoupling the graphene sheet from the metallic substrate underneath. Another beautiful manifestation of this is the fading out of the moiré structure captured with the help of STM and LEED imaging by S. Ulstrup et al [129] as shown in Figure 4.5. The STM image after oxygen intercalation appears less corrugated while the higher order moiré spots in the LEED image of GR/Ir(111) becomes vague on oxygen intercalation.

2. The Dirac cone shifts upwards by about $0.57\,eV$ on oxygen intercalation compared to pristine graphene on Ir(111) i.e. the Fermi level lies $0.67\,eV$ below the Dirac point in the

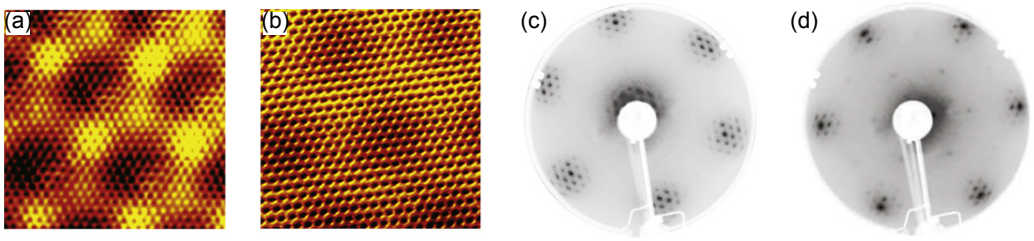

Figure 4.5: Fading moiré after decoupling of graphene by oxygen intercalation. Atomically resolved STM images showing the moiré sub-lattices (a) as grown GR/Ir(111) under UHV conditions (b) after oxygen intercalation. LEED images showing the reciprocal space of GR/Ir(111) (c) before and (d) after oxygen intercalation [129].

valence band implying a strong positive doping by the intercalated oxygen molecules. This is attributed to electron transfer from the graphene to the electronegative oxygen molecules.

3. The momentum distribution curve (MDC) in the ARPES spectrum is seen to broaden after oxygen intercalation. This could of course be due to increased phase-space scattering due to higher p-doping or due to inferior structural quality of the iridium. But one important reason pointed out was the presence of doping inhomogeneity in the graphene due to non-uniform oxygen intercalation that would locally shift the Dirac point and lead to broadening of the Dirac cone in the ARPES spectrum from the bulk sample.

4.2 Decoupled Graphene on Ir(111)

Having gained a detailed understanding of graphene-metal systems in general and GR/Ir(111) system in particular, in the previous section, we now begin our discussion on the system that has been investigated in the present work. This is also CVD grown graphene on iridium. However, prior to measurement, the samples had been subjected to atmospheric conditions. Hence, as we will discover in the subsequent sections, the properties of this system is very different from samples that have been both prepared and characterized in situ under UHV conditions. The samples were provided by the group of Dr. Johann Coraux at Institut Néel.

Using the scanning probe techniques of STM/STS, AFM and KPFM (sections 3.2.1, 3.2.2, 3.2.3), we investigate, in detail, the local properties of this system. At first, the important topographic features on the GR/Ir(111) surface are introduced: i.e. the graphene itself, the regions devoid of graphene and the graphene wrinkles. Detailed characterization of the graphene free regions reveal their oxidized nature while STS on graphene wrinkles show a vanishing doping, thus implying a negligible influence of the metallic substrate in such regions. Next, we study a freshly prepared sample that has faced exposure to ambient conditions for a very small duration of time. This helps us to particularly understand the dynamics of the intercalation processes at

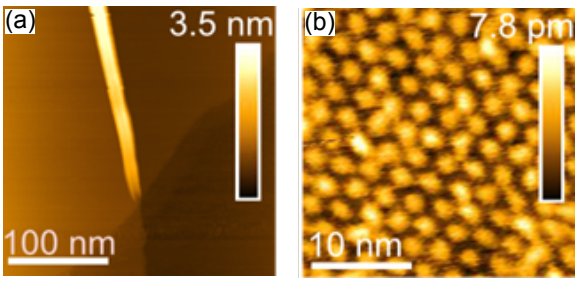

Figure 4.6: STM topographs of an as-grown sample of GR/Ir(111) in UHV conditions prior to exposure to ambient conditions. (a) Graphene wrinkle ending at a graphene edge. Imaging conditions: $I_t = 1.7\,\text{nA}$, $V_{bias} = 1.2\,\text{V}$. (b) Triangular moiré lattice formed due to lattice mismatch of the graphene and the Ir substrate. Imaging conditions: $I_t = 30\,\text{nA}$, $V_{bias} = 0.5\,\text{V}$ [8].

work when exposed to ambient conditions and elucidates the role of the wrinkles, in particular, as pathways for such intercalation. Finally, we investigate the state of charge disorder in graphene that has been completely decoupled from the substrate due to sufficient exposure to ambient conditions. We find a strong correlation of this disorder with the topographic corrugations in STM which we relate to the presence of the intercalated molecular species between graphene and the metal substrate.

This work has been conducted in collaboration with the group of Dr. Johann Coraux (for the samples) and Dr. Benjamin Grévin (for the KPFM measurements). I have included some results from the work of Sylvain Martin (charge disorder in graphene, Figure 4.15) and Amina Kimouche (decoupling of graphene, Figures 4.6, 4.13) which were essential for a complete understanding of the subject. Other than that, the rest of the measurements were done by me as well as the analysis of the KPFM data.

4.2.1 Sample Preparation

The samples of graphene on iridium(111) were prepared in accordance with the procedure demonstrated by C. Vo-Van et al. [136]. Iridium, few nm thick, was first grown on C-plane sapphire wafers by pulsed laser deposition in an ultra-high vacuum (UHV) chamber with a base pressure of 5×10^{-11} mbar, at a temperature of 700 K and then later annealed to 1100 K for the best structural quality. This was followed by the growth of graphene by chemical vapour deposition or CVD, which essentially involves the decomposition of the hydrocarbon, ethylene in the presence of the freshly prepared iridium surface, acting as a catalyst, in a second UHV chamber with base pressure of 10^{-10} mbar, at a temperature of 1300 K. The ethylene is introduced in the vicinity of the iridium via a dosing tube ensuring a higher local partial pressure $\sim 10^{-8}$ mbar.

Figure 4.6 shows STM topographs of the sample, in UHV conditions, just after growth; (a) shows the topography over a larger area with the sheet of graphene containing a wrinkle,

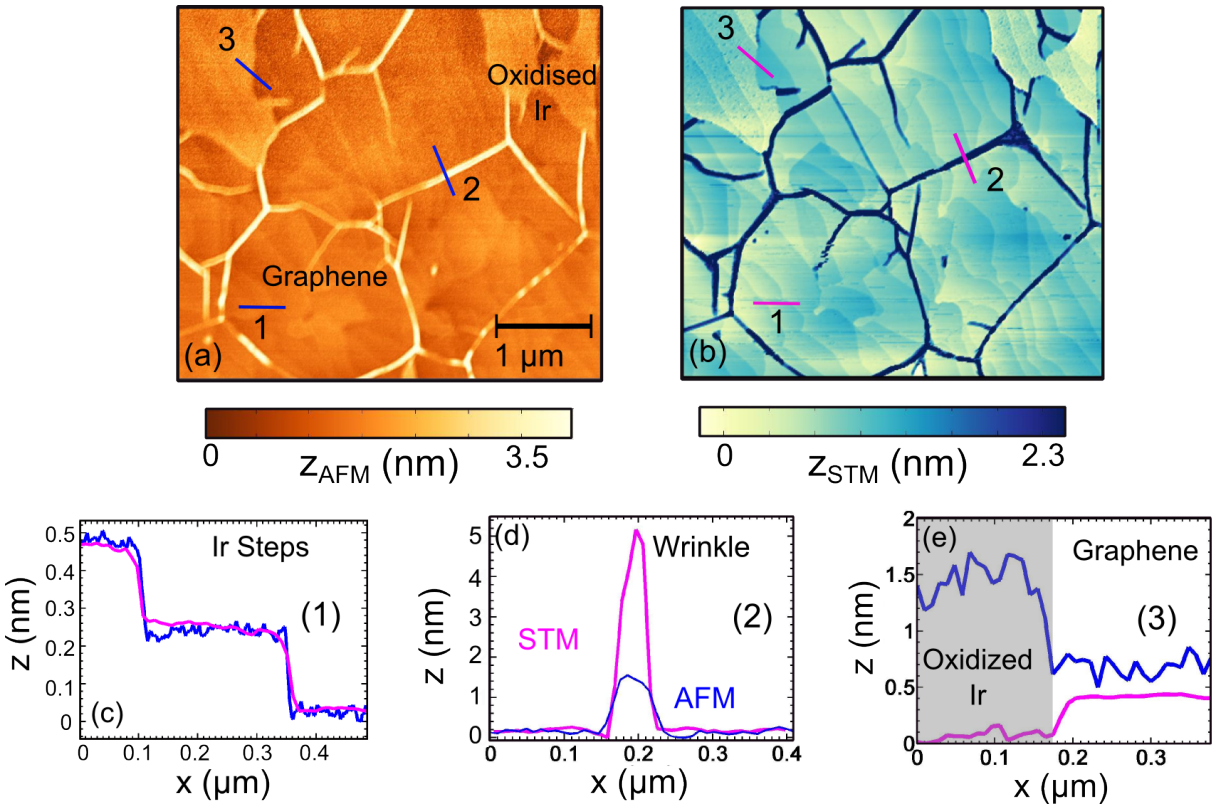

Figure 4.7: Large scale AFM and STM topography of Graphene on Ir acquired one after the other, with the same tip. (a) FM-AFM topography [$\Delta f_{set} = 5\,\text{Hz}, A_{set} = 300\,\text{pm}, V_{bias} = 0.8\,\text{V}$, scan speed $= 200\,\text{nm/s}, f_0 = 974350\,\text{Hz}, Q = 1400$, FIB etched Pt/Ir tip on LER]. (b) STM topography [$I_{set} = 100\,\text{pA}$, $V_{bias} = 0.8\,\text{V}$ at RT, pressure $\sim 10^{-4}\,\text{mbar}$]. (c) Height profile along the atomic steps of Ir in AFM (blue) and STM (magenta). (d) Comparison of height of graphene wrinkle recorded in AFM (blue) and STM (magenta). (e) Profile showing the height of oxidized Ir wrt. the surrounding graphene in AFM (blue) and STM (magenta).

terminating in a graphene edge. The region beyond this interface is just exposed iridium; (b) shows the clearly visible moiré lattice characteristic of this weakly lattice mismatched system.

4.2.2 Large scale surface features

Figure 4.7(a) and (b) shows the AFM and STM topography, acquired one after the other (with the same tip), of the same region of the sample surface. This region is large enough to introduce the main features that the system has to offer.

1. **Graphene** covering most of the surface. The roughness of graphene is about $\sim 50-100\,\text{pm}$ over an area $\sim 100\,\text{nm} \times 100\,\text{nm}$ in STM, somewhat lower than what is usually found in graphene on SiO_2. We note that for pristine graphene that has not been exposed to ambient conditions after growth, the only roughness observed is due to the moiré which shows a lateral periodicity of 2.5 nm.

2. **Atomic steps of Iridium**. The graphene sheet extends over step like features of height $\sim 220\,\text{pm}$ with separation of $\sim 250\,\text{pm}$ between them. These correspond to the atomic terraces of the underlying iridium substrate. Figure 4.7(c) shows a comparison of the height profiles of these Ir steps recorded in AFM and STM. Both imaging techniques give the same dimensions in this case.

3. **Graphene wrinkles** 'criss-crossing' the graphene sheet. These appear as folds in the graphene of height $\sim 1-5\,\text{nm}$ and width $\sim 20-25\,\text{nm}$ (Figure 4.7(d)).The presence of these wrinkles makes it easy to distinguish the regions with and without graphene. These features are discussed in detail in section 4.2.4.

4. **Oxidized Ir** implies the regions devoid of graphene where the bare Ir substrate is exposed. They appear as terminations of many wrinkles. Section 4.2.3 contains further discussion on these oxidized regions of the iridium substrate.

4.2.3 Regions devoid of Graphene : Oxidised Ir

We first discuss the regions devoid of graphene where the bare substrate is exposed. As has been mentioned before, a lot of current research on metal-graphene systems is being directed towards decoupling graphene to liberate it from the metallic influence. In this respect, it is important to understand the intercalation mechanisms at work along the surface, in particular the role that defects have to play in initiating and propagating such processes. Since these exposed regions devoid of graphene actually represent macroscopic defects in the graphene sheet, it is important to examine the nature of these surfaces.

AFM vs STM Topography

These regions appear as depressions in STM and as elevations in AFM with respect to the surrounding graphene. Figure 4.7(e) shows the line profile comparison over such a Graphene/exposed Ir interface recorded in STM and AFM. The elevation in AFM (h_{AFM}) is observed to be about $0.9\,\text{nm}$ and the depression in STM ($-h_{STM}$) to be $\approx 0.4\,\text{nm}$.

This difference can be explained if we consider that the two regions, with and without graphene are electronically very different with a high probability of the latter being oxidized as a result of being subjected to atmospheric oxidation. This would result in reduced conductivity of the exposed part, as associated with oxides, causing the STM tip to move closer to the surface with respect to the surrounding graphene covered region, to maintain the set-point tunneling current. This would account for the depression recorded in STM. On the contrary, since AFM scanning is not affected by electronic properties of the surface, the topography given by AFM should give a more accurate description in this case. The elevation of the exposed regions is then real and justified by an increase in volume that accompanies the oxidation process.

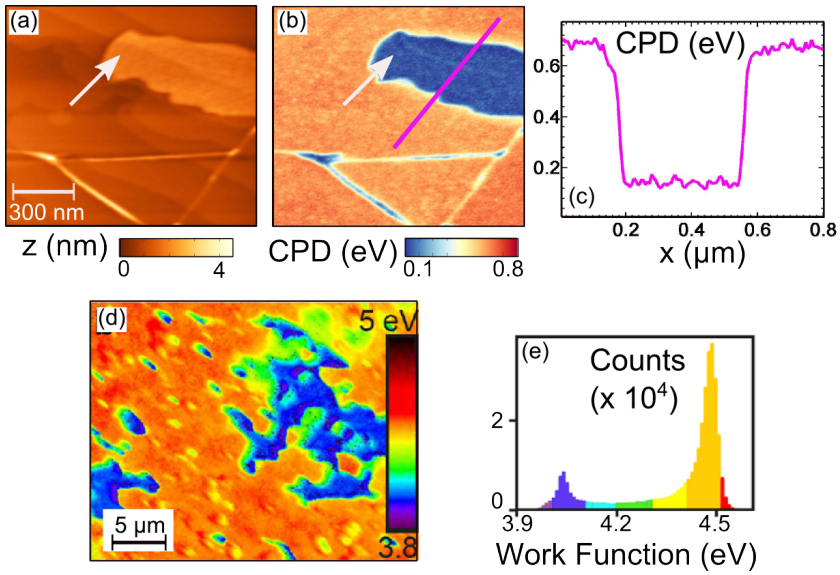

Figure 4.8: Signatures of oxygen in regions devoid of graphene. (a) AFM topography and (b) CPD map (in FM mode) of GR/Ir(111) showing wrinkles as well as Ir substrate devoid of graphene (indicated by white arrow). Imaging parameters: $\Delta f = -3\,\text{Hz}$, $A_{set} = 8.4\,\text{nm}$ (RT, UHV). (c) CPD profile corresponding to the path highlighted by the magenta line in (b). *Courtesy F. Fuchs and B. Grévin.* (d) Work-Function (WF) map of GR/Ir(111) surface (different sample than in (a)-(c)) measured with PEEM. (e) Histogram showing the corresponding WF distribution [8].

Work-function analysis with KPFM and PEEM

Spatially resolved work-function (WF) anaysis using KPFM and Photoemission Electron Microscopy or PEEM confirmed the presence of oxygen in the regions devoid of graphene, as speculated in the previous section. PEEM measurements were done in the group of Dr. Olivier Fruchart in Institut Néel while the KPFM measurements were performed by Dr. Benjamin Grévin.

Figure 4.8(a) and (b) show the AFM topograph and the simultaneously acquired map of contact potential difference or CPD (in frequency-modulated mode) of a region on GR/Ir(111) surface that includes one of these voids in the graphene sheet indicated by the white arrow. The CPD over this region is seen to drop by 0.5 eV as compared to the surrounding graphene covered regions (sub-figure (c)) implying a decrease in WF by the same amount 3.2.3. This is consistent with local WF analysis carried out using PEEM, as shown in Figure 4.8(d),(e). The work-function over the graphene is $\approx 4.5\,\text{eV}$ with a variation of $\approx 0.1\,\text{eV}$ over micrometer distances which is similar to what has been reported for carbon adlayers on iridium [137]. For the parts devoid of graphene, WF is found to be $4-4.1\,\text{eV}$ which is close to 4.2 eV, that has been reported for IrO_2 using ultraviolet photoelectron spectroscopy [138].

Hence, it is quite clear that the regions in the iridium substrate that are left uncovered by the graphene sheet have indeed undergone oxidation under ambient conditions.

4.2.4 Graphene Wrinkles

Probably the most striking feature in the presented surface topography (Figure 4.7) are the graphene *wrinkles*. These are local delaminations on the graphene, formed during cooldown to room temperature after high temperature CVD growth ($\sim$ 1300 K), due to unequal contraction of the graphene and the iridium substrate. The wrinkling of the graphene sheet does not exclusively apply to the GR/Ir(111) system but is a common occurrence for graphene on various substrates. Examples include CVD grown graphene on Cu that has been transferred onto SiO_2 [139], graphene on SiC [140] as well as exfoliated graphene on SiO_2 [141]. This class of corrugations are expected to represent one of the major type of defects in graphene. Hence, understanding their properties and role in influencing the bulk electronic properties is important both fundamentally as well as for industrial applications.

AFM vs STM Topography

Graphene on the wrinkles possesses structural and electronic properties that can be very different from graphene on the flat part. Recent STM studies on wrinkles of graphene on SiO_2 [141] have revealed triangular atomic patterns on the wrinkles in comparison to the expected hexagonal C arrangement on the flat part. The strain created by the increased local curvature on the wrinkle was thought to be the reason for this observed breaking of the six fold symmetry. The authors of [141] further observed distortions between subsequent images of the triangular lattices on wrinkles while no such distortion was observed on the flat graphene. This prompted them to conclude that these distortions probably arose from the higher flexibility of the wrinkled surface.

By combining the techniques of STM and AFM, we examine the scenario, in particular the topography of the wrinkles on graphene on iridium. Figure 4.7 (d) shows a comparison of the height profile over the same graphene wrinkle acquired in AFM and STM mode. The differences are quite remarkable and consistent. In AFM, the wrinkles appear as rounded dome-like folds of the graphene whereas in STM, the very same wrinkle along the exact cross-section appears more like a sharply spiked protrusion. What is even more surprising is that the measured height in STM is far greater than in AFM, more that ~ 3 times in this case.

A possible explanation for this observation could be due to STM tip induced deformation of the graphene on the wrinkle. During scanning in STM mode the tip-sample distance is of the order of a few Å while in non-contact AFM, scanning distances are much higher (about 5 nm further away from STM contact in this case). It has been shown by Altenburg et al. [142], that for tip-sample separations below ≈ 5 Å, the graphene sheet on Ir gets lifted significantly, as high as 12 pm, by Van der Waals' forces between the graphene and the STM tip. In view of this finding, we can expect the STM tip induced deformation to be enhanced on the wrinkle where the graphene is far away from the Ir substrate ($1 - 5$ nm) than on the flat part where the Van der Waals' force between the substrate and the graphene will partly cancel the pull from the tip.

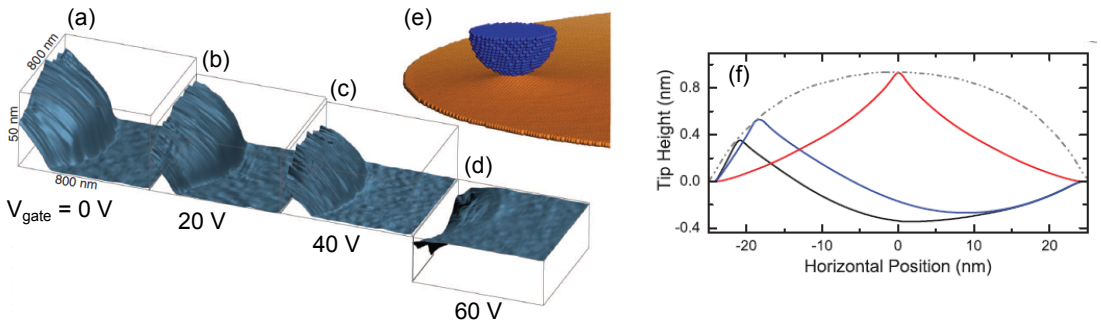

Figure 4.9: Deformation of graphene membrane by competing forces of the STM tip (pulling upwards) and the back-gate electric field (pulling downwards). (a-d) STM topographs at the indicated backgate voltages (V_{gate}). (e) Atomistic model showing deformations in the graphene membrane interacting with the STM tip. (f) Calculated membrane shapes at the critical tip height for horizontal tip positions of 2.5 nm (black curve), 5.2 nm (blue curve), and 25 nm (red curve) from the membrane edge. A back-gate force of 0.012 pN was applied to each atom in the membrane. The gray dot-dashed curve is an envelope showing the membrane height as seen in a STM measurement [143]

Figure 4.9 shows an interesting experiment performed on suspended graphene membranes on SiO_2 substrate which demonstrates this mechanical *pulling* by the STM tip. A convex shape of the membrane implies an increased Van der Waals' force of the tip while a concave shape is produced when the electrostatic force of the backgate overcomes this upward pull by the tip [143].

In AFM mode of scanning, since the tip-sample distances are far higher than 5 Å, the Van der Waals' pull from the tip should be significantly smaller and hence the AFM topography should give us the real height and shape of the wrinkles.

Hence, from a comparative study of topography of wrinkles in AFM and STM, we can clearly see that the wrinkle shape and height is significantly distorted by the STM tip. From this observed distortion, we can conclude that structurally the graphene in the wrinkle is more flexible due to the reduced influence of the Van der Waals' force from the iridium substrate as compared tp *flat* graphene.

Dissipation Microscopy

Another interesting aspect is the consistent observation of reduced energy loss of the scanning resonator or in other words, reduced dissipation over the wrinkles in comparison to *flat* graphene. Figure 4.10 shows the large scale topography of the GR/Ir(111) surface, already shown before, together with the simultaneously acquired map of excitation signal or V_{exc} and the oscillation amplitude A of the scan probe. V_{exc} is the modulation voltage supplied to the scanning resonator to maintain it at the set-point amplitude A at resonance (section 3.2.2). Hence $V_{exc} \propto A_{drive}$ where A_{drive} is the drive amplitude in units of displacement. In frequency modulated AFM, the

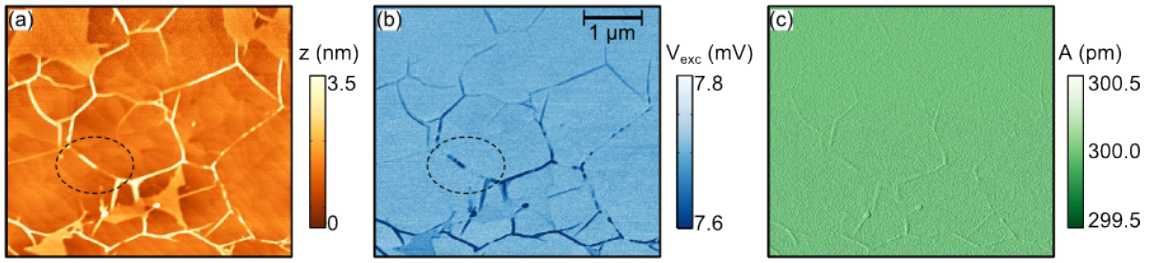

Figure 4.10: Reduced dissipation over wrinkles. (a) AFM topography same as shown in Figure 4.7(a). (b) Corresponding excitation signal (V_{exc}) map which directly gives the spatial variation of the energy dissipation over the surface. (c) Oscillation amplitude A of scan probe.

scan probe is always maintained at resonance, hence $f_{drive} = f_0$ where f_0 is the eigen frequency of the probe. Then, it is rather straightforward to show that [Eq.(3.2.14)]

$$\left|\frac{A}{A_{drive}}\right| = Q = \frac{1}{2\zeta}. \tag{4.2.1}$$

where Q is the quality factor and ζ is the damping ratio. Since A is maintained constant during scanning, by an amplitude controller, it follows, therefore that a map of V_{exc} or A_{drive} would directly produce a map of dissipation encountered by the probing resonator while scanning the surface. Figure 4.10(c) verifies that the amplitude A is maintained constant to within 0.3 % of its mean value of 300 pm. Hence, in the V_{exc} or local dissipation map in figure 4.10(b), we clearly see that the energy loss is reduced over the wrinkles. Moreover, if we compare the wrinkled graphene in the encircled region between the AFM and the dissipation map, we find that the higher the elevation of the graphene wrt to the underlying substrate, the lesser is the dissipation encountered by the probe. Interestingly, this observation is rather consistent with the observation reported in section 1.3.3, for exfoliated graphene on SiO_2.

Dissipation in scanning probe measurements could have multiple origins: electrical, magnetic, due to Brownian motion or hysteresis related dissipation [144]. In the present situation, differences in the extent of dissipation on the wrinkles could be of electrical origin. The metallic tip and the sample can be considered to form the two plates of a capacitor maintained at a potential difference equal to their work-function mismatch i.e. their contact potential difference V_{CPD}, as explained in section 3.2.3 (assuming externally applied bias voltage on the sample to be zero). While scanning in non-contact AFM mode, the periodic modulations of the tip-sample distance z_{ts} causes the tip-sample capacitance C_{ts} to change periodically. If the tip and sample resistances are high, this will lead to currents at finite frequency, thus resulting in energy dissipation. According to Denk and Pohl [145], this dissipation is proportional to V_{CPD}^2/z_{ts}^2. Hence, a difference in dissipation observed indicates a difference in V_{CPD} which is ultimately related to work-function differences in graphene between the two regions. In fact, we shall see shortly, that this is indeed the case.

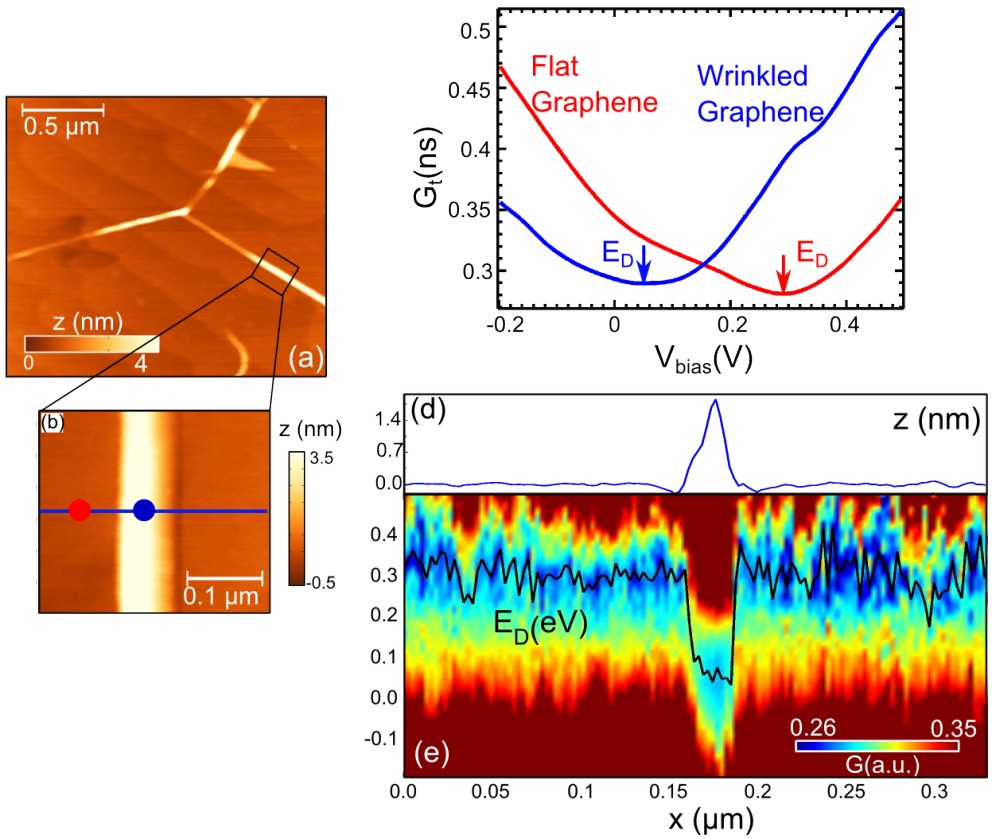

Figure 4.11: Scanning tunneling spectroscopy over graphene wrinkle. (a) FM-AFM topograph showing a large scale view of graphene, wrinkled in certain parts. Imaging parameters: $\Delta f_{set} = 2\,\text{Hz}, A_{set} = 700\,\text{pm}, V_{bias} = 0.8\,\text{V}$, scan speed $= 300\,\text{nm/s}, f_0 = 994967\,\text{Hz}, Q = 120000$, Pt/Ir coated Si cantilever tip on LER, RT. (b) Zoomed in view of the graphene wrinkle. (c) Differential tunneling conductance $G_t$spectrum over *flat* (red) vs *wrinkled* (blue) graphene. (d) Height profile of the wrinkle along blue line in (b), recorded before tunneling spectroscopy at each point along this line. (e) Tunneling conductance map across the wrinkle shown in (b).

Vanishing doping over Wriinkled Graphene by STS

The reduced influence of the iridium substrate on the wrinkled graphene should imply different electronic properties than graphene on the flat part as had been suggested by the observation of reduced dissipation over these folds in graphene. Here, we directly measure the local density of states (LDOS) across the wrinkle via scanning tunneling spectroscopy (STS) to analyze these differences.

Figure 4.11(a),(b) shows the large scale AFM topograph of the surface and the zoomed in view over a graphene wrinkle respectively. The blue line passing across the wrinkle, as indicated in (b), is chosen as the path for performing point to point differential tunneling conductance spectroscopy with inter-point spacing of 2.6 nm. The differential tunneling conductance spectra G_t are measured by the lock-in technique as described in section 3.2.1. A modulation of 6 mV and frequency 407 Hz is superposed on the DC bias V_{bias} applied to the sample to measure the

tunneling conductance.

Figure 4.11(c) shows the average G_t spectrum on *flat* (red) vs *wrinkled* graphene (blue). For graphene on metal, the position of the minimum of G_t vs V_{bias} curve approximately represents the position of the local Dirac point wrt. the Fermi level of graphene, i.e. $|E_D - E_F|$ which is related to the doping concentration by Eq.(2.2.21) [1]. This will be explained in detail in section 5.3.3. In our setup, since the voltage bias is applied to the sample while the tip is maintained at ground by the tunneling current amplifier (Figure 3.1), a positive value of E_D implies a hole doping while a negative value would have implied electron doping. Therefore Figure 4.11(c) indicates that the flat graphene is positively doped while on the wrinkle, the doping is still positive but far less than in the flat part. This is reasonable as the doping existing on the graphene can be either due to the iridium substrate itself or some intercalated molecules present in the space between it and the graphene. Hence further the graphene from the substrate, less should be the influence which in this case translates into negligible doping on the wrinkle.

Figure 4.11(e), shows the spatial variation of the G_t spectrum along a line passing over the wrinkle (indicated in (b)) while (d) gives the simultaneously acquired STM topography. E_D has been indicated in (e) (black curve). By considering the E_D and the z profiles across the wrinkle simultaneously, we are able to track the manner in which E_D, or equivalently, doping changes from the flat to wrinkled graphene. We list here the significant features:

1. Graphene on the flat part is positively doped with mean value of Dirac point as $\bar{E_D} \sim 290\,\text{meV}$ which implies a mean doping level of $\bar{n} \sim 6 \times 10^{12}\,\text{cm}^{-2}$. The local fluctuations in the Dirac point is found to be $\sigma_{E_D} = 30\,\text{meV}$ corresponding to a doping inhomogeneity of $\sigma_n \sim 1.3 \times 10^{12}\,\text{cm}^{-2}$, using Eq.(2.2.21).

2. Graphene on the wrinkle is significantly less doped. Mean value of Dirac point and doping are $\bar{E_D} \sim 40\,\text{meV}$ and $\bar{n} \sim 1.4 \times 10^{11}\,\text{cm}^{-2}$ respectively. Corresponding fluctuations are $\sigma_{E_D} \sim 18\,\text{meV}$ and $\sigma_n \sim 1.0 \times 10^{11}\,\text{cm}^{-2}$, but these fluctuations are not very accurate since the number of measurement points considered in this case is only 10.

3. While approching the wrinkle from the flat region, E_D rapidly decreases to almost zero as the wrinkle height exceeds $\sim 0.6\,\text{nm}$. In other words, this measurement gives us the metal-graphene distance at which the latter is liberated from the influence of the former.

Hence, we see that electronic properties are indeed very different on the wrinkle than on graphene closer to the substrate i.e. on the flat part. The E_D fluctuations on the flat graphene show a weak correlation with topography (≈ 0.3) in this case. However, we are probably limited by the spatial ($= 2.6\,\text{nm}$) and energy resolution to do such an analysis, since the measurement was performed at room temperature. Nevertheless, the comparison of the doping disorder with topography on the flat graphene is reported, in detail, in a subsequent section.

[1] Because of close proximity to the metallic substrate which acts as a screening plate, local gating effect by the tip is weak

Kelvin Probe Microscopy

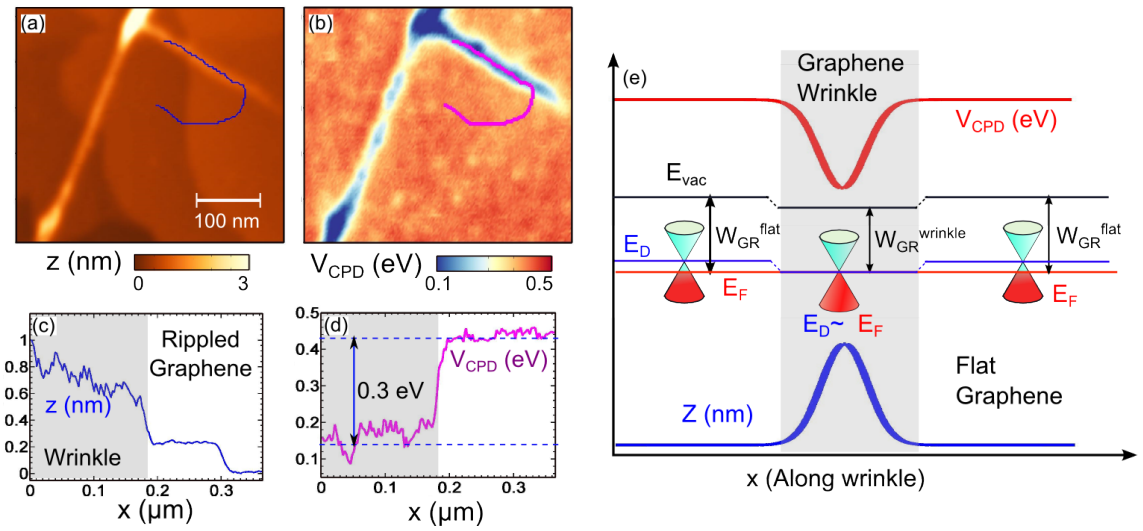

Figure 4.12: Kelvin probe force microscopy on graphene wrinkles. (a) Topography by FM-AFM and (b) corresponding contact potential difference (V_{CPD}) image by frequency modulated KPFM of GR/Ir(111) surface, (UHV, 300 K). Imaging parameters: $\Delta f = -15\,\mathrm{Hz}$, $A_{set} = 8.4\,\mathrm{nm}$. (c) Height profile of the wrinkle along the blue line marked in (a). (d) V_{CPD} profile of wrinkle over the same path, marked by the magenta line in (b). (e) Schematic explaining the V_{CPD} change across graphene wrinkle. E_F = Fermi energy, E_D = Dirac Point, E_{vac} = Vacuum energy level. *Courtesy F. Fuchs and B. Grévin.*

We further employ frequency modulated Kelvin probe force microscopy (FM-KPFM) to map out the spatial variations of the contact potential difference V_{CPD} (section 3.2.3). V_{CPD} is directly related to the work-function of the sample W_s as given by Eq.(3.2.24). The V_{CPD} map can, therefore, be equivalently interpreted as the work-function map of the surface provided we assume absence of any surface charge, dipoles or bonding of the scanning cantilever to the surface which might cause additional changes. This is useful in the present situation because any existing local doping difference will be directly detected in a V_{CPD} map of the surface.

Figure 4.12(a) and (b) show the FM-AFM topography and V_{CPD} map respectively of the GR/Ir(111) surface, acquired with a Si cantilever tip. We observe that the wrinkled regions are manifested as a depression in the V_{CPD} map. This implies that the work-function decreases over the wrinkle, indicating a decrease in the Dirac point E_D [146]. Figures (c) and (d) show the topography and the V_{CPD} profile respectively along a path starting from the graphene wrinkle and terminating on flat graphene. V_{CPD} measured over wrinkled graphene is $\approx 0.3\,\mathrm{eV}$ lower than what is measured on the flat part. This equivalently means that the Dirac point over wrinkle is lower by 0.3 eV. This confirms quantitatively the tunneling spectroscopy measurements (Figure 4.11) where hole doping reduces from $\approx 0.290\,\mathrm{eV}$ on the flat to ≈ 0 on the wrinkled graphene. The schematic in (e) illustrates this situation.

Hence, by employing two complimentary microscopy techniques, scanning tunneling spec-

troscopy and Kevin probe force microscopy, we clearly demonstrate the difference in the electronic properties found on the graphene on the flat part as compared to the graphene on the wrinkle. Both methods lead to the same conclusion that the doping level changes from strongly p-doped nature on the flat region where graphene is closer to the substrate to negligibly small doping value on the wrinkle where it is $\sim 1\,\text{nm}$ from the influence of the substrate.

4.3 Dynamics of Decoupling of Graphene

So far, we have concentrated on GR/Ir(111) systems that had experienced exposure to ambient conditions for prolonged durations (several months in some cases). This system is very different from the same system that had always remained in UHV. From our analysis so far, we can already cite one prominent difference. The positive doping observed in an as-grown sample leads to a Dirac point energy of $< 100\,\text{meV}$ wrt. the Fermi energy, as has been discussed in section 4.1.3. In our case, E_D on graphene on the flat part is $\approx 300\,\text{meV}$, which is considerably higher. And this is yet less than on GR/Ir(111) systems with perfect coverage of the iridium substrate that has been subjected to controlled oxygen intercalation under UHV conditions in which case, it is $\approx 600\,\text{meV}$. An obvious and important question is what causes this difference.

To answer this question, in this section, we study a freshly prepared sample of GR/Ir(111), of intermediate coverage, that has been subjected to ambient conditions for a very short duration of time[2]. AFM observation at room temperature reveals a gradual decoupling of the graphene, starting from the wrinkles. This suggests some intercalation processes at work which is confirmed by the detection of oxygen via chemical analysis, throughout the sample. The role of the wrinkles is then discussed as tunnels for such intercalation process. Scanning tunneling spectroscopy is finally performed to investigate the difference in the electronic properties between well-coupled and decoupled graphene.

The AFM measurements for visualization of the decoupling process has been performed by Amina Kimouche while I have performed the STS measurements in the subsequent section.

4.3.1 Wrinkles as pathways for intercalation

Figure 4.13(a) shows a large scale AFM topograph of a freshly prepared sample of graphene on iridium, acquired right after exposing it to ambient conditions. We observe that apart from the usual features that has been discussed (section 4.2.2), there is an additional new feature: graphene surrounding the wrinkles is elevated wrt. graphene further away, forming a kind of *halo* around the wrinkles. To distinguish the graphene in these regions from graphene in the flat part, we will refer to it as *decoupled graphene* based on the fact that in these ribbon-like regions adjoining the wrinkles, graphene-metal distance is higher than on the flat part, which we will refer to as *well-coupled*, henceforth.

[2]Time duration mentioned before each measurement.

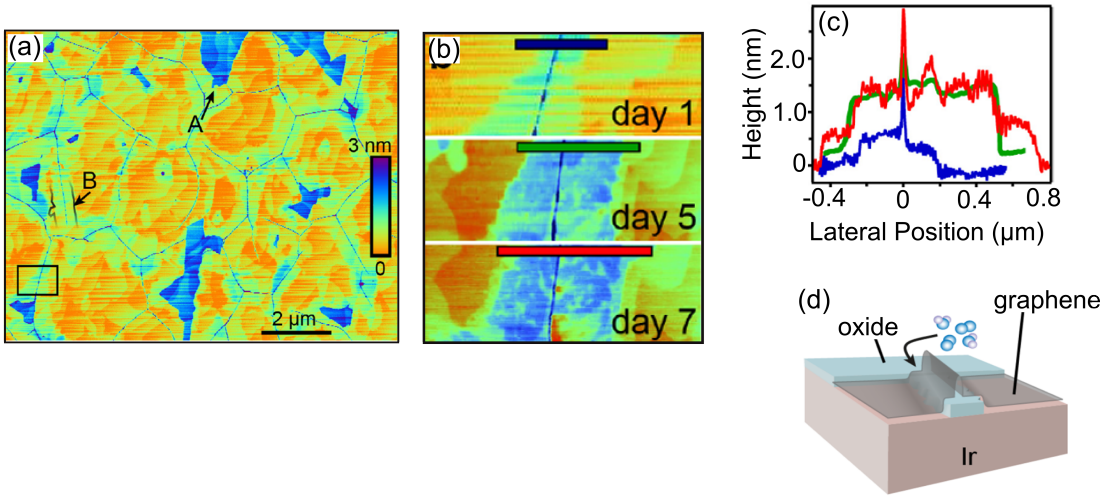

Figure 4.13: Gradual oxygen intercalation around graphene wrinkles. (a) Large scale AFM topograph (tapping mode) of a sample of GR/Ir(111) right after exposure to ambient conditions. The regions devoid of graphene have been indicated as 'A' while the ribbon-like regions in the graphene surrounding the wrinkles are labelled as B. (b) Zoom-in on the rectangular region indicated in (a) after 1,5 and 7 days of exposure to ambient conditions. (c) Height profiles along the lines marked in (b). (d) Schematic demonstrating the role of graphene wrinkles as pathways of oxygen intercalation [8]

Figure 4.13(b)and (c) shows the gradual evolution of these regions with time. From 0.4 nm and several 10 nm after 1 h of exposure to air, the height and width of the regions of decoupled graphene increases, rapidly at first, then slower and slower. After a few days they do not increase much and reach about 1.5 nm and a few 100 nm, respectively. The increase can be stopped at any stage by simply placing the sample under UHV.

This observation suggests that there is some intercalation process at work that gradually decouples the graphene from the metallic substrate underneath, starting from the wrinkles. A closer look at the topography (Figure 4.13(a)) shows that there are several wrinkle terminations at any given hole in the graphene sheet. Without the presence of these terminations, intercalation of molecules would have been difficult since graphene is known to bind strongly to the iridium substrate at the edges [147]. Hence the wrinkle terminations serve as entry points for the intercalation of molecules while the wrinkle themselves act as tunnels for their propagation underneath the graphene. The schematic shown in Figure 4.13(d) demonstrates this process.

We expect the diffusing molecular species to be predominantly oxygen because chemical analysis of the sample via area selected X-ray photo-emission performed with PEEM confirms the presence of oxygen all over the surface [8]. It is important to note that such an intercalation would not have been possible in samples with 100 % graphene coverage under ambient conditions [128][148]. The presence of the large number of free edges in the graphene sheet in the present system containing multiple wrinkle terminations is therefore necessary for the observed oxygen

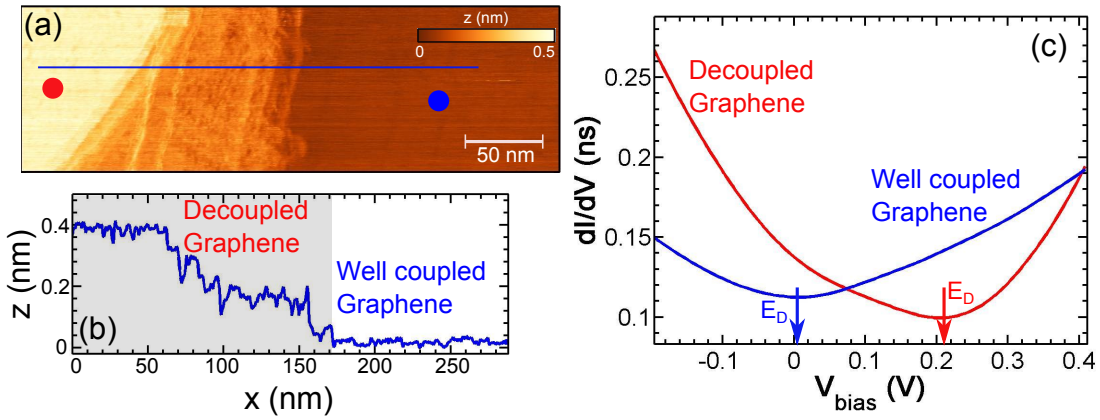

Figure 4.14: Tunneling Spectroscopy over well coupled and decoupled graphene. (a) STM topograph showing the boundary between coupled and decoupled graphene. Imaging parameters: $I_t = 100\,\text{pA}$, $V_{bias} = 0.6\,\text{V}$, scan speed $= 40\,\text{nm/s}$. (b) Height profile along the blue line indicated in (a). (c) Tunneling conductance as a function of V_{bias} over graphene well coupled to Ir substrate (blue) and that decoupled from it (red). The tunneling conductance is obtained by taking the numerical derivative of the tunneling current, see text for details.

intercalation.

4.3.2 Electronic Properties of well-coupled vs decoupled graphene

To understand the effect of intercalated oxygen molecules on the electronic properties of the graphene, we perform STM and STS. Figure 4.14(a) shows the STM topograph of the boundary between decoupled and well coupled graphene. The height profile across this boundary in (b) shows that the graphene on the decoupled part is lifted by about 0.4 nm wrt. graphene in the well-coupled region. We note that this height is different from the equilibrium height of 1.5 nm reported in the previous section. This could be because of several reasons: (1) this sample is different from the sample in Figure 4.13, (2) Figure 4.14(a) shows a STM topograph while Figure 4.13(a)-(c) presents the AFM topograph and the heights recorded in AFM and STM can be different, as we saw in the case of wrinkles (section 4.2.4) and (3) time of exposure to ambient conditions was quite different for the two samples. In the present case, time duration is longer (> 1 week). Hence, possibly, some non-zero quantity of oxygen must have intercalated throughout the system, in this time, which might lead to a reduced step height at the interface.

The roughness (STM) of graphene increases on decoupling in general, in this case being about 22 pm which is almost double the value measured on the well coupled region. This is consistent with the fact that the moiré pattern (Figure 4.1) that is found in the pristine samples, is absent in samples which has faced prolonged exposure to ambient conditions ([9], Figure 1).

Figure 4.14(c) shows the tunneling conductance spectra over well-coupled graphene (blue) and decoupled graphene (blue). Each tunneling spectrum represents the average of 100 spectra,

acquired over a total area of 50 nm × 50 nm. The main findings are enumerated below.

1. On well-coupled graphene: $\bar{E_D} \approx 8\,\text{meV}$ i.e. almost no doping with $\sigma_{E_D} \approx 15\,\text{meV}$.
2. On decoupled graphene: $\bar{E_D} = 180\,\text{meV}$, $\bar{n} = 2.9 \times 10^{12}\,\text{cm}^{-2}$ and the corresponding fluctuations are $\sigma_{E_D} = 23\,\text{meV}$, $\sigma_n = 7.8 \times 10^{11}\,\text{cm}^{-2}$, i.e positively doped but less than what is usually measured on samples subjected to prolonged exposure to ambient conditions as discussed in section 4.2.4.

The reason for observing lower positive doping in the decoupled regions in this sample as compared to other samples presented before (section 4.2.4) is related to the difference in exposure time to the atmospheric conditions, (about a week, which is far less than usual) before the STM measurements. The fact that the decoupled graphene has a higher positive doping over well-coupled graphene clearly demonstrates the role that the intercalated oxygen molecules play as positive dopants of the graphene sheet besides decoupling it from the influence of the metallic substrate.

4.3.3 Conclusion

In conclusion, ex-situ prepared GR/Ir(111), that has faced exposure to ambient conditions for prolonged durations of time, is different from both pristine GR/Ir(111) grown and preserved in UHV or perfectly graphene covered iridium that has been subjected to controlled oxygen intercalation, also under UHV conditions. It is kind of an intermediate between the two, indicated by the level of positive doping which lies midway between that of pristine GR/Ir(111) and decoupled graphene in GR/O/Ir(111) systems. The natural intercalation of oxygen molecules, starting at the graphene edges and propagating via wrinkles, accounts for this intermediate level of doping. This natural decoupling process transforms the moiré lattices into a corrugated landscape with typical roughness $\sim 50 - 100\,\text{pm}$.

4.4 Charge disorder in decoupled graphene

In this final section, we return to a system of GR/Ir(111) that has been exposed to ambient conditions for a prolonged duration of time. This, therefore, offers a system where the graphene is decoupled from the substrate by the intercalation of oxygen molecules from the atmosphere. Importantly, we note that the linear dispersion, which is missing in the corresponding pristine system in UHV (Figure 4.2(b),(c)), is completely restored in this decoupled system as shown by us in [9] (primarily the work of S. C. Martin). The Fermi velocity is found to be $v_F = 0.9 \pm 0.04\,\text{m/s}$ which implies that the charge carriers are subjected to a highly screened environment [149] i.e. the dielectric constant $\epsilon \to \infty$, which is probably a consequence of the close proximity to the metallic substrate which acts as an electrostatic screening plate.

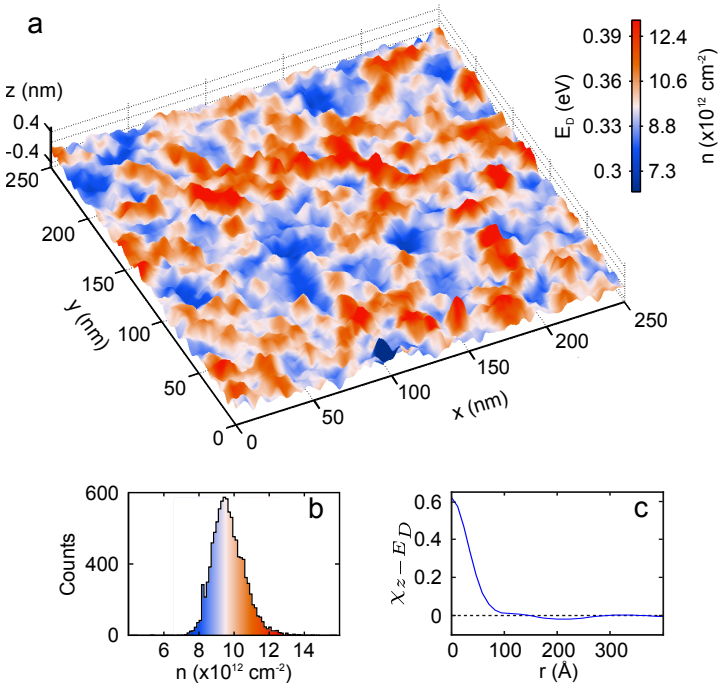

Figure 4.15: Correlation between charge disorder and topography. (a) Dirac point map (color code) superimposed over a 3D plot of the long-wavelength topography. Image of 250 nm × 250 nm. (b) Carrier density distribution extracted from (a) (see text). (c) 2D correlation coefficient $\chi_{z-E_D}(\mathbf{r})$ (see text), between E_D and topography maps given above [9].

We investigate the charge disorder in such a system using STM/STS and then by KPFM. The measurement of charge disorder, presented here, was performed by S. C. Martin, KPFM by Benjamin Grévin while I participated in the data analysis.

4.4.1 STM/STS investigation of charge disorder

To find the doping inhomogeneity in decoupled graphene, we perform point to point tunneling spectroscopy over a region of 250 nm × 250 nm. The Dirac point $E_D(\mathbf{r})$ and the corresponding doping concentration $n(\mathbf{r})$ are then extracted by analyzing each tunneling spectrum following the same procedure as described in (section 4.2.4). The color map shown in Figure 4.15(a) pictures the spatial inhomogeneities of $E_D(\mathbf{r})$ around its mean value, forming a smooth landscape of charge puddles, of about $8-9$ nm in diameter. The standard deviation in charge carrier concentration is found to be $\sigma_n = 1.2 \times 10^{12}\, cm^{-2}$.

We now focus on the comparison between the Dirac point distribution and the topography. Since only topographic variations at length scales similar or larger than the typical puddle size can correlate with the charge inhomogeneities, we filter out the topographic maps from structures of dimensions below half the mean puddle size. Figure 4.15(a) shows the superposition of an $E_D(\mathbf{r})$ map (color scale) along with the long wavelength-pass filtered topography $z(\mathbf{r})$ recorded at the same position [three-dimensional (3D) profile]. A very high degree of correlation between

doping and topography is readily seen. We have quantified this by calculating the normalized cross-correlation function between topography $z(\mathbf{r})$ and the Dirac point map $E_D(\mathbf{r})$, given by

$$\chi_{z-E_D}(\mathbf{r}) = \frac{\sum_i E_D(\mathbf{r_i} - \mathbf{r}) \times z(\mathbf{r_i})}{(\sigma_{E_D}\sigma_z)}. \tag{4.4.1}$$

The local cross correlations $\chi_{z-E_D}(0)$ between $z(\mathbf{r})$ and $E_D(\mathbf{r})$ are in excess of 60% in large area maps [Figure 4.15(c)]. These correlations are independent of the region chosen, but are enhanced in maps with dimensions much larger than the typical puddle size. When correlating spectroscopic maps with topography, one also has to recall that in constant current STM mode, a LDOS variation will lead to a change in the tip-sample distance z. This can misleadingly induce phantom topographic features.

In order to check the influence of the DOS on the topographical images, we performed a calculation to estimate the apparent δz that would be caused by variations of the DOS. Using Eq.(3.2.1) and Eq.(3.2.2), the expression for the tunneling current can be written as

$$I_t = A \exp\left(-\frac{z}{z_0}\right) \int_0^{eV_{bias}} \rho\left(E - E_D(\mathbf{r})\right) dE, \tag{4.4.2}$$

where we assume that the DOS spectra are described by a single function $\rho(E - E_D)$ and spatial dependence is only via $E_D(\mathbf{r})$ and A is a constant. In constant current mode and choosing a specific reference location $\mathbf{r_0}$ at which $E_D(\mathbf{r_0}) = E_D^0$, we can then write the variations of z around $z(\mathbf{r_0})$ as

$$\delta z = z_0 \ln\left(\frac{\int_0^{eV_{bias}} \rho\left(E - E_D(\mathbf{r})\right) dE}{\int_0^{eV_{bias}} \rho\left(E - E_D^0\right) dE}\right). \tag{4.4.3}$$

Starting from the experimental Dirac point map of Figure 4.15(a) and assuming a flat topography, we calculate using 4.4.3, a phantom topography appearing with an apparent roughness of 6 pm at $V_{bias} = 570$ meV (the bias voltage at which the the topography of Figure 4.15(a) was measured), that is more than one order of magnitude smaller than the typical roughness measured on the same region by STM. Hence, the measured topography is weakly affected by the inhomogeneities of the DOS.

The cross-correlation coefficients found between the Dirac point map and topographic images taken on the same region but at different bias voltages are listed in Table 4.1. Except for the highest bias, topographic images at all energies including $V_{bias} < 0$, show similarly strong correlations to the Dirac point map. The lower cross-correlation at $V_{bias} = 700\,mV$ can be attributed to the fact that graphene is transparent at high bias, thus we probably probe the metallic substrate below rather than the graphene.

Hence, from the above analysis we can convincingly state that the doping landscape in this system of naturally decoupled graphene on iridium is disordered and this disordered landscape bears a strong positive correlation with the actual corrugated landscape of the sample measured in STM.

V_{bias} (mV)	700	570 (1)	570 (2)	100	30	-570
$\chi^0_{z-E_D}$	14 %	45 %	56 %	66 %	61 %	40 %

Table 4.1: Cross-Correlation coefficient between the topography images at different bias voltages V_{bias} and the E_D map. The images 570(1) and (2) are two images performed at the same place but successively.

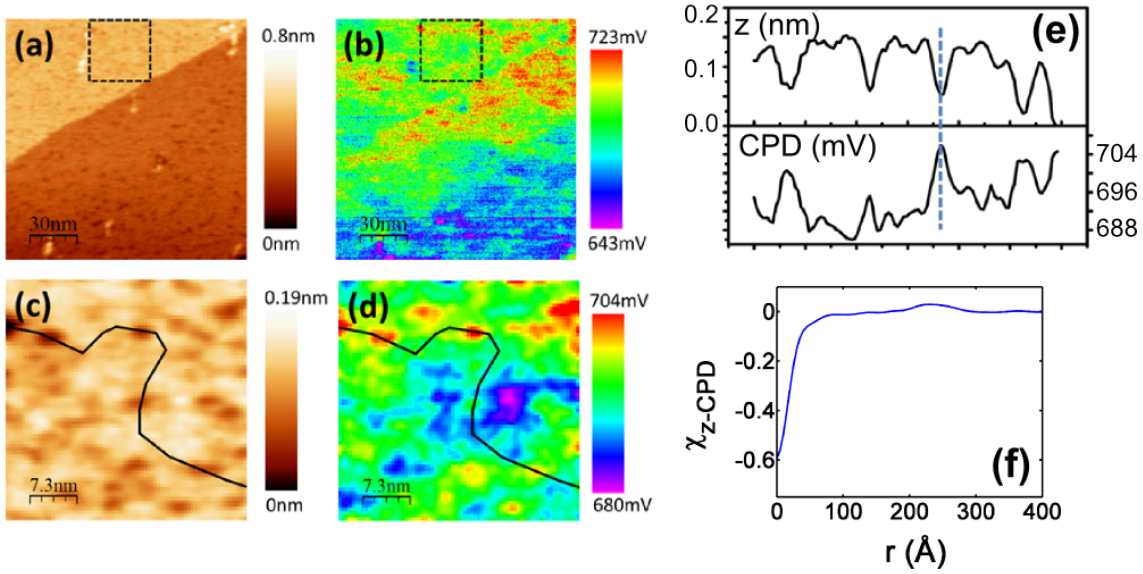

Figure 4.16: Negative correlation between V_{CPD} fluctuations and AFM topography. (a) Topography (by FM-AFM) and (b) and V_{CPD} map (by FM-KPFM) of *flat* graphene. Imaging parameters: $\Delta f = -50\,\mathrm{Hz}$, $A_{set} = 8.4\,\mathrm{nm}$. (c,d) Numerical zoom extracted from the area enclosed by the black dotted square in images (a,b). Both images have been filtered by applying a Gaussian smooth to remove high frequency noise. (e) Topographic and V_{CPD} levels corresponding to the paths highlighted by black lines in (c,d). Depressions in the topography are clearly correlated with local maxima of the V_{CPD}. (f) Angular average of the cross-correlation function, $\chi_{z-CPD}(\mathbf{r})$ between V_{CPD} and topography maps given above. *Courtesy F. Fuchs and Benjamin Grévin*

4.4.2 Charge disorder by KPFM

We now examine the system of decoupled graphene using frequency modulated KPFM to map the fluctuations in local contact potential difference or V_{CPD}. Local fluctuations in doping implies local variations in the work-function of graphene W_{GR} and hence variations in V_{CPD} [Eq.(3.2.24), Eq.(5.3.1)]. As seen from these equations, doping, V_{CPD} and W_{GR} are all directly related. Therefore, a positive correlation between doping and topography should also imply a positive correlation between the V_{CPD} map and the topography.

However, this is not always the case. Both positive and negative correlations are found between V_{CPD} map and the topography with magnitudes $\chi_{z-V_{\mathrm{CPD}}}(0) = 0.1 - 0.6$ where $\chi_{z-V_{\mathrm{CPD}}}$ is the angular averaged, normalized correlation function between them, defined in a manner

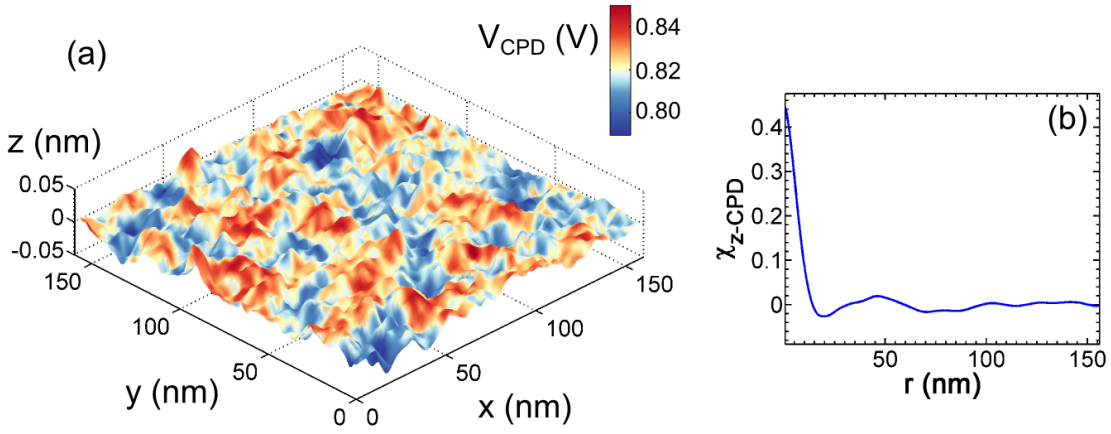

Figure 4.17: Example of a region where a positive correlation between V_{CPD} fluctuations and AFM topography is found. (a) V_{CPD} map (color code) superposed over a 3D plot of the long-wavelength topography. (b) Angular average of the normalized cross-correlation function, $\chi_{z-CPD}(\mathbf{r})$ between the V_{CPD} map and topography. *Courtesy F. Fuchs and Benjamin Grévin.*

equivalent to Eq.(4.4.1). In general, fluctuations in the V_{CPD} map could be characterized by a standard deviation of about 10 meV and a spatial extent of $6 - 14$ nm. Figure 4.16 shows an instance where a strong negative correlation $\approx -60\%$ is found while Figure 4.17 shows another region where a strong positive correlation $\approx 45\%$ is seen.

In our interpretation of V_{CPD} maps so far, we have only considered ideal, charge or dipole free surfaces. Hence, V_{CPD} had a one to one correspondence with the WF distribution along the surface [Eq.(3.2.24)]. However, presence of charges or dipoles in the surface will manifest themselves in the V_{CPD} maps, creating additional features. In particular,

1. A negative V_{CPD} shift (with respect to its reference/background value) will be produced for a local positive charge.

2. A negative V_{CPD} shift will also be produced for an electric dipole pointing upwards.

This has been demonstrated in Figure 4.18. To compensate the electric field created by a positive charge or a positive dipole on the surface, an additional positive voltage needs to be supplied to the tip which equivalently means a negative shift in V_{CPD} (section 3.2.3).

In addition, non-conventional mechanisms (such as local surface polarization effects induced by the AC modulation at the tip) can contribute to the local V_{CPD} contrasts at the sub-10 nm scale, when the nc-AFM/KPFM is operated in the regime where short range forces contribute significantly to the tip-surface interaction [150]. These extra contributions depend on the nature of the sample, and state of the art modeling simulations are needed to carry out quantitative analysis of the V_{CPD} contrasts.

While the above effects can explain the negative correlations sometimes found, a concrete conclusion is not possible at the moment. Efforts continue in this direction for a clearer under-

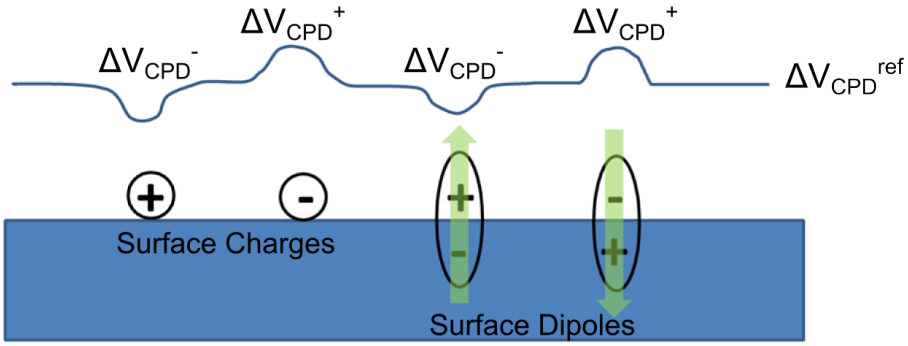

Figure 4.18: Schematic depicting changes in V_{CPD} due to surface charges or dipoles.

standing.

4.4.3 Origin of Disorder

The analysis of charge disorder by tunneling spectroscopy (section 4.4.1) leads to the conclusion that decoupled graphene on a metallic substrate displays a strong local correlation between doping and topography. Several scenarios can be considered for this observation. A contribution of curvature effects [151][62][152][153] could, for example, be anticipated. Figure 4.19 shows the charge disorder induced in the graphene by the strain field associted with the measured topography, theoretically calculated for us by the group of Marco Polini. However, we see that the contribution of the local curvature in this system is nearly two orders of magnitude below the observed amplitude of the doping disorder.

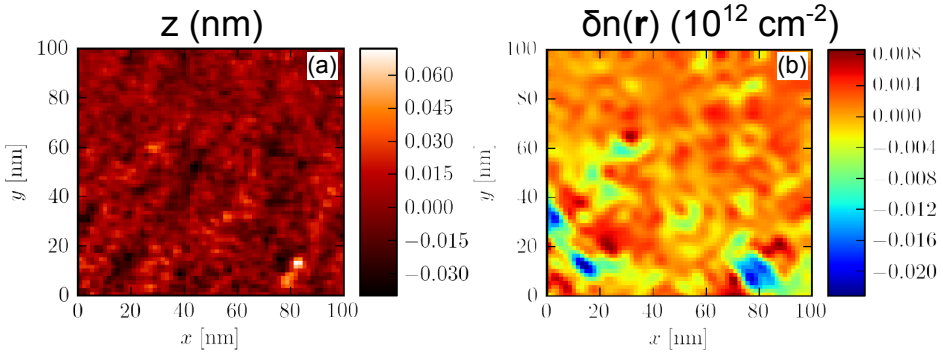

Figure 4.19: Strain field induced charge disorder. (a) Height fluctuations $z(\mathbf{r})$ of decoupled graphene. (b) Charge disorder $\delta n(\mathbf{r})$ induced in the graphene by the strain fields generated by the topography in (a). *Courtesy A. Tomadin, M. Gibertini and M. Polini.*

The graphene doping could further be due to graphene-metal distance dependent charge transfer from the metallic substrate due to finite electronic wave function overlap. Calculations of this effect [120] yield a qualitatively correct description, including the correct sign of χ_{z-E_D} for graphene on iridium. But as we have seen before (4.3.1), the graphene-metal distance $\sim 1\,nm$

in this case of decoupled graphene, a distance at which the above scenario would have negligible contributions as seen in Figure 4.20.

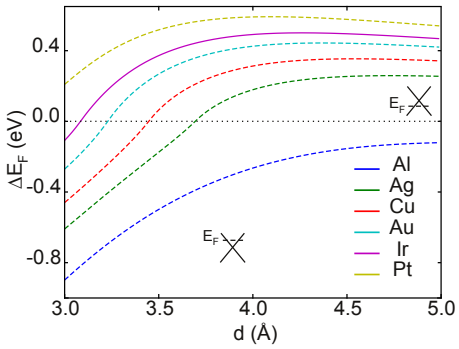

Figure 4.20: Fermi level shifts $\Delta E_F(d)$ as a function of metal-graphene distance calculated by the model proposed by Giovanetti et al.(Eq.(1) of [120]). Work-function of iridium $W_{Ir} = 5.76\,\text{eV}$.

The most likely explanation of the doping bases on the presence of molecular species, in particular oxygen as we have shown above, intercalated between the graphene and its substrate. It has already been demonstrated in section 4.3.2, that oxygen intercalation is accompanied by increase in surface corrugation as well as enhanced p-doping of the graphene. Locally enhanced accumulation of negatively charged intercalates induce a reduction of the Fermi level, that is, enhanced p doping in the graphene. Hence, a random distribution of oxygen intercalates underneath the decoupled graphene sheet seems to be the most probable reason for the observed strong positive correlation between charge disorder and topography.

4.5 Conclusion

In conclusion, we have presented scanning probe measurements on a sample of ex-situ grown graphene on iridium (111) of intermediate coverage. Unlike the corresponding pristine system prepared in UHV, the present system consists of graphene that is decoupled from the influence of the iridium substrate by the natural intercalation of oxygen molecules under ambient conditions. These molecules enter at the free edges of the graphene and propagate along local delaminations called wrinkles which are seen to act as tunnels for their propagation. We find an increase in positive doping on decoupling which confirms the role of the oxygen molecules in inducing this doping. The positive doping is found to disappear almost completely on the wrinkles where the graphene-substrate distance is maximum. Doping inhomogeneities on decoupled graphene are further investigated by STS which show a strong positive correlation with topography measured in STM. The inhomogeneous distribution of negatively charged oxygen intercalates underneath the graphene is identified as the most probable reason for this charge disorder and its strong signature in topography. KPFM measurements of the corresponding distribution of V_{CPD} in decoupled graphene present ambiguous results which calls for the necessity for further measurements.

Chapter 5

Disorder and Screening in Graphene Devices

Contents

5.1 Introduction **139**
5.2 Charge Carrier Transport in Graphene **140**
5.2.1 Sample Description and Experimental Method 141
5.2.2 Electric Field Effect 143
5.2.3 RPA-Boltzmann Conductivity 147
5.3 Local Field Effect with Scanning probe microscopy **147**
5.3.1 Experimental Method 148
5.3.2 Contact Potential Difference with KPFM 149
5.3.3 Tunneling Spectroscopy on graphene 154
5.3.4 Local gating with the tip 155
5.3.5 Tunneling Spectroscopy at different carrier density: The Experiment . 162
5.4 Electron-Hole Puddles in Graphene **167**
5.4.1 Imaging Electron-Hole Puddles 168
5.4.2 Charge Disorder with Point to Point Tunneling Spectroscopy 170
5.4.3 Gradual evolution of Charge disorder with Carrier Concentration . . . 177
5.4.4 Correlations at Different carrier densities 184
5.5 Conclusion **191**

5.1 Introduction

In Chapter 2, we considered the unusual screening properties of monolayer graphene from a purely theoretical point of view. In the absence of interactions, the low energy quasiparticle

spectrum in graphene is purely Dirac like. Switching on these interactions will induce changes in this linear dispersion [154][155][156]. In intrinsic graphene [1], the changes are quite remarkable as the Fermi liquid model for quasiparticles is no longer applicable [154]. The low energy dispersion is profoundly non-linear with the Dirac cone developing an inward curvature as has been reported in transport measurements of effective mass in suspended graphene [60] and in ARPES measurements on free standing graphene on SiC [157]. However, for extrinsic graphene, which encompasses the vast majority of samples prepared in labs for practical device applications, the Fermi liquid model holds true as any kind of doping will induce generic Fermi liquid behaviour. In this case, electron-electron interactions just renormalize the quasiparticle dispersion keeping the linear structure intact [158][154].

These many body interaction effects are well described by the dielectric function of the system which we have studied in detail in section 2.3. This function introduces an important length scale in the problem : the Thomas-Fermi screening length $1/q_{TF}$ which sets the relevant length scale for many body interactions. Whereas in 2D electron gases or bilayer graphene having a parabolic dispersion relation, q_{TF} is independent of carrier concentration, the case of SLG is markedly different. Here, the screening length changes with carrier concentration that can be easily controlled in gated graphene devices. Hence for a given disordered impurity potential, created by random charge impurities in the substrate, the correlations in the screened potential possess an amplitude and spatial extent that both depend on the carrier density. Or equivalently, the doping inhomogeneities induced by the disordered potential change with the gate potential, a fact that is often neglected.

By combining macroscopic transport with *in situ* scanning probe microscopy (AFM + STM) at dilution temperatures, we investigate this screened Coulomb impurity problem in exfoliated graphene devices on SiO_2. Transport will give us an overall characterization of the bulk electronic properties of the sample and in principle should be sufficient to predict the scenario at a local scale, provided the model of scattering by random charge impurities holds true. Hence, combining and correlating the local measurements with the macroscopic characterizations will rigorously test the validity of this model as well as enable a deeper understanding of the problem.

5.2 Charge Carrier Transport in Graphene

In this section, we consider the macroscopic electronic properties of a sample of exfoliated single-layered graphene on SiO_2/Si substrate by means of transport measurements in a two-probe configuration. Carrier transport in any system depends on the mobility of its charge carriers which, in the case of practical graphene samples, is primarily limited by scattering from random

[1] It is undoped or ungated graphene with n and $E_F = 0$ homogenously throughout. It is a theoretical construct. Very "clean" graphene, free from the influence of substrate impurities, like suspended graphene, comes close to this theoretical limit.

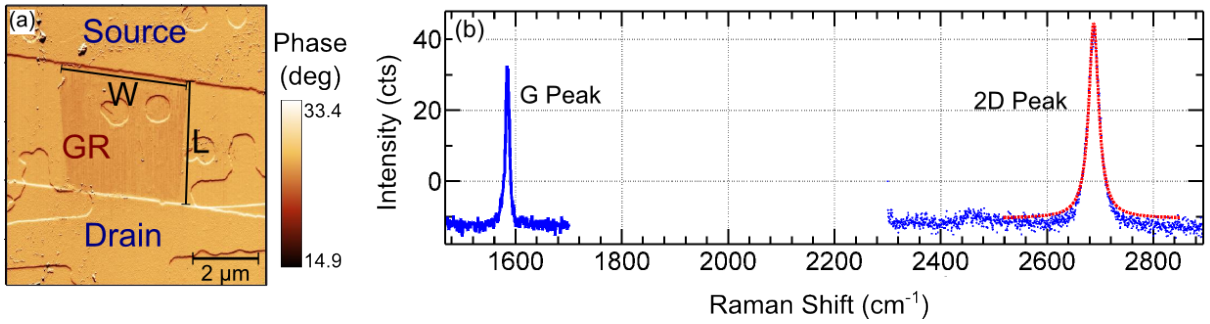

Figure 5.1: Sample Description and Raman Characterization. (a) Device geometry. Phase signal image of contacted monolayer graphene, acquired ex-situ in tapping mode AFM. [$L = 4.3\,\mu$m and $W = 4.2\,\mu$m]. (b) Raman Spectrum of flake (blue line). 2D peak at $2687\,\mathrm{cm}^{-1}$ with Lorentzian fit of width $\Gamma_{2D} \sim 23\,\mathrm{cm}^{-1}$ (red dashed line). G peak position $\sim 1584\,\mathrm{cm}^{-1}$ with line-width $\Gamma_G \sim 7.5\,\mathrm{cm}^{-1}$.

charge impurities [29]. This leads to a constant mobility at high carrier densities and a sample dependent minimum conductivity as explained in section 2.4.2. The other scattering mechanisms that have been pointed out are short range scattering from defects [159] leading to sub-linear conductivity at high n, scattering by graphene phonons [160], substrate surface polar phonon scattering [161], midgap states [162] and local curvature induced gauge fields [62]. However, a vast majority of experiments show the scattering from random charge impurities to be the dominant mechanism determining carrier transport in graphene.

Assuming this is true, it is possible to explain all the important features of carrier dependent conductivity in graphene by just two parameters: (a) concentration of charged impurities in the substrate, n_{imp} and (b) average distance, d, of these impurities from the plane of the graphene sheet (section 2.4.2). In this section, we experimentally analyze the field effect in a graphene device to recover these two fundamental quantities.

5.2.1 Sample Description and Experimental Method

Our sample constitutes of a single-layerd graphene flake prepared by the process of mechanical exfoliation and contacted using the mechanical shadow mask technique as described in section 1.3. Out of seventy samples prepared using this process, sixteen were measured. While the starting samples had a single contact and were multi-layered, the last four were single-layered with two isolated electrical contacts. The final sample measured was by far the best in terms of mobility (factor of two improvement) and interface transparency (section 1.3.5). Hence, we mainly present measurements on this final SLG sample while results on a multi-layered flake has been included in the appendix.

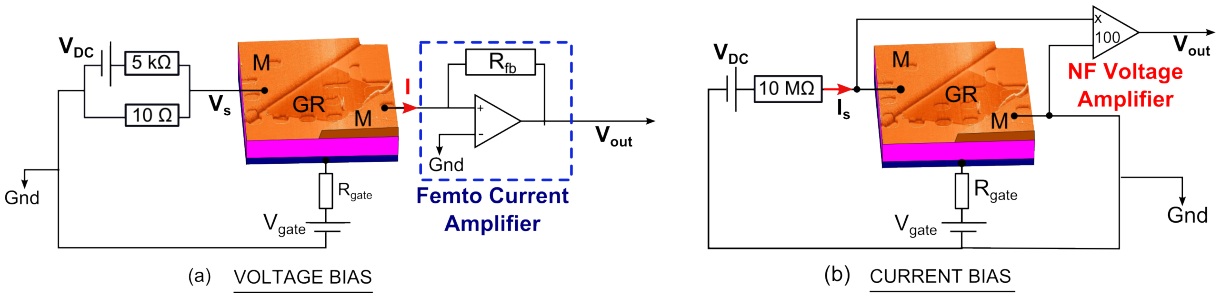

Figure 5.2: Configuration for two probe measurement of resistance of sample by (a) voltage biasing and (b) current biasing. [GR = graphene on SiO_2(285 nm)/Si substrate, M = Metal].

Sample Description

Figure 5.1(a) shows the AFM (phase) image of the contacted graphene flake that forms the subject matter of this chapter. The metal contacts labelled 'Source' and 'Drain' are made of Ti/Nb/Au (1.5 nm/10 nm/2 nm). Details of the sample fabrication procedure together with the reasons for the choice of contact metals have been presented in section 1.3. The holes in the substrate represent binary code markers that are essential for locating the sample in complimentary scanning probe measurements (section 3.5.2). These holes are very shallow, about 10 nm deep and 750 nm in diameter and hence the graphene follows their profile rather than being suspended over them.

Figure 5.1(b) shows the Raman spectrum of the graphene prior to contacting. The Lorentzian profile of the 2D peak with width $\Gamma_{2D} \sim 23\,\mathrm{cm}^{-1}$ proves that the flake is single-layered (section 1.3.2). From the combined observation that (a) the intensity ratio beween the 2D peak and the G peak is about $1.4 < \mathrm{IR}_0 \approx 3$, (b) the position of the G peak is $1584\,\mathrm{cm}^{-1} > \mathrm{G}_0 \approx 1582\mathrm{cm}^{-1}$ and (c) the width of the G peak is $7.5\,\mathrm{cm}^{-1} < \Gamma^0_{\mathrm{G}} \approx 16\,\mathrm{cm}^{-1}$, where $(\mathrm{IR}_0, \mathrm{G}_0, \Gamma^0_{\mathrm{G}})$ indicate the respective quantities in undoped graphene, we can conclude that the flake was already doped by the impurity atoms in the substrate prior to deposition of metal contacts. Further, the 2D peak position of about $2687\,\mathrm{cm}^{-1} > 2\mathrm{D}_0 \approx 2685\,\mathrm{cm}^{-1}$, where $2\mathrm{D}_0$ is the corresponding position in the undoped case, tells us that the nature of doping is p-type [30][34]. The presence of any defect would have been indicated by a peak at about $\sim 1350\,\mathrm{cm}^{-1}$. Unfortunately, spectrum in this range was not measured.

Experimental Method

Figure 5.2(a) and (b) show the two main configurations used to measure the two-probe resistivity of the sample.

1. Voltage Bias: A DC voltage V_{DC} was applied to one of the metal contacts acting as the 'Source' while the other contact, acting as the 'Drain' was maintained at ground potential.

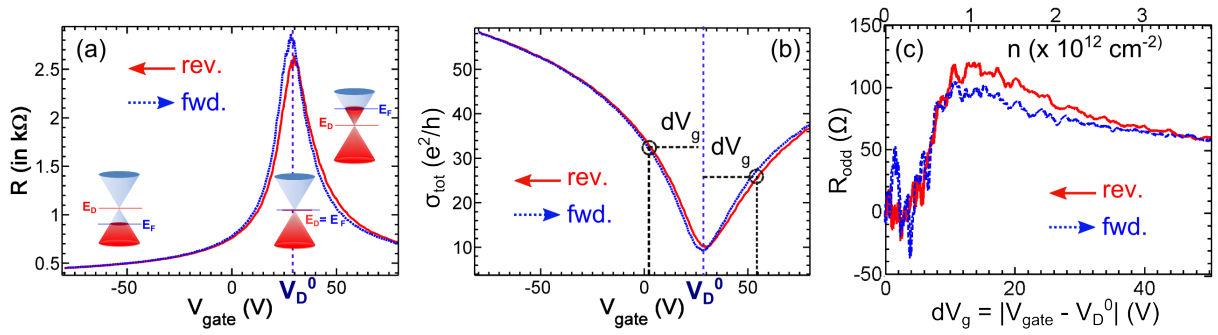

Figure 5.3: Electric field effect in monolayer graphene. (a) Two probe resistance vs backgate voltage V_{gate} for forward and reverse sweeps (maximum slew rate = 30 mV/s), measured at 130 mK. The schematics indicate the position of the Fermi energy E_F wrt. the Dirac point E_D at different V_{gate}. V_D^0 indicates the Charge neutrality point. (b) Two-probe conductivity $\sigma_{tot} = (L/W)/R$ vs V_{gate}. (c) Asymmetry between electron and hole carriers. R_{odd} characterizes this asymmetry, see text.

The two resistors in series to V_{DC}, provide a voltage division by factor 500 to reduce voltage noise. The current is measured from the 'Drain' using a variable gain ($10^3 - 10^{11}$ V/A), low noise current amplifier from Femto [163]. For the measurements presented in this chapter $V_s = 5$ mV and the gain used in the current amplifier was usually 10^5 unless otherwise mentioned. A current density exceeding 3.6×10^{12} A/m^2 was found to be unsafe for the flake, hence V_{DC} was chosen accordingly.

2. Current Bias: In some cases, current biasing was also used to measure the two probe resistance of the sample. Figure 5.2(b) illustrates how this was implemented in our setup. A DC voltage in series with a high resistance $R = 10$ MΩ served as the current source. The voltage difference between the two contacts was measured using a NF Voltage Amplifier [164].

The backgate voltage V_{gate} was applied via a very high resistance $R_{gate} \sim 100$ MΩ. This was done to protect the gate against accidental voltage spikes/jumps and to protect the cryostat in case of defective gate. The room temperature ground was used as the overall ground reference.

5.2.2 Electric Field Effect

The electric field effect in graphene allows tuning its carrier concentration by means of changing a capacitively coupled external voltage V_{gate} [165]. As is usually the practice, V_{gate} is connected to the bottom, highly doped Si layer of the Si/SiO_2 substrate which therefore forms the backgate. By changing V_{gate}, we can continuously tune the relative position of the Dirac point E_D wrt. the Fermi level E_F such that the latter gradually changes its position from the valence band up into the conduction band (schematics in Figure 5.3(a)). To measure the field effect in graphene, the

gate voltage was gradually changed and the corresponding two probe resistance was measured in a manner described above. Figure 5.3 shows the field effect measured in the current device in a voltage bias configuration. The gate voltage at which the conductivity of the sheet is minimum corresponds to the situation where E_F is aligned with the Dirac point (E_D) leading to 'charge neutral' graphene. Hence this gate voltage V_D^0 is called the 'Charge Neutrality Point' or CNP. For $V_{gate} > V_D^0$, the graphene is doped with electrons whereas for $V_{gate} < V_D^0$, hole doping occurs. Due to presence of intrinsic doping, from impurities on the substrate and perhaps the metal contacts, V_D differs from zero and $\sim 30\,\mathrm{V}$ in this case, which corresponds to a hole doping of $\sim 2.3 \times 10^{12}\,\mathrm{cm}^{-2}$.

Hysteresis and Asymmetry

There exists a small but finite hysteresis between forward and reverse sweeps. Presence of polar water molecules in the Graphene/SiO_2 interface could be a reason for this [166]. This is not so surprising since the cleaning of the substrate by oxygen plasma renders the surface hydrophilic (section 1.3.1).

Additionally, we notice that there is a prominent asymmetry between the electron and hole conductivities. We can characterize this asymmetry in the following manner.

$$R_{odd} = \frac{[R(V_D^0 + dV_g) - R(V_D^0 - dV_g)]}{2} \tag{5.2.1}$$

where $dV_g = |V_{gate} - V_D^0|$. Figure 5.3(c) shows R_{odd} as a function of both dV_g and the corresponding carrier concentration n. We find that for $n < 8 \times 10^{11}\,\mathrm{cm}^{-2}$, R_{odd} fluctuates about zero and for higher n, stabilizes to a positive value of $\sim 60\,\Omega$ implying a higher contact resistance at electron doping than in case of hole doping. We will find later that this limiting carrier concentration approximately corresponds to the impurity concentration in the substrate.

Theoretically, the scattering cross-sections off charged impurities for electrons and holes are different and hence in this respect, the transport is expected to be asymmetric for these charge carriers of opposite polarities [167]. Novikov predicted a value of $\mu_{el}/\mu_h = 0.37$ for an impurity charge $Z = 1$. However, this asymmetry is expected to reduce when screening by conduction electrons is taken into account. Chen et al. [61], experimentally found this ratio to be 0.83 ± 0.01. In our case $\mu_{el}/\mu_h = 0.9 \pm 0.2$. The method adopted to extract the mobilities is discussed shortly.

Another important reason for this asymmetry could be due to the metal contacts. By the mechanism of charge transfer, the metal contacts pin the carrier density in graphene underneath them [110, 168]. In case of Ti, as is the case in the present sample, this doping is p-type. This leads to the formation of a p-n junction all along the interface at overall negative doping by V_{gate} and p-p junction at overall positive doping. This provides the reason for positive value of R_{odd} at high n.

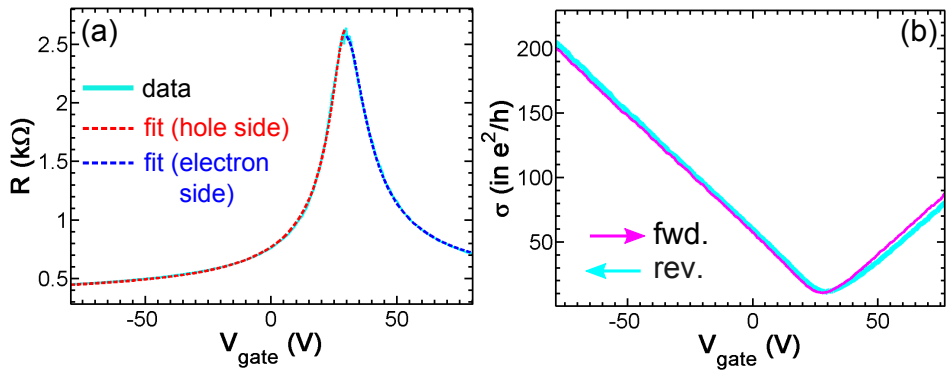

Figure 5.4: Field effect after subtracting contact resistance. (a) Field effect curve for reverse sweep together with fit according to Eq.(5.2.2), electron and hole side fitted separately. Fit parameters: Series resistance $R^h_{series} = 325\,\Omega$, mobility $\mu^h = 6190\,\mathrm{cm^2V^{-1}s^{-1}}$ and intrinsic doping $n^*_h = 4.45 \times 10^{11}\,\mathrm{cm^{-2}}$ (hole side); $R^{el}_{series} = 409\,\Omega$, $\mu^{el} = 5305\,\mathrm{cm^2V^{-1}s^{-1}}$ and $n^*_{el} = 5.55 \times 10^{11}\,\mathrm{cm^{-2}}$ (electron side) . (b) Two-probe conductivity of graphene after subtracting the corresponding series resistance, R^h_{series} and R^{el}_{series}, from the hole and electron side respectively.

Eliminating contact resistance

Figure 5.3(b) apparently shows the conductivity of the sample to vary non-linearly with gate V_{gate} for $|V_{gate} - V^0_D| \gg 0$. However, this is only the two-probe conductivity, and has contributions from the wires leading up to the sample as well as the metal graphene contact resistances. We can write this additional resistance as $R_{series} = 2(R_{wire} + R_c)$ where $R_{wire} \approx 77\,\Omega$ is the wire resistance (measured at room temperature) and R_c is the graphene-metal contact resistance. The resistance of the metal leads is zero because of their superconducting nature with $T_c \approx 7.2\,\mathrm{K}$ [2] which is well above the temperatures at which the measurements are conducted $T < 4.2\,\mathrm{K}$. Therefore, the resistance shown in Figure 5.3 is $R = R_{GR} + R_{series}$ where R_{GR} is the resistance of the graphene. Using the following procedure we can roughly estimate R_{series} and eleminate it to get the actual conductivity of graphene.

Away from V^0_D, there will be only one type of carriers, and conductivity will be given by $\sigma = ne\mu$ where n is the carrier concentration (either electrons or holes). As $V_{gate} \to V^0_D$, the system will break up into electron and hole puddles. So, in this case, the carrier concentration will not be zero but equal to a finite residual carrier density n^* which had been introduced in section 2.4.1. Assuming carrier mobilities to be the same, $\sigma = (n_e + n_h)e\mu = n^*e\mu$. Combining these two limiting cases in a single expression and incorporating R_{series}, we get [169]:

$$R = R_{series} + \left(\frac{L}{W}\right) \frac{1}{\mu\sqrt{(n^*e)^2 + \left[C_g\left(V_{gate} - V^0_D\right)\right]^2}} \tag{5.2.2}$$

where the number of carriers induced by V_{gate} is $n = C_g\left(V_{gate} - V^0_D\right)$ and $C_g = K\epsilon_0/t$ is the gate

[2] Carbon thermometers used were not precise in this range

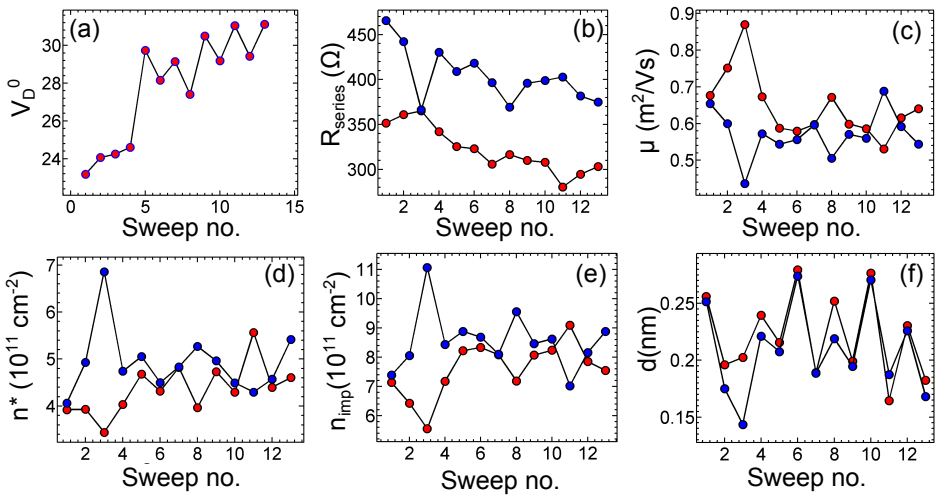

Figure 5.5: Evolution of the different transport parameters with time. V_D^0 is the charge neutrality point, R_{series} is the series resistance, μ is the mobility, n^* is the induced residual charge density, n_{imp} is the impurity concentration and d is the distance of impurities from the graphene plane. The thirteen sweeps have been acquired over seventeen days at temperature 4 K or 130 mK. Parameters extracted from fit to hole side indicated by red circles and electron side by blue circles.

capacitance. Here $K = 3.9$ is the dielectric constant of the SiO_2, $\epsilon_0 = 8.85 \times 10^{-12}\,\mathrm{Fm}^{-1}$ is the vacuum permittivity and $t = 285\,\mathrm{nm}$ is the thickness of SiO_2 in the substrate.

Because of the asymmetry, it is not possible to fit the conductivity for the full range of V_{gate} using the above expression. However separately fitting the hole and the electron conductivity with (R_{series}, μ, n^*) as fit parameters is possible. Figure 5.4(a) shows the fit to the above equation done in this way. The mean values of the series resistance for the hole and electron side were found to be $R^h_{series} = 320\,\Omega$ and $R^{el}_{series} = 400\,\Omega$ respectively.

The conductivity of graphene is then obtained by subtracting out R^{el}_{series} and R^h_{series} from the electron and hole sides respectively i.e. $\sigma_{el} = \left[\frac{1}{\sigma^{el}_{tot}} - R^{el}_{series}\left(\frac{W}{L}\right)\right]^{-1}$ and similarly for the hole side. This has been shown in Figure 5.4(b). The conductivity of graphene, so obtained, shows a linear dependence on V_{gate} on both sides with minor deviations in some cases. This linear dependence is in accordance with the model for Coulomb scattering by random charge impurities (section 2.4.2).

We note here that a gradual decrease of both resistances i.e. R^{el}_{series} and R^h_{series} was observed during the course of measurement (Figure 5.5(c)) while their difference $(R^{el}_{series} - R^h_{series}) = (80 \pm 30)\,\Omega$ fluctuates about the mean value. This seems to suggest a gradual improvement of interface transparency with time.

5.2.3 RPA-Boltzmann Conductivity

The RPA-Boltzmann model, that we discussed in section 2.4.1, predicts a constant mobility at high carrier densities for random-charge impurity scattering, described by Eq.(2.4.6). From this equation, we can relate this constant mobility to the concentration of charge impurities in the substrate n_{imp} i.e.

$$\mu = 20\left(\frac{e}{h}\right)\frac{1}{n_{imp}}. \tag{5.2.3}$$

This allows us to obtain n_{imp} from the previously extracted mobility. Knowing (n_{imp}, n^*), we finally invoke the self-consistency relation Eq.(2.4.17), to obtain the value of d (distance of impurities from the 2D plane of graphene) that best satisfies it.

Hence, from the measurement of conductivity as a function of carrier concentration, we are able to extract all the important parameters that determine the carrier dynamics in the system i.e. $V_D^0, \mu, n^*, n_{imp}, d$. In Figure 5.5(a)-(f), all these quantities have been plotted so as to track their evolution with time during the course of the experiment. Although, initially conditions changed, towards the end, they were more steady. In the following table, we enumerate the mean values of these different quantities extracted from transport for electron and hole doped graphene.

Carrier	R_{series} (Ω)	V_D^0 (V)	μ ($\mathrm{cm^2V^{-1}s^{-1}}$)	n_{imp} ($10^{11}\,\mathrm{cm^{-2}}$)	n^* ($10^{11}\,\mathrm{cm^{-2}}$)	d (nm)
Electron	400	29 ± 1	5706 ± 600	8.56 ± 0.99	4.92 ± 0.69	0.21 ± 0.03
Hole	320	29 ± 1	6450 ± 900	7.61 ± 0.90	4.36 ± 0.54	0.22 ± 0.04

Table 5.1: Summary of Parameters extracted from Transport. R_{series} is the series resistance due to the connecting wires leading up to the sample and the metal-graphene contact resistance, V_D^0 is the charge neutrality point, μ is the mobility of graphene, n_{imp} is the concentration of impurities, n^* is the residual charge concentration and d is the average distance of the charge impurities from the graphene plane.

5.3 Local Field Effect with Scanning probe microscopy

The transport measurements that we have considered so far have helped in looking into the bulk electronic properties of the sample which are primarily determined by carriers at the Fermi energy. In this section, we go beyond this by implementing the techniques of Kelvin Probe Force microscopy (KPFM) (section 3.2.3) and Scanning tunneling spectroscopy (STS) (section 3.2.1). This allows us to look into the details of the energy dispersion for energies ranging from the valence band to the conduction band with a high resolution both energetically and spatially.

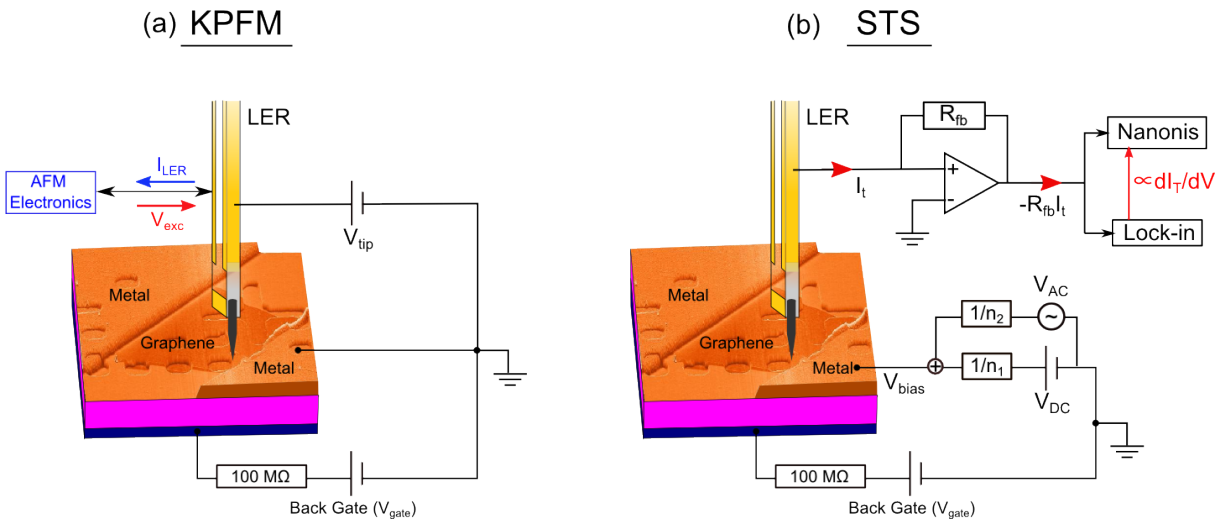

Figure 5.6: Experimental configuration for (a) CPD measurement with KPFM and (b) STS.

Changing the backgate will enable us to look into how the band structure of graphene responds to this change.

While KPFM acts as a tool to track the change in work-function as a function of V_{gate} without itself inducing any change, the resolution offered is inferior to STS because of the large tip-sample distance ($d_{KPFM} \sim (10 - 20)\,\text{nm} \gg d_{STS}$). On the other hand, STS is capable of incredibly superior resolution but the close proximity of the tip to the graphene complicates the interpretation of the tunneling conductance spectrum. Combining the two techniques will enable us to overcome the individual limitations and benefit from their combined advantages, eventually leading to a better understanding of the problem.

5.3.1 Experimental Method

The experimental arrangement for performing KPFM and STS on the gated single-layered graphene device have been shown in Figure 5.6. In particular, we note that:

1. **KPFM:** A DC voltage is applied to the tip V_{tip} via the LER electrode connected to it whereas the other electrode is used for AFM operation. The sample is maintained at ground (RT). The CPD is measured in the manner described in section 3.2.3.

2. **STS:** A DC voltage V_{DC}, sometimes superposed with an AC modulation V_{AC} is supplied to the connected graphene flake via voltage divisions n_1 and n_2 respectively while the tip is maintained at ground (RT) via the ground of the tunneling current amplifier.

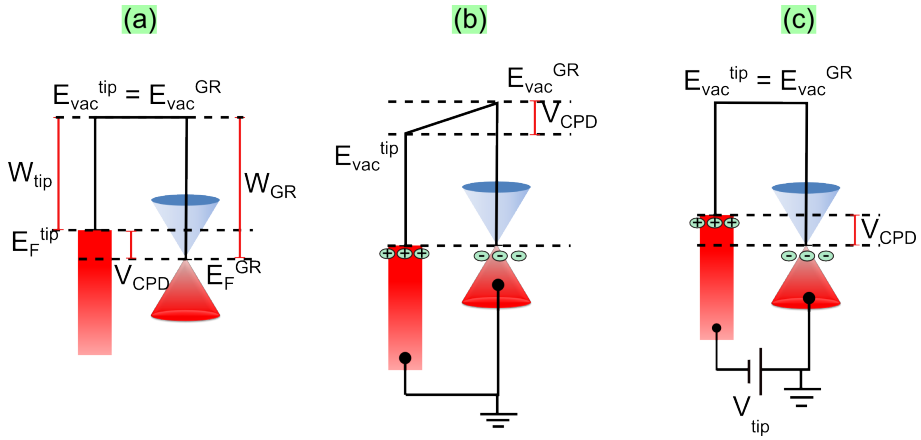

Figure 5.7: Schematics explaining V_{CPD} measurement on graphene. (a)-(c) Band structure schematics showing band alignment between AFM tip and undoped graphene at charge neutrality ($V_{gate} = V_D^0$). (a) Tip and sample not in electric contact. (b) Tip and sample in electric contact that causes Fermi level in tip and graphene to align and corresponding vacuum levels to E_{vac}^{tip} and E_{vac}^{GR} to misalign by an amount equal to the V_{CPD}. (c) The misalignment in vacuum level is compensated by the applying a voltage to the tip equal to $-V_{\text{CPD}}$.

5.3.2 Contact Potential Difference with KPFM

The working principle and measurement of contact potential difference V_{CPD} between the sample surface and the tip by KPFM (force spectroscopy), has already been explained in section 3.2.3. In the case of graphene, V_{CPD} will change with V_{gate}. This is because, changing the carrier concentration by V_{gate} implies shifting the entire band-structure of graphene (i.e. Dirac point position E_D and vacuum energy E_{vac}^{GR}) wrt. its Fermi energy E_F^{GR}, thus causing a change in its work-function $W_{GR} = E_{vac}^{GR} - E_F^{GR}$ and consequently a change in V_{CPD} [Eq.(3.2.24)]. Figure 5.7(b) demonstrates the measurement of V_{CPD} in graphene at different V_{gate} by KPFM. It is quite straight-forward to show then that

$$V_{\text{CPD}} = -V_{tip} = W_{GR} - W_{tip} = \Delta + E_D. \tag{5.3.1}$$

where $\Delta = W_{GR}^0 - W_{tip}$ i.e. the work-function mismatch between undoped graphene W_{GR}^0 and the tip. Using Eq.(2.2.21), we can write down the dependence of E_D on V_{gate} (with E_F^{GR} as reference).

$$\begin{aligned} E_D &= -\hbar v_F \,\text{sgn}(n)\sqrt{\pi|n|} = -\hbar v_F \,\text{sgn}(V_{gate} - V_D^0)\sqrt{\frac{\pi K \epsilon_0}{et}(V_{gate} - V_D^0)} \\ \Rightarrow E_D &= -\gamma e \,\text{sgn}\left(V_{gate} - V_D^0\right)\sqrt{|V_{gate} - V_D^0|} \end{aligned} \tag{5.3.2}$$

where $\gamma = \hbar v_F \sqrt{\frac{\pi K \epsilon_0}{e^3 t}} \sim 0.035\,\text{V}^{1/2}$, V_D^0 is the charge neutrality point which for the present sample is 30 V, $K = 3.9$ is the dielectric constant for SiO_2 and $t = 285$ nm is its thickness in the substrate, $v_F = 1.1 \times 10^6$ m/s is the Fermi velocity of graphene on SiO_2 [170].

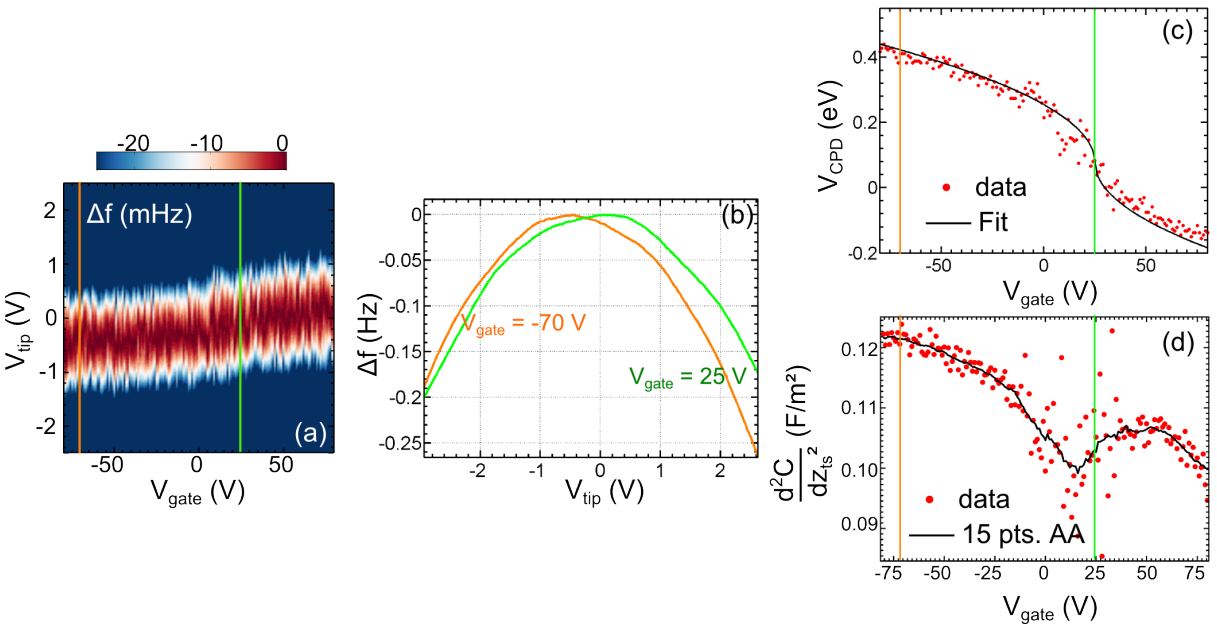

Figure 5.8: Variation of V_{CPD} with backgate. (a) Frequency shift Δf as a function of backgate V_{gate} and tip voltage V_{tip}. The Δf vs V_{bias} parabolic curves at each V_{gate} have been shifted vertically such that $\Delta f = 0$ at the maximum position. (b) Δf vs V_{tip} along the vertical cuts indicated in (a) at high (orange) and low carrier densities (green). (c) Variation of CPD with backgate. Red dots indicate data points and black solid line indicates fit to Eq.(5.3.1). Fit parameters $\Delta = 80\,\mathrm{meV}$ and $V_D^0 = 25\,\mathrm{V}$. (d) Variation of curvature of the Δf vs V_{tip} parabolas as a function of V_{gate}. Red dots indicate data points while black solid line indicates an average over 15 adjacent points.

Measurement of CPD as a function of backgate

To measure the variation of the local contact potential difference of graphene wrt. the scan probe (tungsten tip mounted on LER) with backgate, the following procedure is adopted.

1. The tip is approached close to the surface in FM-AFM mode with setpoint parameters $\Delta f_{set} = -1\,\mathrm{Hz}$, $A_{set} = 500\,\mathrm{pm}$ and $V_{tip} = 0\,\mathrm{V}$. After stabilization of the tip-sample distance, z-regulation is turned off and tip retracted by about 5 nm from this position. This causes the frequency shift Δf to drop to zero due to negligible contribution from Van der Waals force.

2. The voltage applied to the tip V_{tip} is gradually ramped up leading to a finite Δf due to the resulting electrostatic interaction between the tip and the sample.

3. Parabolic dependence of Δf on V_{tip} is measured after adjusting the back-gate voltage to the desired value. By repeating this tip voltage sweep at several gate voltages, we get a complete gate map of Δf.

This measurement was performed at base temperature of 130 mK with minimum thermal drift [3]. This enabled us to stabilize the tip at about 10 nm above the sample surface for a total duration of about 3.5 hrs of the experiment, without any z-regulation. The measurement location was chosen to be about 1 μm away from one of the metal-graphene interfaces.

Assuming negligible contribution from Van der Waals interaction, the frequency shift of the scanning resonator due to the electrostatic tip-sample interaction is given by Eq.(3.2.26). This equation gives the condition that $\Delta f = 0$ at $V_{tip} = -V_{\mathrm{CPD}}$ implying a perfect compensation of the work-function mismatch induced electric field by the tip voltage. In the experiment, however, since Δf is adjusted to zero only once in the beginning under the conditions $(V_{gate}, V_{tip}) = 0\,\mathrm{V}$, the maximum value of Δf is found to vary slightly from 25 mHz to -10 mHz. This is a natural consequence of the variation of the maximum position of the parabolas i.e. $-V_{\mathrm{CPD}}$ with V_{gate}. To remove this artifact and recover the above condition, the individual parabolic curves are vertically shifted. Figure 5.8(a) shows the color plot of Δf as a function of V_{gate} and V_{tip} after this adjustment. We clearly see the position of maximum Δf to change from negative to positive tip voltages as V_{gate} is increased, implying a Fermi level moving from the valence band into the conduction band as expected.

To extract V_{CPD}, the individual Δf vs V_{tip} curves are fitted to a second order polynomial. The position of the maximum of this polynomial gives V_{CPD} [4] (Figure 5.8(c)). We see that this can be well fit with Eq.(5.3.1) with V_D^0 and Δ as the free parameters. This gives us $V_D^0 \sim 25\,\mathrm{V}$ and $\Delta \sim 80$ meV. The value for charge neutrality, although not exactly the same as measured in transport, comes reasonably close. This discrepancy could be due to measurement on a locally doped region that causes charge neutrality to be achieved at a gate voltage which is different from the bulk value. We additionally note that unlike at high carrier densities where the V_{CPD} data is less noisy and have a better agreement with Eq.(5.3.1), at low carrier densities $n < 8{\times}10^{11} cm^{-2} \sim n_{imp}$ (section 5.2.3), the data points are rather scattered. This is probably pointing to electron-hole puddles at low carrier concentrations which cause local random deviations from the gate dependence of the charge carrier concentration as assumed in Eq.(5.3.1).

Along with V_{CPD}, the curvature of the Δf vs V_{tip} parabolas also change with the backgate. This curvature is $\propto \frac{d^2}{dz_{ts}^2}$ [Eq.(3.2.26)] where C is the tip-sample capacitance and z_{ts} is the tip-sample distance. Figure 5.8(d) shows the variation of $\frac{d^2C}{dz_{ts}^2} = -\frac{4k}{f_0}p_2$ with backgate voltage. p_2 is the coefficient of the second order polynomial to which the data is fitted. The reason for this observed variation is not very clear. At backgate voltages away from charge neutrality, with plenty of charge carriers, graphene strongly screens this potential such that the tip-sample capacitor model assumed in Eq.(3.2.26) holds good. But close to charge neutrality, with very few carriers, screening by graphene is very weak and the probe will sense this potential more directly. This could account for the drop in $\frac{d^2C}{dz_{ts}^2}$ as $V_{gate} \to V_D^0$. However, it does not explain

[3] This was verified by AFM imaging of the surrounding structures in the surface before and after measurement.
[4] This procedure produces the CPD dependence on backgate with the least noise

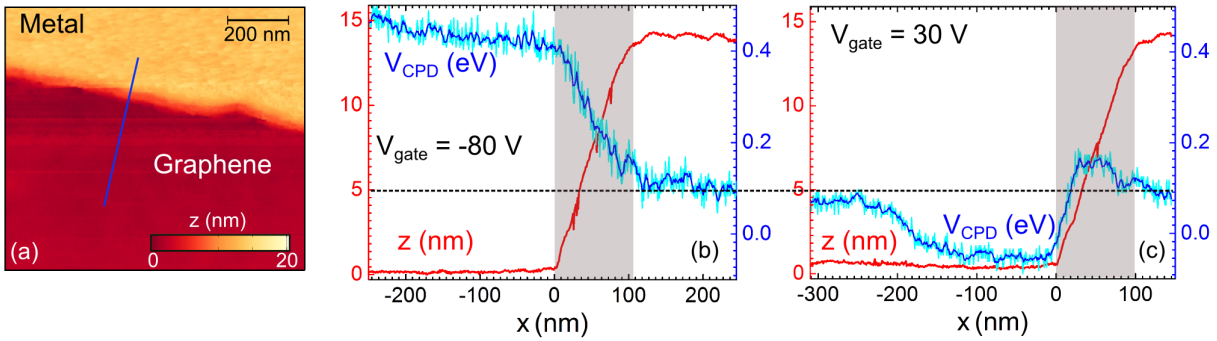

Figure 5.9: Change of V_{CPD} across the metal-graphene interface. (a) STM topograph of the metal-graphene interface. Imaging parameters: $I_t = 50\,\mathrm{pA}$, $V_{bias} = 0.8\,\mathrm{V}$, scan speed $= 50\,\mathrm{nm/s}$ at 130 mK. (b) Change of V_{CPD} and height profile across the metal-graphene interface at high hole doping $V_{gate} - 80\,\mathrm{V} \ll V_D^0$ and (c) at low carrier concentration $V_{gate} = 30\,\mathrm{V} \rightarrow V_D^0$. The grey window indicates the transition region between metal and graphene and the black dashed horizontal line runs along the V_{CPD} of the metal for a comparison between the two situations at high and low carrier doping.

the gradual decrease observed as V_{gate} is changed from negative to positive values. Eq.(5.3.1) also assumes an infinite extent of the graphene which is not the case. The probe will sense the electric field due to the backgate from the sides which might account for the linear background.

Local CPD change across the Metal-Graphene Interface

With this method of V_{CPD} detection by Kelvin probe, it is possible to measure the work-function mismatch between graphene and the metal contacts as well as measure how the local V_{CPD} gradually evolves across the interface. Figure 5.9 shows the change of V_{CPD} along the interface at high hole doping ($V_{gate} = -80\,\mathrm{V}$) and close to the charge neutrality point V_D^0 ($V_{gate} = 30\,\mathrm{V}$). To do this measurement, the tip-sample distance was adjusted at each point along the line running across the interface (blue line in sub-figure (a)) to the same set-point conditions as before at $V_{tip} = 0\,\mathrm{V}$. After this, the z-regulation was turned off and the tip lifted by 5 nm to perform the Δf spectroscopy. On completion of the measurement, the z-regulation was turned back on, tip approched and moved to the next point. This ensured a safe, reproducible and crash-free positioning of the tip as well as minimum drift in frequency shift during the course of the measurement.

At high hole concentrations (Figure 5.9(b)), we observe a higher V_{CPD} on the graphene than on the metal which is expected since the Fermi level in the graphene lies deep in the valence band. As the metal interface is approached, V_{CPD} decreases and stabilizes as soon as the tip moves fully on the metal. The transition in the V_{CPD} profile fully coincides with the transition in the height profile of the metal contact as indicated by the rectangular gray window. The broadening of the interface observed in the topography is predominantly due to the finite curvature of the tip apex,

as explained in section 1.3.4. On the graphene itself, V_{CPD} profile is not completely horizontal but possesses a gentle slope, which could imply a gradual decrease of p-doping as the interface is approached. Another plausible reason could be that close to the interface, the tip-sample force is shared between interaction with graphene and the metal which has a lower V_{CPD} and therefore produces a gradual decrease. However, this second reason is proven wrong by repeating this measurement near charge neutrality.

Figure 5.9(c) shows the simultaneous change of V_{CPD} and height profile across the metal-graphene interface at low carrier concentrations. Now V_{CPD} in the graphene is more or less aligned with V_{CPD} in the metal of about 110 meV. But the profile does not monotonically change from graphene to the metal anymore. There is a significant drop of about ~ 110 meV in the graphene close to the interface over a spatial width of ~ 150 nm before rising up on the metal. This implies that next to the interface, graphene is more n-doped than further away which is consistent with the observation at high hole doping. We can safely dismiss the possibility of the metal contributing to the tip-sample force close to the interface because if it were true, then we should have observed a gradual increase in graphene on approaching the metal contact which has higher V_{CPD} now. The presence of this relatively higher e-doping next to the interface is somewhat surprising as the titanium contacts are expected to induce a positive doping in the graphene (section 5.2.2). Another prominent difference with the high density situation is that V_{CPD} transition from graphene to metal is much more rapid in this case.

This measurement allows us to quantify the work-functions of the different materials involved. The average V_{CPD} of the metal contact (Au) is (110 ± 20) meV. If we assume the work-function of Au to be 4.83 eV [171], then this gives a tip work-function $W_{tip} = 4.72$ eV, which is within the range expected for tungsten. From the variation of V_{CPD} of graphene with back-gate (Figure 5.8), we can say that the work-function of graphene changes from (5.16 ± 0.02)eV at $V_{gate} = -80$ V to 4.58 eV at $V_{gate} = 80$ V [Eq.(3.2.24)].

The work-function mismatch between the upper gold surface of the metal contact and graphene at high hole doping is $\Delta W_{MG} = 330$ meV. If we assume that work-function of the Ti bottom layer of the metal electrode is approximately the same as this top layer, then we can crudely estimate the carrier transmission probability of the interface T using Landauer's approach [172]. In this approach, the contact conductance is understood by $G = 1/R_c = \left(\frac{4e^2}{h}\right) TM$, M being the number of quantum modes. For a graphene channel of width W, $M = \left(\frac{|\Delta W_{GM}|}{\pi \hbar v_F}\right) W$ [172]. This gives a transmission probability $T \sim 0.13$ at $V_{gate} = -80$ V if we cosider $R_c \sim 80\,\Omega$ as found from transport (section 5.2.2).

Summary of CPD measurements

From the measurements of contact potential difference by KPFM, we conclude the following.

1. For undoped graphene, the contact potential difference wrt. the tungsten tip is found to

be $V_{\mathrm{CPD}} = 80\,\mathrm{meV}$ at a single location. As we will see later, this value is not fixed but dependent on tip condition as well as spatial doping inhomogeneities.

2. Both the maximum position as well as the curvature of the Δf vs V_{tip} parabolic curves are found to change with backgate. V_{CPD} change with V_{gate} at a point in graphene follows the expected symmetric dependence given by Eq.(5.3.1) while the curvature shows a non-monotonic decrease from high hole to electron doping.

3. From the variation of V_{CPD} profile across the metal-graphene interface, we find a 150 nm broad region of significantly higher n-doping on the graphene, right next to the interface. This inhomogeneity is clearly observed as a step of 110 meV in the V_{CPD} profile at low overall doping while at high hole doping, it causes a gradual decrease in V_{CPD} towards the interface. This clearly reveals that inhomogeneities are magnified as the charge neutrality point is approached, completely consistent with expectations (section 2.4.2).

5.3.3 Tunneling Spectroscopy on graphene

Scanning tunneling spectroscopy provides an ingenious way to measure the local density of states of a given sample by simply aligning the Fermi level of a metallic tip (flat DOS), to the energy E at which DOS of the sample needs to be measured as discussed in section 3.2.1. This process is illustrated in the following Figure 5.10(a) for the simple case of undoped graphene.

When the voltage applied to the sample $V_{bias} = 0$, the Fermi level of the tip E_F^{tip}, graphene E_F^{GR} and the Dirac point E_D, are all perfectly aligned (Case 1 of Figure 5.10(a)). For the moment we consider the work-function mismatch between tip and graphene to be zero. Now, if we apply a positive bias voltage to the graphene wrt. the tip, we displace all the energy bands and the Fermi level in graphene downwards by an amount eV_{bias} wrt. E_F^{tip}. If we fix E_F^{GR} as our reference, then from this reference, it equivalently means that E_F^{tip} has moved up by eV_{bias} (case 2). Similarly, applying a negative bias means shifting E_F^{tip} downwards (case 3). Therefore, using [Eq.(3.2.9)], the tip-graphene differential tunneling conductance at $T = 0\,\mathrm{K}$ is given by

$$G(V_{bias}, T = 0\,\mathrm{K}) \propto \rho_{GR}(eV_{bias}) = \frac{2}{\pi\hbar^2 v_F^2} |eV_{bias} - E_D| \tag{5.3.3}$$

where ρ_{GR} refers to the DOS of graphene given by Eq.(2.2.19). The above equation suggests the minimum of the differential conductance to be zero and occurring at $eV_{bias} = E_D$, i.e. when E_F^{tip} is aligned with the Dirac point. However, the minimum conductance measured in STS experiments in graphene is never zero because of thermal smearing as well as smearing due to spatial doping disorder. Inducing charge carriers in graphene by means of the backgate V_{gate}, will change E_D [Eq.(5.3.2)] and consequently the position of this minimum. Figure 5.10(b) shows the functional dependence of the differential tunneling conductance $G_t(V_{bias}, T = 0)$ on V_{gate} and V_{bias}. For simplicity, we have assumed $V_D^0 = 0$ whereas in the present sample, it is about 30 V

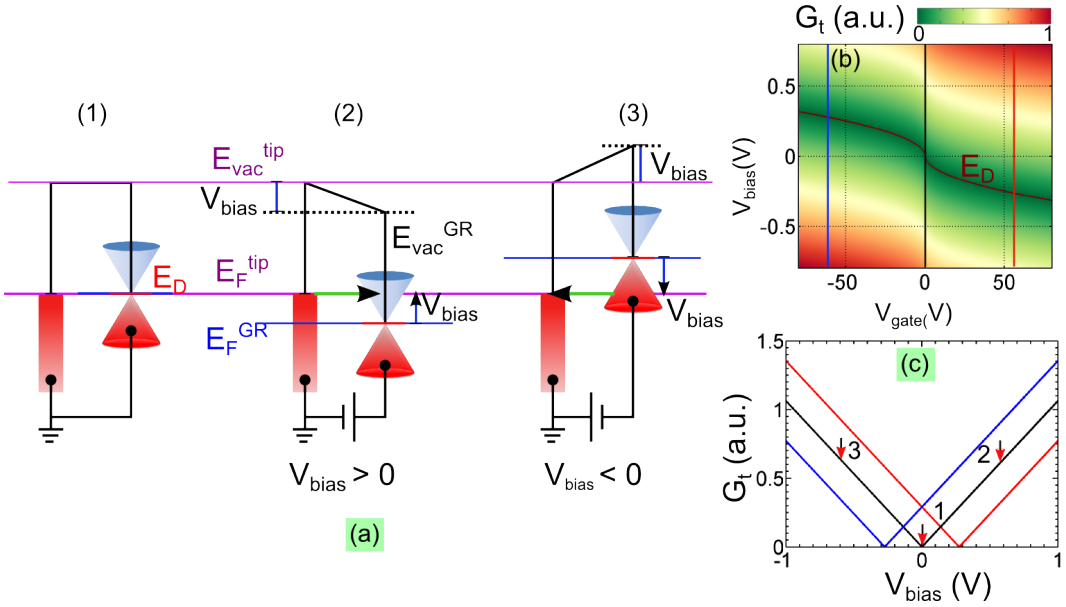

Figure 5.10: Schematic of STS on graphene at different carrier densities. (a) Band-structure schematics explaining the relative position of the Fermi level of undoped graphene wrt. the Fermi level of the metallic tip for varying bias voltage V_{bias} on the graphene, see text. (b) Calculated differential tunneling conductance G_t as a function of V_{bias} and V_{gate} according to Eq.(5.3.3) and Eq.(5.3.2). The 'maroon' line along the minimum of G_t gives E_D vs. V_{gate} according to Eq.(5.3.2). (c) G_t vs. V_{bias} at different V_{gate} along the vertical cuts indicated in (b). The arrows indicate the situation corresponding to case (1)-(3) in (a).

(table 5.1). The 'S' like dependence of E_D on V_{gate} is prominently visible as the locus of the minimum of the conductance curves for each V_{bias}, additionally indicated by the maroon line. The lines of constant carrier density run parallel to the V_{bias} axis.

5.3.4 Local gating with the tip

So far we have only considered the metallic tip as a measurement probe and completely ignored any effect that it might have on the graphene as a local gate. This issue was addressed in detail by S.K Choudhary et al. [173] and later on by Y. Zhao et al. [174]. In the latter case, the authors incorporated the additional effect of having a finite work-function mismatch between the tip and the graphene, thus significantly improving our understanding of the effect of the tip as a local gate. In this section, we first follow the reasoning of S.K. Choudhary et al., to derive the changes induced in the STS gate maps as a result of tip-gating. Later on, we will improve on these results with the help of Zhao et al.

If a voltage V_{bias} is applied to the graphene with the tip grounded, then the potential with which the tip gates the graphene is $-V_{bias}$. So the total carrier density induced by the combined gating of V_{gate} and V_{bias} is[5]

[5]Actually $n = \frac{K\epsilon_0}{et}[(V_{gate} - V_{bias}) - \beta V_{bias}]$. Since $\beta \gg 1$, we can approximately use Eq.(5.3.4) without

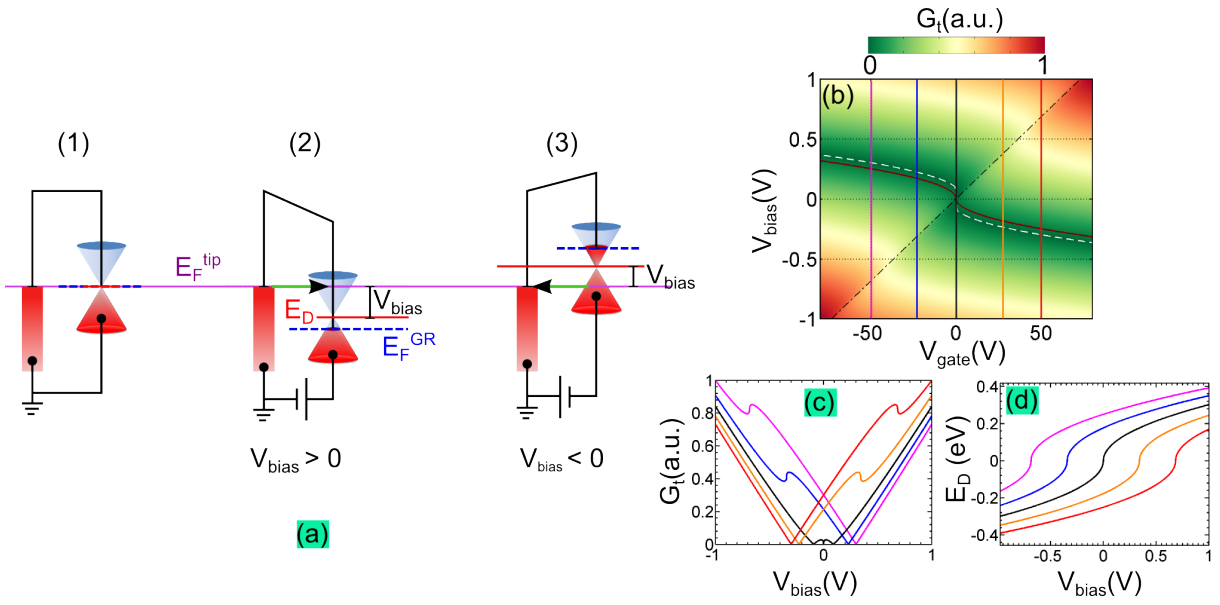

Figure 5.11: Effect of tip-induced gating in tunneling spectroscopy in graphene. (a) Schematic showing the position of the energy bands in graphene wrt. E_F^{tip} in the course of changing V_{bias}. (b) Calculated differential tunneling conductance G_t ($T = 0\,\mathrm{K}$) as a function of V_{gate} and V_{bias} ($z_{ts} = 1\mathrm{nm}$). Dirac point dependence (maroon line) without considering tip-induced gating [Eq.(5.3.2)], position of the primary minimum V'_{min} (white dashed line) and secondary minimum V''_{min} (black dashed line) [Eq.(5.3.7)] has been indicated. (c) G_t and (d) E_D as a function of V_{bias} at different V_{gate} along the vertical cuts indicated in (b).

$$n = \frac{K\epsilon_0}{et}\left(V_{gate} - \beta V_{bias}\right). \tag{5.3.4}$$

Assuming a parallel plate capacitor configuration, $\beta = t/z_{ts}K$, z_{ts} being the tip-sample distance. This approximation is quite reasonable. The authors in [173], have explicitly calculated the induced charge-density using a sphere-plane capacitor model and found that for a tip radius of about 30 nm and $z_{ts} = 1\,\mathrm{nm}$, the parallel plate model overestimates the charge induced by only 1%. Also, we must remember that the induced charge has been assumed to be of infinite extent for simplicity but this is not true. So, the results are valid only for the point exactly under the tip. For $z_{ts} \sim 1\,\mathrm{nm}$, which is quite often the case in STM operation, $\beta \sim 75$ and hence gating by the tip has quite a significant impact in influencing the differential tunneling conductance measured.

The Dirac point position will now be given by

$$E_D = -\gamma e\,\mathrm{sgn}(V_{gate} - \beta V_{bias})\sqrt{|V_{gate} - \beta V_{bias}|}. \tag{5.3.5}$$

Here, for simplicity, we have assumed $V_D^0 = 0$. To incorporate a finite V_D^0, we should just replace

introducing too much error.

V_{gate} by $(V_{gate} - V_D^0)$. Substituting E_D in Eq.(5.3.3), gives the necessary modification in the tunneling conductance.

$$G_t(V_{bias}, T = 0\,\mathrm{K}) \propto \left| V_{bias} + \gamma\, \mathrm{sgn}(V_{gate} - \beta V_{bias}) \sqrt{|V_{gate} - \beta V_{bias}|} \right|. \tag{5.3.6}$$

This has been plotted in Figure 5.11(b). Instead of one minimum in each G_t vs. V_{bias} curve occurring at the actual Dirac point of sample E_D^0, there are two local minima now (sub-figure (b)) moving in opposite directions with V_{gate}. The primary minimum occurs when $V_{bias} = E_D$ where E_D itself is dependent on V_{bias} (sub-figure (c)) and the secondary minimum occurs when $E_D = 0$ wrt. E_F^{GR} at which point it has a sharp jump due to the square root dependence on $|n| \propto |V_{gate} - \beta V_{bias}|$. The position of the primary and secondary minima is given respectively by

$$\begin{aligned} V'_{min} &= -\mathrm{sgn}(V_{gate})\, \frac{\beta\gamma^2 + \gamma\sqrt{4\,|V_{gate}| + \beta^2\gamma^2}}{2}, \\ V''_{min} &= \frac{V_{gate}}{\beta}. \end{aligned} \tag{5.3.7}$$

Therefore, from the slope of V''_{min} vs V_{gate}, we are able to extract β and hence estimate the tip-sample distance z_{ts}. The smaller the tip-sample distance, the smaller will be the slope of the position of the secondary minimum vs backgate which implies a stronger gating by the tip. We also note that along the inclined line of the secondary minimum, indicated in Figure 5.11(b), $n = 0$. Along any parallel line to this, n is constant.

From the knowledge of β and V'_{min}, it will be possible to recover the value of E_D^0 which is the main objective and hence correct for the error introduced due to this local gating by the tip. Using Eq.(5.3.7) and Eq.(5.3.2), we can formulate the relation between V'_{min} and E_D^0.

$$E_D^0 = \left[\frac{2\gamma\sqrt{|V_{gate}|}}{\beta\gamma^2 + \gamma\sqrt{4\,|V_{gate}| + \beta^2\gamma^2}} \right] V'_{min}. \tag{5.3.8}$$

In Figure 5.12, using the above equation, the differences between E_D^0 and V'_{min} has been plotted. It becomes clear that the presence of the tip causes a significant difference between the two at tip-sample distances $z_{ts} < 1\,\mathrm{nm}$ whereas beyond $\sim 5\,\mathrm{nm}$, we can ignore the contribution of the tip as a local gate. Hence, while considering the V_{CPD} measurements (section 5.3.2), where $z_{ts} > 10\,\mathrm{nm}$, we were justified in ignoring this effect. At high gate voltages ($V_{gate} \gg \beta^2\gamma^2/4$), this difference can be approximated by the following expression,

$$V'_{min} - E_D^0 = -\mathrm{sgn}(V_{gate})\, \frac{\beta\gamma^2}{2}. \tag{5.3.9}$$

Hence the tip-induced gating has the effect of enhancing the discontinuity in the primary minimum as compared to E_D^0, seen clearly in Figure 5.11(b) or Figure 5.12(a). However, the discontinuity itself still occurs at the charge neutrality point of the entire sample.

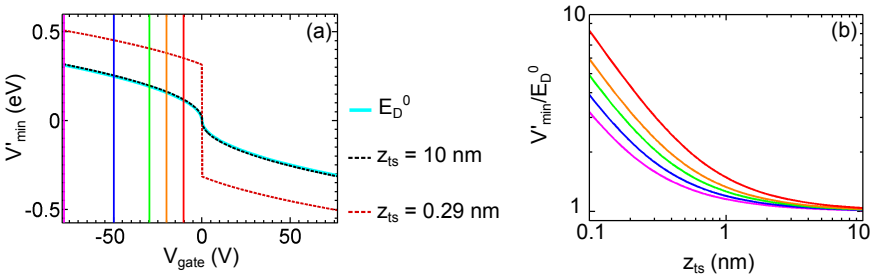

Figure 5.12: Change in the position of the primary minimum of G_t vs V_{bias} in the presence of tip-induced gating. (a) Comparison between E_D^0 and V'_{min} at different tip-sample distances (z_{ts}). (b) V'_{min}/E_D^0 as a function of z_{ts} for different V_{gate} indicated by the vertical lines in (a).

Work-Function mismatch

A finite work-function mismatch between the tip and the graphene will induce further modifications in the differential tunneling conductance gate maps as pointed out by Y. Zhao et al. [174]. As already discussed in section 5.3.2, due to this work-function mismatch, the potential difference between the tip and the graphene will not be zero when they are electrically connected but equal to their contact potential difference V_{CPD} given by Eq.(5.3.1). This potential difference will also act as a local gate if z_{ts} is sufficiently small. When a finite bias voltage is applied to graphene, the total potential of the tip wrt. graphene will be $(-V_{bias} + V_{\mathrm{CPD}})$. Again assuming a parallel plate capacitor model, the total carrier density induced in the graphene by the combined effect of the tip and the backgate is

$$n = \frac{K\epsilon_0}{et}\left[V_{gate} - \beta\left\{V_{bias} - (\Delta + E_D)\right\}\right]. \tag{5.3.10}$$

This leads to a Dirac point position given by

$$\begin{aligned} E_D &= -\gamma e\,\mathrm{sgn}\left[V_{gate} - \beta\left(V_{bias} - \Delta - E_D\right)\right]\sqrt{\left|V_{gate} - \beta\left(V_{bias} - \Delta - E_D\right)\right|} \\ \Rightarrow E_D &= -\mathrm{sgn}\left[V_{gate} - \beta\left(V_{bias} - \Delta\right)\right]\frac{\left[-\beta\gamma^2 + \gamma\sqrt{4\left|V_{gate} - \beta\left(V_{bias} - \Delta\right)\right| + \beta^2\gamma^2}\right]}{2}. \end{aligned} \tag{5.3.11}$$

Inserting E_D, given by the above expression, in Eq.(5.3.6) gives the differential tunneling conductance as a function of V_{bias} and V_{gate} which has been plotted in Figure 5.13 for three different tip-sample distances. Most importantly we note that now V'_{min} has approximately the same functional dependence on V_{gate} as E_D^0 with the significant difference that unlike E_D^0 which becomes zero at $V_{gate} = V_D^0$ (= 0 in this example), the primary minimum becomes zero at a different value of V_{gate}. Let us call this point of discontinuity of V'_{min} as V'_D which is related to the charge neutrality point in the following manner.

$$V'_D = V_D^0 - \beta\Delta. \tag{5.3.12}$$

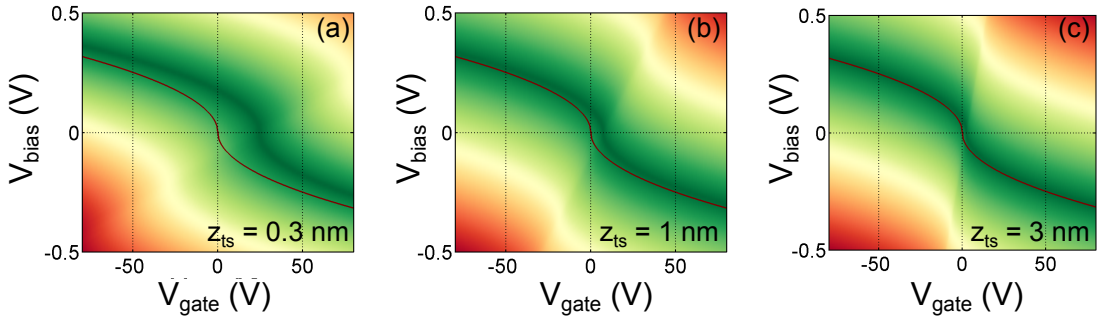

Figure 5.13: Tunneling conductance as a function of V_{bias} and V_{gate} after incorporating the effect of work-function mismatch induced doping described by Eq.(5.3.11) for $\Delta = -0.1\,\mathrm{V}$ and tip-sample distances z_{ts} indicated at bottom right. Maroon line indicates the Dirac point position wrt. E_F^{GR} without considering additional doping due to the tip.

We note that V_D' can be either higher or lower than V_D^0 depending on the sign of Δ which can change in the course of a scanning probe experiment. The secondary minimum V_{min}'' also becomes zero at $V_{gate} = V_D'$. Hence, experimentally, V_D' can be identified as the point of intersection of the curves corresponding to V_{min}' and V_{min}'' in the differential tunneling conductance gate map as also seen in Figure 5.13.

The position of the primary and the secondary minimum are, therefore, approximately given by

$$\begin{aligned} V_{min}' &= -\gamma\,\mathrm{sgn}(V_{gate} - V_D')\sqrt{|V_{gate} - V_D'|}, \\ V_{min}'' &= \frac{V_{gate} - V_D^0}{\beta} + \Delta. \end{aligned} \tag{5.3.13}$$

Using the above equation and Eq.(5.3.2), we can now find the relationship between the primary minimum and the position of the Dirac point E_D^0 unperturbed by the tip.

$$E_D^0 = \begin{cases} -\sqrt{(V_{min}')^2 - \gamma^2(V_D^0 - V_D')} & \text{for } V_{gate} > V_D' \\ \sqrt{(V_{min}')^2 - \gamma^2(V_D' - V_D^0)} & \text{for } V_{gate} < V_D' \end{cases} \tag{5.3.14}$$

This equation should correct for the complication introduced by the tip-gating. We note that only at high doping, when $|V_{min}'| \gg \gamma\sqrt{|V_D^0 - V_D'|}$, we can ignore the second term above and hence, have $E_D^0 \approx V_{min}'$. As V_{min}' becomes comparable to $\gamma\sqrt{|V_D^0 - V_D'|}$, E_D^0 increasingly deviates from V_{min}'. At charge neutrality when $E_D^0 = 0$, the above equation gives $V_{min}' = \gamma\sqrt{|\beta\Delta|}$ which is just the finite Dirac point resulting from the doping induced by the tip-neutral graphene work-function mismatch (Δ).

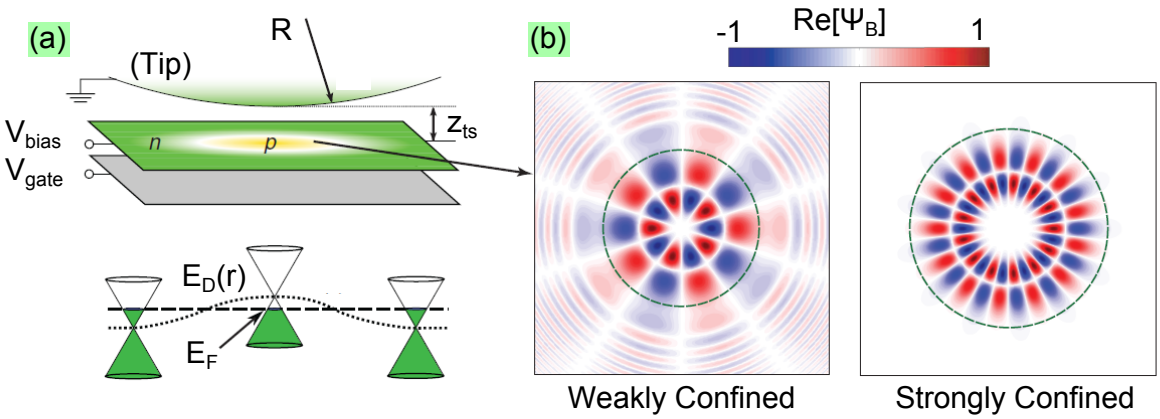

Figure 5.14: Local doping induced in the graphene by the STM tip. (a) Schematic demonstrating the situation where (V_{bias}) and V_{gate} are adjusted so as to reverse the polarity of the charge carriers underneath the STM tip by local gating, wrt. the background polarity. (b) Spatial profile of graphene wavefunction (real part of the second spinor component) underneath the tip. Electronic confinement results from the interference of incident and reflected waves at the p-n junction rings created by the STM tip. Confinement is stronger for larger angular momentum m i.e. for larger incidence angles. This is demonstrated for $m = 5$ (weak confinement) and $m = 13$ (strong confinement) [174].

Confinement effects due to tip-induced circular p-n junctions

The results derived so far are true only for the point directly under the tip $r = 0$. Due to the finite curvature of the tip, the charge density induced by it in the graphene will have a finite spatial extent. This means a finite region is created underneath the tip with doping that is different from the doping present in the rest of the flake. When we sweep V_{bias}, in the course of performing tunneling spectroscopy, we are therefore tuning this doping difference. If V_{bias} is such that the polarity of charges is reversed underneath the tip wrt. the surrounding, then a circular p-n or n-p junction is created. Figure 5.14(a) shows a schematic illustrating this situation. This leads to confinement of electronic states. This is because, even though Klein tunneling ensures 100% transmission of the normally incident chiral charge carriers across such a barrier, for oblique incidences the transmission is strongly suppressed [3]. Interference between incident and reflected electronic waves will then lead to spatially distributed resonances as shown in Figure 5.14(b). These resonances in the DOS are in turn detected as local maxima and minima in the tunneling spectrum. Hence, we add one more set of features to the differential tunneling conductance gate maps that are a manifestation of the gating effect of the tip.

This effect was most prominently visible in the gate maps presented by Y. Zhao et al [174] for graphene on boron nitride while others found in literature show vague but definite signatures of such tip-induced resonances [170][158]. They occur as two sets of fringes, where one follows

the primary minimum V'_{min} and the other follows the secondary minimum V''_{min}. The energy spacing between the fringes is given by the formula $\Delta\epsilon = \pi\hbar v_F/r$ where r is the radius of the p or n doped cavity created by the tip where the electronic states are confined. The reason behind the presence of two sets of fringes instead of one is the same as the reason for the presence of two local minima related to the Dirac point. Any feature in the LDOS of graphene is manifested twice in the tunneling spectrum, once when E_F^{tip} is aligned with it (this will follow the primary minimum) and next time when E_F^{GR} is aligned with it (this will follow the secondary minimum).

To be more quantitative, let us assume a spherical tip with radius R, located at a distance z_{ts} from the graphene plane (Figure 5.14(a)). Using the method of images, we find the induced surface charge density at a position r to be $\Delta n(r) \propto \frac{1}{z_{ts}+r^2/2R}$, provided $R >> z_{ts}$ which is a fair assumption in STM experiments. Now, if we consider the voltage applied to graphene to be V_{bias} such that the effective voltage of the tip wrt. graphene is $-(V_{bias} - \Delta - E_D)$, then the total charge density induced by the combined effect of the tip and the gate is

$$\begin{aligned} n(r) &= \frac{K\epsilon_0}{et}\left(V_{gate} - V_D^0\right) - \frac{\epsilon_0}{z_{ts} + r^2/2R}\left(V_{bias} - \Delta - E_D(r)\right) \\ \Rightarrow n(r) &= \frac{K\epsilon_0}{et}\left[\left(V_{gate} - V_D^0\right) - \beta(r)\left(V_{bias} - \Delta - E_D(r)\right)\right] \end{aligned} \tag{5.3.15}$$

The above equation is the same as Eq.(5.3.10), the only difference being that in this case β has a spatial dependence given by $\beta(r) = \frac{t}{2K}\frac{1}{z_{ts}+r^2/2R}$. For $r \to \infty$, $\beta \to 0$, implying that far away from the tip-center, the doping induced is only set by the backgate while directly under the tip at $r = 0$, we recover the results of the previous section. In Figure 5.15, the $E_D(r)$ profiles under the tip have been plotted as V_{bias} is changed from negative to positive values keeping V_{gate} fixed, using Eq.(5.3.11) but with the modified value of $\beta(r)$. In sub-figure (a), $E_D(r)$ crosses the Fermi level of graphene. This imposes a p-n junction for states with energy $|\varepsilon| < |E_D(r) - E_F^{GR}|$, ϵ being defined wrt. $E_D(r)$. This gives rise to the second set of fringes following V''_{min}. In sub-figure (b), Fermi level of tip is raised further up, such that $E_D(r)$ lies in between E_F^{GR} and E_F^{tip} but crosses neither. In this situation, graphene is p-doped throughout and no resonances occur. In sub-figure (c), E_F^{tip} is raised further up such that now $E_D(r)$ crosses it. Once again p-n junctions are formed for states with energy $|\varepsilon| < |E_D(r) - eV_{bias}|$ which will now result in the first set of fringes that run parallel to V'_{min}. States with energies $|\varepsilon| > |E_D(r = 0) - E_D(r \to \infty)|$ will never face a p-n junction barrier and will therefore be free of fringes.

Hence, we see that tunneling spectroscopy is an excellent tool to probe the local density of states of the sample but one has to proceed with caution when the sample in question is graphene. This is because unlike metallic surfaces, carrier concentration in graphene is sensitive to external electric fields and the applied tip-sample potential difference meant for measuring the DOS will in turn modify it via local gating. The above analysis should therefore be helpful in the interpretation of the experimentally measured differential tunneling conductance gate maps that is presented in the following section.

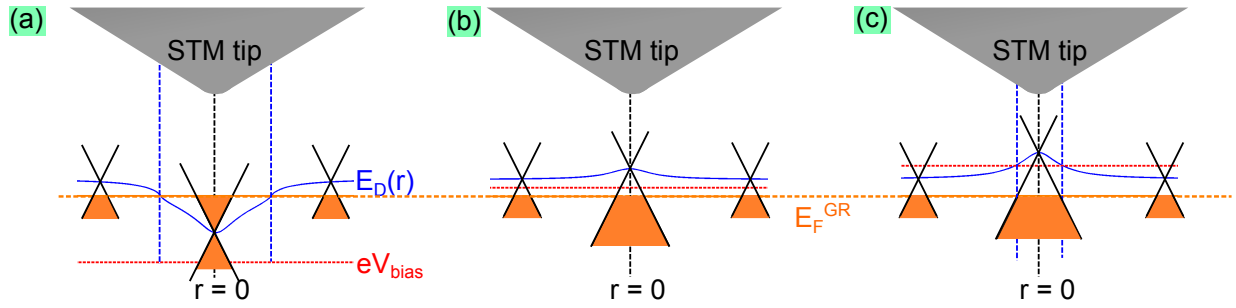

Figure 5.15: Change of the Dirac point E_D profile (blue line) of the graphene underneath the tip with change in V_{bias} at a fixed backgate voltage, calculated according to Eq.(5.3.11) with $\beta = \beta(r)$ [$V_{gate} = 25\,\mathrm{V}$, $V_D^0 = 30\,\mathrm{V}$, $z_{ts} = 0.1\,\mathrm{nm}$ and $\Delta = -0.1\,\mathrm{V}$]. The tip Fermi level E_F^{tip} (red dashed line) is set at eV_{bias} wrt. graphene Fermi level E_F^{GR} (orange line) . Idea from [174], supplementary information.

5.3.5 Tunneling Spectroscopy at different carrier density: The Experiment

We perform tunneling spectroscopy in graphene in the configuration discussed in Section 5.3.1. With tunneling current I_t as the feedback parameter, the tip is approached close to the surface, the set-point adjusted at the starting bias voltage V_{bias} for STS. The gate voltage is then gradually ramped up/down ($0.1\,\mathrm{V/s}$) to the desired value. After a wait time of about $5 - 10\,\mathrm{s}$ for the tip conditions to stabilize, the z-feedback is turned off followed by tunneling spectroscopy, at the end of which V_{bias} is restored to its starting value. For minimizing noise, a voltage division by factor of 10 is used on V_{bias}. All tunneling conductances measured in this section refer to the numerical derivative of the tunneling current. Due to the low temperature $T \sim 130\,\mathrm{mK}$ in which the measurements were performed, thermal drift was minimum.

Figure 5.16(b) shows the complete gate map i.e. dependence of the differential tunneling conductance as a function of V_{gate} and V_{bias} at a single point in graphene (Point 1) located approximately midway between the two metallic contacts, i.e. about $2\,\mu\mathrm{m}$ from each. The features that have been discussed in the previous section due to local gating by the tip are visible apart from some additional features. Let us go through these one by one.

Local Minimum at Fermi Energy of Graphene

There is a prominent dip at Fermi energy i.e. at $V_{bias} = 0\,\mathrm{V}$ that does not change its position with backgate. This feature has been observed by quite a few groups by now and is famously referred to as the zero bias anomaly or ZBA. The group of Michael F. Chrommie consistently reported on observation of such a gap of width $\sim 130\,\mathrm{meV}$ for graphene on SiO_2 [175][6] as well as on boron nitride [176], and attributed it to phonon mediated inelastic tunneling processes. Others like A. Deshpande et al. [177] or S. K. Choudhary et. al. [173] observed no such gap.

In the present measurements, the gap width was seen to be about $60 - 100\,\mathrm{meV}$ and the

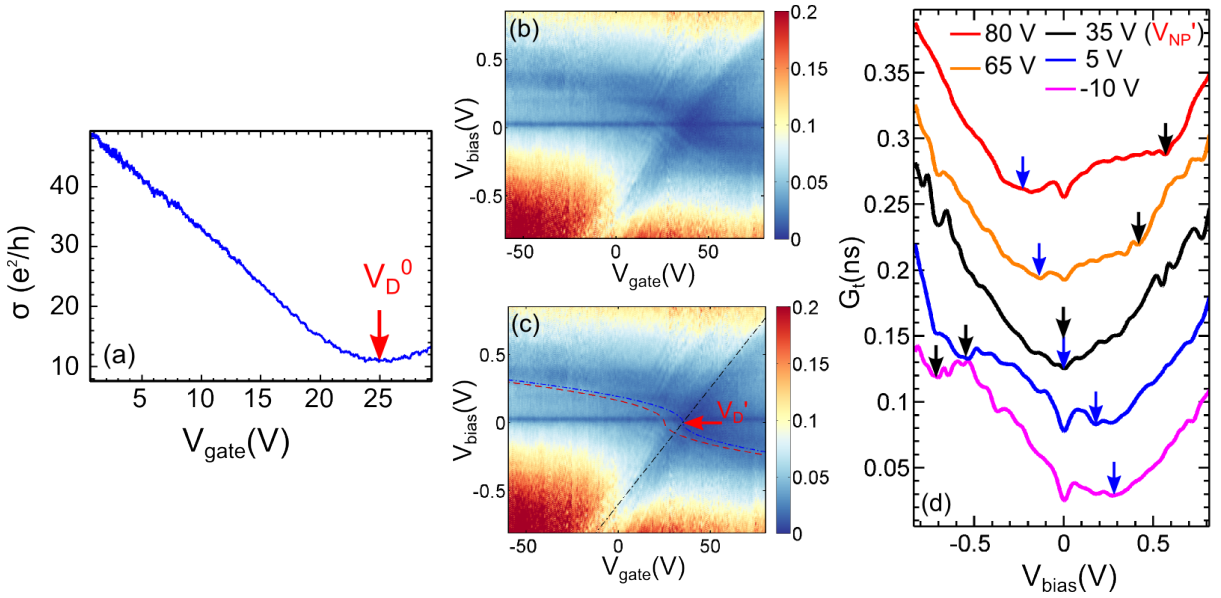

Figure 5.16: Tunneling spectroscopy at different V_{gate}. (a) Macroscopic two-probe conductivity vs. V_{gate} measured just before STS measurement giving the charge neutrality point $V_D^0 \approx 25\,\mathrm{V}$. (b) Differential tunneling conductance in ns as a function of V_{gate} and V_{bias}. (c) The same as in (b) but with E_D^0 (maroon line) [Eq.(5.3.2)], primary minimum V'_{min} (blue dashed line) and secondary minimum V''_{min} (black dashed line) [Eq.(5.3.13) with $V'_D = 35\,\mathrm{V}, \Delta = -0.171\,\mathrm{V}$ and $\beta = 58.5$] vs V_{gate} superposed. (d) Differential tunneling conductance G_t vs. V_{bias} at different gate voltages (curves displaced by 0.06 ns for clarity). Blue arrows indicate V'_{min} and black arrows indicate V''_{min}.

depth was more for hole doped graphene than when it is doped by an equivalent amount of electrons [Figure 5.16(c)]. A decrease of DOS at the Fermi level is a known characteristic of low dimensional disordered systems like graphene due to long range Coloumb interactions [178] and could offer an explanation for this ZBA as also pointed out by Jung et. al [170]. Interestingly this gap is camouflaged when the gate voltage is adjusted such that the primary minimum V'_{min} coincides with it at the Fermi level as clearly seen in Figure 5.16(c) for $V_{gate} = 35\,\mathrm{V}$ (which is close to local charge neutrality point V'_D).

The Primary and the Secondary Minima

Apart from this, we can clearly identify a global minimum for each tunneling spectrum. For $V_{gate} < 38\,\mathrm{V}$ ($\approx V'_D$), this minimum is located at positive values of V_{bias} while for $V_{gate} > 38\,\mathrm{V}$, it shifts to negative V_{bias} as indicated by the blue arrows in Figure 5.16(c). In the gate map shown in sub-figure (b), the blue dashed line approximately traces this feature. We see that it follows a Dirac point E_D^0 like dependence with V_{gate} (maroon dashed line in sub-figure (b)). As discussed in the previous section, this is the primary minimum V'_{min}.

The secondary minimum V''_{min} is also visible in the gate map in sub-figure (b), as indicated by

the black dashed line. In sub-figure (c), the black arrows indicate their position in each tunneling spectrum. The position of this local minimum is seen to move in exactly the opposite direction with V_{gate} as compared to V'_{min} in a linear fashion, as expected.

The two curves, representing V'_{min} vs V_{gate} and V''_{min} vs V_{gate}, are seen to approximately coincide at $V_{gate} = V'_D \approx 38\,\mathrm{V}$, $V_{bias} = 0$. V'_D is clearly different from the CNP measured in transport where $V^0_D = 25\,\mathrm{V}$ recorded just prior to STS measurement (Figure 5.16(a)). This is consistent with our discussion in section 5.3.4. The slope of $V''_{min} = 1/\beta$ [Eq.(5.3.13)] and this gives us an estimate for the tip-sample distance z_{ts}. Also, the value of Δ i.e. work-function mismatch between undoped graphene and the tip can be extracted using Eq.(5.3.12).

Figure 5.17 shows all the gate maps acquired during the course of this experiment over a period of one month at different locations on the graphene. This is followed by a table 5.2 that lists all the relevant parameters extracted from the gate maps using the above procedure.

We see that the crossing of V'_{min} and V''_{min} is a common feature in all the gate maps. However, values of V^0_D, V'_D and Δ are all seen to vary with time. We note the stark difference between 'Point 4' and rest of the location points where, in contrast to the other locations, V'_D is much lower than V^0_D. From Eq.(5.3.12), a change in V'_D from point to point can occur due to two reasons: firstly due to doping inhomogeneities which results in a spatially varying charge neutrality point $V_D(\mathbf{r}) = V^0_D + \delta V_D(\mathbf{r})$, which is bound to be different at the four chosen locations. Secondly, due to the change in tip work-function in the course scanning resulting in change of Δ which is also perfectly possible given the long time differences between the different measurements (5.2).

β, which is independently determined from the slope of V''_{min} vs V_{gate}, is expected to depend on the set tunneling resistance R_t which is a measure of the tip-sample distance. However, positive correlation expected between R_t and z_{ts} is not clear in the data sets. The significant time difference between measurements at Point 2, 3 and 4 is once again the possible explanation, during which tip conditions changed (the decay length of tunneling current I_t i.e. z_0 given by Eq.(3.2.1) changed). R_t is therefore not a good estimate for z_{ts} in this case and a more systematic study would have been useful. Also, an unambiguous determination of V''_{min} is difficult due to the presence of several smaller resonances near it leading to a blurring effect.

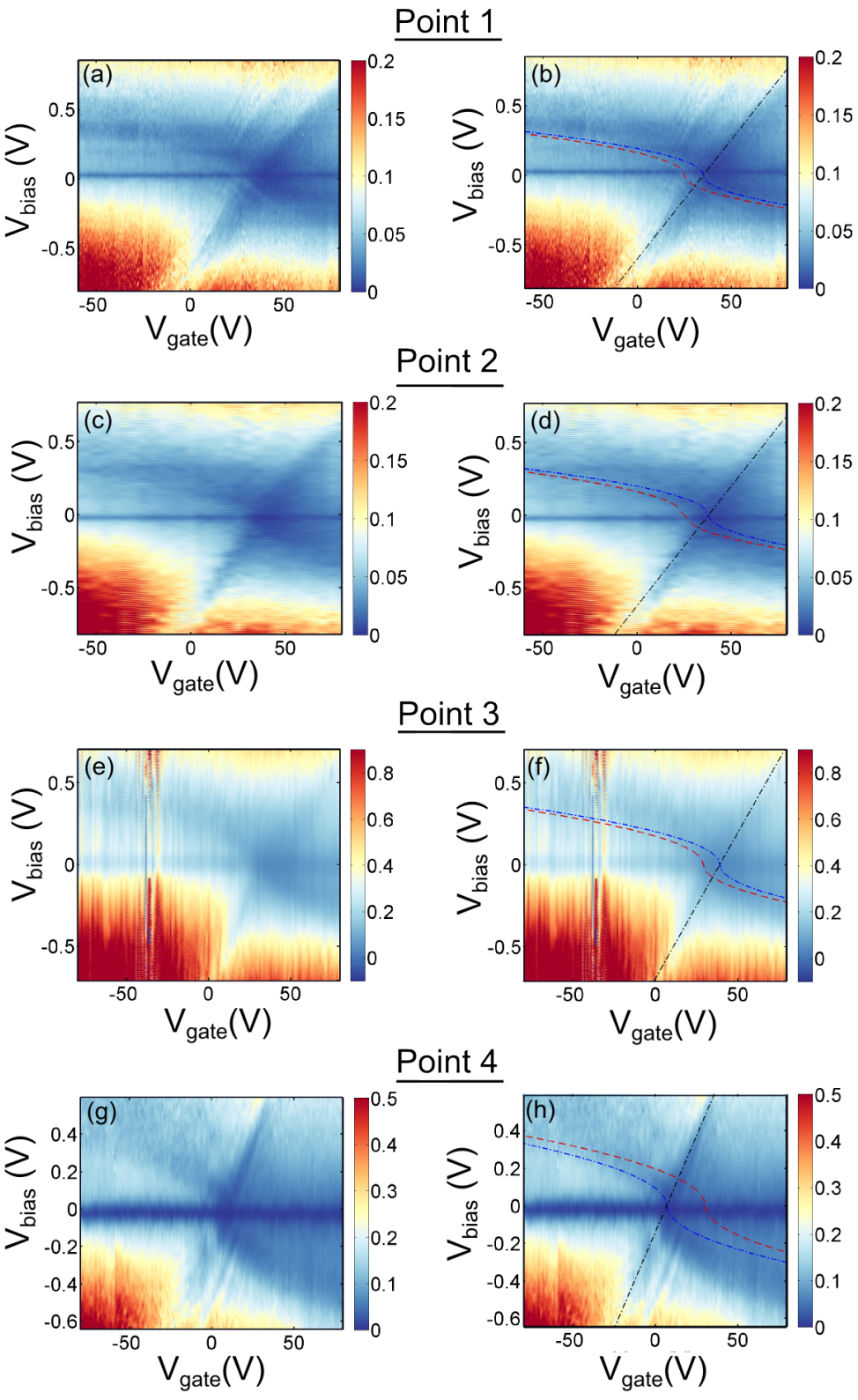

Figure 5.17: Tunneling conductance in 'ns' as a function of V_{bias} and V_{gate} measured at different locations (Points 1-4) over a span of one month, see table (5.2). In each row, first image [(a), (c), (e)] gives $G_t(V_{bias}, V_{gate})$ in ns while the second image [(b), (d), (f)] is the first image along with lines drawn along the three relevant quantities $(E_D^0, V'_{min}, V''_{min})$. Maroon curve gives E_D^0 for charge neutrality at V_D^0 from transport. V'_{min} and V''_{min} are indicated by blue and black dashed lines respectively.

Location	Date	R_t (GΩ)	V_D^0 (V)	V_D' (V)	z_{ts} (nm)	β	Δ (eV)
Point 1	13/02/2015	18	25	35	1.2	58.5	-0.171
Point 2	14/02/2015	18	25	38	1.2	60.9	-0.213
Point 3	18/02/2015	4	29	38	1.3	56.2	-0.178
Point 4	02/03/2015	8	30	7	1.5	48.7	0.478

Table 5.2: Parameters extracted from differential tunneling conductance on graphene as a function of V_{bias} and V_{gate} at different locations and at different times. R_t is the tunneling resistance at the beginning of each G_t vs. V_{bias} measurement when z-regulation was turned off, V_D^0 is the charge neutrality point (CNP) measured from transport just before the corresponding STS. (c) V_D' is the value of V_{gate} at which V_{min}' and V_{min}'' intersect, z_{ts} is the tip-sample distance, $\beta = t/(K z_{ts})$ and Δ is the work-function difference between undoped graphene and the tip.

The Fringes

Finally, we turn our attention to the resonances accompanying V_{min}' and V_{min}''. In the gate map shown in Figure 5.16, we see two sets of fringe like patterns, one set moving parallel to V_{min}' and the other set moving parallel to V_{min}''. As we discussed before in section 5.3.4, the origin of these fringes is related to the formation of p-n or n-p junctions underneath the tip which leads to confinement in the electronic states. The fringe width in this case is observed to be $\approx 100\,\text{meV}$. This allows us to roughly estimate the dimension of the confinement cavity created by the tip $r_0 = \pi\hbar v_F/\Delta\varepsilon \approx 23\,\text{nm}$. If we consider a tip-sample distance $z_{ts} = 1.2\,\text{nm}$ (table 5.2) and assume a spherical shape of the metallic tip, then a lateral extent r_0 of induced doping would imply a tip radius of $R = r_0^2/2z_{ts} \approx 220\,\text{nm}$. In this experiment, the STM tip used had a pyramidal shape (Figure 3.26(c)) with a slanting horizontal apex of length $\approx 600\,\text{nm}$ (from SEM image). However, the actual shape and dimension of the tip that participates in the tip-sample tunneling process can be quite different. In this sense, the estimate obtained from the G_t gate map above could provide a better estimate. However, the broadening observed at the metal-graphene interface (Figure 5.9(b),(c)) of about 100 nm, suggests a tip apex radius of about 50 nm.

We note that the fringes occur only close to V_{min}' and V_{min}''. This is because, as explained before (section 5.3.4), states lying away from $E_D(r)$ do not face any tip-induced p-n junction barrier and hence no confinement. Only states close to the $E_D(r)$ with energy $|\varepsilon| < |E_D(r = 0) - E_D(r \to \infty)|$ will form p-n junctions for certain values of V_{bias}. We also notice that the fringes are rather vague, the most prominent being at Point 1 (Figure 5.17), especially if we compare these maps to those acquired by Y. Zhao et al., [174] on graphene on BN. This could be related to the fact that graphene on SiO_2 has significantly more charge inhomogeneity than graphene on BN [176]. The visibility of the fringes is expected to improve by decreasing the tip-sample distance as this would induce a higher distortion of the $E_D(r)$ profile under the tip.

Conclusion

In conclusion, we find that the experimentally measured differential tunneling conductance gate maps on graphene are reasonably well explained if we incorporate the effect of (1) tip-induced gating (2) doping induced by the gate dependent tip-graphene work-fuction mismatch and (3) confinement of electronic states induced in graphene due to the finite curvature of the tip. Together, they account for the two important minima in the tunneling spectrum i.e. V'_{min} and V''_{min} and the fringes observed at low energies. However, what is not accounted for is the zero bias anomaly (ZBA), found at all gate voltages which we attribute to a Coulomb gap present in low dimensional disordered systems.

We importantly realize that in gated graphene devices where the tip acts as a local gate, the primary minimum of the differential tunneling conductance spectrum is different from the Dirac point E_D^0 unperturbed by the tip. Only at very high doping $V'_{min} \approx E_D^0$ but at low doping, the deviations become increasingly more pronounced. This is in contrast with graphene on metals where the presence of the metal substrate prevents local gating by the tip and hence, we can safely say $E_D^0 = V'_{min}$, as done in Chapter 4 for the case of graphene on iridium.

Plenty of rich literature is available on STS measurements of graphene on SiO_2 at different gate voltages. While many of them target investigation of eletron-hole puddles in graphene [6, 179], implicitly assuming that the primary minimum is the same as E_D^0, few delve into the details of interpreting the G_t gate maps. The G_t spectrum is actually a 'zoo' of gate dependent/independent features and many researches have been directed towards finding the origin of these features. Many-body interactions like electron-electron, electron-phonon, electron-plasmon etc have been suggested to contribute additional features to the spectrum [180], E_D^0 vs V_{gate} dependence has been suggested to be modified due to Fermi velocity renormalization [158], to name a few. Incorporating these effects might lead to further advancement in our analysis. However, in our opinion, the role that the STM tip has to play in influencing the G_t spectrum is quite dramatic and will contribute in a major way. Hence, our interpretations have been primarily influenced by the work of S. K. Choudhuri et. al [173] and Y. Zhao et al.[174] who have directly addressed this issue in detail. What our experiment adds to this is the fact that we can constantly correlate the measured gate maps with the bulk behavior of the sample obtained from in-situ measurement of transport characteristics of the device.

5.4 Electron-Hole Puddles in Graphene

Finally we come to our main objective, which is the investigation of local charge disorder in graphene. In Section 5.2, we have discussed in detail, the transport properties of the present sample which allowed us to extract the impurity concentration n_{imp} and their average distance from the plane of graphene d. Assuming the origin of this disorder to be random charge impurities embedded in the substrate, these two quantities should be sufficient to completely characterize

the correlations of the screened disorder potential $\tilde{V_D}(r)$ as discussed in Chapter 3. In this section, we use Scanning tunneling spectroscopy to directly image the doping inhomogeneities present in graphene at different carrier concentrations and hence experimentally measure these local correlations. This will allow us to directly compare the theoretical predictions with what we measure experimentally.

5.4.1 Imaging Electron-Hole Puddles

To measure the doping fluctuations present in a given region of graphene by STS, there are two ways. One way is to acquire the full differential tunneling conductance $G_t = dI_t/dV$ spectrum at each point which is called Constant imaging tunneling spectroscopy or CITS. Using the position of the primary minimum of this spectrum, we can then find the local Dirac point $E_D^0(r)$ using Eq.(5.3.14) [6]. By this process, we can accurately measure the Dirac point distribution present in the given region. However, the high measurement time involved poses a major disadvantage for the implementation of this technique. For example, if the measurement time for one point is adjusted at about 30 s, then for 64×64 pxls, the whole CITS would last for about 34 hours! Since our experiment involves investigating the charge disorder at several gate voltages at low temperatures ($T \sim 130$ mK) in an inverted dilution cryostat, such long duration measurements are not feasible.

The second alternative is the spatial mapping of G_t using a lock-in amplifier, at a fixed value of V_{bias} with the z-feedback on. This technique was demonstrated by Y. Zhang et al. to image electron-hole puddles in graphene on SiO_2 [6]. The measurement time involved in this case (85 mins for an image of 256×256 pxls at a speed of 10 nm/s for the images presented), is orders of magnitude less than in the previous case. Hence, for the bulk of the measurements presented in this section, we adopt this method.

The principle behind the spatial mapping of the differential tunneling conductance G_t to visualize the existent charge inhomogeneity is that if V_{bias} is chosen in the vicinity of the primary minimum V'_{min}, then an infinitesimal fluctuation in the position of the Dirac point $\delta E_D^0(r)$ due to doping inhomogeneity will lead to an infinitesimal change in V'_{min} which in turn should produce an infinitesimal change in $G_t(V_{bias})$ given by $\delta(dI_t/dV) \propto \delta V'_{min} \propto \delta E_D^0$ [7]. The upper-right and lower-left insets of Figure 5.18(a) demonstrate this schematically for the hole and electron doped case respectively.

If the tunneling spectrum on graphene would be perfectly linear about the Dirac point or rather the primary minimum as in the insets in the schematic of Figure 5.19(a), then this method should provide an accurate image of the doping inhomogeneities up to a multiplicative factor provided the voltage bias chosen for imaging $(V_{bias})_{set}$ lies sufficiently far from $(V'_{min} \pm \delta V'_{min})$.

[6] E_D^0 refers to the actual Dirac point of graphene without any perturbation from the tip.

[7] The proportionality should hold, at least at high doping [Eq.(5.3.14)], because V'_{min} follows the same dependence on V_{gate} as E_D^0 except that their origins are horizontally shifted by $\Delta\beta$.

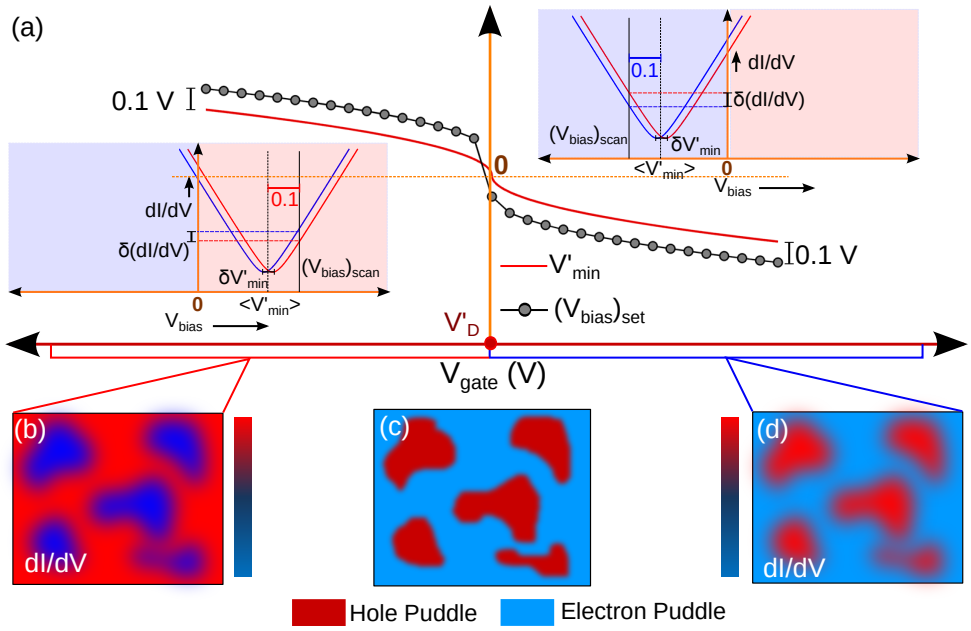

Figure 5.18: Imaging of electron-hole puddles at different backgate voltages. (a) Schematic demonstrating the choice of V_{bias}, i.e. $(V_{bias})_{set}$, for acquiring the LDOS maps at different gate voltages based on the variation of the primary minimum V'_{min} of the differential tunneling conductance spectrum (due to the variation in E_D). Inset at upper-right demonstrates the proportionality of doping disorder ($\delta E_D \propto \delta V'_{min}$) to fluctuations in tunneling conductance $\delta(dI/dV)$ at a given V_{bias} for $V_{gate} > V'_D$ where V'_D is the CNP under the joint action of the tip and the backgate. Lower-left inset demonstrates the same for $V_{gate} < V'_D$. (c) Schematic of a given distribution of electron-hole puddles and (b) its corresponding dI_t/dV images for hole-doped and (d) electron-doped graphene.

However, measuring at bias voltages located too far from the primary minimum is not recommended. This is because the perturbations that induce these doping inhomogeneities also act as scattering centers and at high energies, will give rise to quasiparticle interference patterns in the $G_t(x, y)$ maps as clearly seen in Figure 5.19. Therefore for $|(V_{bias})_{set}| \gg |V'_{min}|$, the $G_t(x, y)$ maps will contain spatial modulations induced by the QPIs superposed on the doping distribution. The characteristic spatial dimension of features extracted from such an image would mainly correspond to the QPI patterns rather than the charge inhomogenieties.

Measuring at V_{bias} located too close to the primary minimum is not recommended either. As we had discussed in section 5.3.4, the tunneling spectrum close to V'_{min} is not linear but complicated by the presence of a series of fringes due to tip-induced confinement of the electronic states close to the Dirac point. We also found it best to avoid energies lying in the range $0 < |(V_{bias})_{set}| < |V'_{min}|$ because of the presence of the zero bias anomaly at $V_{bias} = 0$.

Keeping all these conditions in mind, it is important to find an optimum value of V_{bias} at which we can correctly implement the second technique to image the charge inhomogenieties. From our discussion so far, it is quite obvious that the choice of this bias voltage will depend

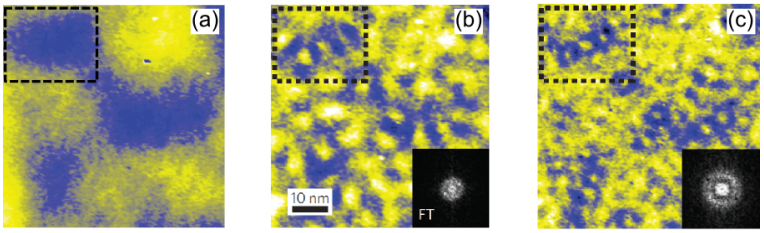

Figure 5.19: Charge Disorder and Quasiparticle Interferences on graphene on SiO_2 by Y. Zhang et al. [6]. (a) Spatial map of differential tunneling conductance G_t that gives the charge disorder. Bias voltage used for scanning $(V_{bias})_{set} = -0.25\,\mathrm{V}$ at $V_{gate} = 15\,\mathrm{V}$ when the average Dirac point is at $\approx -0.1\,\mathrm{V}$. (b) $G_t(x, y)$ map of the same region, at the same gate voltage but at $(V_{bias})_{set} = 0.35\,\mathrm{V}$ and (c) at $0.6\,\mathrm{V}$. These maps are a superposition of the charge disorder and the spatial modulations induced by QPI. The insets show the corresponding Fourier transform indicating the characteristic spatial dimension of the features in the map.

on the position of E_D or rather the primary minimum V'_{min} which in turn is dependent on the backgate voltage. In Figure 5.18(a), the choice of $(V_{bias})_{set}$ for each V_{gate} has been demonstrated. The following briefly summarizes our selection criteria.

$$(V_{bias})_{set} = \begin{cases} \langle V'_{min} \rangle + 0.1\,\mathrm{V} & \text{for } \langle V'_{min} \rangle > 0 \\ \langle V'_{min} \rangle - 0.1\,\mathrm{V} & \text{for } \langle V'_{min} \rangle \leq 0 \end{cases} \tag{5.4.1}$$

From Figure 5.17, we clearly see that the above criteria select the optimum bias voltage at which the tunneling spectrum is approximately linear and featureless. At the same time, the difference of $0.1\,\mathrm{V}$ ensures that it is neither too far from nor too close to the primary minimum. However, we must note that the two different conditions used for hole and electron doping will result in a contrast reversal as demonstrated in Figure 5.18(b)-(d). For a given doping distribution shown in (c), following the positive doping criteria will produce the same image as the given distribution [(d)]. But choosing the negative doping criteria will produce the complimentary image. However, this is not a problem as the quantities of interest i.e. amplitude and spatial extent of disorder remain identical in the two cases.

5.4.2 Charge Disorder with Point to Point Tunneling Spectroscopy

Let us start with a detailed investigation of the local charge disorder in the present sample by acquiring the full differential tunneling conductance spectrum at each point in a given region i.e. a complete CITS. Although quite time consuming, it remains the best and the most direct way to quantitatively measure the fluctuations in the local Dirac point by Scanning tunneling spectroscopy. They serve the additional purpose of validating our imaging criteria of the electron-hole puddle landscape using the second method.

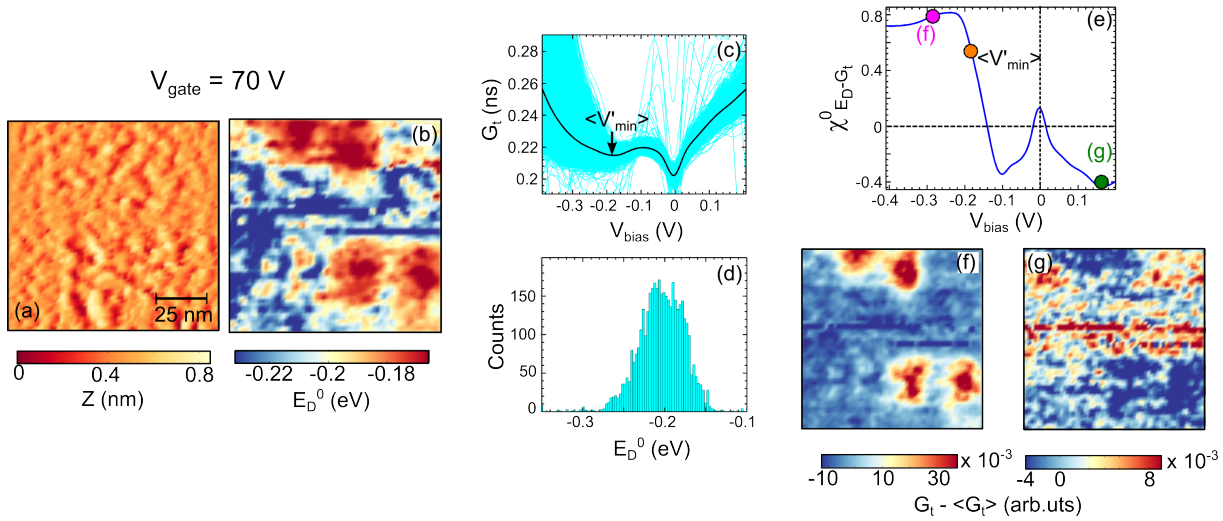

Figure 5.20: Dirac point fluctuations at high electron doping $V_{gate} = 70\,\mathrm{V}$ using point to point tunneling spectroscopy (64×64 points over $100\,\mathrm{nm} \times 100\,\mathrm{nm}$). (a) Simultaneously acquired topography in STM ($I_{set} = 100\,\mathrm{pA}$, $V_{bias} = 0.3\,\mathrm{V}$). (b) Dirac Point map composed of the position of the primary minimum V'_{min} of the tunneling spectrum acquired at each point. (c) Differential tunneling conductance G_t as a function of V_{bias} measured using lock-in technique ($V_{AC} = 6\,\mathrm{mV}$, $f_{AC} = 322.4\,\mathrm{Hz}$). Cyan curves indicate all the tunneling spectra at different spatial locations while the black curve represents their average. (d) Histogram of Dirac point. (e) Correlation coefficient $\chi_{E_D - G_t}$ between Dirac point map in (b) and spatial map of tunneling conductance $G_t(x, y)$ as a function of V_{bias}. (f) $G_t(x, y)$ at $V_{bias} = -283.7\,\mathrm{mV}$ and (g) at $V_{bias} = 201\,\mathrm{mV}$.

CITS at high electron concentration

Figure 5.20 presents the thorough investigation of the local doping inhomogeneities found at high electron concentrations corresponding to a backgate voltage of 70 V by the method of CITS. Since, the charge neutrality point was observed at $V_D^0 = 30\,\mathrm{V}$, this backgate voltage should correspond to an electron concentration of $n_g = 3.0 \times 10^{12}\,\mathrm{cm}^{-2}$ (2.1). Considering an average impurity distance of $d = 0.21\,\mathrm{nm}$, as suggested by transport measurements for electron doping (table 5.1), this value of n_g lies in the intermediate regime where the theory is not very well developed (section 2.4.2). It would have been interesting to measure beyond the complete screening limit but since this would mean $V_{gate} > 600\,\mathrm{V}$, it was not feasible. (a) and (b) shows the topography and the Dirac point map of the given region on graphene. The two images do not seem to be correlated. This is expected on graphene on SiO_2 as the source of E_D fluctuations are randomly charged impurities embedded in the substrate and is consistent with the measurements by Y. Zhang et al. [6] or A. Deshpande et al [177]. The topographic roughness is about 110 pm.

To obtain the Dirac point distribution in the given region, as a first step, we extract the primary minimum from each G_t vs V_{bias} curve. This is done by means of a parabolic fit over

an energy window spanning from $-400\,\text{mV}$ to $-60\,\text{mV}$ in this case [8]. Not all spectra are perfect and a selection procedure is needed to shortlist the better ones. Ensuring a positive curvature of the best fit parabola serves as a good criterion for this purpose. From the primary minimum, the Dirac point $E_D^0(r)$ is obtained using Eq.(5.3.14). Figure 5.20(c) shows the collection of all selected spectra with the black line showing the mean differential tunneling conductance. (d) gives the histogram of the distribution of $E_D^0(r)$ found in the above way with a mean value of $-203.7\,\text{meV}$ and a standard deviation of $\sigma_{E_D} = 28.3\,\text{meV}$. Using Eq.(2.2.21), we also find the associated distribution of doping concentration $n(r)$ with an average value of $\langle n \rangle = 31 \times 10^{11}\,\text{cm}^{-2}$ and standard deviation $n_{rms} = 9 \times 10^{11}\,\text{cm}^{-2}$. All these have been listed together in the table 5.3 along with the corresponding values extracted from CITS at other gate voltages.

Since the CITS measurement involves probing the spatial variations in the LDOS at different energies, it becomes possible to cross-check if $G_t(x,y)$ maps acquired at V_{bias} that follows the selection criteria given by Eq.(5.4.1) actually resembles the Dirac point map. The standard way to quantify the resemblance between two given images, A and B with dimensions (M,N), is via their correlation coefficient which is given by

$$\chi^0_{A-B} = \frac{\sum_{m=1}^{M}\sum_{n=1}^{N}\left(A_{mn}-\bar{A}\right)\left(B_{mn}-\bar{B}\right)}{\sigma_A \sigma_B}. \tag{5.4.2}$$

As is evident, a perfect resemblance would correspond to $\chi^0_{A-B} = 1$ while completely uncorrelated images would correspond to $\chi^0_{A-B} \to 0$. Figure 5.20(e) shows the variation of the 2D correlation coefficient between $G_t(x,y)$ and the Dirac point map as a function of V_{bias}. At the average primary minimum i.e. $V_{bias} =< V'_{min} >$, $\chi^0_{E_D-G_t} \approx 0.5$ (orange dot) and is clearly seen (Figure 5.20(e)) to increase to about 0.8 at $V_{bias} =< V'_{min} > -0.1\,\text{V}$ (magenta dot) beyond which it saturates. Therefore, this implies that the $G_t(x,y)$ maps for $V_{bias} \lesssim (< V'_{min} > -0.1\,\text{V})$ show maximum positive correlation with the $E_D^0(x,y)$ map and hence justifies our criteria for choosing $(V_{bias})_{set}$ according to Eq.(5.4.1) for imaging the inhomogeneities at high electron densities. This is further verified by the $G_t(x,y)$ map at $V_{bias} =< V'_{min} > -0.1\,\text{V}$ shown in (f) which indeed shows a strong resemblance to $E_D^0(x,y)$ map in (b). On the right of $V_{bias} =< V'_{min} >$, $\chi^0_{E_D-G_t}$ decreases and becomes negative at around ($V_{bias} = -0.1\,\text{V}$), then rises again to almost zero at $V_{bias} = 0\,\text{V}$ and then once again drops to negative values. The reason for the change in sign is expected as explained clearly by the schematic in Figure 5.18. Had the G_t vs V_{bias} dependence been perfectly linear about V'_{min}, the change in sign of $\chi^0_{E_D-G_t}$ would have been instantaneous. The finite slope in (e) about $V_{bias} =< V'_{min} >$ therefore arises due to the flattening of the G_t spectrum about the primary minimum. The presence of the zero bias anomaly at $V_{bias} = 0\,\text{V}$ (section 5.3.5) obscures the existing correlations i.e. $\chi^0_{E_D-G_t} \approx 0$ and hence justifies the need to optimally choose the bias voltages for imaging the doping inhomogeneities.

[8] Care is taken to avoid the Zero bias anomaly (ZBA)

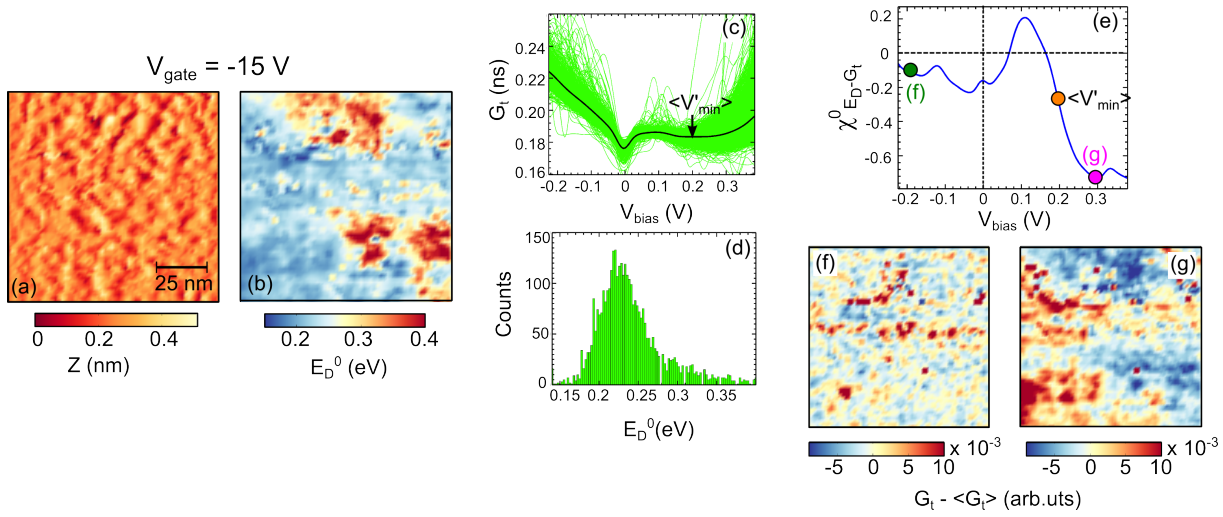

Figure 5.21: Dirac point fluctuations at high hole doping $V_{gate} = -15\,\mathrm{V}$. Region under consideration is the same as in Figure 5.20. (a) Simultaneously acquired topography in STM ($I_{set} = -100\,\mathrm{pA}$, $V_{bias} = -0.32\,\mathrm{V}$). (b)-(e) Analogous to (a)-(e) of Figure 5.20. $G_t(x, y)$ as a function of V_{bias}. (f) $G_t(x, y)$ at $V_{bias} = -200.8\,\mathrm{mV}$ and (g) at $V_{bias} = 296.5\,\mathrm{mV}$.

CITS at high hole concentration

Figure 5.21 shows the main results acquired from a CITS at $V_{gate} = -15\,\mathrm{V}$ on the same region as above that is clearly identified by the well-matched topography in the two cases as seen from Figure 5.20(a) and Figure 5.21(a).$V_{gate} = -15\,\mathrm{V}$ corresponds to hole doped graphene with carrier concentration $n_g = 34 \times 10^{11}\,\mathrm{cm}^{-2}$ considering $V_D^0 = 30\,\mathrm{V}$, as seen from transport. Proceeding in a similar manner as before, we obtain the distribution of E_D^0 and the charge carrier concentration n which enables us to calculate the fluctuations in these quantities present in the given region. Our results show a stronger disorder in the present case with $n_{rms} = 13 \times 10^{11}\,\mathrm{cm}^{-2}$ and $\sigma_{E_D} = 42.1\,\mathrm{meV}$, both of which are higher than at $V_{gate} = 70\,\mathrm{V}$.

A comparison of the Dirac point maps at the two gate voltages i.e. Figure 5.20(b) and Figure 5.21(b) clearly illustrates how the relatively lower electron doped regions at $V_{gate} = 70\,\mathrm{V}$ (red circular regions at lower right and upper middle) transforms into regions with higher hole doping wrt. the surroundings at $V_{gate} = -15\,\mathrm{V}$.

The interpretation of $\chi^0_{E_D-G_t}$ vs V_{bias} (Figure 5.21(e)) is more complicated in this case. The highest correlation $\chi^0_{E_D-G_t} \approx -0.8$ is almost the same in magnitude as before but with an inverted sign and develops for $V_{bias} \gtrsim (< V'_{min} > +0.1\,\mathrm{V})$ (magenta dot) which is expected (Figure 5.18) and also in accordance with our prediction (section 5.4.1). At $V_{bias} < V'_{min}$, $|\chi^0_{E_D-G_t}|$ decreases and turns positive at about $V_{bias} = 0.1\,\mathrm{V}$, beyond which it reduces once again to weakly negative values at about $V_{bias} = 0\,\mathrm{V}$ and remains fluctuating there, unable to recover a high positive value as would have been expected. This is the fundamental difference measured between high electron doping (Figure 5.20) and high hole doping (Figure 5.21). The reason for this difference

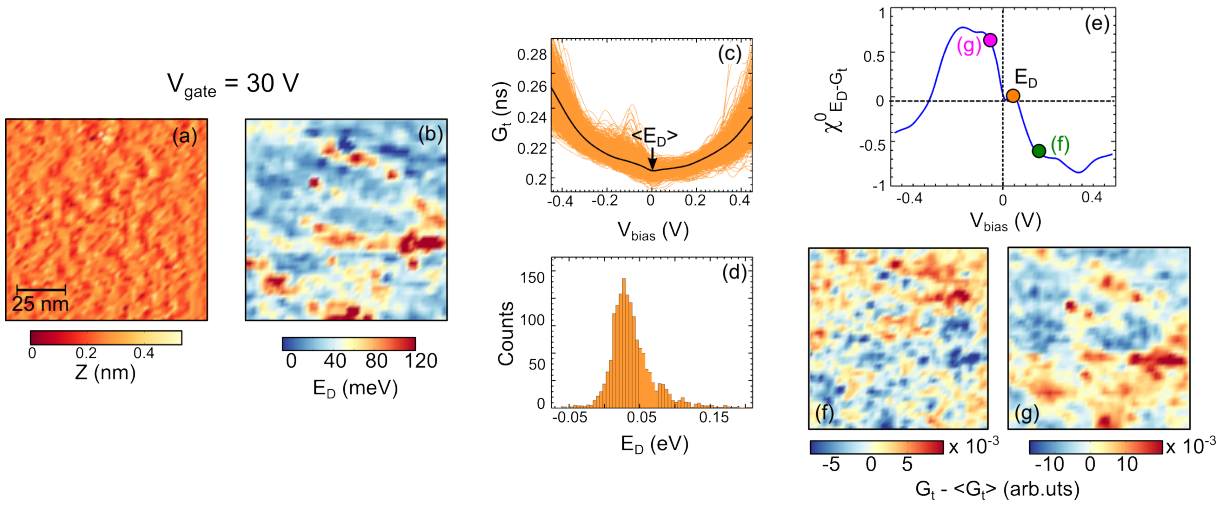

Figure 5.22: Dirac Point fluctuations close to Charge Neutrality $V_{gate} = 30\,\mathrm{V}$ (50×50 points over $100\,\mathrm{nm} \times 100\,\mathrm{nm}$). Region under consideration is different from that in Figures 5.20 and 5.21. (a) Simultaneously acquired topography in STM ($I_{set} = 200\,\mathrm{pA}$, $V_{bias} = 0.6\,\mathrm{V}$). (b)-(e) Analogous to (a)-(e) of Figures 5.20 and 5.21. $G_t(x, y)$ as a function of V_{bias}. (f) $G_t(x, y)$ at $V_{bias} = 140\,\mathrm{mV}$ and (g) at $V_bias = -60\,\mathrm{mV}$.

is not very clear but seems to be related to the different shape of the tunneling spectrum in the two situations, as seen from Figure 5.20(c) and Figure 5.21(c), which is very much flatter about $< V'_{min} >$ in the hole doped case in comparison to the situation at high electron doping. This fact is also visible in the all the $G_t(V_{bias}, V_{gate})$ maps shown in Figure 5.17.

For the imaging of doping inhomogeneities by mapping of tunneling conductance $G_t(x, y)$ at a set V_{bias}, this asymmetry between high electron and hole doping implies that imaging at high hole densities will be trickier than imaging at high electron densities, and would rely heavily on a careful choice of V_{bias} for scanning. The flatter G_t spectrum at high hole doping also implies lower sensitivity to a given spatial inhomogeneity which manifests as a lower standard deviation in the $G_t(x, y)$ maps (notice color bar scale of Figure 5.20(f) and 5.21(g)).

CITS near charge neutrality

Figure 5.22, summarizes the main findings from the complete CITS at $V_{gate} = 30\,\mathrm{V}$ which corresponds to the charge neutrality point in transport. However, the region under investigation is different from that in Figure 5.20 or Figure 5.21 [9], hence a direct comparison is not possible as before. Nevertheless, it is still possible to find out the statistics related to the local E_D^0 distribution as before. We find the Dirac point fluctuations to be about 36 meV and the corresponding doping fluctuations $n_{rms} = 4.77 \times 10^{11}\,\mathrm{cm}^{-2}$. We note that in this case $\bar{n} = 1.79 \times 10^{11}\,\mathrm{cm}^{-2} \ll n_{rms}$, hence this indeed corresponds to the low density regime.

[9] Due to technical difficulties.

We note here, that the values of σ_{E_D} and n_{rms} that we measure in this case, also listed in table 5.3, may be erroneous. This is because the ZBA and V'_{min} lies in close proximity in the G_t spectra. This renders an unambiguous detection of V'_{min} difficult. In this respect, measuring away from the primary minimum, as in Method 2 presented in the subsequent section, may give a more accurate description of the amplitude of the inhomogeneities. For example, the correlation length ξ (section 2.4.2) associated with the features in the Dirac point map is only 4.2 nm while it increases in the correlated $G_t(x, y)$ maps (g) to 7 nm which is perhaps closer to the actual value.

The 2D correlation coefficient $\chi^0_{E_D-G_t}$ (Figure 5.22(e)) is zero at $V_{bias} = 0$ and rises equally on both sides of the primary minimum which is expected and well understood. Therefore choosing either side i.e. $(< V'_{min} > +0.1\,\text{V})$ or $(< V'_{min} > -0.1\,\text{V})$ for measuring the carrier density fluctuations would give a proper visualization of the E^0_D distributions as additionally verified in (f) and (g). For $V_{bias} > (< V'_{min} > +0.1\,\text{V})$, $\chi^0_{E_D-G_t}$ remains at ≈ -0.6, at least within the measurement window, but drops rapidly at high negative V_{bias}. This drop in correlation is probably related to the onset of scattering from doping inhomogeneities at high energies resulting in lower puddle sizes as seen in Figure 5.19. However, the situation is once again found to be asymmetric for hole states ($V_{bias} < 0$) and electron states ($V_{bias} > 0$).

The following table lists the summary of the main results found from the three CITS presented above.

V_{gate} (V)	$\bar{E_D}$ (meV)	$\bar{n}$ ($\times 10^{11}\,\text{cm}^{-2}$)	V'_D (V)	σ_{E_D} (meV)	n_{rms} ($\times 10^{11}\,\text{cm}^{-2}$)	ξ (nm)
70	-203.7	30.98	36.8	28.3	8.99	7.3
30	40.7	1.79	31.3	36.1	4.77	4.2
-15	238.7	35.59	16.0	42.1	13.51	7.8

Table 5.3: Comparison of parameters extracted from CITS at high electron doping $V_{gate} = 70\,\text{V}$, high hole doping $V_{gate} = -15\,\text{V}$ and near charge neutrality $V_{gate} = 30\,\text{V}$. $\bar{E_D}$ and $\bar{n}$ are the mean Dirac point and carrier concentration respectively, σ_{E_D} and n_{rms} are the standard deviations in E_D and n respectively, V'_D is the gate voltage at which the primary minimum V'_{min} of $< G_t >$ would be zero.

Comparison with theory

The question now is whether σ_{E_D} that we find at the three different carrier concentrations agree with what is expected from the value of (n_{imp}, d) found from transport (table 5.1)? The inhomogeneities being induced by the disordered impurity potential on the substrate, should be related to the screened disorder potential $\tilde{V}_{rms}$ as discussed in section 2.4.2. In the complete screening limit obtained at large carrier densities, the fluctuations in the Dirac point should be

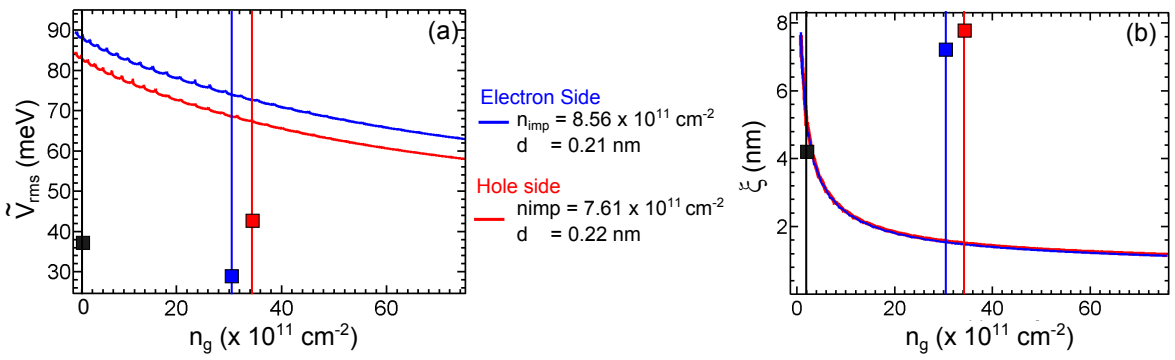

Figure 5.23: Comparison of local fluctuations with expected values from transport. (a) Variation of the fluctuations in the screened disorder potential $\tilde{V}_{rms}$ with carrier concentration n_g. (b) Variations in the correlation length of the screened disorder potential with n_g. Solid lines are calculated using (n_{imp}, d) obtained from transport (table 5.1). For calculation method, see text 5.4.2.

equal to the fluctuations in the screened disorder potential (section 2.4.2) i.e.

$$\sigma_{E_D} = \tilde{V}_{rms} = \sqrt{C(0)} \tag{5.4.3}$$

where $C(0)$ is given by Eq.(2.4.15). To calculate $C(0)$ at a given carrier concentration n_g, we consider a Gaussian distribution $n(r)$ with mean $\bar{n} = n_g$ and standard deviation n_{rms} calculated self-consistently following the procedure outlined in 6. The mean $C(0)$ of this distribution has been considered as the value of $C(0)$ at n_g.

Figure 5.23(a) shows the variation of this $C(0)$ with n_g for two different sets of (n_{imp}, d). The red and blue solid lines are calculated assuming (n_{imp}, d) obtained from transport (table 5.1) for the electron and hole side respectively. The red, blue and black squares represent the experimentally measured values for the CITS at the three different carrier concentrations [10].

It is quite obvious that the fluctuations measured in the CITS do not agree with what is derived from the parameters extracted from transport. The amplitude of disorder is significantly less. We must note here that Eq.(5.4.3) is true only in the complete screening limit whereas in the present experiment, this limit was never reached. For both CITS, at $V_{gate} = -15\,\mathrm{V}$ and $V_{gate} = 70\,\mathrm{V}$, the carrier densities lie in the intermediate regime where the theory is not well described, as discussed in section 2.4.2. We must also note that due to lack of a good spatial resolution in the CITS, σ_{E_D} and n_{rms} measured is subjected to finite error.

Figure 5.23(b) shows the change in the correlation length as a function of n_g, calculated using Eq.(2.4.27) [11] also for the two different sets of (n_{imp}, d) as discussed above (indicated in figure).

[10] n_g for the CITS at $V_{gate} = -15\,\mathrm{V}$ and $70\,\mathrm{V}$ is not $\bar{n}$ of the distribution but calculated from the relation given in table 2.1

[11] By method 2 discussed in section 2.4.2

In table 5.3, ξ found from the Dirac point maps at the three different carrier concentrations have been listed. Once again, the poor agreement is due to the lack of sufficient spatial resolution. However, for the CITS conducted at charge neutrality point i.e. $V_{gate} = 30\,\mathrm{V}$, we find $\xi = 4.2\,\mathrm{nm}$ and for the best correlated $G_t(x, y)$ map (Figure 5.22(g)), $\xi = 7\,\mathrm{nm}$ which comes very close to the theoretically predicted value.

To summarize, using the CITS measurements, the doping inhomogeneities in graphene has been probed at high electron and hole concentrations as well as close to charge neutrality. Although a clear quantitative comparison with theory is not possible at this stage due to lack of spatial resolution, the measurements clearly validate the technique for imaging the charge puddles, that has been discussed in section 5.18.

5.4.3 Gradual evolution of Charge disorder with Carrier Concentration

In the last section, we employed the process of acquiring the full differential tunneling conductance spectrum at each designated spatial location of a given region to investigate the fluctuations in the Dirac point E_D^0. Although we were able to measure σ_{E_D} at three different carrier concentrations, the measurements lacked the spatial resolution needed to observe the small coherence lengths at large carrier concentrations. Also, because of the large measurement time involved, we were unable to track the gradual evolution $\tilde{V}_{rms}$ or ξ with carrier concentration. In this section, we overcome these limitations by employing the second method of imaging $G_t(x, y)$ at a well chosen bias voltage $(V_{bias})_{set}$ [Eq.(5.4.1)], to track the evolution of the disordered landscape of the screened impurity potential with carrier concentration at two different locations.

Experimental Details

To acquire a series of $G_t(x, y)$ maps at different backgate voltages using method 2 (section 5.4.1), the first step involves the preparation of a list of bias voltages $(V_{bias})_{set}$ at which the image scans are to be conducted. This requires the knowledge of the variation of V'_{min} wrt. V_{gate} in order to follow our imaging criteria described by Eq.(5.4.1). Hence, a $G_t(V_{bias}, V_{gate})$ map is obtained at a given location just prior to this measurement. This gives the required information about the primary minimum which enables the preparation of the list of $(V_{bias})_{set}$ [12].

However, this is not very trivial as an unambiguous determination of V'_{min} is difficult in most cases, especially at low densities. Also, it must be clarified, that at the time of performing the measurements, the difference between the V'_{min} and E_D^0 was not very well understood. Hence at the two locations, two different selection criteria for $(V_{bias})_{set}$ were eventually implemented, different from that given by Eq.(5.4.1). Figure 5.24 shows the chosen $(V_{bias})_{set}$ wrt. V'_{min} at the two different locations. For Location 1 in (a), the selection was done based on the position of

[12] Perhaps a better method would have been to measure at G_t vs V_{bias} spectrum for a given V_{gate} at multiple locations and then determine the average spectrum for identifying V'_{min}.

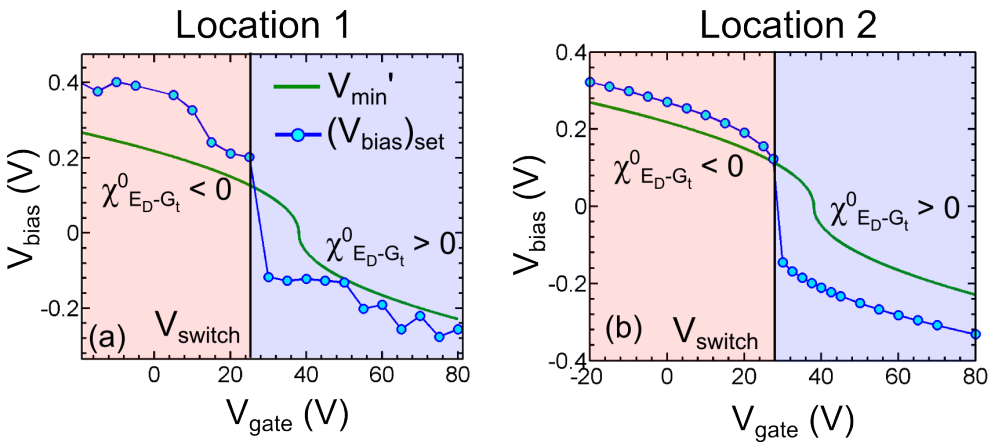

Figure 5.24: The voltage bias set for scanning $(V_{bias})_{set}$ at different V_{gate} wrt. the location of the primary minimum V'_{min} (Eq.(5.3.13) with $V'_D = 38\,\mathrm{V}$ in accordance with point 2 and 3 of table 5.2). $\chi^0_{E_D-G_t}$ gives the 2D correlation coefficient of the differential tunneling conductance map $G_t(x, y)$ with the Dirac point map $E_D(x, y)$. The sign is assigned based on our discussion in section 5.4.2. (a) For Location 1 and (b) for Location 2. V_{switch} gives the gate voltage beyond which $(V_{bias})_{set}$ switches sign which for Location 1 ia at 25 V and for Location 2 is at 27.5 V.

V'_{min} extracted from the G_t spectrum at different V_{gate}. The uneven choice of $(V_{bias})_{set}$ reflects the crudeness of detection of V'_{min} in this way. For Location 2, the theoretical Eq.(5.3.2) (with $V^0_D = 30\,\mathrm{V}$) was used to obtain E^0_D at different V_{gate}. Then assuming $E^0_D = V'_{min}$, $(V_{bias})_{set}$ was chosen in a manner given by Eq.(5.4.1).

In Figures (5.25 and 5.26) (a) gives the G_t gate map measured at a single point right before imaging the puddles while (b) gives the same but with different curves superposed. Table 5.4 lists the definition of each.

Quantity	Definition
E^0_D	Dirac point position without considering tip induced gating [Eq.(5.3.2)]
V'_{min}	The primary minimum of the tunneling conductance G_t spectrum.
$(V_{bias})_{set}$	Bias voltage set for imaging puddles.
$[V'_{min}]_1$	V'_{min} extracted by fitting a parabola about the minimum (also described in section 5.4.2).
$[V'_{min}]_2$	Derived by visually estimating the position of V'_{min} from the gate map in a manner discussed in section 5.3.5

Table 5.4: Summary of the different relevant voltages for mapping the puddles.

Once the list of $(V_{bias})_{set}$ has been decided, the following steps just involve setting V_{gate} and V_{bias} according to the prepared list with tip in retracted position for safety, then approaching

and stabilizing the tip before scanning and finally scanning over the given region with closed z-feedback i.e. in constant current mode.

The Puddles

Figures (5.25 and 5.26) (c) show the set of $G_t(x, y)$ maps that track the gradual evolution of the 'electron-hole puddle ' landscape as V_{gate} is tuned from high hole concentration ($V_{gate} \ll V_D^0 = 30\,\mathrm{V}$) to charge neutrality ($V_{gate} = V_D^0$) and eventually to high electron concentration ($V_{gate} \gg V_D^0$). Both the spatial dimension as well as the amplitude of the features in the $G_t(x, y)$ maps is clearly seen to increase as the gate voltage approaches charge neutrality i.e. $V_{gate} \to V_D^0$. This is a direct consequence of the fact that at high carrier concentrations, the underlying disordered potential is strongly screened leading to reduction in induced inhomogeneity whereas at low carrier densities, screening is week and the underlying disordered potential renders the graphene strongly disordered, hence accounting for the large e-h puddles.

To better understand the evolution with V_{gate}, let us go over the $G_t(x, y)$ maps from high hole doping to high electron doping. At Location 1 (Figure 5.25(c)), from $V_{gate} = -20\,\mathrm{V}$ to 25 V, we do observe the puddles to gradually grow in size and come into prominence. A contrast reversal occurs between 25 V and 30 V which is related to the sign change in $(V_{bias})_{set}$. We can explain this by once again considering the 2D correlation coefficient $\chi^0_{E_D-G_t}$ between $G_t(x, y)$ and the Dirac point map $E_D(x, y)$. Based on our analysis of $\chi^0_{E_D-G_t}$ in section 5.4.2, the positive or negative sign of the correlation has been depicted in Figure 5.24 for the different $(V_{bias})_{set}$ for both locations. For location 1 [in (a)], the switch in sign of $\chi^0_{E_D-G_t}$ occurs between 25 V and 30 V which explains the contrast reversal. However, another contrast inversion occurs between 40 V and 45 V. From Figure 5.24(a), this cannot be explained but if we consider the possibility that due to the uneven nature of $(V_{bias})_{set}$, the V'_{min} vs V_{gate} curve intersects it between 40 V and 45 V, then this would account for the contrast change. Beyond 45 V, the puddle sizes decrease in a consistent manner. For Location 2 (Figure 5.26), the choice of $(V_{bias})_{set}$ captures the evolution of the puddles in a more consistent fashion. In this case, the puddles grow systematically in size till $V_{gate} = 27.5\,\mathrm{V}$ beyond which the switch in contrast occurs, clearly explained by Figure 5.24(b). On further increasing V_{gate}, the large puddles are gradually fragmented to give rise to smaller ones at high electron densities.

We distinctly notice that a stronger disorder persists at higher electron doping than in the equivalently hole doped graphene at both locations (first and last G_t image at each location, for example). In case of Location 2, one might suspect this to be the result of scanning too close to the primary minimum (Figure 5.26(a)) in the hole doped side which causes confinement of the electronic states being probed (situation demonstrated schematically in Figure 5.15(c)), and hence QPIs may follow leading to decrease in size of the features. However, at Location 1, on the hole doped side, the scan voltages chosen were sufficiently far from V'_{min} (Figure 5.25(a)). On the contrary, scan voltages used for probing electron doped graphene were perhaps too close to

the primary minimum in this case. Nevertheless, we continue to observe this asymmetry between electron and hole doped graphene. This seems to be related to the asymmetry that was found in the CITS measurements discussed in section 5.4.2 where the tunneling spectrum at high hole doping (Figure 5.21(c)) was found to be flatter about V'_{min} than at high electron doping (Figure 5.20(c)). Both observations tend to imply a relative difficulty in imaging of puddles at high hole concentrations.

Therefore, we see that tuning the gate voltage causes the lateral and longitudinal scale of screened potential fluctuations to change. The fluctuations increase as the charge neutrality point is approached (maximum achieved near V'_D) and subside away from it at high carrier concentrations. A distinct asymmetry exists between electron and hole doping as larger puddle sizes persist at higher electron doping than at an equivalent amount of hole doping. This observation is common to all locations measured, although different criteria were used to set the bias voltage.

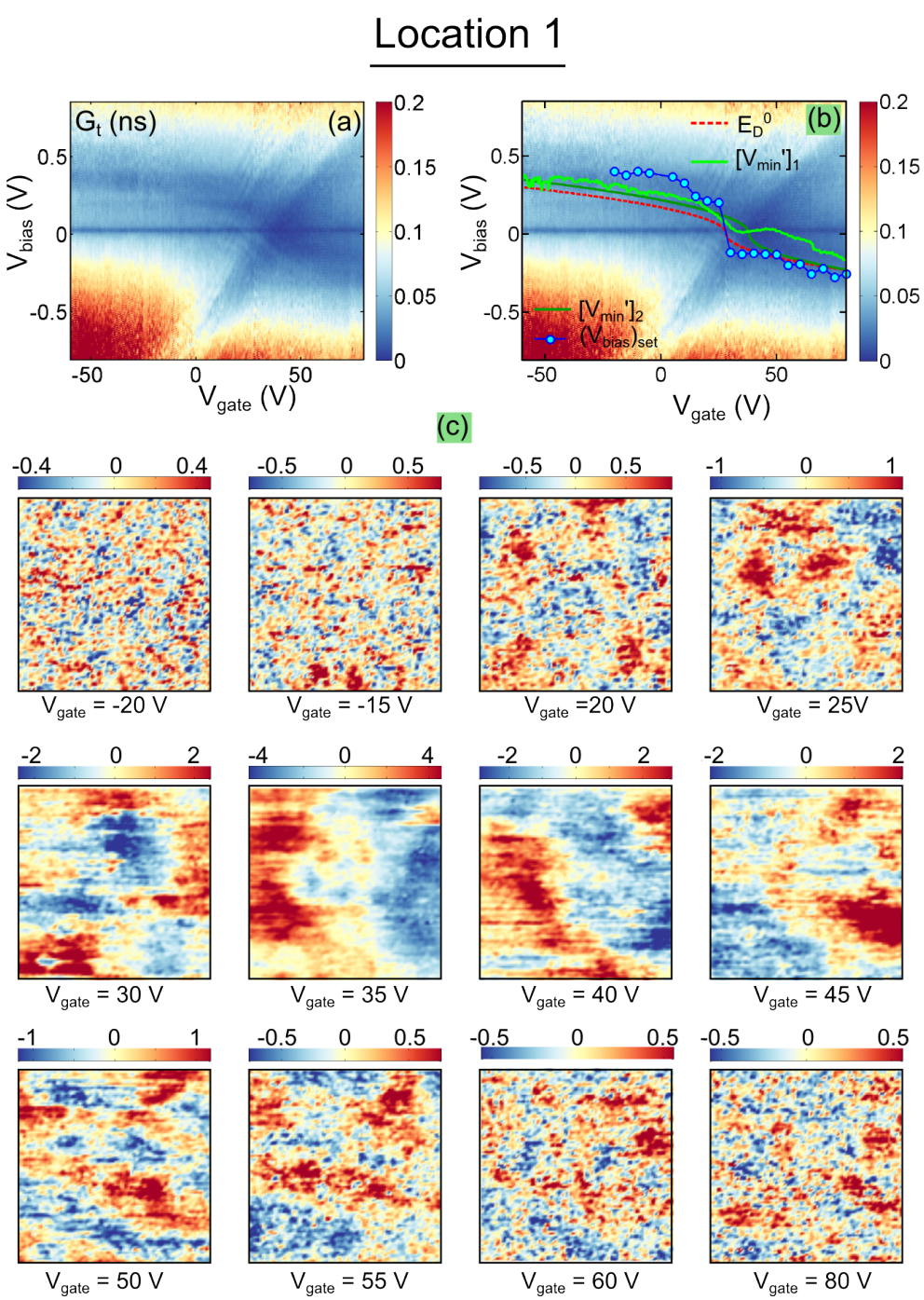

Figure 5.25: Evolution of charge disorder with carrier concentration at Location 1. (a) G_t gate map (in ns) acquired at a single point, just before imaging the charge disorder (same as Point 1 in Figure 5.17). (b) The same as (a) but with different relevant voltages superposed which are described in table 5.4. (c) Spatial maps of differential tunneling conductance at different V_{gate} for Location 1 over an area of 40 nm × 40 nm, resolution = 0.39 nm. Imaging parameters : $I_t = 100\,\text{pA}$, $V_{bias} = (V_{bias})_{set}$, $V_{AC} = 6\,\text{mV}$, $f_{AC} = 322.4\,\text{Hz}$, $\tau_{lock-in} = 10\,\text{ms}$, scan speed = 10 nm/s.

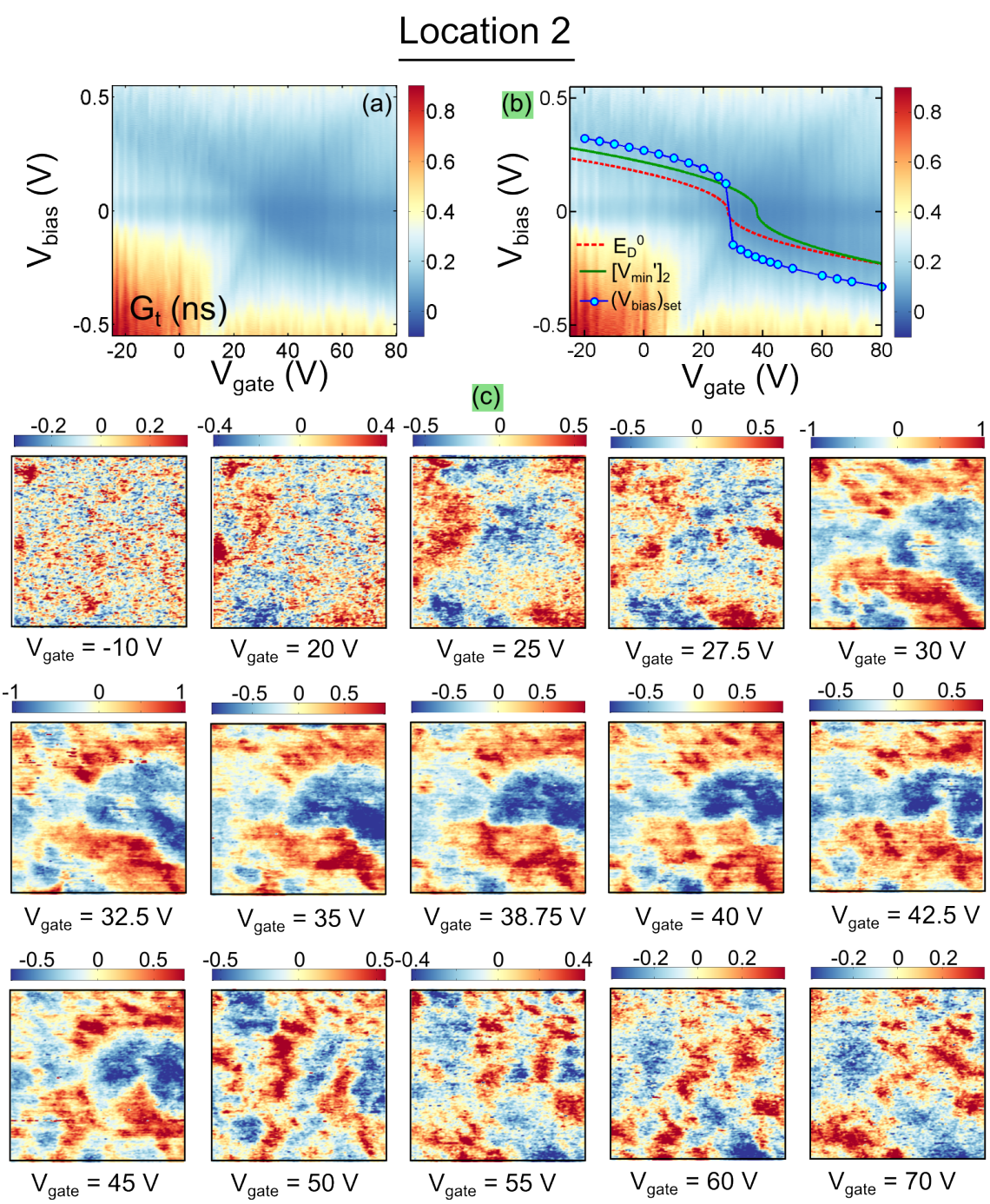

Figure 5.26: Evolution of charge disorder with carrier concentration at Location 2. (a) G_t gate map (in ns) acquired at a single point, just before imaging the charge disorder (same as Point 3 in Figure 5.17). (b) The same as (a) but with different relevant voltages superposed which are described in table 5.4. (b) Spatial maps of differential tunneling conductance at different V_{gate} for Location 2 over an area of 100 nm × 100 nm, resolution = 256 pxls.. Imaging parameters : I_t = 50 pA, V_{bias} = $(V_{bias})_{set}$, V_{AC} = 12 mV, f_{AC} = 322.4 Hz, $\tau_{lock-in}$ = 10 ms, scan speed = 10 nm/s.

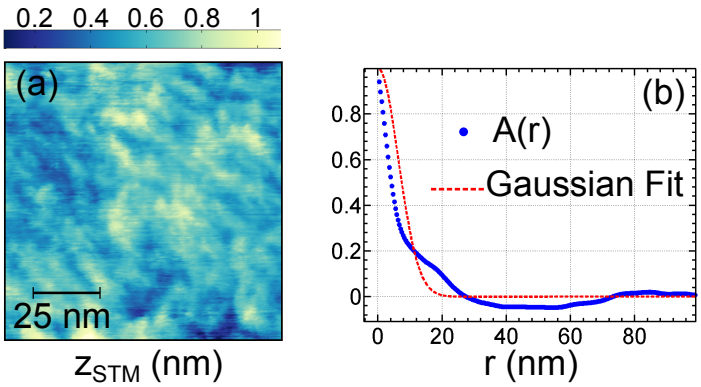

Figure 5.27: Topography of graphene in STM. (a) STM topography of Location 2 in Figure 5.26 at $V_{gate} = 27.5\,\mathrm{V}$. Roughness is about 0.124 nm. (b) Angular averaged, normalized auto-correlation $A(r)$ of the STM topography shown in (a). FWHM extracted from Gaussian fit (red dashed line) is about10 nm which gives the lateral roughness.

Correlation with Topography

In the previous section, we have studied the gradual evolution of the $G_t(x, y)$ maps with V_{gate}. Now let us look at the corresponding changes in the simultaneously acquired STM topography. Figure 5.27(a) shows the STM topograph of $100\,\mathrm{nm} \times 100\,\mathrm{nm}$ region corresponding to Location 2 (Figure 5.26) at $V_{gate} = 27.5\,\mathrm{V}$. The roughness is found to vary between $(0.06 - 0.2)\,\mathrm{nm}$ and the spatial dimension of the corrugations is about 10 nm (Figure 5.27(b)) which is consistent with what is found in literature [181].

Figure 5.28 shows the change in the STM topography with backgate, in particular, the apparent surface roughness in (a) and the 2D correlation coefficient with the simultaneously acquired $G_t(x, y)$ map in (b). We find that at both locations, the STM surface roughness increases as charge neutrality point V_D^0 is approached and reduces at higher concentrations. The maximum roughness is achieved at $V_{gate} = 35\,\mathrm{V}$ at Location 1 and at $V_{gate} = 27.5\,\mathrm{V}$ at Location 2. For the second case, this maximum position coincides with V_{switch} (Figure 5.24(a)) but for the first location, this is not the case since $V_{switch} = 25\,\mathrm{V}$ (Figure 5.24(b)). $\chi^0_{z-G_t}$ also shows a dependence on V_{gate}. Approaching V_D^0 from high hole doping, $\chi^0_{z-G_t}$ first decreases from ≈ 0 to negative values, then increases to positive values and then subsides again to smaller positive values at high electron doping. In (c),(d) and (e),(f), topography and the simultaneously acquired $G_t(x, y)$ maps are shown corresponding to largest negative and positive correlation respectively which do show a small resemblance to each other.

The reason for the variation of the STM topography with V_{gate}, found at both locations, is clearly related to the increase in inhomogeneities in the DOS at low carrier concentrations. This is because in STM, the topography is the convolution of the actual topography and the DOS Eq.(3.2.2), hence strong fluctuations in the DOS will tend to produce strong variations in

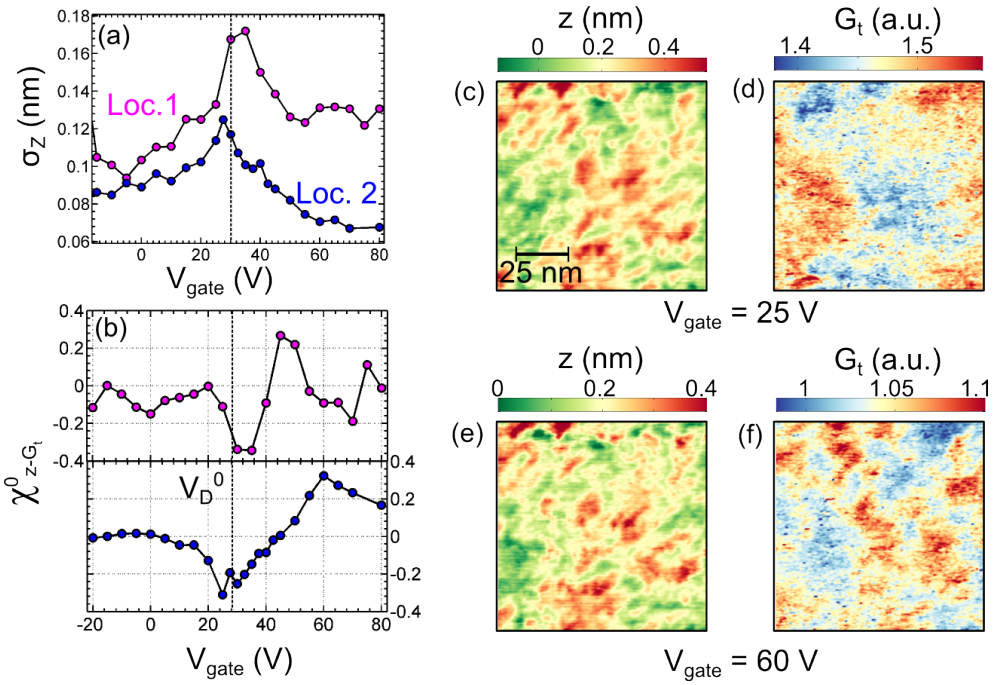

Figure 5.28: Change of (a) surface roughness σ_z and (b) 2D correlation coefficient between topography and the simultaneously acquired $G_t(x,y)$ map $\chi^0_{z-G_t}$ [Eq.(5.4.2)] with V_{gate} for Location 1 (Figure 5.25) and 2 (Figure 5.26). (c) STM Topography and (d) the corresponding $G_t(x,y)$ map for $V_{gate} = 25\,\mathrm{V}$ (maximum negative correlation), for Location 2. (e) STM Topography and (f) the corresponding $G_t(x,y)$ map for $V_{gate} = 60\,\mathrm{V}$ (maximum positive correlation), for Location 2.

the tunneling current I_t. I_t being maintained constant during imaging of the puddles in STM, the fluctuations will be reflected as an apparent topography with higher corrugations. However, the explanation for the observed variation in χ_{z-G_t} is not very clear, and would require further investigation.

5.4.4 Correlations at Different carrier densities

The differential tunneling conductance maps presented in Figure 5.25 and 5.26 have shown quite explicitly that both the lateral and longitudinal scale of screened disorder potential fluctuations dramatically increase as charge neutrality point is approached. The correlation function $C(r)$, that we have discussed in detail in section 2.4.2, provides a good way to quantitatively characterize these fluctuations. It can be considered to be composed of two distinct parts: (1) the amplitude of the fluctuations and (2) the spatial extent, as given by Eq.(2.4.11). In this section, we calculate these two quantities for the measured DOS maps and compare them with what is expected from the transport measurements, summarized in table 5.1.

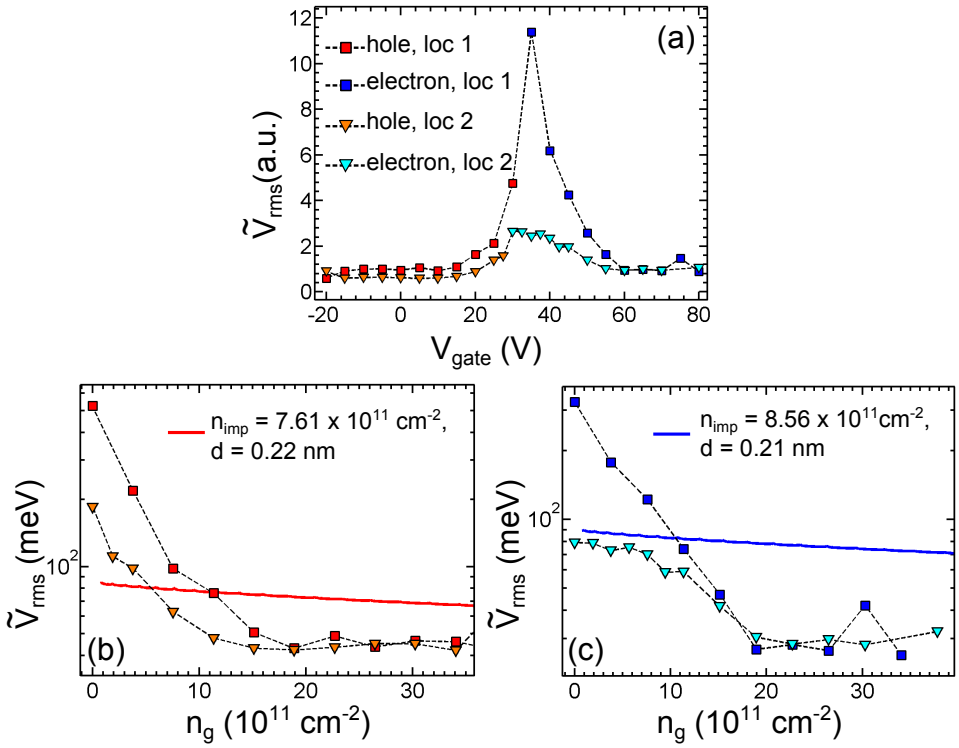

Figure 5.29: RMS amplitude of fluctuations of screened disorder potential. (a) Experimentally measured $\tilde{V}_{rms}$ at the two different locations as a function of V_{gate}. Curves have been normalized wrt. value at high electron densities. (b) Variation of $\tilde{V}_{rms}$ with carrier concentration n_g for hole doped and (c) for electron doped graphene. The solid line is the same as shown in Figure 5.23, calculated using (n_{imp}, d) found in transport (table 5.1).

Amplitude of Fluctuations of the Screened disorder potential

The amplitude of fluctuations in the screened disorder potential or $\tilde{V}_{rms}$ can be considered to be directly proportional to the standard deviation of the $G_t(x, y)$ maps. This is because, as explained in section 5.4.1, an infinitesimal fluctuation in the screened potential translates into an infinitesimal fluctuation of the Dirac point which in turn causes an infinitesimal change in G_t. Hence, up to a multiplicative factor, the two fluctuations should be related. Alternatively, the central element of the cross-correlation matrix can be used to find the RMS amplitude of the fluctuations. The cross-correlation of a matrix $(A - \bar{A})$ of dimension $M \times N$ and mean $\bar{A}$, with itself is given by

$$C(i,j) = \frac{\sum_{m=1}^{M}\sum_{n=1}^{N}\left(A_{m,n} - \bar{A}\right)\left(A_{m-i,n-j} - \bar{A}\right)}{M \times N}. \tag{5.4.4}$$

From this definition, it is easy to see that $C(0) = \sigma_A^2/MN$. Therefore, the standard deviation of the $G_t(x, y)$ images can be obtained either in this way or directly. The fluctuations in the screened disorder potential is then simply $\tilde{V}_{rms} \propto \sigma_{G_t}$.

In Figure 5.29(a), $\tilde{V}_{rms}$ obtained in the above way, for the set of $G_t(x, y)$ maps shown in

Figure 5.25 and 5.26, has been plotted as a function of V_{gate} for the two different locations. The curves have been normalized wrt. their value at high electron doping. We now see quantitatively that the amplitude of the fluctuations gradually build up towards charge neutrality and subside away from it. The extent of increase measured in the two locations is different. This is certainly related to the difference in set-point parameters used for acquiring the images in the two cases in terms of choice of both V_{bias} and I_t ($I_t = 100\,\text{pA}$ in the case of Location 1 and 50 pA for Location 2).

In section 5.4.2, we had quantitatively measured the RMS value of the Dirac point fluctuations ($= \tilde{V}_{rms}$) at high hole and electron doping (table 5.3). Using these values, we can rescale the curves plotted in (a). This allows us to convert the RMS fluctuations in differential tunneling conductance i.e. σ_{G_t} in units of energy. This has been separately carried out for the electron and the hole side. In Figure 5.29(b) and (c), the rescaled values have been plotted together with theoretically calculated ones using the procedure described in section 5.4.2. The solid lines have been calculated for (n_{imp}, d) suggested by transport while to calculate the dashed lines, d has been changed to match the value at high doping suggested by the CITS measurements. However, we see clearly that the observations are not in agreement with the theoretical fits.

The discrepancy could be related to the gating effect exerted by the tip on the graphene which causes the Dirac point of the graphene right below it to change from E_D^0 [Eq.(5.3.2)] to E_D' [Eq.(5.3.11)]. Additionally, the primary minimum V'_{min} in the G_t spectrum no longer corresponds to E_D^0 as we have discussed in section 5.3.4. In such a situation, it is actually not so obvious that all three of these important energy locations will follow the same inhomogeneous doping profile existing on the sample. From a differential tunneling conductance spectrum in graphene, since the directly measurable quantity is V'_{min}, it is important to understand whether this correctly reproduces a given doping profile along the graphene surface.

Figure 5.30(a) shows the schematic of a STM tip positioned over graphene with inhomogeneous doping indicated by the red and blue regions. The actual doping profile without influence of the tip is given by E_D^0 which is indicated by the orange lines in (b),(c) and (d). The change in E_D^0 is considered to be equal to the RMS value of the screened disorder potential i.e. $\Delta E_D^0 = \tilde{V}_{rms}$. Since $\tilde{V}_{rms}$ changes with V_{gate}, ΔE_D^0 changes accordingly. In (e), the orange curve shows this change as a function of V_{gate} which is calculated using the same parameters as the red dashed curve in Figure 5.29(b). To correctly measure this doping profile, we would require V'_{min} (indicated by the green line) to reproduce the behavior of E_D^0. However, we see that this is not the case. Away from charge neutrality, the agreement is reasonable but towards it, $\Delta V'_{min}$ is magnified to almost 2.5 times the actual value (ΔE_D^0) in the present example.

The maximum value of $\Delta V'_{min}$ depends directly on the work-function mismatch Δ and inversely on the tip-sample distance z_{ts}. This might account for the difference in the increase of $\tilde{V}_{rms}$ observed in the two locations (Setpoint current I_t at location 1 was 100 pA and at Location 2 was 50 pA as stated in Figure 5.25 and 5.26). Further, this seems to roughly explain the other

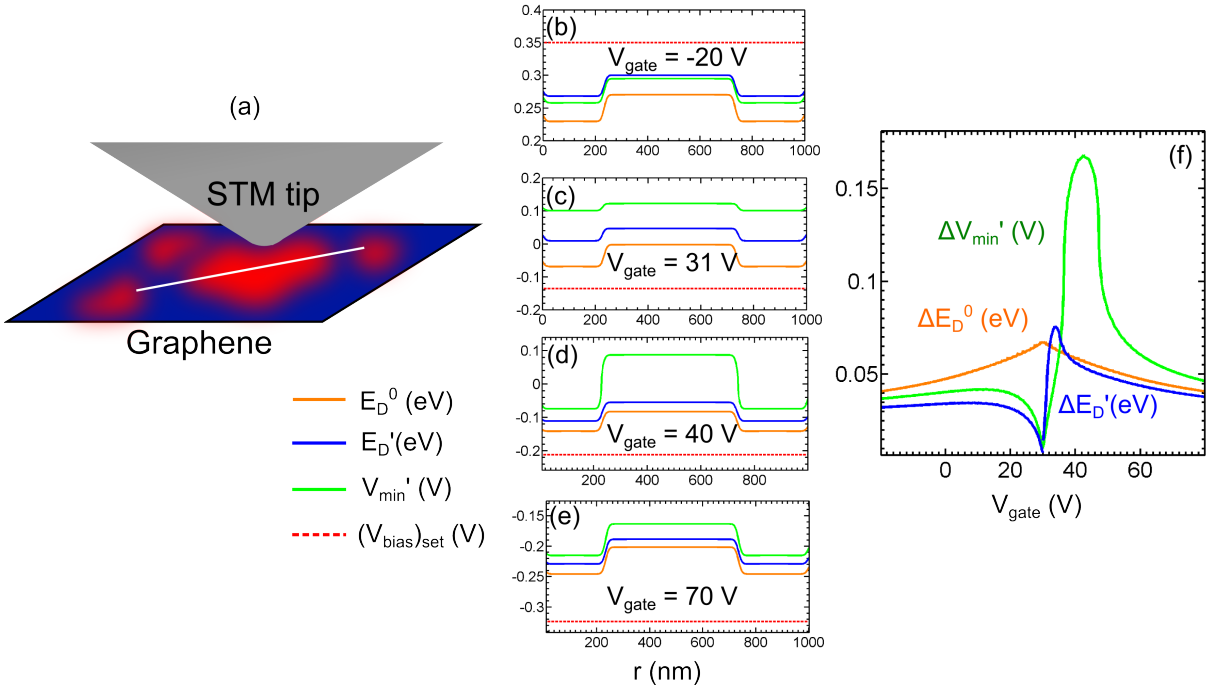

Figure 5.30: Calculation of the role of the tip in influencing the Inhomogeneity. (a) Schematic showing the STM tip positioned on graphene with inhomogeneous doping. (b)-(e) Profile along the white line in (a) of the Dirac point unperturbed by tip E_D^0 [Eq.(5.3.2)], with tip influence E_D' (Eq.(5.3.11), $\Delta = -0.213\,\mathrm{V}$, $z_{ts} = 1.4\,\mathrm{nm}$) and the primary minimum V'_{min} wrt. the bias voltage chosen for scanning $(V_{bias})_{set}$ at four different gate voltages. The charge neutrality point is at $V_D^0 = 30\,\mathrm{V}$. The inhomogeneity in the E_D^0 distribution is given by $\Delta E_D^0 = \tilde{V}_{rms} = \max(E_D^0) - \min(E_D^0)$ where $\tilde{V}_{rms}$ is calculated for $n_i mp = 7.6 \times 10^{11}\,\mathrm{cm}^{-2}$ and $d = 0.7\,\mathrm{nm}$, following the process discussed in section 5.4.2.

observations in the experimentally measured $\tilde{V}_{rms}$ vs V_{gate} curves shown in Figure 5.29(a): that the maximum value of V'_{min} is shifted wrt. V_D^0 and that the rise in $\Delta V'_{min}$ from high doping to low doping is asymmetric for hole doped and electron doped graphene.

Method to extract Puddle Size

Although quantitative detection of the amplitude of screened potential fluctuations by STS is difficult, as illustrated in Figure 5.30, the spatial extent of the inhomogeneities is correctly tracked by V'_{min} as seen in (b),(c) and (d). Hence, let us now discuss the method by which we can extract the spatial dimension of the fluctuations in the $G_t(x, y)$ maps at different backgate voltages.

Figure 5.31 demonstrates the procedure that has been adopted to extract the lateral scale of fluctuations in the $G_t(x, y)$ maps shown in Figures 5.25 and 5.26. We start with a given image of electron-hole puddles, Ψ. As a first step, the mean is subtracted to obtain $\Psi - \langle\Psi\rangle$ (Figure 5.31(a)). The images are then filtered using a Gaussian filter with FWHM of about 0.55 nm. Since, the smallest size of puddles at high carrier densities $\approx 1.5\,\mathrm{nm}$, this level of filtering should

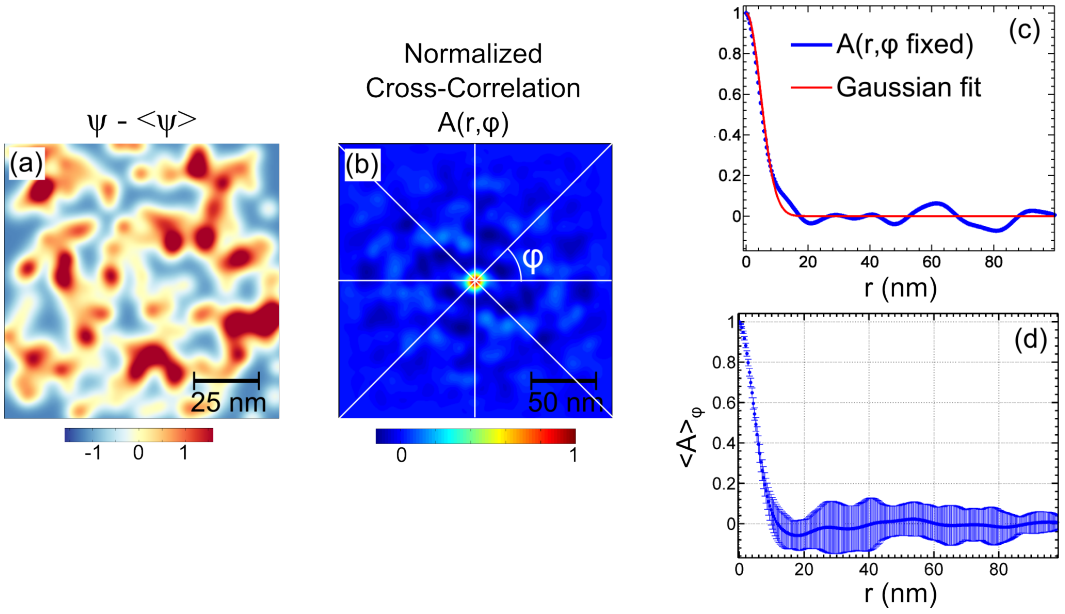

Figure 5.31: Demonstration of finding correlations from a given image of charge puddles. (a) Simulated image of charge puddles. Each puddle is constructed from a Gaussian function. The size and position of the puddles are randomly generated. This image contains 200 puddles with $\sigma = (3.1 \pm 0.3)\,\text{nm}$. (b) Corresponding normalized cross-correlation matrix $A(r, \phi) = C(r, \phi)/C(0)$. (c) Profile of A along a single cut in a given direction ϕ as indicated in (b) with a Gaussian fit. (d) Angular average of A. Length of error bars $Err(r) = [max\{A(r, all\phi)\} - min\{A(r, all\phi)\}]/2$.

be permissible. Next, we find the cross-correlation matrix of image $\Psi - \langle\Psi\rangle$ with itself using Eq.(5.4.4). Dividing by the central element i.e. $C(0)$ gives the normalized cross-correlation matrix $A = C/C(0)$. (c) shows a cut in this matrix $A(r, \phi)$ along a fixed direction ϕ. Fitting this curve with a Gaussian function of the form $G(r) = \exp\left(-\frac{r^2}{4\sigma^2}\right)$ (indicated by the red line in (c)), gives us the decay length σ of the correlation curve for this direction. Repeating this process for several directions and considering the mean curve gives the angular averaged, normalized correlation function $\langle A\rangle_\phi$. The mean of σ gives the average decay length of the correlation curve and the standard deviation can be considered as the associated error. This error is an indication of the non circular shape of the puddles and can be significant for large puddle sizes.

This forms a standard way to extract the characteristic dimension of repetitive features in a given image, which in our case are the puddles. Since this is a statistical process, we have to bear in mind that the lengths extracted in this manner are a rough estimate and not entirely accurate. This is especially true when the size of the puddles are significantly large compared to the image area and when large number of puddles fuse to form a huge blob. To get an estimate of the amount of error we introduce in this process, let us consider the table 5.5 which lists the results of applying the above process to simulated images of Gaussian puddles.

The first column lists the size (σ) of the Gaussian puddles considered for the simulations. We see that for one single puddle, fit with the function $G(x)$ accurately determines the puddle size.

σ_p^{In}	$\left[\sigma_p^{Out}(\Psi)\right]_{N=1}$	$\left[\sigma_p^{Out}(\Psi-\langle\Psi\rangle)\right]_{N=1}$	$Err_{N=1}$	$\left[\sigma_p^{Out}(\Psi-\langle\Psi\rangle)\right]_{N=86}$	$Err_{N=86}$
(10.0 ± 0.4) nm	9.9 nm	8.6 nm	16.3%	(6.1 ± 0.6) nm	38%
(8.0 ± 0.4) nm	8.0 nm	7.6 nm	11.0%	(6.4 ± 0.7) nm	21%
(5.9 ± 0.4) nm	5.9 nm	5.5 nm	6.2%	(5.1 ± 0.8) nm	14%
(4.0 ± 0.4) nm	4.0 nm	3.8 nm	2.7%	(3.8 ± 0.3) nm	3%

Table 5.5: Estimation of error for extraction of the puddle size from the Correlation method. The image size considered for simulation is about 100 nm × 100 nm. σ_p^{In} denotes the size of of the Gaussian puddles (σ of the Gaussian function) considered for the simulation, $\left[\sigma_p^{Out}(\Psi)\right]_{N=1}$ is the size extracted from an image consisting of a single puddle Ψ, $\left[\sigma_p^{Out}(\Psi-\langle\Psi\rangle)\right]_{N=1}$ is the same but with mean subtracted i.e. for $\Psi-\langle\Psi\rangle$ and $Err_{N=1}$ is the percentage error in estimating the size of a single puddle from image $\Psi-\langle\Psi\rangle$. $\left[\sigma_p^{Out}(\Psi-\langle\Psi\rangle)\right]_{N=86}$ and $Err_{N=86}$ is the same as above but for 86 puddles per 100 nm × 100 nm.

The act of subtracting the mean from the image of the single puddle already introduces a finite error ($Err_{N=1}$) that increases with the puddle size. Now if we consider number of puddles to be $N = 86$ in an area of 100 nm × 100 nm (since $n_{imp} \approx 8.6 \times 10^{11}$ cm^{-2}, table 5.1), then we find that the error percentage increases even more $Err_{N=86}$. In particular, this process underestimates the puddle size by an amount dependent on the size itself.

Nevertheless, in lack of a better solution, we adopt the process of fitting the angular averaged, normalized correlation curves with a Gaussian function of the form $G(r)$, to extract the puddle size. Moreover, Gaussian mapping of the Coulombic impurity potential happens to be a popular choice among theoreticians [56] which allows one to relate the correlation length ξ to the carrier concentration n_g using Eq.(2.4.27). Note that the correlation length and puddle size are related by $\xi = \sigma\sqrt{2}$.

Lateral Extent of Disorder: The Puddle Size

Using the method described in the previous section 5.4.4, the angular averaged, normalized correlation curves $A(r) = \langle A\rangle_\phi$ have been extracted for the $G_t(x, y)$ maps shown in Figure 5.25 and 5.26. Figures 5.32(a) and (c) show the evolution $A(r)$ at different gate voltages for Location 1 and 2 respectively. We clearly observe the width of the yellow region, in the color plots, to gradually increase near the center as $V_{gate} \to V_D'$ and subside towards the edges at higher carrier concentrations. This is a manifestation of the way the puddle sizes change with gate voltage. The red triangles in (a) and (c) indicate the correlation length ξ extracted in the manner described in section 5.4.4. However, wee see that the profile of ξ does not correctly follow the upper boundary of the yellow (intense) region in the color plots (a) and (c). By adjusting the weightage of the points in the first 15 nm and last 4 nm of the $A(r)$ curves while fitting it with a Gaussian, causes

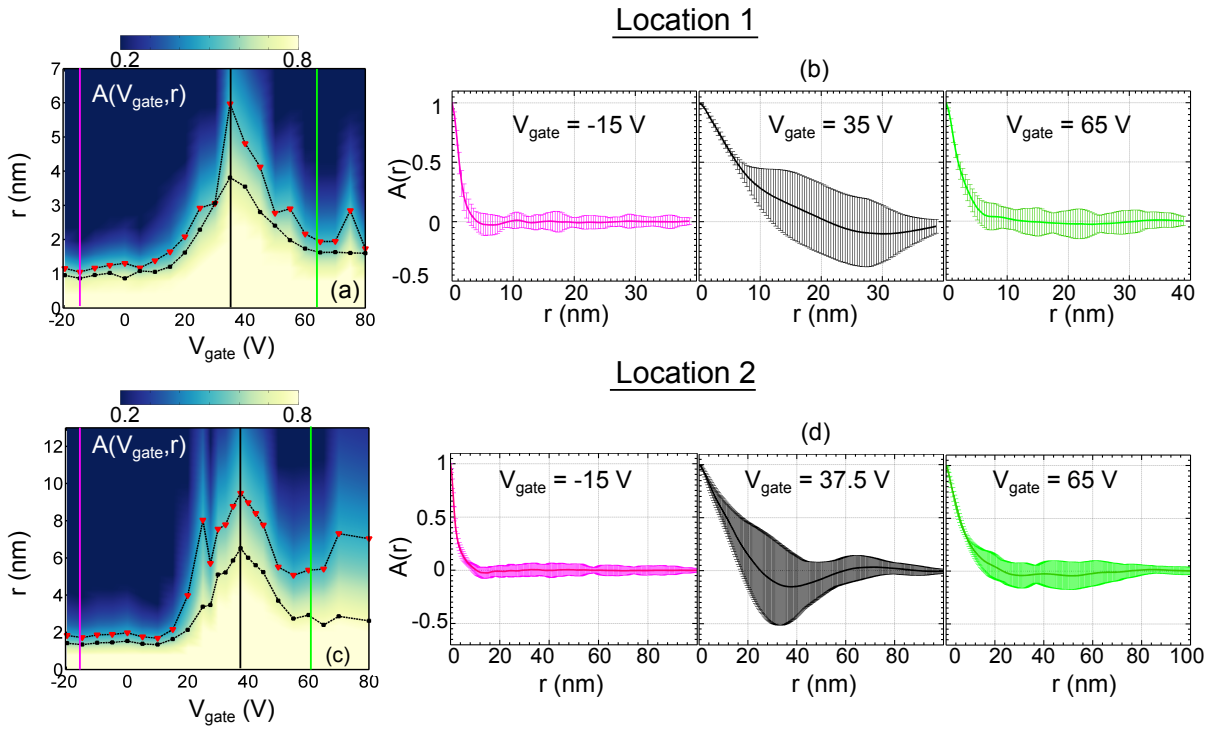

Figure 5.32: The angular averaged, normalized correlation $A(V_{gate}, r)$ of $G_t(x, y)$ maps at different carrier concentrations. (a) $A(V_{gate}, r)$ at Location 1 of $G_t(x, y)$ maps shown in Figure 5.25. The black squares and the red triangles give the correlation length ξ with two different methods, see text.(b) $A(r)$ at different V_{gate} along the vertical cuts in (a). Error is extracted in the manner demonstrated in Figure 5.31. (c) $A(V_{gate}, r)$ at Location 2 for $G_t(x, y)$ maps shown in Figure 5.26. (d) $A(r)$ at different V_{gate} along the vertical cuts in (c).

the extracted values of ξ to better follow this boundary as seen by the black-bullets. An example of this weight adjustment is shown in Figure 5.33.

The difference between ξ extracted by the two methods is considered as the error introduced by this preferential weighting procedure which is additionally represented by the width of the transition region between yellow and blue in the color plots of Figure 5.32.

In Figure 5.34, we superpose the values of these experimentally measured correlation lengths with what we expect from the value of (n_{imp}, d) found from transport (solid lines) and from the CITS measurements (dashed lines). We find that the agreement is rather good for hole doped graphene as seen in (a) and also for electron doped graphene at location 2. At high hole concentrations, the correlation length is about 13 % smaller than expected at location 1 while for location 2, the agreement is much better. Perhaps the best agreement with transport is found for electron doped graphene at location 2 (bullets almost exactly follow the blue solid line). In this case ξ seems to saturate for $n_g < 4 \times 10^{11}$ cm^{-2} which is of the order of the induced residual doping n^* (table 5.1). In the low density regime, the agreement is weaker for hole doped graphene

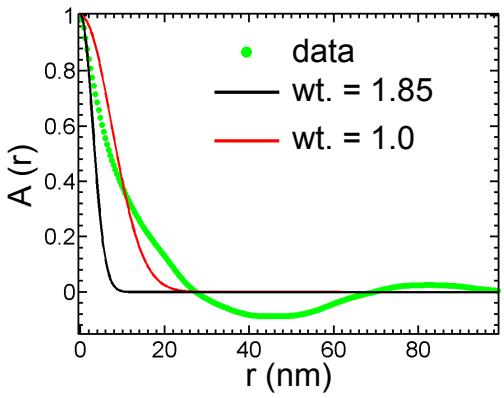

Figure 5.33: Gaussian fits to $A(r)$ (red,blue) using Eq.(2.4.25) by increasing weightage (wt.) of points in the first 15 nm and the last 4 nm wrt. the middle points. $A(r)$ shown here corresponds to G_t map at $V_{gate} = 70\,\mathrm{V}$ for Location 2 (Figure 5.26).

(both locations) and electron doped graphene (location 1). But this is not so surprising as in this regime, with large size of inhomogeneities, the error is expected to be higher; correlation curves deviate significantly from a Gaussian due to finite size effects (Figure 5.32(b),(d), for example.

By employing Scanning tunneling spectroscopy, we are able to measure a carrier density dependent correlation length of fluctuations that follows the trend predicted by transport theories for charge carriers in graphene. Hence, this once again constitutes a strong validation of the fact that the origin of the charge disorder in graphene on SiO_2 is indeed random charge impurities on the substrate.

5.5 Conclusion

In conclusion, we have presented a detailed investigation of the field effect in graphene by combining in-situ transport with scanning probe microscopy at dilution temperatures. The same Coulombic impurity potential that causes a linear conductivity in graphene at high carrier densities, renders the local electrostatic landscape of graphene disordered. By transport, we measure the average properties of this impurity potential i.e. (n_{imp}, d) which we find to be asymmetric for electrons and holes. Using STS, we investigate the screened impurity potential locally at different gate voltages where we find a dramatic increase of both the spatial extent and amplitude of inhomogeneities at low carrier densities. While the variations of the spatial extent of the fluctuations with back-gate show very good agreement with (n_{imp}, d) extracted from transport, the observed amplitude of inhomogeneities show a larger than expected increase at low densities. We explain this as a result of the local gating effect exerted by the tip on graphene which amplifies any change in the intrinsic doping at low carrier concentrations.

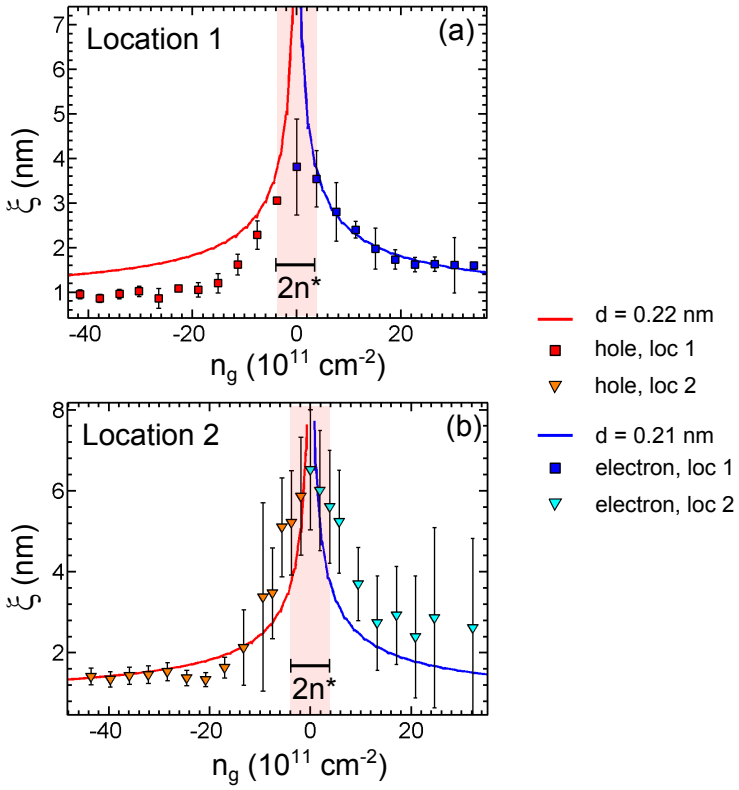

Figure 5.34: Comparison of the experimentally measured correlation length with theory. (a) Variation of correlation length ξ as a function of carrier concentration n_g at Location 1 and (b) Location 2. Solid lines are calculated theoretically using Eq.(2.4.27) for (n_{imp}, d) obtained from transport (table 5.1). Squares and triangles represent measurements at location 1 and 2 respectively. $n^* \approx 4 \times 10^{11}\,\mathrm{cm}^{-2}$ is the residual charge density found from transport 5.1.

Conclusion

In monolayer graphene, the disorder induced charge puddles are predicted to grow as the Fermi level approaches the Dirac point. This is a unique feature of MLG amongst 2DEGs. This thesis is the first experimental quantitative verification on the microscopic scale of this prediction.

In our quest, we have realized that the role of the metallic tip, employed in measuring these puddles by STM, can in no way be neglected. Being over a hundred times closer to graphene than the backgate, the tip acts as a local gate that induces a p-n or n-p junction right underneath. This leads to significant effect in the tunneling spectrum. The situation is very different on graphene on iridium where the close proximity to the metal substrate weakens any local gating by the tip. The interpretation of the tunneling spectrum on graphene has, therefore, been far more simple in that case.

In this thesis, I had the fascinating opportunity to explore Scanning probe microscopy. The primary motivation for combining AFM with STM in our setup was to conduct site-specific STM where the role of the AFM is just like a blind man's tool to guide the tip to the sample that is placed on a vast insulating substrate. Although this application was extensively used, we additionally experimented with other techniques like Kelvin probe force microscopy, dynamic STM, dissipation microscopy, scanning gate microscopy, to name a few. AFM also enabled us to directly visualize the effect the STM tip created on the sample such as cleaning action of the tip, any destructive effect, etc. In brief, we realized that the AFM, especially when combined with STM, is so much more than just a guiding tool for the tip. More innovative applications trying to combine the two techniques, can lead to significant progress towards realizing the true potential of this microscope.

There has been quite some failures on the way. One of the initial targets of this thesis had been the investigation of the superconducting proximity effect in superconductor-graphene hybrid devices using STM/STS. As a first try, we probed HOPG (highly oriented pyrolytic graphite) covered with tin islands. Such a system was difficult to probe as the soft islands were easily picked up by the tip. Eventually, we succeeded in measuring such an interface with the tin showing the superconducting DOS but failed to observe a proximity induced gap on the graphite itself. This measurement continued on the exfoliated graphene devices that were contacted with Ti/Nb/Au,

as discussed in chapter 1. Although a small gap in the DOS was found on some occasions, a systematic spatial evolution could not be measured as the interface was approached.

Perhaps, measuring proximity induced superconductivity in graphene by STM might not be possible in the first place. Our measurements have shown that the metallic tip induces a confinement of electronic states right beneath it. Because charge and phase are conjugate variables, charge confinement implies large phase fluctuations, which in turn suppresses superconductivity.

References

[1] Kostya S Novoselov, Andre K Geim, SV Morozov, D Jiang, Y_ Zhang, SV Dubonos, IV Grigorieva, and AA Firsov. Electric field effect in atomically thin carbon films. *science*, 306(5696):666–669, 2004.

[2] V. P. Gusynin and S. G. Sharapov. Unconventional Integer Quantum Hall Effect in Graphene. *Physical Review Letters*, 95(14), Sep 2005.

[3] M. I. Katsnelson, K. S. Novoselov, and A. K. Geim. Chiral tunnelling and the Klein paradox in graphene. *Nat Phys*, 2(9):620–625, Aug 2006.

[4] Andreas W. W. Ludwig, Matthew P. A. Fisher, R. Shankar, and G. Grinstein. Integer quantum Hall transition: An alternative approach and exact results. *Phys. Rev. B*, 50(11):7526–7552, Sep 1994.

[5] Nguyen Hong Shon and Tsuneya Ando. Quantum Transport in Two-Dimensional Graphite System. *J. Phys. Soc. Jpn.*, 67(7):2421–2429, Jul 1998.

[6] Yuanbo Zhang, Victor W. Brar, Caglar Girit, Alex Zettl, and Michael F. Crommie. Origin of spatial charge inhomogeneity in graphene. *Nat Phys*, 6(1):74–74, Jan 2010.

[7] S Samaddar, D van Zanten, A Fay, B Sacépé, H Courtois, and C B Winkelmann. Niobium-based superconducting nano-device fabrication using all-metal suspended masks. *Nanotechnology*, 24(37):375304, Aug 2013.

[8] Amina Kimouche, Olivier Renault, Sayanti Samaddar, Clemens Winkelmann, Hervé Courtois, Olivier Fruchart, and Johann Coraux. Modulating charge density and inelastic optical response in graphene by atmospheric pressure localized intercalation through wrinkles, Supplementary Information. *Carbon*, 68:73–79, Mar 2014.

[9] S. C. Martin, S. Samaddar, B. Sacépé, A. Kimouche, J. Coraux, F. Fuchs, B. Grévin, H. Courtois, and C. B. Winkelmann. Disorder and screening in decoupled graphene on a metallic substrate. *Phys. Rev. B*, 91(4), Jan 2015.

[10] P Dubos, P Charlat, Th Crozes, P Paniez, and B Pannetier. Thermostable trilayer resist for niobium lift-off. *Journal of Vacuum Science & Technology B*, 18(1):122–126, 2000.

[11] C. Varmazis M. Strongin and A. Joshi. *Metallurgy of Superconducting Materials: Treatise on Materials Science and Technology*, volume 14. Elsevier, 1979.

[12] Kohei Ohnishi, Takashi Kimura, and Yoshichika Otani. Improvement of superconductive properties of mesoscopic Nb wires by Ti passivation layers. *Applied physics express*, 1(2):021701, 2008.

[13] Nam Kim, Klavs Hansen, Jussi Toppari, Tarmo Suppula, and Jukka Pekola. Fabrication of mesoscopic superconducting Nb wires using conventional electron-beam lithographic techniques. *Journal of Vacuum Science & Technology B*, 20(1):386–388, 2002.

[14] Wenzhong Bao, Gang Liu, Zeng Zhao, Hang Zhang, Dong Yan, Aparna Deshpande, Brian LeRoy, and Chun Ning Lau. Lithography-free fabrication of high quality substrate-supported and freestanding graphene devices. *Nano Research*, 3(2):98–102, 2010.

[15] L Angers, F Chiodi, G Montambaux, M Ferrier, S Guéron, H Bouchiat, and JC Cuevas. Proximity dc squids in the long-junction limit. *Physical Review B*, 77(16):165408, 2008.

[16] T Hoss, C Strunk, and C Schönenberger. Nonorganic evaporation mask for superconducting nanodevices. *Microelectronic engineering*, 46(1):149–152, 1999.

[17] T Hoss, Christoph Strunk, C Sürgers, and Christian Schönenberger. UHV compatible nanostructuring technique for mesoscopic hybrid devices: application to superconductor/ferromagnet Josephson contacts. *Physica E: Low-dimensional Systems and Nanostructures*, 14(3):341–345, 2002.

[18] RE Howard. A refractory lift-off process with applications to high-Tc superconducting circuits. *Applied Physics Letters*, 33(12):1034–1035, 1978.

[19] HSJ Van der Zant, HA Rijken, and JE Mooij. The superconducting transition of 2-D Josephson-junction arrays in a small perpendicular magnetic field. *Journal of low temperature physics*, 79(5-6):289–310, 1990.

[20] Hervé Courtois, M Meschke, JT Peltonen, and JP Pekola. Origin of hysteresis in a proximity Josephson junction. *Physical review letters*, 101(6):067002, 2008.

[21] E. S. ROSENBLUM, S. H. AUTLER, and K. H. GOOEN. The Dependence of the Upper Critical Field of Niobium on Temperature and Resistivity. *Rev. Mod. Phys.*, 36(1):77–80, Jan 1964.

[22] Michael Tinkham. *Introduction to superconductivity*. Courier Corporation, second edition, 2012.

[23] P Dubos, H Courtois, B Pannetier, FK Wilhelm, AD Zaikin, and G Schön. Josephson critical current in a long mesoscopic SNS junction. *Physical Review B*, 63(6):064502, 2001.

[24] Alessandro De Cecco. High-critical current Nb based proximity Josephson junctions. Master's thesis, 2012-2013.

[25] KS Novoselov, D Jiang, F Schedin, TJ Booth, VV Khotkevich, SV Morozov, and AK Geim. Two-dimensional atomic crystals. *Proceedings of the National Academy of Sciences of the United States of America*, 102(30):10451–10453, 2005.

[26] DSL Abergel, Alan Russell, and Vladimir I Falko. Visibility of graphene flakes on a dielectric substrate. *Applied Physics Letters*, 91(6):063125–063125, 2007.

[27] P Blake, EW Hill, AH Castro Neto, KS Novoselov, D Jiang, R Yang, TJ Booth, and AK Geim. Making graphene visible. *Applied Physics Letters*, 91(6):063124, 2007.

[28] K Nagashio, T Yamashita, T Nishimura, K Kita, and A Toriumi. Electrical transport properties of graphene on SiO2 with specific surface structures. *Journal of Applied Physics*, 110(2):024513, 2011.

[29] Shaffique Adam, EH Hwang, VM Galitski, and S Das Sarma. A self-consistent theory for graphene transport. *Proceedings of the National Academy of Sciences*, 104(47):18392–18397, 2007.

[30] AC Ferrari, JC Meyer, V Scardaci, C Casiraghi, Michele Lazzeri, Francesco Mauri, S Piscanec, Da Jiang, KS Novoselov, S Roth, et al. Raman spectrum of graphene and graphene layers. *Physical review letters*, 97(18):187401, 2006.

[31] Jun Yan, Yuanbo Zhang, Philip Kim, and Aron Pinczuk. Electric field effect tuning of electron-phonon coupling in graphene. *Physical review letters*, 98(16):166802, 2007.

[32] Simone Pisana, Michele Lazzeri, Cinzia Casiraghi, Kostya S Novoselov, Andre K Geim, Andrea C Ferrari, and Francesco Mauri. Breakdown of the adiabatic Born–Oppenheimer approximation in graphene. *Nature materials*, 6(3):198–201, 2007.

[33] C Stampfer, F Molitor, D Graf, K Ensslin, A Jungen, C Hierold, and Ludger Wirtz. Raman imaging of doping domains in graphene on SiO2. *Applied Physics Letters*, 91(24):241907, 2007.

[34] Anindya Das, S Pisana, B Chakraborty, S Piscanec, SK Saha, UV Waghmare, KS Novoselov, HR Krishnamurthy, AK Geim, AC Ferrari, et al. Monitoring dopants by Raman scattering in an electrochemically top-gated graphene transistor. *Nature nanotechnology*, 3(4):210–215, 2008.

[35] Duhee Yoon, Young-Woo Son, and Hyeonsik Cheong. Negative thermal expansion coefficient of graphene measured by Raman spectroscopy. *Nano letters*, 11(8):3227–3231, 2011.

[36] K. S. Novoselov, A. K. Geim, S. V. Morozov, D. Jiang, M. I. Katsnelson, I. V. Grigorieva, S. V. Dubonos, and A. A. Firsov. Two-dimensional gas of massless Dirac fermions in graphene. *Nature*, 438(7065):197–200, Nov 2005.

[37] N. D. Mermin and H. Wagner. Absence of Ferromagnetism or Antiferromagnetism in One- or Two-Dimensional Isotropic Heisenberg Models. *Physical Review Letters*, 17(22):1133–1136, Nov 1966.

[38] Rachel Won. Photovoltaics: Graphene–silicon solar cells. *Nature Photon*, 4(7):411–411, Jul 2010.

[39] Sukang Bae, Hyeongkeun Kim, Youngbin Lee, Xiangfan Xu, Jae-Sung Park, Yi Zheng, Jayakumar Balakrishnan, Tian Lei, Hye Ri Kim, Young Il Song, and et al. Roll-to-roll production of 30-inch graphene films for transparent electrodes. *Nature Nanotechnology*, 5(8):574–578, Jun 2010.

[40] Sumit Goenka, Vinayak Sant, and Shilpa Sant. Graphene-based nanomaterials for drug delivery and tissue engineering. *Journal of Controlled Release*, 173:75–88, Jan 2014.

[41] ChengWei Chiu, Xingliang He, and Hong Liang. Surface modification of a neural sensor using graphene. *Electrochimica Acta*, 94:42–48, Apr 2013.

[42] Andrei V. Shytov, Mark S. Rudner, and Leonid S. Levitov. Klein Backscattering and Fabry-Pérot Interference in Graphene Heterojunctions. *Physical Review Letters*, 101(15), Oct 2008.

[43] A. V. Shytov, M. I. Katsnelson, and L. S. Levitov. Vacuum Polarization and Screening of Supercritical Impurities in Graphene. *Physical Review Letters*, 99(23), Dec 2007.

[44] A. F. Morpurgo and F. Guinea. Intervalley Scattering, Long-Range Disorder, and Effective Time-Reversal Symmetry Breaking in Graphene. *Physical Review Letters*, 97(19), Nov 2006.

[45] S. V. Morozov, K. S. Novoselov, M. I. Katsnelson, F. Schedin, L. A. Ponomarenko, D. Jiang, and A. K. Geim. Strong Suppression of Weak Localization in Graphene. *Physical Review Letters*, 97(1), Jul 2006.

[46] J. Martin, N. Akerman, G. Ulbricht, T. Lohmann, J. H. Smet, K. von Klitzing, and A. Yacoby. Observation of electron–hole puddles in graphene using a scanning single-electron transistor. *Nat Phys*, 4(2):144–148, Nov 2007.

[47] S. Das Sarma, Shaffique Adam, E. H. Hwang, and Enrico Rossi. Electronic transport in two-dimensional graphene. *Rev. Mod. Phys.*, 83(2):407–470, May 2011.

[48] S. Adam, Suyong Jung, Nikolai N. Klimov, Nikolai B. Zhitenev, Joseph A. Stroscio, and M. D. Stiles. Mechanism for puddle formation in graphene. *Phys. Rev. B*, 84(23), Dec 2011.

[49] A. H. Castro Neto, F. Guinea, N. M. R. Peres, K. S. Novoselov, and A. K. Geim. The electronic properties of graphene. *Rev. Mod. Phys.*, 81(1):109–162, Jan 2009.

[50] Guohong Li, Adina Luican, and Eva Y. Andrei. Scanning Tunneling Spectroscopy of Graphene on Graphite. *Physical Review Letters*, 102(17), Apr 2009.

[51] P. R. Wallace. The Band Theory of Graphite. *Phys. Rev.*, 71(9):622–634, May 1947.

[52] Neil W Ashcroft and N David Mermin. *Solid State Physics*. Harcourt College Publishers, 1976.

[53] Jiamin Xue. Berry phase and the unconventional quantum Hall effect in graphene. *arXiv preprint arXiv:1309.6714*, 2013.

[54] Johan Nilsson, A. H. Castro Neto, F. Guinea, and N. M. R. Peres. Electronic properties of bilayer and multilayer graphene. *Phys. Rev. B*, 78(4), Jul 2008.

[55] Neil W Ashcroft and N David Mermin. *Solid State Physics*. Harcourt College Publishers, 1976.

[56] Shaffique Adam. Graphene Carrier Transport Theory. In Hassan Raza, editor, *Graphene Nanoelectronics*, NanoScience and Technology, pages 357–394. Springer Berlin Heidelberg, 2012.

[57] E. H. Hwang and S. Das Sarma. Dielectric function, screening, and plasmons in two-dimensional graphene. *Phys. Rev. B*, 75(20), May 2007.

[58] Aaron Bostwick, Taisuke Ohta, Thomas Seyller, Karsten Horn, and Eli Rotenberg. Quasiparticle dynamics in graphene. *Nat Phys*, 3(1):36–40, Dec 2006.

[59] E. H. Hwang and S. Das Sarma. Quasiparticle spectral function in doped graphene: Electron-electron interaction effects in ARPES. *Phys. Rev. B*, 77(8), Feb 2008.

[60] D. C. Elias, R. V. Gorbachev, A. S. Mayorov, S. V. Morozov, A. A. Zhukov, P. Blake, L. A. Ponomarenko, I. V. Grigorieva, K. S. Novoselov, F. Guinea, and et al. Dirac cones reshaped by interaction effects in suspended graphene. *Nat Phys*, 7(9):701–704, Jul 2011.

[61] J.-H. Chen, C. Jang, S. Adam, M. S. Fuhrer, E. D. Williams, and M. Ishigami. Charged-impurity scattering in graphene. *Nat Phys*, 4(5):377–381, Apr 2008.

[62] Marco Gibertini, Andrea Tomadin, Marco Polini, A. Fasolino, and M. I. Katsnelson. Electron density distribution and screening in rippled graphene sheets. *Phys. Rev. B*, 81(12), Mar 2010.

[63] G. M. Rutter, J. N. Crain, N. P. Guisinger, T. Li, P. N. First, and J. A. Stroscio. Scattering and Interference in Epitaxial Graphene. *Science*, 317(5835):219–222, Jul 2007.

[64] E. Rossi. http://scienceisbeauty.tumblr.com/post/964600043/density-distribution-at-the-dirac-point-for-a.

[65] Enrico Rossi, S. Adam, and S. Das Sarma. Effective medium theory for disordered two-dimensional graphene. *Phys. Rev. B*, 79(24), Jun 2009.

[66] Gerd Binnig, Heinrich Rohrer, Ch Gerber, and Eddie Weibel. Tunneling through a controllable vacuum gap. *Applied Physics Letters*, 40(2):178–180, 1982.

[67] Gerd Binnig, Calvin F Quate, and Ch Gerber. Atomic force microscope. *Physical review letters*, 56(9):930, 1986.

[68] Øystein Fischer, Martin Kugler, Ivan Maggio-Aprile, Christophe Berthod, and Christoph Renner. Scanning tunneling spectroscopy of high-temperature superconductors. *Reviews of Modern Physics*, 79(1):353, 2007.

[69] Michael Tinkham. *Introduction to superconductivity*. Courier Corporation, second edition, 2012.

[70] J.N. Israelachvili. *Intermolecular and Surface Forces*. Academic, London, 1992.

[71] Neil W Ashcroft and N David Mermin. *Solid State Physics*. Harcourt College Publishers, 1976.

[72] Franz J. Giessibl, Florian Pielmeier, Toyoaki Eguchi, Toshu An, and Yukio Hasegawa. Comparison of force sensors for atomic force microscopy based on quartz tuning forks and length-extensional resonators. *Physical Review B*, 84(12), Sep 2011.

[73] Franz J. Giessibl. High-speed force sensor for force microscopy and profilometry utilizing a quartz tuning fork. *Applied Physics Letters*, 73(26):3956, 1998.

[74] Franz J. Giessibl. Atomic resolution on Si(111) (7×7) by noncontact atomic force microscopy with a force sensor based on a quartz tuning fork. *Applied Physics Letters*, 76(11):1470, 2000.

[75] Seiji Heike and Tomihiro Hashizume. Atomic resolution noncontact atomic force/scanning tunneling microscopy using a 1 MHz quartz resonator. *Applied Physics Letters*, 83(17):3620, 2003.

[76] Toshu An, Toyoaki Eguchi, Kotone Akiyama, and Yukio Hasegawa. Atomically-resolved imaging by frequency-modulation atomic force microscopy using a quartz length-extension resonator. *Applied Physics Letters*, 87(13):133114, 2005.

[77] T. R. Albrecht, P. Grütter, D. Horne, and D. Rugar. Frequency modulation detection using high-Q cantilevers for enhanced force microscope sensitivity. *Journal of Applied Physics*, 69(2):668, 1991.

[78] Sylvain Martin. *Systèmes nanoélectroniques hybrides : cartographies de la densité d'états locale*. PhD thesis, 2012. Thèse de doctorat dirigée par Courtois, Hervé Physique Grenoble 2012.

[79] S. H. Pan, E. W. Hudson, and J. C. Davis. [sup 3]He refrigerator based very low temperature scanning tunneling microscope. *Review of Scientific Instruments*, 70(2):1459, 1999.

[80] B. Young B. Cabrera A. L.Woodcraft, A. Gray and A. Miller. A low temperature thermal conductivity database. *Low Temperature Detectors LTD 13, Proceedings of the 13th International Workshop,*, page 681, 2009.

[81] Frank Pobell. *Matter and Methods at Low Temperatures*. Third edition.

[82] Physik Instrumente (PI) GmbH.

[83] Cryostat Sionludi developed by A. Benoît and M. Caussignac.

[84] Frank Pobell. *Matter and Methods at Low Temperatures*. Springer Science + Business Media, 2007.

[85] Service electronique de l'Institut Néel. http://neel.cnrs.fr/spip.php?rubrique82.

[86] *Nanonis, SPM Control System*.

[87] Paul Horowitz and Winfield Hill. *The art of electronics*. Cambridge Univ. Press, 1989.

[88] SPECS. Kolibri Sensor, Advanced Quartz Sensor Technology for FM-AFM.

[89] CABLE DESIGNERS GUIDE.

[90] P. Günther, U. Ch. Fischer, and K. Dransfeld. Scanning near-field acoustic microscopy. *Appl. Phys. B*, 48(1):89–92, Jan 1989.

[91] A. Michels, F. Meinen, T. Murdfield, W. Göhde, U.C. Fischer, E. Beckmann, and H. Fuchs. 1 MHz quartz length extension resonator as a probe for scanning near-field acoustic microscopy. *Thin Solid Films*, 264(2):172–175, Aug 1995.

[92] A Castellanos-Gomez, N Agraït, and G Rubio-Bollinger. Carbon fibre tips for scanning probe microscopy based on quartz tuning fork force sensors. *Nanotechnology*, 21(14):145702, Mar 2010.

[93] Arunima Sethi. Towards STM on a gate tunable Quantum Dot. Master's thesis, Nanophysics, University Joseph Fourier, 2014.

[94] Michael Tinkham. *Introduction to superconductivity*. Courier Corporation, second edition, 2012.

[95] R. Baskaran, A. V. Thanikai Arasu, E. P. Amaladass, and M. P. Janawadkar. High upper critical field in disordered niobium nitride superconductor. *Journal of Applied Physics*, 116(16):163908, Oct 2014.

[96] Microcrystal.

[97] Epotecny E207. Technical report.

[98] Epotek H201D. Technical report, $http://www.epotek.com/site/administrator/components/com_products$

[99] Florian Pielmeier, Daniel Meuer, Daniel Schmid, Christoph Strunk, and Franz J Giessibl. Impact of thermal frequency drift on highest precision force microscopy using quartz-based force sensors at low temperatures. *Beilstein Journal of Nanotechnology*, 5:407–412, 2014.

[100] Toshu An, Takahiro Nishio, Toyoaki Eguchi, Masanori Ono, Atsushi Nomura, Kotone Akiyama, and Yukio Hasegawa. Atomically resolved imaging by low-temperature frequency-modulation atomic force microscopy using a quartz length-extension resonator. *Review of Scientific Instruments*, 79(3):033703, 2008.

[101] J. Rychen, T. Ihn, P. Studerus, A. Herrmann, K. Ensslin, H. J. Hug, P. J. A. van Schendel, and H. J. Güntherodt. Operation characteristics of piezoelectric quartz tuning forks in high magnetic fields at liquid helium temperatures. *Review of Scientific Instruments*, 71(4):1695, 2000.

[102] S. Hembacher, F.J. Giessibl, and J. Mannhart. Evaluation of a force sensor based on a quartz tuning fork for operation at low temperatures and ultrahigh vacuum. *Applied Surface Science*, 188(3-4):445–449, Mar 2002.

[103] S. Hembacher, F. J. Giessibl, J. Mannhart, and C. F. Quate. Local Spectroscopy and Atomic Imaging of Tunneling Current, Forces, and Dissipation on Graphite. *Physical Review Letters*, 94(5), Feb 2005.

[104] N. Berdunov, A. J. Pollard, and P. H. Beton. Dynamic scanning probe microscopy of adsorbed molecules on graphite. *Applied Physics Letters*, 94(4):043110, 2009.

[105] Markus Ternes, César González, Christopher P. Lutz, Prokop Hapala, Franz J. Giessibl, Pavel Jelínek, and Andreas J. Heinrich. Interplay of Conductance, Force, and Structural Change in Metallic Point Contacts. *Physical Review Letters*, 106(1), Jan 2011.

[106] T. Quaglio, F. Dahlem, S. Martin, A. Gérardin, C. B. Winkelmann, and H. Courtois. A subKelvin scanning probe microscope for the electronic spectroscopy of an individual nano-device. *Review of Scientific Instruments*, 83(12):123702, 2012.

[107] Hélèn le Sueur. *Cryogenic AFM-STM for Mesoscopic Physics*. PhD thesis, CEA-Saclay, 2007.

[108] John W May. Platinum surface LEED rings. *Surface Science*, 17(1):267–270, 1969.

[109] R Schlögl, M Che, O Clause, Ch Marcilly, C Louis, H Knöinger, E Teglauer, W Keim, B Drieben-Hölscher, JW Geus, et al. *Handbook of Heterogeneous Catalysis*, chapter Preparation of Solid Catalysts, pages 138–264. Wiley Online Library, 2008.

[110] Eduardo J. H. Lee, Kannan Balasubramanian, Ralf Thomas Weitz, Marko Burghard, and Klaus Kern. Contact and edge effects in graphene devices. *Nature Nanotechnology*, 3(8):486–490, Jun 2008.

[111] Yu S Dedkov and M Fonin. Electronic and magnetic properties of the graphene–ferromagnet interface. *New Journal of Physics*, 12(12):125004, Dec 2010.

[112] Johann Coraux, Alpha T. N'Diaye, Carsten Busse, and Thomas Michely. Structural Coherency of Graphene on Ir(111). *Nano Lett.*, 8(2):565–570, Feb 2008.

[113] I. Pletikosić, M. Kralj, P. Pervan, R. Brako, J. Coraux, A. T. N'Diaye, C. Busse, and T. Michely. Dirac Cones and Minigaps for Graphene on Ir(111). *Physical Review Letters*, 102(5), Feb 2009.

[114] J. Vaari, J. Lahtinen, and P. Hautojärvi. The adsorption and decomposition of acetylene on clean and K-covered Co(0001). *Catalysis Letters*, 44(1/2):43–49, 1997.

[115] T.A. Land, T. Michely, R.J. Behm, J.C. Hemminger, and G. Comsa. STM investigation of single layer graphite structures produced on Pt(111) by hydrocarbon decomposition. *Surface Science*, 264(3):261–270, Mar 1992.

[116] Alpha T. N'Diaye, Sebastian Bleikamp, Peter J. Feibelman, and Thomas Michely. Two-Dimensional Ir Cluster Lattice on a Graphene Moiré on Ir(111). *Physical Review Letters*, 97(21), Nov 2006.

[117] S. Marchini, S. Günther, and J. Wintterlin. Scanning tunneling microscopy of graphene on Ru(0001). *Phys. Rev. B*, 76(7), Aug 2007.

[118] Alexander Grüneis and Denis V. Vyalikh. Tunable hybridization between electronic states of graphene and a metal surface. *Phys. Rev. B*, 77(19), May 2008.

[119] Elena Voloshina and Yuriy Dedkov. Graphene on metallic surfaces: problems and perspectives. *Physical Chemistry Chemical Physics*, 14(39):13502, 2012.

[120] G. Giovannetti, P. A. Khomyakov, G. Brocks, V. M. Karpan, J. van den Brink, and P. J. Kelly. Doping Graphene with Metal Contacts. *Physical Review Letters*, 101(2), Jul 2008.

[121] Alexander Grüneis. Synthesis and electronic properties of chemically functionalized graphene on metal surfaces. *J. Phys.: Condens. Matter*, 25(4):043001, Dec 2012.

[122] Alexander Grüneis, Kurt Kummer, and Denis V Vyalikh. Dynamics of graphene growth on a metal surface: a time-dependent photoemission study. *New Journal of Physics*, 11(7):073050, Jul 2009.

[123] D. Haberer, D. V. Vyalikh, S. Taioli, B. Dora, M. Farjam, J. Fink, D. Marchenko, T. Pichler, K. Ziegler, S. Simonucci, and et al. Tunable Band Gap in Hydrogenated Quasi-Free-Standing Graphene. *Nano Lett.*, 10(9):3360–3366, Sep 2010.

[124] Rafik Addou, Arjun Dahal, and Matthias Batzill. Graphene on ordered Ni-alloy surfaces formed by metal (Sn, Al) intercalation between graphene/Ni(111). *Surface Science*, 606(13-14):1108–1112, Jul 2012.

[125] A. Varykhalov, M. R. Scholz, Timur K. Kim, and O. Rader. Effect of noble-metal contacts on doping and band gap of graphene. *Phys. Rev. B*, 82(12), Sep 2010.

[126] A. M. Shikin, G. V. Prudnikova, V. K. Adamchuk, F. Moresco, and K.-H. Rieder. Surface intercalation of gold underneath a graphite monolayer on Ni(111) studied by angle-resolved photoemission and high-resolution electron-energy-loss spectroscopy. *Phys. Rev. B*, 62(19):13202–13208, Nov 2000.

[127] Peter Sutter, Jerzy T. Sadowski, and Eli A. Sutter. Chemistry under Cover: Tuning Metal-Graphene Interaction by Reactive Intercalation. *Journal of the American Chemical Society*, 132(23):8175–8179, Jun 2010.

[128] Rosanna Larciprete, Søren Ulstrup, Paolo Lacovig, Matteo Dalmiglio, Marco Bianchi, Federico Mazzola, Liv Hornekær, Fabrizio Orlando, Alessandro Baraldi, Philip Hofmann, and et al. Oxygen Switching of the Epitaxial Graphene–Metal Interaction. *ACS Nano*, 6(11):9551–9558, Nov 2012.

[129] Søren Ulstrup, Mie Andersen, Marco Bianchi, Lucas Barreto, Bjørk Hammer, Liv Hornekær, and Philip Hofmann. Sequential oxygen and alkali intercalation of epitaxial

graphene on Ir(111): enhanced many-body effects and formation of pn -interfaces. *2D Materials*, 1(2):025002, Aug 2014.

[130] P. Sutter, M. S. Hybertsen, J. T. Sadowski, and E. Sutter. Electronic Structure of Few-Layer Epitaxial Graphene on Ru(0001). *Nano Lett.*, 9(7):2654–2660, Jul 2009.

[131] Myung Ho Kang, Sung Chul Jung, and Jae Whan Park. Density functional study of the Au-intercalated graphene/Ni(111) surface. *Phys. Rev. B*, 82(8), Aug 2010.

[132] Johann Coraux, Alpha T. N'Diaye, Nicolas Rougemaille, Chi Vo-Van, Amina Kimouche, Hong-Xin Yang, Mairbek Chshiev, Nedjma Bendiab, Olivier Fruchart, and Andreas K. Schmid. Air-Protected Epitaxial Graphene/Ferromagnet Hybrids Prepared by Chemical Vapor Deposition and Intercalation. *The Journal of Physical Chemistry Letters*, 3(15):2059–2063, Aug 2012.

[133] Muriel Sicot, Philipp Leicht, Andreas Zusan, Samuel Bouvron, Ole Zander, Martin Weser, Yuriy S. Dedkov, Karsten Horn, and Mikhail Fonin. Size-Selected Epitaxial Nanoislands Underneath Graphene Moiré on Rh(111). *ACS Nano*, 6(1):151–158, Jan 2012.

[134] Jayeeta Lahiri and Matthias Batzill. Graphene destruction by metal-carbide formation: An approach for patterning of metal-supported graphene. *Appl. Phys. Lett.*, 97(2):023102, 2010.

[135] Peter J. Feibelman. Pinning of graphene to Ir(111) by flat Ir dots. *Phys. Rev. B*, 77(16), Apr 2008.

[136] Chi Vo-Van, Amina Kimouche, Antoine Reserbat-Plantey, Olivier Fruchart, Pascale Bayle-Guillemaud, Nedjma Bendiab, and Johann Coraux. Epitaxial graphene prepared by chemical vapor deposition on single crystal thin iridium films on sapphire. *Appl. Phys. Lett.*, 98(18):181903, 2011.

[137] EV Rut'kov and A Ya Tontegode. A study of the carbon adlayer on iridium. *Surface Science*, 161(2):373–389, 1985.

[138] Babu R. Chalamala, Yi Wei, Robert H. Reuss, Sanjeev Aggarwal, Bruce E. Gnade, R. Ramesh, John M. Bernhard, Edward D. Sosa, and David E. Golden. Effect of growth conditions on surface morphology and photoelectric work function characteristics of iridium oxide thin films. *Appl. Phys. Lett.*, 74(10):1394, 1999.

[139] Wenjuan Zhu, Tony Low, Vasili Perebeinos, Ageeth A. Bol, Yu Zhu, Hugen Yan, Jerry Tersoff, and Phaedon Avouris. Structure and Electronic Transport in Graphene Wrinkles. *Nano Lett.*, 12(7):3431–3436, Jul 2012.

[140] B. Lalmi, J. C. Girard, E. Pallecchi, M. Silly, C. David, S. Latil, F. Sirotti, and A. Ouerghi. Flower-Shaped Domains and Wrinkles in Trilayer Epitaxial Graphene on Silicon Carbide. *Sci. Rep.*, 4, Feb 2014.

[141] Ke Xu, Peigen Cao, and James R. Heath. Scanning Tunneling Microscopy Characterization of the Electrical Properties of Wrinkles in Exfoliated Graphene Monolayers. *Nano Lett.*, 9(12):4446–4451, Dec 2009.

[142] S J Altenburg and R Berndt. Local work function and STM tip-induced distortion of graphene on Ir(111). *New Journal of Physics*, 16(5):053036, May 2014.

[143] N. N. Klimov, S. Jung, S. Zhu, T. Li, C. A. Wright, S. D. Solares, D. B. Newell, N. B. Zhitenev, and J. A. Stroscio. Electromechanical Properties of Graphene Drumheads. *Science*, 336(6088):1557–1561, Jun 2012.

[144] H. J. Hug and A. Baratoff. Measurement of Dissipation Induced by Tip-Sample Interactions. *NanoScience and Technology*, page 395–431, 2002.

[145] Winfried Denk and Dieter W. Pohl. Local electrical dissipation imaged by scanning force microscopy. *Appl. Phys. Lett.*, 59(17):2171, 1991.

[146] Young-Jun Yu, Yue Zhao, Sunmin Ryu, Louis E. Brus, Kwang S. Kim, and Philip Kim. Tuning the Graphene Work Function by Electric Field Effect. *Nano Lett.*, 9(10):3430–3434, Oct 2009.

[147] D. Subramaniam, F. Libisch, Y. Li, C. Pauly, V. Geringer, R. Reiter, T. Mashoff, M. Liebmann, J. Burgdörfer, C. Busse, and et al. Wave-Function Mapping of Graphene Quantum Dots with Soft Confinement. *Physical Review Letters*, 108(4), Jan 2012.

[148] Elin Grånäs, Jan Knudsen, Ulrike A. Schröder, Timm Gerber, Carsten Busse, Mohammad A. Arman, Karina Schulte, Jesper N. Andersen, and Thomas Michely. Oxygen Intercalation under Graphene on Ir(111): Energetics, Kinetics, and the Role of Graphene Edges. *ACS Nano*, 6(11):9951–9963, Nov 2012.

[149] Choongyu Hwang, David A. Siegel, Sung-Kwan Mo, William Regan, Ariel Ismach, Yuegang Zhang, Alex Zettl, and Alessandra Lanzara. Fermi velocity engineering in graphene by substrate modification. *Sci. Rep.*, 2, Aug 2012.

[150] Laurent Nony, Adam S. Foster, Franck Bocquet, and Christian Loppacher. Understanding the Atomic-Scale Contrast in Kelvin Probe Force Microscopy. *Physical Review Letters*, 103(3), Jul 2009.

[151] Doron Gazit. Correlation between charge inhomogeneities and structure in graphene and other electronic crystalline membranes. *Phys. Rev. B*, 80(16), Oct 2009.

[152] Marco Gibertini, Andrea Tomadin, Francisco Guinea, Mikhail I. Katsnelson, and Marco Polini. Electron-hole puddles in the absence of charged impurities. *Phys. Rev. B*, 85(20), May 2012.

[153] Eun-Ah Kim and A. H. Castro Neto. Graphene as an electronic membrane. *EPL (Europhysics Letters)*, 84(5):57007, Dec 2008.

[154] S. Das Sarma, E. H. Hwang, and Wang-Kong Tse. Many-body interaction effects in doped and undoped graphene: Fermi liquid versus non-Fermi liquid. *Phys. Rev. B*, 75(12), Mar 2007.

[155] J. González, F. Guinea, and M. A. H. Vozmediano. Marginal-Fermi-liquid behavior from two-dimensional Coulomb interaction. *Phys. Rev. B*, 59(4):R2474–R2477, Jan 1999.

[156] Marco Polini, Reza Asgari, Yafis Barlas, T. Pereg-Barnea, and A.H. MacDonald. Graphene: A pseudochiral Fermi liquid. *Solid State Communications*, 143(1-2):58–62, Jul 2007.

[157] D. A. Siegel, C.-H. Park, C. Hwang, J. Deslippe, A. V. Fedorov, S. G. Louie, and A. Lanzara. Many-body interactions in quasi-freestanding graphene. *Proceedings of the National Academy of Sciences*, 108(28):11365–11369, Jun 2011.

[158] Jungseok Chae, Suyong Jung, Andrea F. Young, Cory R. Dean, Lei Wang, Yuanda Gao, Kenji Watanabe, Takashi Taniguchi, James Hone, Kenneth L. Shepard, and et al. Renormalization of the Graphene Dispersion Velocity Determined from Scanning Tunneling Spectroscopy. *Physical Review Letters*, 109(11), Sep 2012.

[159] Jian-Hao Chen, W. G. Cullen, C. Jang, M. S. Fuhrer, and E. D. Williams. Defect Scattering in Graphene. *Physical Review Letters*, 102(23), Jun 2009.

[160] E. H. Hwang and S. Das Sarma. Acoustic phonon scattering limited carrier mobility in two-dimensional extrinsic graphene. *Phys. Rev. B*, 77(11), Mar 2008.

[161] S. Fratini and F. Guinea. Substrate-limited electron dynamics in graphene. *Phys. Rev. B*, 77(19), May 2008.

[162] T. Stauber, N. M. R. Peres, and F. Guinea. Electronic transport in graphene: A semiclassical approach including midgap states. *Phys. Rev. B*, 76(20), Nov 2007.

[163] VARIABLE GAIN LOW NOISE CURRENT AMPLIFIER DLPCA-200. http://www.femto.de/en/products/current-amplifiers/variable-gain-up-to-500-khz-dlpca.html. *Femto*.

[164] High Speed Bipolar Amplifier. https : //www.nfcorp.co.jp/english/pro/pp/p$_a$mp/h$_s$pe/hsa/index.html. *NF Corporation*.

[165] K. S. Novoselov. Electric Field Effect in Atomically Thin Carbon Films. *Science*, 306(5696):666–669, Oct 2004.

[166] Timm Lohmann, Klaus von Klitzing, and Jurgen H. Smet. Four-Terminal Magneto-Transport in Graphene p-n Junctions Created by Spatially Selective Doping. *Nano Lett.*, 9(5):1973–1979, May 2009.

[167] D. S. Novikov. Numbers of donors and acceptors from transport measurements in graphene. *Appl. Phys. Lett.*, 91(10):102102, 2007.

[168] B. Huard, N. Stander, J. A. Sulpizio, and D. Goldhaber-Gordon. Evidence of the role of contacts on the observed electron-hole asymmetry in graphene. *Phys. Rev. B*, 78(12), Sep 2008.

[169] Wenjuan Zhu, Vasili Perebeinos, Marcus Freitag, and Phaedon Avouris. Carrier scattering, mobilities, and electrostatic potential in monolayer, bilayer, and trilayer graphene. *Phys. Rev. B*, 80(23), Dec 2009.

[170] Suyong Jung, Gregory M. Rutter, Nikolai N. Klimov, David B. Newell, Irene Calizo, Angela R. Hight-Walker, Nikolai B. Zhitenev, and Joseph A. Stroscio. Evolution of microscopic localization in graphene in a magnetic field from scattering resonances to quantum dots. *Nat Phys*, 7(3):245–251, Jan 2011.

[171] Paul A. Anderson. Work Function of Gold. *Phys. Rev.*, 115(3):553–554, Aug 1959.

[172] Fengnian Xia, Vasili Perebeinos, Yu-ming Lin, Yanqing Wu, and Phaedon Avouris. The origins and limits of metal–graphene junction resistance. *Nature Nanotechnology*, 6(3):179–184, 2011.

[173] Shyam K. Choudhary and Anjan K. Gupta. Effects of tip induced carrier density in local tunnel spectra of graphene. *Appl. Phys. Lett.*, 98(10):102109, 2011.

[174] Y. Zhao, J. Wyrick, F. D. Natterer, J. F. Rodriguez-Nieva, C. Lewandowski, K. Watanabe, T. Taniguchi, L. S. Levitov, N. B. Zhitenev, and J. A. Stroscio. Creating and probing electron whispering-gallery modes in graphene. *Science*, 348(6235):672–675, May 2015.

[175] Yuanbo Zhang, Victor W. Brar, Feng Wang, Caglar Girit, Yossi Yayon, Melissa Panlasigui, Alex Zettl, and Michael F. Crommie. Giant phonon-induced conductance in scanning tunnelling spectroscopy of gate-tunable graphene. *Nat Phys*, 4(8):627–630, Jul 2008.

[176] Régis Decker, Yang Wang, Victor W. Brar, William Regan, Hsin-Zon Tsai, Qiong Wu, William Gannett, Alex Zettl, and Michael F. Crommie. Local Electronic Properties of Graphene on a BN Substrate via Scanning Tunneling Microscopy. *Nano Lett.*, 11(6):2291–2295, 2011.

[177] A. Deshpande, W. Bao, F. Miao, C. N. Lau, and B. J. LeRoy. Spatially resolved spectroscopy of monolayer graphene on SiO 2. *Phys. Rev. B*, 79(20), May 2009.

[178] AL Efros and BI Shklovskii. Coulomb gap and low temperature conductivity of disordered systems. *Journal of Physics C: Solid State Physics*, 8(4):L49, 1975.

[179] A. Deshpande, W. Bao, Z. Zhao, C. N. Lau, and B. J. LeRoy. Imaging charge density fluctuations in graphene using Coulomb blockade spectroscopy. *Physical Review B*, 83(15), Apr 2011.

[180] Victor W. Brar, Sebastian Wickenburg, Melissa Panlasigui, Cheol-Hwan Park, Tim O. Wehling, Yuanbo Zhang, Régis Decker, Çağlar Girit, Alexander V. Balatsky, Steven G. Louie, and et al. Observation of Carrier-Density-Dependent Many-Body Effects in Graphene via Tunneling Spectroscopy. *Physical Review Letters*, 104(3), Jan 2010.

[181] V. Geringer, M. Liebmann, T. Echtermeyer, S. Runte, M. Schmidt, R. Rückamp, M. C. Lemme, and M. Morgenstern. Intrinsic and extrinsic corrugation of monolayer graphene deposited on SiO 2. *Physical Review Letters*, 102(7), Feb 2009.